LUND UNIVERSITY

Crack growth and development of fracture zones in plain concrete and similar materials

Petersson, Per-Erik

1981

DIVISION OF BUILDING MATERIALS
LUND INSTITUTE OF TECHNOLOGY

CRACK GROWTH AND DEVELOPMENT OF FRACTURE ZONES IN PLAIN CONCRETE AND SIMILAR MATERIALS

PER-ERIK PETERSSON

REPORT TVBM - 1006
LUND SWEDEN 1981

DIVISION OF BUILDING MATERIALS
LUND INSTITUTE OF TECHNOLOGY

CRACK GROWTH AND DEVELOPMENT OF FRACTURE ZONES IN PLAIN CONCRETE AND SIMILAR MATERIALS

PER-ERIK PETERSSON

REPORT TVBM - 1006
LUND SWEDEN 1981

CODEN: LUTVDG/(TVBM-1006)/1-174/(1981)

CRACK GROWTH AND DEVELOPMENT OF FRACTURE ZONES IN PLAIN CONCRETE AND SIMILAR MATERIALS

PER-ERIK PETERSSON

ISSN - 0348-7911

PREFACE

This work has been carried out at the Division of Building Materials at the Lund Institute of Technology in Sweden. The project was financially supported by grants from the Swedish Board for Technical Development.

All the members of the staff at the Division of Building Materials have, more or less, contributed to the performance of this project and the author wants to express his thanks to them all and especially to

Professor Arne Hillerborg for his encouragement and his experienced and clever guidance in planning and carrying out the project.

Leif Erlandsson for his invaluable help during the development of new testing equipment.

Bo Johansson for his skill and efficiency when carrying out the tests.

Britt Andersson (drawing) and Anni-Britt Nilsson (typing) for their interest and ability in producing a good result.

Lund, October 1981

Per-Erik Petersson

Per-Erik Petersson

CONTENTS

LIST OF SYMBOLS

A	area
a	crack depth and notch depth
b	width
COD	crack opening displacement
d	depth
d_F	depth of the fracture zone
d_ℓ	ligament depth
E	Young's modulus
E_d	dynamic Young's modulus
F	load
F_c	fracture load
f	resonance frequency
f_c	compression strength
f_f	flexural tensile strength
f_t	tensile strength
f_f^{net}	net flexural tensile strength
G	strain energy release rate
G_c	critical strain energy release rate
G_F	fracture energy
J	value of the J-integral
J_c	critical value of the J-integral
K	stress intensity factor
K_c	critical stress intensity factor
K_R	resistance to crack growth
k	stiffness
ℓ	length
ℓ_{ch}	characteristic length ($\ell_{ch}=G_F E/f_t^2$)
ℓ_g	gauge length
M	moment
M	mass
m	mass per unit length
P	force
Q	energy
U	energy
W_o/C	water-cement ratio
w	width of the fictitious crack
w_c	critical value of the width of the fictitious crack

γ	surface energy
δ	deformation or displacement
ε	strain
ε_m	mean strain
ν	Poisson's ratio
σ	stress
σ_c	critical stress
σ_y	yield stress
σ_s	shrinkage stress

SUMMARY

When a notched specimen of a linear elastic material becomes subjected to load, the region in front of the notch tip will be highly stressed. A real material cannot stand these high stresses and a damage zone will develop in front of the notch tip. For concrete and other non-yielding materials, the damage zone is caused by the development of micro-cracks. The material in this micro-cracked material volume, or *fracture zone*, is partly destroyed but is still able to transfer stress. The stress transferring capability normally decreases when the local deformation of the zone increases, i.e. when the number of micro-cracks increases. This thesis deals with the *development of fracture zones* and how the fracture zones affect the *crack propagation* and the *fracture process* for *plain concrete* and similar materials.

In the calculation model presented here, the fracture zone is modelled by a crack that is able to transfer stress and the stress transferring capability depends on the width of the crack in the stressed direction (see Fig 3.6). As the stress transferring crack is not a real crack but a fictitious crack, the model is called the *Fictitious Crack Model*. In the calculations the fictitious crack (i.e. the fracture zone) is assumed to start developing at one point when the first principal stress reaches the tensile strength and the fictitious crack develops perpendicular to the first principal stress. The deformation properties are given by two relations; one relation between the stress and the relative strain, i.e. a σ-ε *curve*, for the material outside the fictitious crack and one relation between the stress and the opening of the fictitious crack, i.e. a σ-w *curve* (see Fig 3.4). These curves are considered as material properties and they are, together with Poisson's ratio, the only parameters necessary to know when carrying out calculations by using the Fictitious Crack Model.

The Fictitious Crack Model cannot normally be treated analytically but numerical methods have to be used. In this thesis calculation methods are presented which are based on the *finite element method*.

A number of calculations have been carried out by using the Fictitious Crack Model and the results seem to be in good agreement with experimental results (cf Tables 6:1 and 6:3, Fig:s 6.33, 6.35, 7.1 and 8.16).

Calculation results are presented which indicate that up to 150 mm long fracture zones develop in front of notches in concrete structures (see

Fig 5.6). These results are in good agreement with test results presented in literature.

The applicability of linear elastic fracture mechanics to concrete and similar materials is analysed by use of the Fictitious Crack Model. It is found that linear elastic fracture mechanics is too dependent on, among other things, specimen dimensions to be useful as a fracture approach, unless the dimensions, for concrete structures, are in order of meters. The usefulness of the J-integral, the Crack Opening Displacement-approach and the R-curve analysis is also found to be very limited where cementitious materials are concerned.

The σ-ε and σ-w curves can be approximately determined if the *tensile strength* (f_t), the *Young's modulus* (E) and the *fracture energy* (G_F) are known (see Fig 4.10). G_F is defined as the amount of energy necessary to create one unit of area of a crack and consequently G_F equals the area under the σ-w curve. G_F can be determined by use of a *stable* three-point bend test on a notched beam and this test method is dealt with in detail. Among other things, the stability conditions for the three-point bend test are given and test results are presented which imply that G_F is suitable for use as a material property for concrete. The direct tensile test is also dealt with and a new type of clamping grips is presented, which can be used for determination of the tensile strength on prismatic concrete specimens (see Fig 7.3)

Test results of f_t, E and G_F are presented for a number of concrete qualities (see Fig:s 7.31-7.35). G_F normally appears to be 70-140 N/m and is especially dependent on the quality of aggregate, water-cement-ratio and age.

The σ-w curve can be directly determined from the *stable* tensile stress-strain curve and in the last Chapter a new type of very stiff testing machine is presented by which it is possible to carry out stable tensile tests on concrete (see Fig 8.5). The complete stress-deformation curves, and thus the σ-w curves, have been determined for a number of concrete qualities (see Fig:s 8.10-8.13). It was found that the shapes of the σ-w curves are similar for the different concrete qualities. A result of this is that no "complicated" stable tensile tests have to be carried out in order to determine σ-w curves for concrete but good approximations of the curves can be determined by use of the "simple" f_t- and G_F-tests. Furthermore, due to the small variations of the shapes of the σ-w curves for concrete, the fracture pro-

perties can be expressed by a single parameter called the *characteristic length* (ℓ_{ch}). ℓ_{ch} is defined as $G_F E/f_t^2$ and the smaller the value of ℓ_{ch} is, the more "brittle" the material is. For most concrete qualities ℓ_{ch} seems to be 200-400 mm.

The description above covers a complete system for analysing crack propagation in concrete as it includes a realistic material model, a functional calculation model and methods for determining the material parameters necessary for the calculations. Therefore this work ought to be of use as a base for further studies of the fracture process of concrete and similar materials.

1 INTRODUCTION

In the field of fracture mechanics stresses and strains around crack tips in loaded structures are analysed. The fracture of non-yielding materials is always caused by crack propagation and therefore it was logical when Kaplan (1961) started to study the fracture process of concrete by means of fracture mechanics. Since then numereous reports have been published about crack stability, crack propagation, fracture mechanical test methods and so on for concrete and similar materials. Almost all of these publications have one thing in common; concrete is treated as a linear elastic material and the well-known K- and G-approaches, more or less modified, are used. A few researches have used other methods such as the J-integral approach and R-curve analysis.

The results of all these efforts are discouraging; in fact, to date there exist no working fracture mechanical calculation models for concrete, no well defined fracture mechanical material parameters, no well established test methods and so on. This has given rise to some doubt regarding the usefulness of fracture mechanics when applied to concrete. However, the fracture of concrete is caused by cracks and consequently it is necessary to use fracture mechanics when describing the fracture process of concrete but one has to be aware of the fact that fracture mechanics is not the same as linear elastic fracture mechanics. As linear elastic fracture mechanics seems unsuitable for concrete it is consequently necessary to develop approaches that take material properties other than the linear elastic ones into consideration, especially the properties of the highly strained region in front of the crack tip. Such an approach is presented in this thesis.

The work presented in this report is a part of a research program aimed at developing a fracture mechanical model suitable for analysing the micro- and macro-fracture of plain and reinforced concrete and similar materials. In connection with this research program a number of papers have been published, for example Hillerborg, Modéer and Petersson (1976), Modéer (1979), Petersson (1980a, 1980b, 1980c), Petersson and Gustafsson (1980), Hillerborg (1980), Hillerborg and Petersson (1981).

This report deals with the macro-fracture of plain concrete and similar materials. The physical properties of the fracture zone in front of a crack tip in a stressed material are discussed and a calculation model is presented by which the crack growth and the development of local fracture zones can be analysed. The calculation model can however be used for quantitative estimations only if a number of essential material parameters are known. For this reason

the work, to a large extent, is concentrated on the development of suitable methods for determining the fracture mechanical properties of cementitious materials and such properties are also presented for a number of qualities of plain concrete.

This project has, as all other projects, a number of limitations of which some are listed and discussed below.

a) Concrete is a composite material where the components are cement paste, aggregate particles and pores but in the calculations concrete and other cementitious materials are assumed to be homogeneous and isotropic. This ought to be a fair assumption when the dimensions of the structure exceed the dimensions of the largest irregularities in the material by a few times.

b) In the calculations only the development of a single crack (opening mode) is analysed but in principle the model can also be used when two or more cracks develop simultaneously.

c) For a yielding material plastic deformations take place close to the crack tip and so called shear lips develop. Due to these plastic deformations the fracture mechanical properties of yielding materials are strongly affected by the state of stress; plane stress or plane strain. For non-yielding materials the irreversible deformations are due to the formation of micro-cracks and therefore no plastic deformations take place and the difference between plane stress and plane strain is small. In the calculations presented in this report plane stress is used and Poisson's ratio (ν) is assumed to be 0.2.

d) Most of the calculations and tests are relevant for wet specimens, i.e. the effect of shrinkage stresses is not dealt with, although this can be done with the model, see 4.2.

2 FRACTURE MECHANICS

2.1 Introduction

The reference list in this Chapter is incomplete. However, most of the definitions and expressions are well known in the field of fracture mechanics and can be found, for example, in Knott (1973) and Carlsson (1976).

Fig 2.1 illustrates an infinitely large plate of linear elastic material and the plate is subjected to a uniform tensile stress σ_0. The stress distribution will be disturbed if there is a circular hole in the plate. At the most critical point of the boundary of the hole, the stress will, independently of the size of the hole, reach three times the applied stress. This means that holes or other irregularities will considerably reduce the strength of a material.

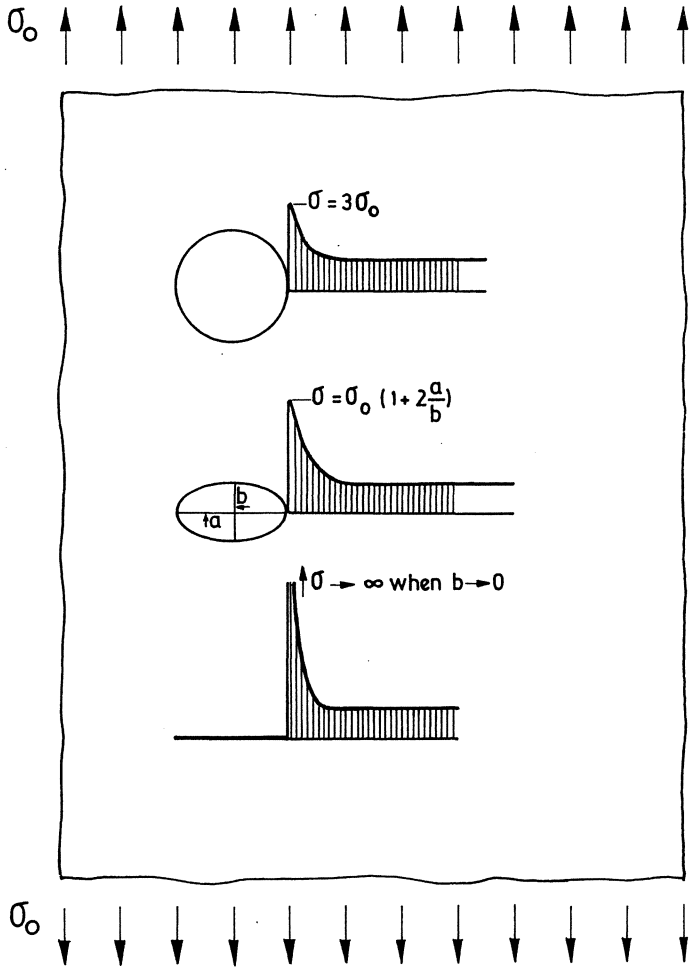

Fig 2.1 The stress distributions close to a circular hole, an elliptical hole and a crack in an infinitely large plate subjected to the uniform stress σ_0.

If the circular hole is replaced by an elliptical hole, the stress at the tip of the elliptical hole becomes 1 + 2a/b times the applied stress, where a and b are the major and minor axes of the ellipse respectively. If the minor axis is much smaller than the major axis, i.e. $b \ll a$, then the elliptical hole is a crack and the stress at the crack tip grows unlimitedly as the ratio a/b approaches infinity. This means that ordinary stress criterions cannot be used in this case as the material would then fail as soon as it became subjected to load.

A material always contains irregularities. However, a real material is never perfectly linear elastic, at least not at high stresses, and crack tips are never infinitely sharp and these are the reasons why materials can exist at all.

2.2 Linear elastic fracture mechanics

2.2.1 Energy criterion

Even if materials never behave perfectly linear elastic it is sometimes possible to approximate the material behaviour with a linear elastic model. As stress criterions cannot be used, one has to use so called fracture mechanics approaches. The first approach of this type was proposed by Griffith (1921).

Fig 2.2 shows an infinitely large plate subjected to a uniform tensile stress σ_0. The plate contains a 2a long crack, which is oriented perpendicular to the applied stress. By equating the elastic strain energy that is released when the crack advances a small distance Δa at each crack tip and the energy necessary to create the new crack surfaces, Griffith found an expression for the critical stress (σ_c) at which the crack propagates:

$$\sigma_c = \sqrt{\frac{2\gamma E}{\pi a}}\,\alpha \qquad (2:1)$$

where E is the Young's modulus and γ is the surface energy per unit area. α is 1 for plane stress and $\sqrt{1/(1-\nu^2)}$ for plane strain, where ν is Poisson's ratio. For concrete ν is normally less than 0.2, which means that $1 < \alpha < 1.02$. The discrepancy between plane stress and plane strain is so small for concrete that it can be neglected and below all the relations are relevant for plane stress, i.e. $\alpha=1$.

By introducing the critical strain energy release rate (G_c), (2:1) can be extended to be relevant also for materials where small, irreversible deformations take place close to the crack tip. G_c includes not only 2γ but also the

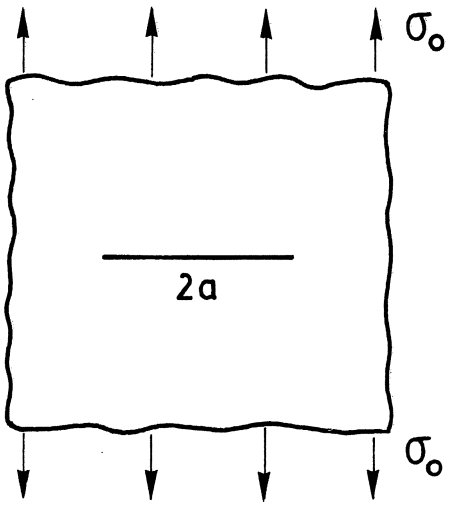

Fig 2.2 An infinitely large plate with a 2a long crack oriented perpendicular to the applied stress σ_o.

energy consumption due to plastic deformations close to the crack tip and (2:1) becomes:

$$\sigma_c = \sqrt{\frac{G_c E}{\pi a}} \qquad (2:2)$$

Normally (2:2) is seen as:

$$G = G_c \qquad (2:3)$$

and G, the strain energy release rate is defined as:

$$G = \frac{\sigma_o^2 \pi a}{E} \times g \qquad (2:4)$$

where g is a correction factor dependent on the specimen geometry and the loading case. g equals unity for the infinitely large plate in Fig 2.2.

2.2.2 Stress intensity criterion

The stress distribution in front of a crack tip, perpendicular to the crack and on a line parallel with the crack, see Fig 2.3, can be expressed as:

$$\sigma = \frac{K}{\sqrt{2\pi x}} + \ldots\ldots\ldots \qquad (2:5)$$

where x is the distance from the crack tip and K is the stress intensity factor. The points represent terms that are small compared with the main term for

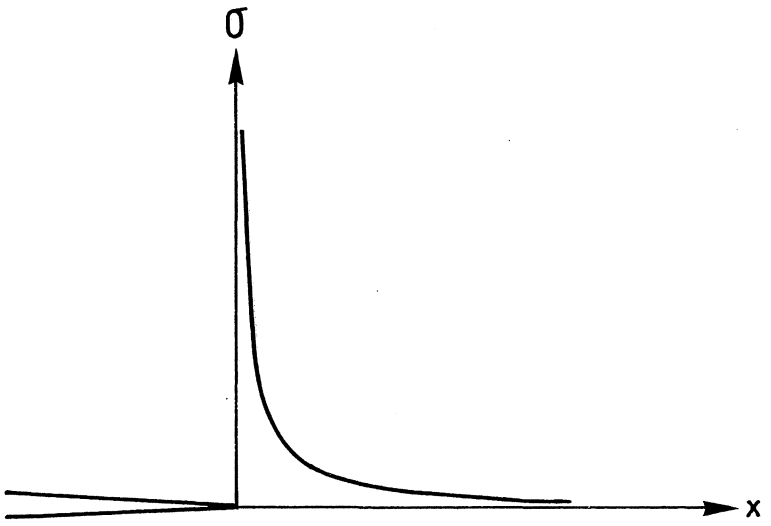

Fig 2.3 The stress distribution in front of a crack tip in a linear elastic material.

small values of x and therefore the main term itself describes the stress distribution close to the crack tip.

As seen in (2:5), the stress distribution is unaffected by the geometry of the specimen and the intensity of the stress is only dependent on K. For this reason a stress intensity criterion for initiation of crack growth can be used:

$$K = K_c \qquad (2:6)$$

where K_c is the critical stress intensity factor. For the infinitely large plate according to Fig 2.2, $K=\sigma_o\sqrt{a\pi}$ and thus:

$$\sigma_c = K_c/\sqrt{a\pi} \qquad (2:7)$$

By comparing (2:7) with (2:2) it becomes obvious that a connection between K_c and G_c (or K and G) for the infinitely large plate exists:

$$K_c = \sqrt{G_c E} \qquad (2:8)$$

(2:8) can also be shown to be relevant for other geometries and load cases.

Normally K_c is expressed as:

$$K_c = \sigma_c\sqrt{a} \times f \qquad (2:9)$$

where f is a correction factor dependent on geometry and type of loading. $f = \sqrt{\pi}$ for the infinitely large plate in Fig 2.2.

2.2.3 Cohesive zones

In linear elastic fracture mechanics one neglects the fact that the stress at the crack tip theoretically approaches infinity, while the stress in reality can never exceed the cohesive strength of the material. Barenblatt (1962) found that a small cohesive zone must exist in a region close to the crack tip, i.e. a zone where closing stresses act between the crack surfaces. Barenblatt assumed the zone to be very small (the length of the zone << length of the crack) and therefore the linear elastic approaches previously discussed can be used for calculation purposes but the existence of cohesive zones explain why linear elastic fracture mechanics can be used at all

2.3 Elastic plastic fracture mechanics

2.3.1 Introduction

A perfectly linear elastic material follows a straight-lined stress-strain curve (σ-ε curve) all the way to fracture. A more realistic σ-ε curve for a real material is shown in Fig 2.4.

The material in front of a propagating crack will be highly strained and all the points of the σ-ε curve will be represented. Three different zones can be separated around the crack tip, see Fig 2.5.

1. The linear elastic zone: Far from the crack tip the stress is so low that the material still behaves in a linear elastic way.
2. The plastic zone: In this zone the stress-strain relation is non-linear and the stress increases or at least remains constant as the strain increases
3. The fracture zone (or process zone): In this zone the stress decreases as the strain increases.

If the plastic zone and the fracture zone are small compared with the specimen dimensions and the crack depth, then linear elastic fracture mechanics can be used but otherwise other methods have to be used. For yielding materials, for example most metals, a large plastic zone develops and one has to use elastic-plastic fracture mechanics approaches. In these approaches the extent of the fracture zone is normally reduced to a point, which is probab-

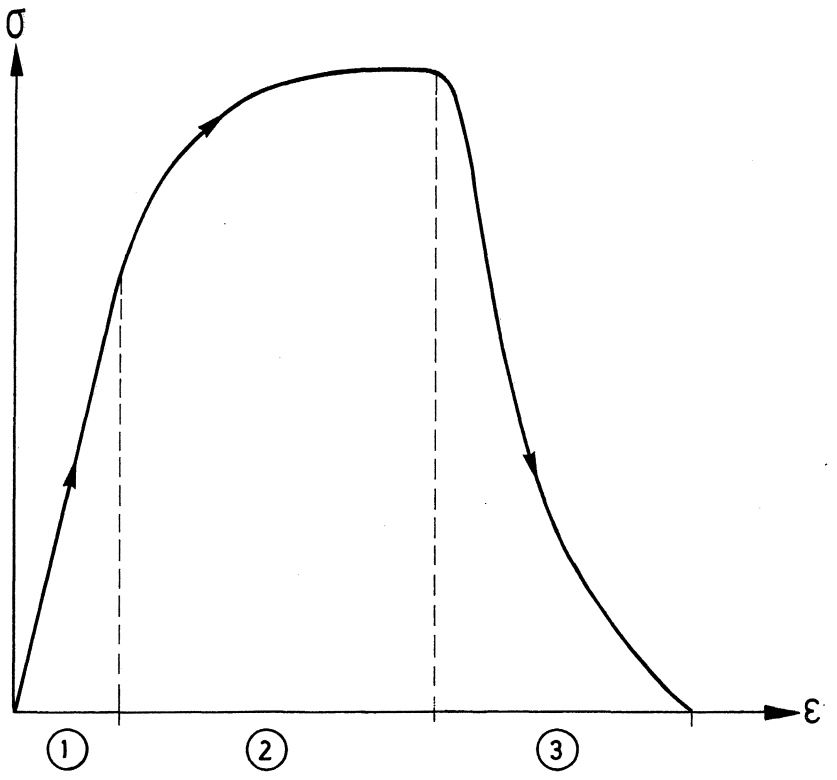

Fig 2.4 A schematic illustration of a σ-ε curve. Three parts of the curve can be separated; (1)=linear elastic deformations, (2)=plastic deformations and increasing stress, (3)=plastic deformations and decreasing stress.

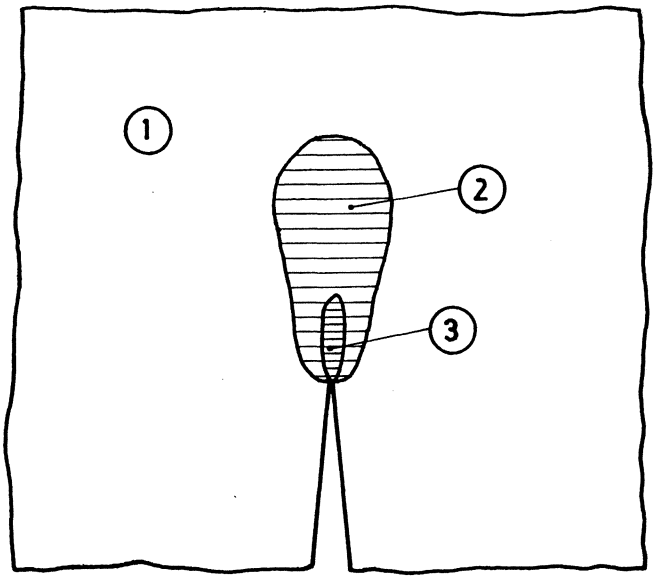

Fig 2.5 In front of a crack in a stressed material there is a plastic zone (2) and a fracture zone (3). Far from the crack tip the material behaves in a linear elastic way (1).

ly a fair approximation for most yielding materials. For non-yielding materials, however, the influence of the fracture zone is much more important, while the plastic deformations are small. This thesis in fact deals with how the fracture zone affects the fracture process of concrete and similar materials.

2.3.2 The Dugdale model

For an elastic-ideal plastic material the stress can never exceed the yield stress (σ_y). In the model according to Dugdale (1960) it is assumed that a narrow yield zone develops in front of the crack tip along the line of the crack, see Fig 2.6. The stresses in the yield zone never exceed the yield stress and consequently loadcase a) in Fig 2.6 equals the sum of the loadcases b) and c).

The stress at the tip of the yield zone will approach infinity unless the sum of the stress intensity factors for the loadcases b) and c) is zero and this condition gives the extension of the fracture zone as a function of the applied stress. The Dugdale model is, for example, suitable for describing the development of fracture zones in thin sheets of yielding materials.

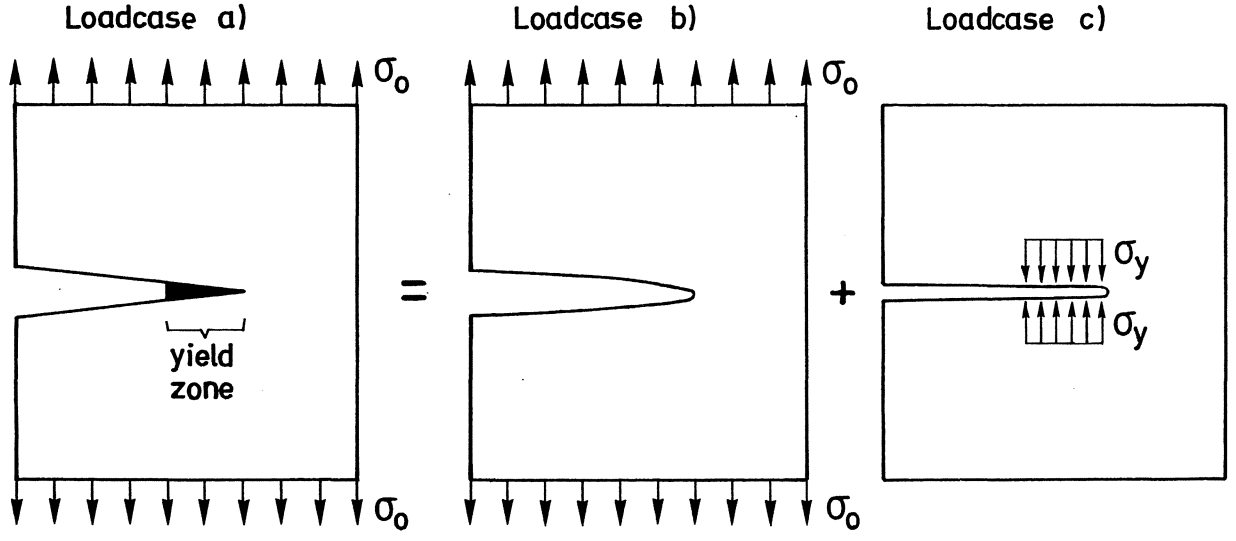

Fig 2.6 The loadcase a) according to Dugdale is identical with the sum of the loadcases b) and c).

2.3.3 The J-integral

A fracture approach similar to the G_c-approach can of course also be used for non-linear elastic materials. For this reason a parameter called the J-integral has been proposed (Rice, 1968). This method is based on the change in potential energy when a crack extends:

$$J = -\frac{1}{b}\frac{\partial U}{\partial a} \qquad (2:10)$$

where b is the the specimen width, U is the potential energy and a is the crack length. When using the J-integral the criterion for crack propagation is:

$$J = J_c \qquad (2:11)$$

where J_c is a material property for elastic materials.

The J-integral is only strictly relevant for elastic materials where the loading and unloading take place along the same curve. Normally this is unrealistic for real materials and this considerably restricts the applicability of the J-integral. However, as long as no unloading takes place in any point of the specimen, the material itself "does not know" whether it is elastic or not and then the J-integral can also be used for materials where irreversible deformations take place. In all real materials a fracture zone develops in front of the crack tip before the crack starts to propagate. In the fracture zone, and in the material volume close to this zone, unloading takes place and consequently the fracture zone must be small compared with the specimen dimensions and the crack length if the J-integral is to be useful as a fracture mechanical approach.

2.3.4 The Crack Opening Displacement (COD)

COD represents the widening of the crack tip when a cracked specimen is subjected to load, see Fig 2.7. It has been suggested that there exists a critical value, COD_c, of the crack opening displacement that, at least for some materials, can be used as a criterion for the initiation of crack growth.

2.3.5 R-curve analysis

Sometimes it is possible to observe stable crack growth even if K increases. The only explanation for this is that K_c increases as the crack propagates. This is observed especially for metals in the intermediate range, i.e. in the range, where neither plane stress nor plane strain is dominating and the

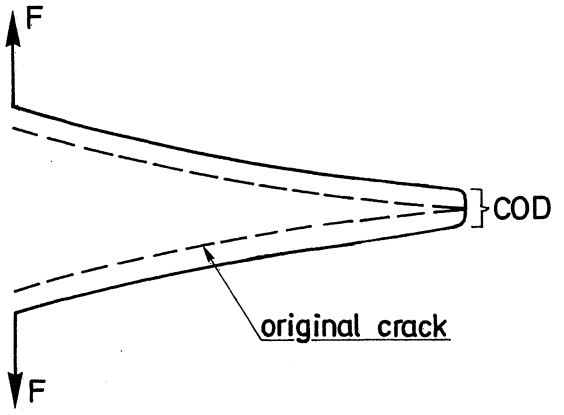

Fig 2.7 The Crack Opening Displacement (COD) representing the widening of the crack tip.

explanation is that the plastic deformations (width of the shear lips) in front of the crack tip increase as the crack advances.

The resistance to crack growth (K_R) has been introduced as a material parameter in order to describe the variation of the critical strain energy release rate when the crack advances. K_R is defined in the same way as K_c but instead of the original crack length one uses the actual crack length, i.e. the original crack length (a) + the crack advance (Δa).

Some test results indicate that plots of K_R against the crack advance, (i.e. R-curves), are, for a specific specimen width, independent of the specimen geometry and method of loading and therefore might be used as a material property. An example of such a plot is shown in Fig 2.8.

When using the R-curves for predicting crack growth the curves are put into a diagram where the axes represent the resistance to crack growth (K_R) and the actual crack length ($a + \Delta a$) respectively, see Fig 2.9. R-curves starting at different original crack lengths (a_1 and a_2 in the Figure) are identical as they are supposed to be independent of the specimen geometry (except for the width). The R-curves are compared with curves representing the stress intensity factor (K) as a function of the actual crack length. In the Figure the K-curve representing the load F_1 touches the R-curve for the original crack length a_1 at a point where the K-curve increases more than the R-curve and thus the crack propagation will be unstable. For the load F_2 the crack propagation will be stable if the original crack length is a_1 but unstable if the original crack length is a_2.

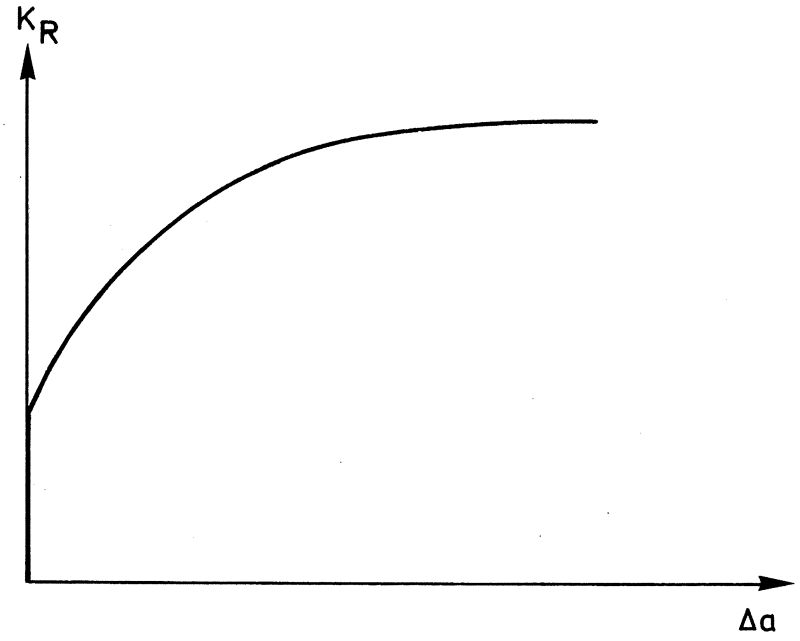

Fig 2.8 An example of a crack growth resistance curve (R-curve).

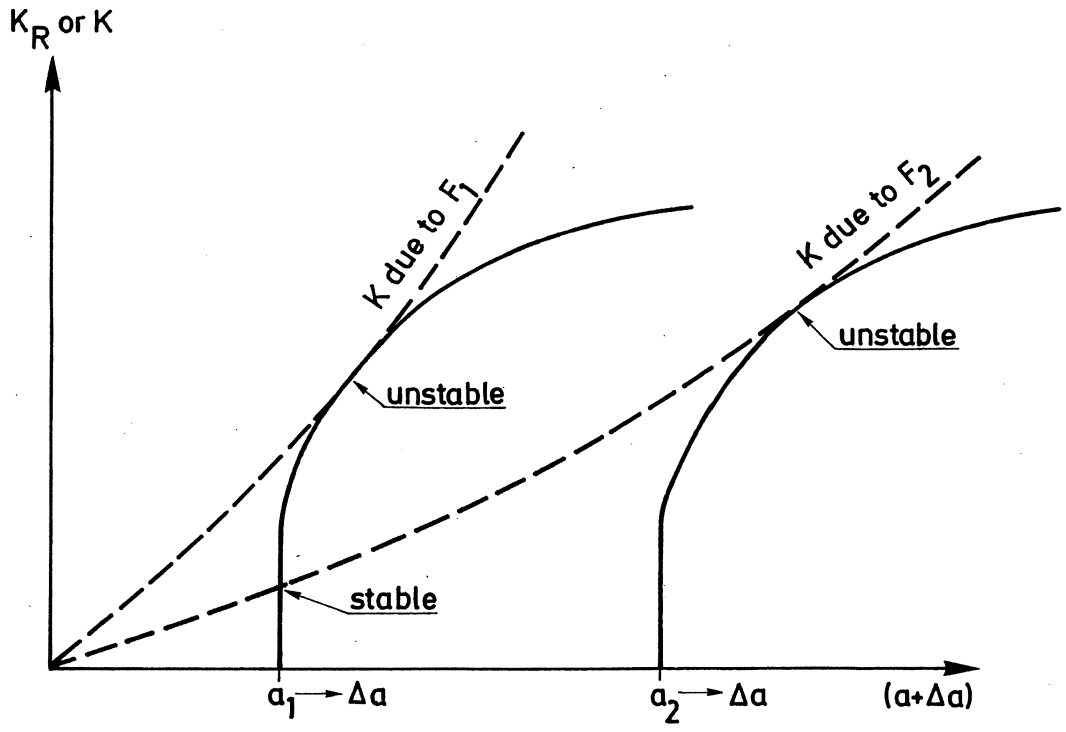

Fig 2.9 The principles of predicting crack propagation by use of R-curves.

K_R-curves can be used only if linear elastic fracture mechanics is applicable for each value of the crack advance but the R-curve analysis of course can also be relevant for J_R-curves, COD_R-curves and so on.

2.4 Fracture mechanical models considering the influence of the fracture zone

The crack model presented in Fig 2.10a was used by Andersson and Bergqvist (1970). A layer of thickness d was inserted between two semi-infinite, linearly elastic media and by interrupting the layer a crack could be modelled. The layer was given a stress-deformation relation according to Fig 2.10b. The slope of the ascending part of the stress-deformation curve was chosen so that it was in agreement with the stress-strain curve for the semi-infinite media. For different assumptions of the slope of the descending part of the curve in Fig 2.10b, the stress-distribution in front of the crack tip could be calculated by use of numerical methods. However, the results are primarily of theoretical interest due to poor knowledge about the material properties necessary to determine the stress-deformation curve in Fig 2.10b.

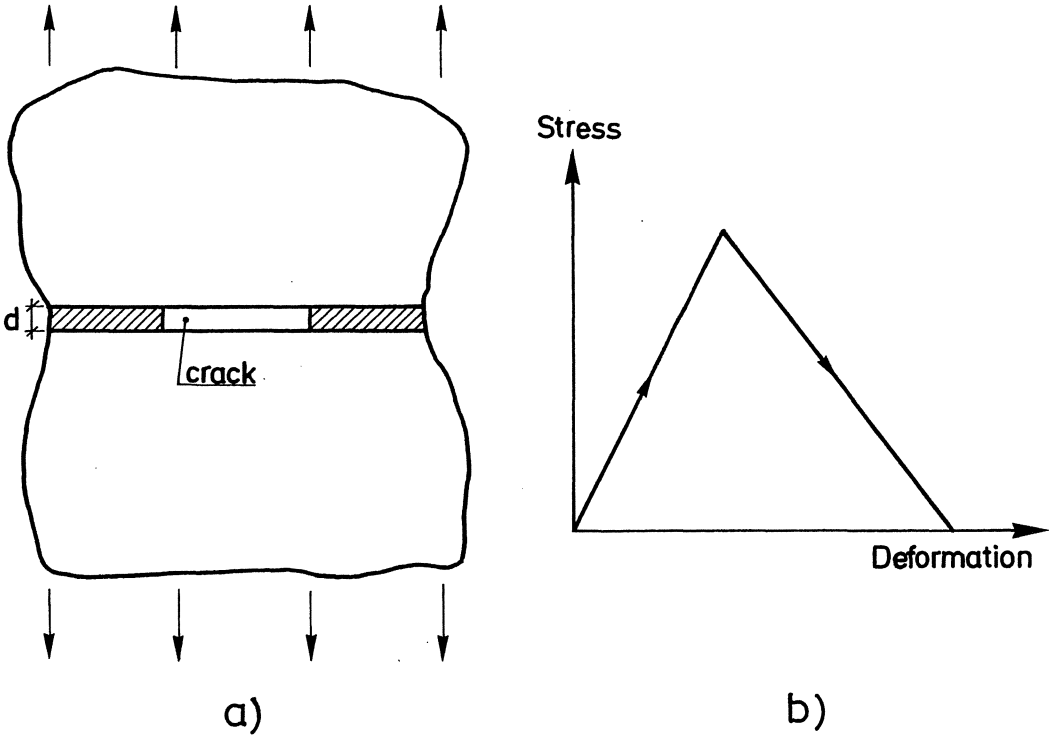

Fig 2.10 a) The crack model according to Andersson and Bergqvist (1970).
b) Stress-deformation relation for the thin layer in Fig 2.10a.

In damage mechanics (Kachanov, 1958) the strength of a loaded structure is determined by the deterioration of the material caused by the loading. The value of the deterioration is characterized by a parameter ω, which is a measure of the decrease in the load carrying internal area of the material. The net stress in the undamaged material (s) then equals $\sigma/(1-\omega)$ where σ is the conventional stress applied to the material.

Janson and Hult (1977) combined damage mechanics and the Dugdale model. In the Dugdale model the stress is constant along the plastic zone in front of the crack tip. Janson and Hult replaced the constant stress by a constant net stress (s) and let ω be dependent on the distance from the crack tip, which resulted in a varying stress along the yield zone. The same principles as used for the Dugdale solution could then be used for calculating the length of the yield zone as a function of the applied stress for different assumptions of the distribution of ω. All the calculations were carried out on an infinite plate containing a slit. In another paper (Janson, 1978) calculations were presented, where ω increases linearly with the widening, in the stressed direction, of the fracture zone. The calculation results are in good agreement with the solution according to Dugdale for small values of the crack length and in good agreement with the solution according to linear elastic fracture mechanics for large values of the crack length. However, in an intermediate range the varying stress along the yield zone, or fracture zone, affects the calculation results considerably.

Naus and Lott (1968) used a crack model similar to that in Fig 2.10 in order to estimate the length of the fracture zone in front of a crack tip in cement paste. However, they did not relate the stress in the thin layer to the deformation of the layer but assumed a certain stress distribution along the fracture zone.

By use of damage mechanics and the finite element method Mazars (1981) studied the development of fracture zones in plain and reinforced concrete specimens. The method is not a pure fracture mechanical method and so far only initially unnotched specimens have been analysed.

3 THE FICTITIOUS CRACK MODEL

3.1 The tensile fracture of concrete

By using a very stiff tensile testing machine and small specimens it is possible to determine the complete tensile stress-strain curve of concrete, see for example Hughes and Chapman (1966), Evans and Marathe (1968) and Chapter 8 below. An example of such a curve is shown in Fig 3.1.

At first the material behaves almost linear elastic but when the stress increases, the curve becomes non-linear due to micro-cracks, which are distributed over the entire specimen. When the maximum stress is reached, one cross section is unable to carry more load and it is fair to assume that the development of micro-cracks will be concentrated on a small material volume close to this cross section when the specimen becomes more deformed. This means that, after the maximum load is reached, additional deformations will take place in the micro-cracked material volume, or fracture zone, while the material outside the fracture zone will be elastically unloaded. The load decreases when the first fracture zone develops and consequently only a single zone develops.

Some very interesting results regarding local deformations at direct tensile

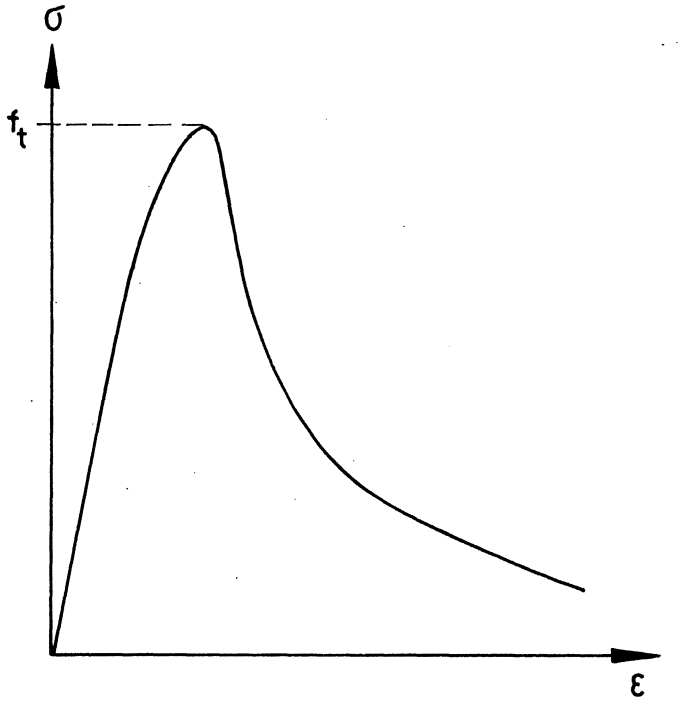

Fig. 3.1 An example of the complete tensile stress-strain curve (σ-ε curve) for concrete.

tests were presented by Heilmann, Hilsdorf and Finsterwalder (1969). Results from one of their tests are presented in Fig 3.2. Strain gauges were glued at different positions on a 600 mm long concrete specimen with a cross sectional area of 80 x 150 mm^2, see Fig 3.2a. The load was excentrically applied, which made it possible to achieve a stable fracture. In the Figure the position of the final crack is shown.

In Fig 3.2b the local strains are shown as a function of the mean strain of the specimen. The local strains are separated into two groups; one group representing the cross section where the final crack develops (gauges 2-3) and one group representing the material outside the position of the final crack (gauges 1, 4-9). As can be seen in the Figure, the strain represented by the gauges crossing the final crack increases rapidly from the moment when the maximum stress is reached. At the same time the strain outside the fracture zone decreases. This clearly shows that a local fracture zone starts developing when the tensile stress is reached. In this case the fracture zone in fact starts developing already before the maximum stress is reached, but this is explained by the excentricity of the load, which means that the fracture zone propagates from one side of the specimen, through the material, to the other side. However, the development of the fracture zone mainly takes place after the maximum stress is reached.

In Fig 3.2c the local strains for the individual gauges are shown for different stress levels. The strains increase very rapidly for the two gauges over the fracture zone while the strains over the other gauges remain fairly low. This implies that the fracture zone is located to a narrow band across the specimen.

As the width of the fracture zone in the stressed direction seems to be small it ought to be possible to describe the tensile test by a simple model according to Fig 3.3.

In the model the fracture zone is replaced by a slit that is able to transfer stress and the stress transferring capability depends on the width (w) of the slit. The width of the slit is zero when it starts opening and consequently the length of the specimen outside the slit (or fracture zone) equals the original specimen length (ℓ)+strain deformations. The total deformation ($\Delta\ell$) of the specimen then becomes:

$$\Delta\ell = \varepsilon_0 \ell + w \qquad (3:1)$$

where ε_0 is the strain in the material outside the fracture zone.

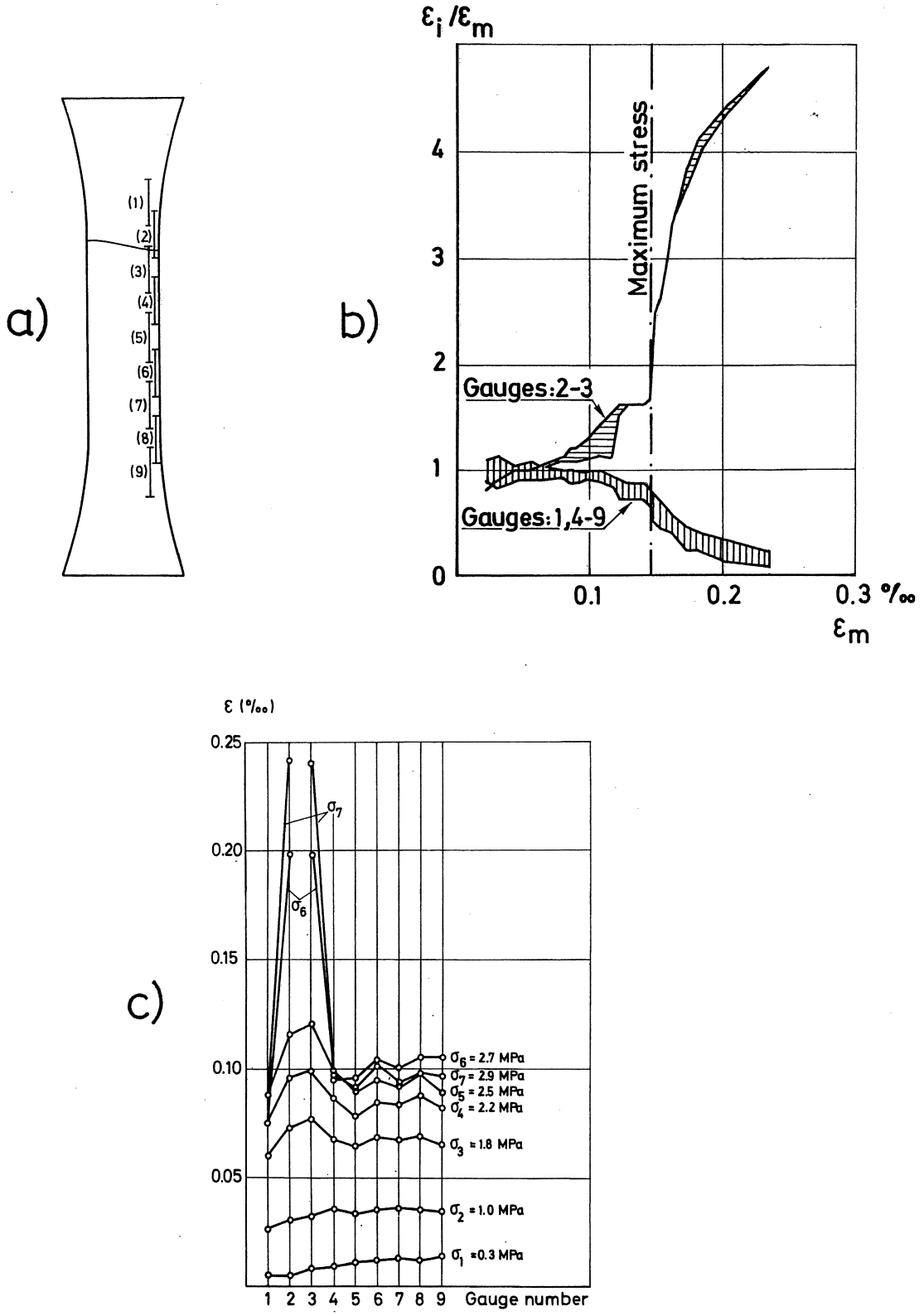

Fig. 3.2 a) The position of the 9 strain gauges.

b) Strains for the gauges crossing the fracture zone (2-3) and for those outside the zone (1, 4-9). ε_i=strain for gauge No i, ε_m= =mean strain for the specimen.

c) Strains for the individual gauges for different stresses. (Heilmann, Hilsdorf and Finsterwalder, 1969)

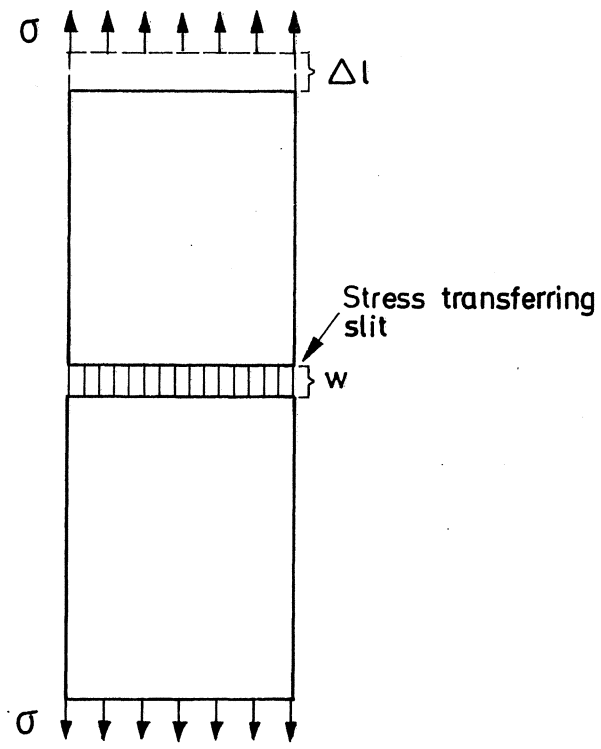

Fig. 3.3 A simple model of the direct tensile test. The fracture zone is replaced by a slit that is able to transfer stress. The stress transferring capability depends on the width (w) of the slit.

From (3:1) it is obvious that the mean strain (ε_m) of the specimen in Fig 3.3 is:

$$\varepsilon_m = \varepsilon_o + w/\ell \qquad (3:2)$$

w is zero before the tensile strength is reached and consequently the mean strain is independent of the specimen length for the increasing part of the stress-strain curve. However, after the maximum stress is reached, the deformation of the fracture zone affects the mean strain and consequently the stress-strain curve of concrete, and of other non-yielding materials, is dependent on the specimen length. This means that it is unsuitable to use the stress-strain curve as a material property. A better way of describing the deformation properties of a material therefore is to use two relations; one relation between the stress and the relative strain for the material outside the fracture zone (Fig 3.4a) and one relation between the stress and the absolute deformation of the fracture zone (Fig 3.4b)

The fracture zone of a non-yielding material can be compared with the necking of a yielding material. However, there is one fundamental difference. The necking is caused by shear deformations and therefore the properties of the

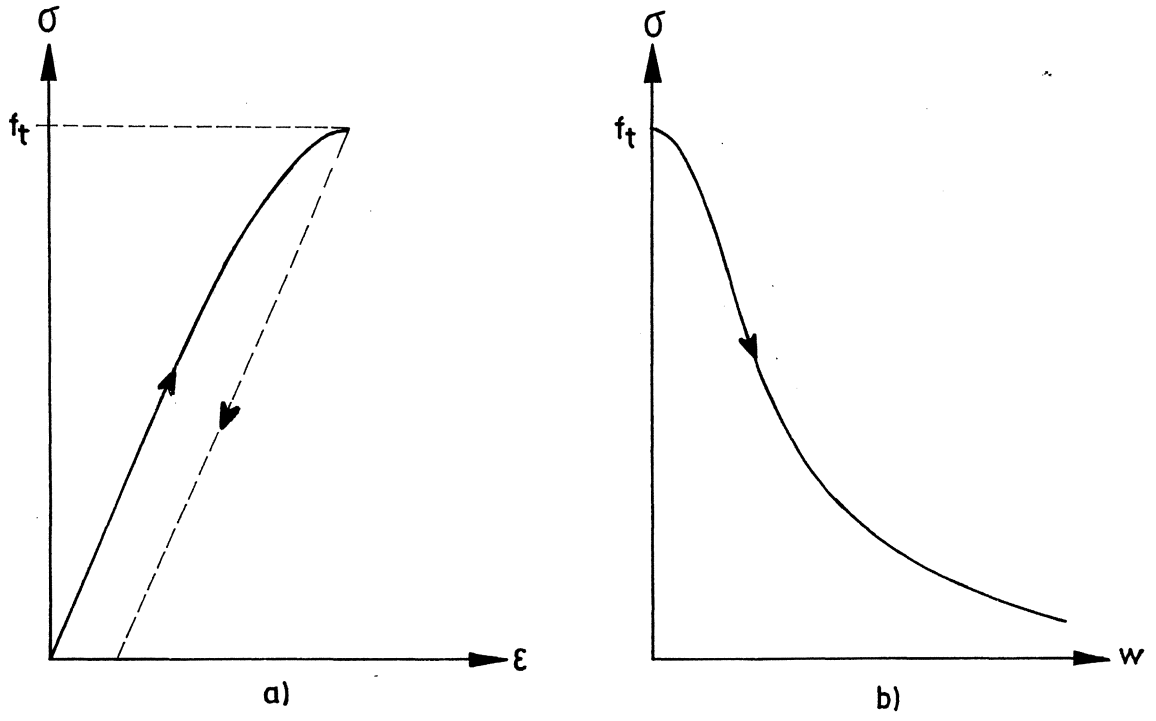

Fig. 3.4 a) The deformation properties of the material outside the fracture zone are given by a relation between the stress and the relative strain, i.e. a σ-ε curve.

b) The deformation properties of the fracture zone are given by a relation between the stress and the absolute widening of the zone in the stressed direction, i.e. a σ-w curve.

necking zone are strongly affected by the state of stress, plane stress or plane strain, which means that the properties of the necking zone depend on the specimen thickness. The fracture zone of a non-yielding material is caused by the development of micro-cracks and no shear deformations take place. This means that the difference between plane stress and plane strain is small for concrete and therefore the σ-ε and σ-w curves ought to be independent of the specimen thickness and, consequently, the curves in Fig 3.4 can be considered as material properties.

3.2 The Fictitious Crack Model and its applicability

When a notched specimen of a linear elastic material is subjected to load, the stress in front of the notch will, at least theoretically, approach infinity. This of course is impossible for a real material. In the case of concrete, or other non-yielding materials, a zone of micro-cracks will develop in front of the notch and this fracture zone considerably reduces the stress

concentration and this results in a much more realistic description of the stress distribution than the linear elastic solution, see Fig 3.5.

The fracture zone in front of a notch normally develops in a tensile stress field and consequently the properties of this zone are similar to those of the fracture zone in a direct tensile test. This means that it ought to be possible to approximate the fracture zone in front of a notch with a slit, or crack, that is able to transfer stress, see Fig 3.6. The stress transferring capability depends on the width of the slit in the stressed direction. In the Figure the load is represented by a point load but of course this description is relevant for all types of loads, including volume stresses due to shrinkage - or temperature gradients.

The stress transferring crack is not a real crack but can be considered as a fictitious crack and therefore the model described above is called the Fictitious Crack Model. When using the Fictitious Crack Model the following assumptions are made:

* The fracture zone starts developing at one point when the first principal stress reaches the tensile strength. Of course other more complicated fracture criteria can be used but often the simple tensile strength criteria is sufficient.

* The fracture zone develops perpendicular to the first principal stress.

* The material in the fracture zone is partly destroyed but is still able to transfer stress. The stress transferring capability depends on the local deformation of the fracture zone in the direction of the first principal stress. In the calculations the fracture zone is normally replaced by a stress transferring crack and the stress transferring capability depends on the width of the crack in the stressed direction according to a σ-w curve, see Fig 3.4b.

* The width of the fracture zone in the stressed direction is assumed to equal the widening of the zone, i.e. the width of the zone is zero when it starts developing. For non-yielding materials this should be a fair assumption.

* The properties of the material outside the fracture zone are given in a σ-ε curve, see Fig 3.4a.

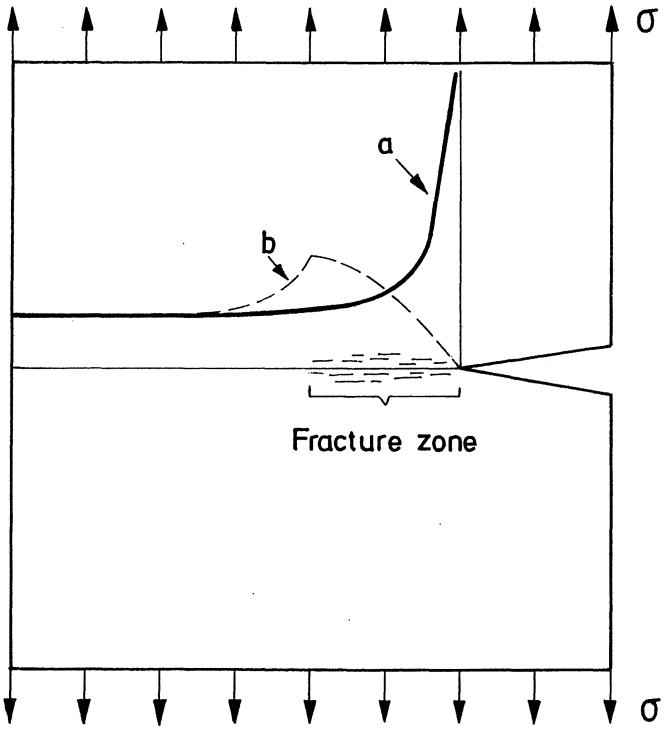

Fig 3.5 Probable stress distribution in front of a notch for a linear elastic material (a) and for a non-yielding material with a micro-cracked zone in front of the notch tip (b).

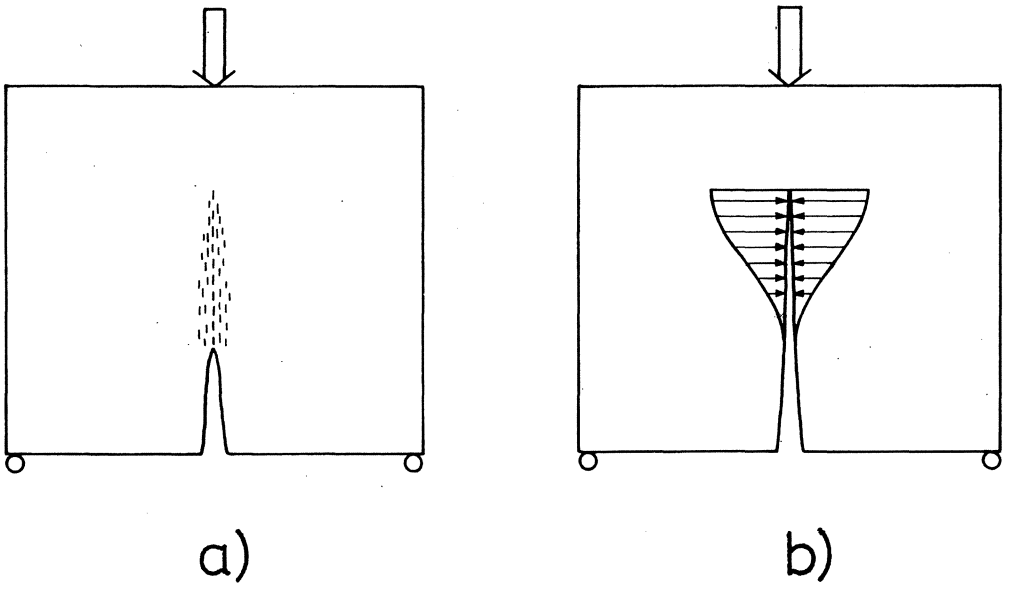

Fig 3.6 When using the Fictitious Crack Model, the fracture zone in front of a crack tip (a) is replaced by a crack that is able to transfer stress (b). The stress transferring capability depends on the width of the crack according to a σ-w curve.

The fracture zone starts developing in one point when the first principal stress reaches the tensile strength even if the high stress is due to other reasons than a stress concentration in front of a notch tip. This means that the Fictitious Crack Model is not a pure fracture mechanics model but initially unnotched structures can also be analysed. This is one thing that makes the Fictitious Crack Model differ from most other approaches. Another advantage is that, by using the Fictitious Crack Model, it is possible to study the development of the fracture zone, the initiation of crack growth and the propagation of the crack through the material. When other models are used, normally only the initiation of crack growth is analysed.

The description of the Fictitious Crack Model above is relevant for a homogeneous material, i.e. a material that has the same properties in all points. In reality no materials are perfectly homogeneous, at least not in the atomic scale. However, if the analysed structure is a few times greater than the largest irregularities in the material, then the material in the structure can be assumed to be approximatively homogeneous and the σ-w curve is then a function of the fractions and the properties of the components of the material.

In this thesis the materials are always assumed to be homogeneous but the Fictitious Crack Model can be used for analysing heterogeneous materials as well. For example, the Barenblatt model is identical to the Fictitious Crack Model when applied on the atomic scale, where, as mentioned above, materials can never be considered as homogeneous. When studying materials that are heterogeneous on the macroscale, for example reinforced concrete, it is necessary to know the material properties, including the σ-w curves, for the different components of the material as well as the properties of the contact zones between the components. Some results from such calculations are presented by Modéer (1979) and Petersson and Gustafsson (1980).

4 THE FINITE ELEMENT METHOD APPLIED TO THE FICTITIOUS CRACK MODEL

4.1 Introduction

The Dugdale model is a special example of the Fictitious Crack Model which can be treated analytically. However, the Fictitious Crack Model normally has to be treated by using numerical methods and the Finite Element Method (FEM) then seems to be the most suitable method. When using FEM the closing stresses acting across the fracture zone (Fig 4.1a) are replaced by nodal forces (Fig 4.1b). The intensity of these forces of course depends on the width of the "fictitious" crack according to the σ-w curve of the material. When the tensile strength, or another fracture criterion, is reached in the top node, see Fig 4.1b, this node is "opened" and forces start acting across the crack at this point. In this way it is possible to follow the crack growth through the material.

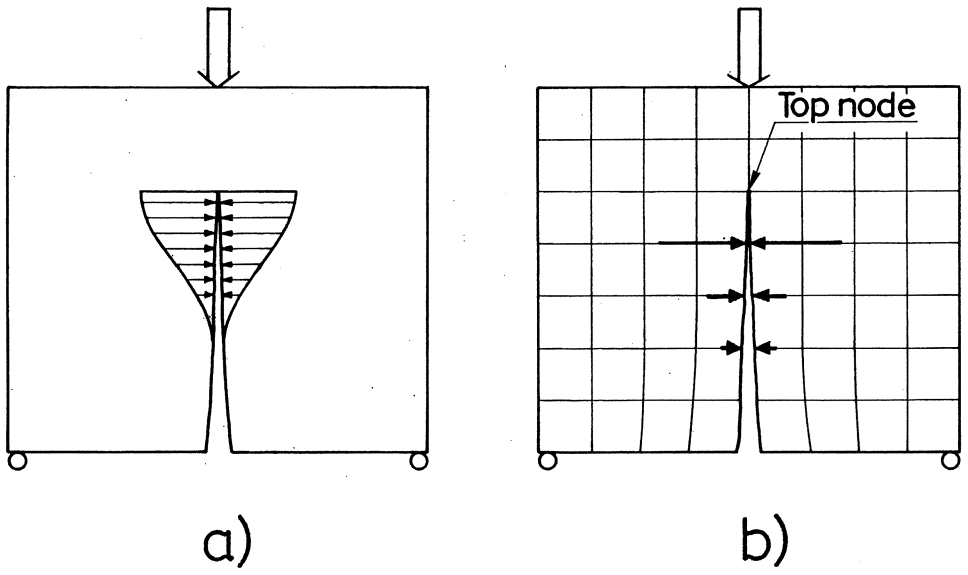

Fig 4.1 When using FEM, the stresses acting across the "fictitious" crack (a) are replaced by nodal forces (b).

4.2 Calculation method I: substucture

In Fig 4.2 a schematic illustration of a deeply cracked structure that is subjected to load is shown. This type of structure is used as a base in this calculation method and at the calculations the fracture zone can develop only along the crack, see below. The dots on the boundaries of the crack represent finite element nodes. The position of the two nodes in each node pair (a node

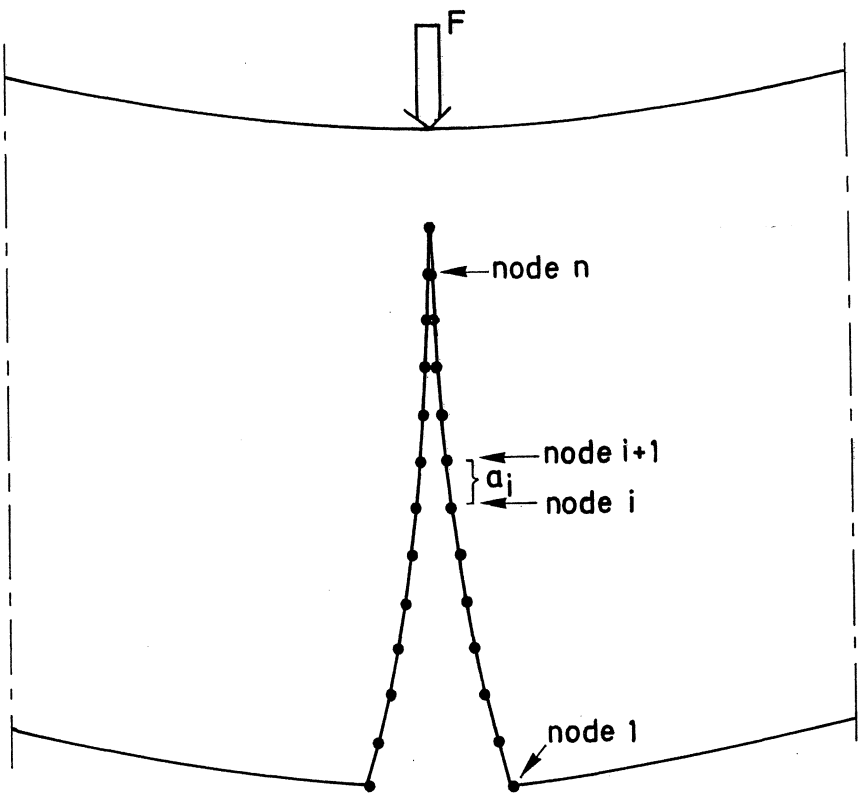

Fig 4.2 A schematic illustration of the finite element nodes along the crack boundaries in a deeply cracked specimen.

pair is the two nodes on the opposite crack surfaces at the same distance from the crack tip) will coincide when the structure is unloaded. The node pairs are numbered from 1 at the base of the crack to n+1 at the crack tip. The distance between two pairs of nodes i and i+1 is denoted a_i.

As the development of the fracture zone is restricted to take place along the crack it is favourable if the crack is as deep as possible. However, to describe the stresses and strains in a realistic way, a sufficiently number of nodes must be left between the crack tip and the loading point and for a given finite element mesh this is the only restriction for the largest possible value of the crack depth.

By introducing closing forces over the crack it is possible to make the structure in Fig 4.2 relevant for an arbitrary notch depth, see Fig 4.3 where an example of a notch with the tip at node k is illustrated. If the material is linear elastic and if the deformations are small, the widening of the crack at each node point from node 1 to node n can be expressed by the n equations:

$$w(i) = \sum_{j=1}^{n} K(i,j)P(j) + C(i)F \qquad (4:1)$$

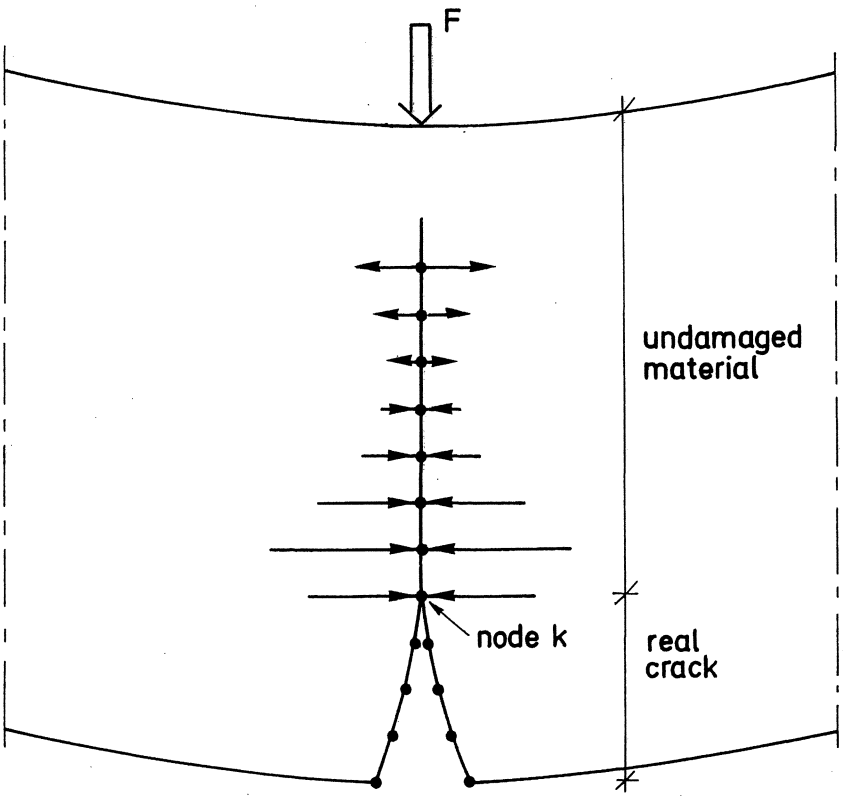

Fig 4.3 A schematic illustration of the first load step in calculation method I.

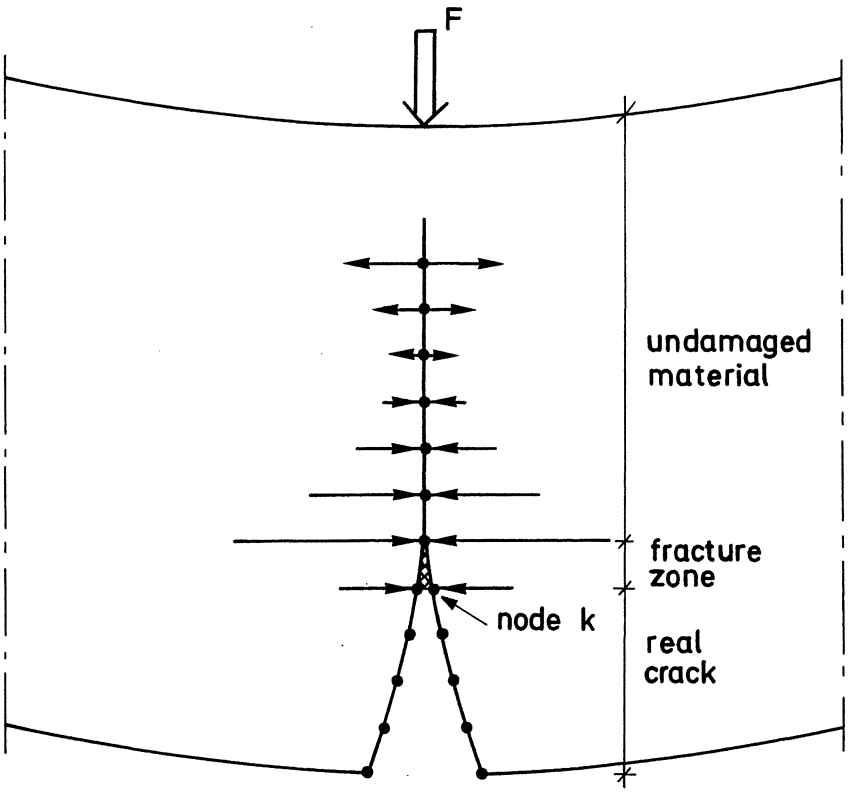

Fig 4.4 A schematic illustration of the second load step in calculation method I.

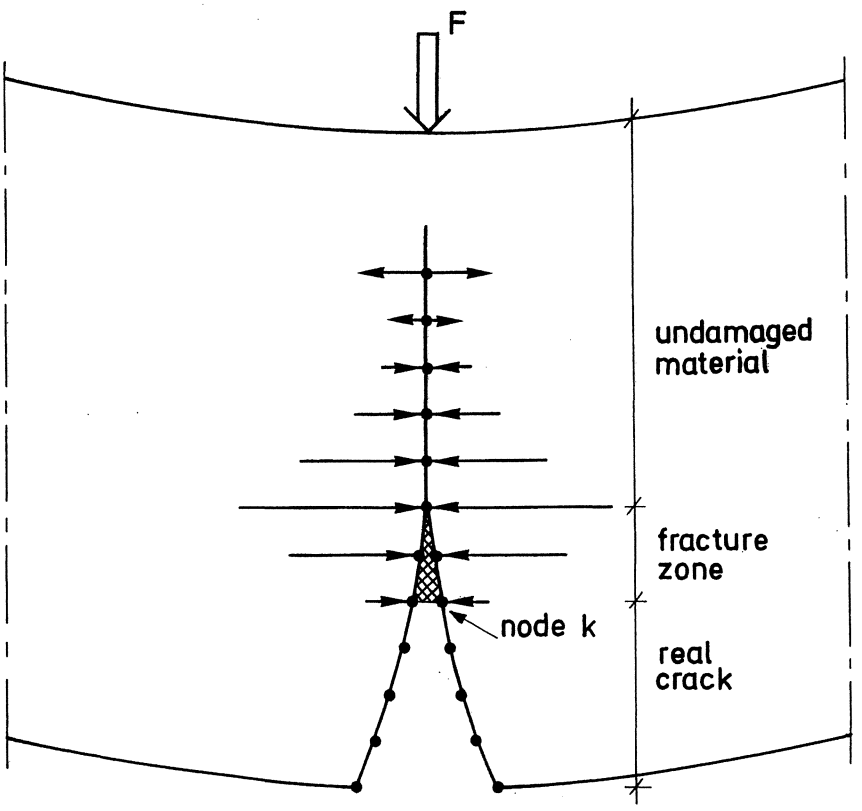

Fig 4.5 A schematic illustration of the third load step in calculation method I.

where w(i) is the width of the crack at node i, P(j) is the closing force acting at node j, F is the load applied to the structure, K(i,j) is the widening of the crack at node i of the structure in Fig 4.2 when unity load is acting at node j and C(i) is the widening of the crack at node i of the structure in Fig 4.2 when the applied load equals unity load.

There are no closing stresses acting across the notch and the widening of the crack is zero at the nodes in front of the notch. This gives:

for the nodes i=1 to k-1

$$P(i) = 0 \qquad (4:2)$$

and for the nodes i=k to n

$$w(i) = 0 \qquad (4:3)$$

For a given load F it is possible to find the n deformations w(i) and the n closing forces P(i) by solving the system of 2n equations defined by (4:1), (4:2) and (4:3).

The displacement (δ) of the loading point is:

$$\delta = \sum_{i=1}^{n} D(i)P(i) + D_F F \qquad (4:4)$$

where D(i) is the displacement of the loading point of the structure in Fig 4.2 when unity load acts at node i and D_F is the displacement of the loading point of the structure in Fig 4.2 when the applied load equals unity load.

All the constants above, K(i,j), C(i), D(i) and D_F, are determined by means of finite element calculations. When determining the constants a number of different load cases are solved but the same global stiffness matrix can be used for all the load cases and consequently it is only necessary to carry out a single invertation of the stiffness matrix.

The solving of the system of equations above, which is the first step of this calculation method, results in the initial slope of the load-displacement curve (F-δ curve).

The structure in Fig 4.3 is linear elastic and consequently the stress at the notch tip will exceed the tensile strength as soon as the structure becomes subjected to load (unless the structure is initially unnotched). Therefore the second step in this calculation method is to "open" the node pair k at the notch tip and to introduce a closing force at this point, see Fig 4.4. The intensity of this closing force depends on the widening of the crack accordingto the σ-w curve:

$$P(k) = a_k b\sigma(w(k))/2 \qquad (4:5a)$$

where a_k is the distance between the nodes k and k+1, b is the width of the structure and $\sigma(w)$ is the stress transferring capability as a function of the widening of the crack according to the σ-w curve. As the closing stresses are zero on the "notch" side of the node k, it is only the stresses acting on the area $a_k b/2$ that affect the force P(k).

In order to facilitate the calculations it is suitable to approximate the σ-w curve with straight lines. The simplest approximation is a single, descending, straight line, see Fig 4.6a. In the Figure f_t is the tensile strength and w_c is the maximum widening of the fracture zone when it is still able to transfer stress. The area under the curve represents the amount of energy necessary to create one unit of area of a crack and consequently the

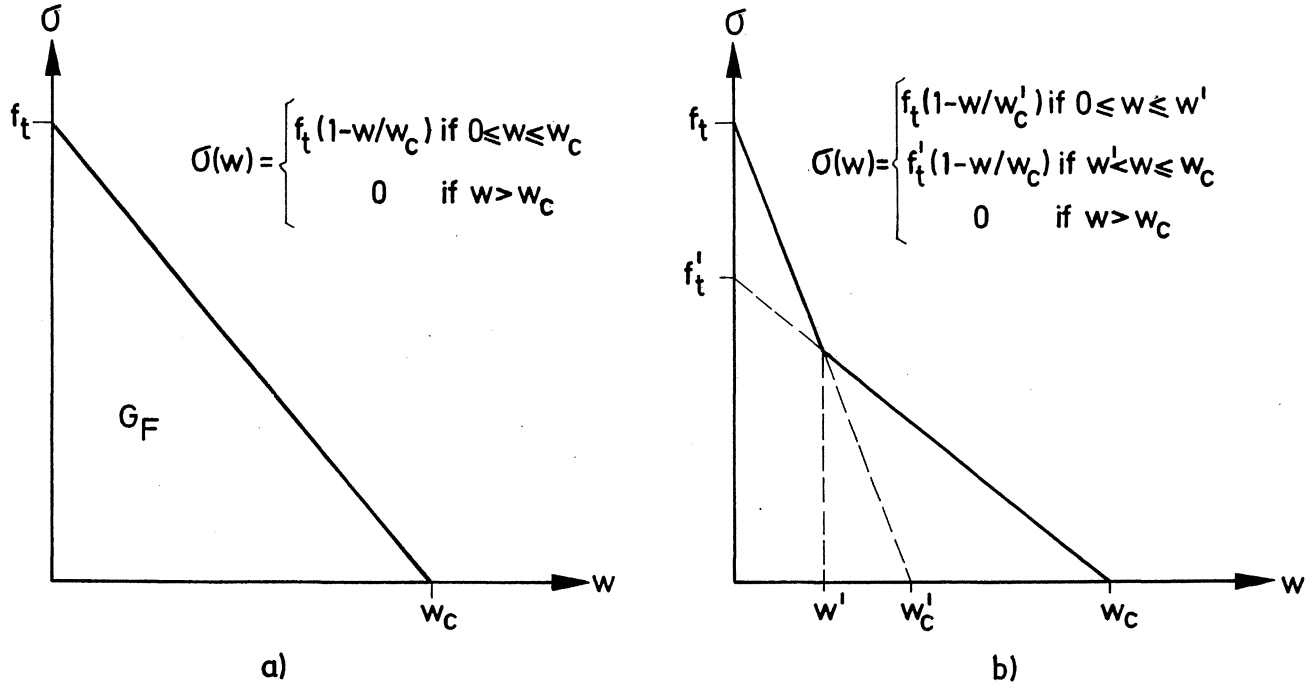

Fig 4.6 a) The simplest approximation of the σ-w curve is a single, descending, straight line.

b) The σ-w curve approximated with two straight lines.

area equals the fracture energy (G_F). This means that in the example in Fig 4.6a w_c equals $2G_F/f_t$.

If the simple single line approximation of the σ-w curve is used then:

$$\sigma(w) = \begin{cases} f_t(1-w/w_c) & \text{if } 0 \leq w \leq w_c \\ 0 & \text{if } w > w_c \end{cases} \qquad (4:6)$$

This relation can be used for calculating P(k) in (4:5a). If more complicated straight-lined approximations are used, then relations similar to those presented in Fig 4.6b can be used. These of course can be extended to straight-lined σ-w curves with an arbitrary number of break-points.

As the deformation of the structure in Fig 4.4 increases, the stress at the top of the fracture zone increases and finally it reaches the tensile strength which means:

$$P(k+1) = f_t b(a_k + a_{k+1})/2 \qquad (4:7)$$

During the first step of the calculation the deformation at node k was zero. If this condition is replaced by (4:5a), then (4:1), (4:2), (4:3) and (4:7) result in a system of 2n+1 equations and by solving this system it is possible to determine the n nodal deformations, the n nodal forces and the load for the moment when the tip of the fracture zone will advance. After this one has to check the widening of the fracture zone at node k. If this exceeds a critical point of the σ-w curve, see Fig 4.6, it is necessary to change (4:5a) so it fulfils the σ-w relation, and then this new system of equations has to be solved. This is repeated until the σ-w relation is fulfilled.

The displacement at the point of the applied load is calculated by using (4:4), which together with F produces the first point of the load-displacement curve. All the calculations in this second step can be carried out without any finite element calculations as all the constants are the same as for the first step.

During the third step the node pair k+1 is "opened" and a closing force starts acting at this point, see Fig 4.5. For this interior node pair, closing stresses act on both sides of the node and therefore the closing force becomes:

$$P(k+1) = (a_k+a_{k+1})b\sigma(w(k+1))/2 \qquad (4:5b)$$

The criterion for propagation of the fracture zone is that P(k+2) exceeds $f_t b(a_{k+1}+a_{k+2})/2$ (compare (4:7)). This criterion plus (4:1), (4:2) and (4:3) (where the conditions w(k)=0 and w(k+1)=0 are replaced by (4:5a) and (4:5b) respectively) give the necessary 2n+1 equations. After solving this system of equations the widening of the fracture zone is controlled and eventually some adjustments of the system of equations have to be carried out. The calculated value of F together with (4:4) give the second point of the load-displacement curve. Note that no new finite element calculations are necessary for this third step either.

The development of the fracture zone and the growth of the real crack can then be followed step by step in the same way until the fracture zone reaches node n and the load-displacement curve of the structure is derived.

The node number (k) for the position of the notch tip can be chosen between 1 and n and consequently it is possible to change the initial notch depth without changing the constants in the system of equations. If k=1 then the structure is initially unnotched.

The stresses along the crack can, for each step, be calculated as:

$$\sigma(i) = \begin{cases} \dfrac{2P(i)}{a_i b} & \text{for } i=k \text{ (at the notch tip)} \\ \dfrac{2P(i)}{(a_{i-1}+a_i)b} & \text{for } i \neq k \end{cases} \qquad (4:8)$$

where $\sigma(i)$ is the stress at node i. The stresses and strains in the elements outside the crack propagation path can be derived from equations similar to (4:4).

All the constants K(i,j), C(i), D(i) and D_F are determined on structures similar to the one presented in Fig 4.2. When the material in the structure is linear elastic, the constants can be converted, by using simple linear elastic relations, to be relevant also for other dimensions and other deformation properties (Young's modulus). In Table 4:1 the proportionality factors are given for the different constants. In the Table the proportionality factor for the distance (a_i) between two nodes is also shown.

Table 4:1 Proportionality factors for the constants in (4:2)-(4:8). d=some characteristic dimension of the structure in the plane. b=the width of the structure perpendicular to the plane, E=Young's modulus.

Constant	Proportionality factor
K(i,j)	1/bE
C(i)	1/bE
D(i)	1/bE
D_F	1/bE
a_i	d

The proportionality factors in Table 4:1 are relevant only if the dimensions in the plane are uniformly changed. For example, where a beam is concerned it is necessary for the ratio beam depth/beam length to remain constant. However, in some cases it is possible to approximately convert the constants to be relevant for other dimensions even if the dimensions in the plane are non-uniformly changed. For a notched beam in three-point bending the values of K(i,j) ought to be independent of the beam length, at least when the ratio beam length/beam depth is not too small. The opening of the crack depends only on the moment at the notched cross section. This moment increases li-

nearly with the beam length and therefore C(i) ought to be proportional to the length. Then according to the Maxwell-Bettis theorem D(i) is also proportional to the beam length. D_F is the deflection of the loading point when the applied load F equals unity load. The value of D_F for a linear elastic material can be calculated for an arbitrary beam length (Carlsson, 1976):

$$D_F = \frac{1}{4bE}\left(\frac{\ell}{d}\right)^3\left[1 + 3.15\left(\frac{d}{\ell}\right)^2\right] + \frac{2}{bE}\left(\frac{\ell}{d}\right)^2 g_1\left(\frac{a}{d}\right) \qquad (4:12)$$

where b=beam width, d=beam depth, ℓ=beam length, a=notch depth, E=Young's modulus. The function $g_1(a/d)$ is shown in Fig 4.7. In (4:12) the influence of Poisson's ratio is neglected which, at least where concrete and similar materials are concerned, affects the value of D_F very little.

Cementitious materials are often subjected to volume stresses due to drying shrinkage and temperature gradients for example. Most available FEM-programs can be used for treating this type of loading for linear elastic materials. When the structure in Fig 4.2 is subjected to shrinkage stresses for example, the separation of the nodes in each node pair along the crack can be de-

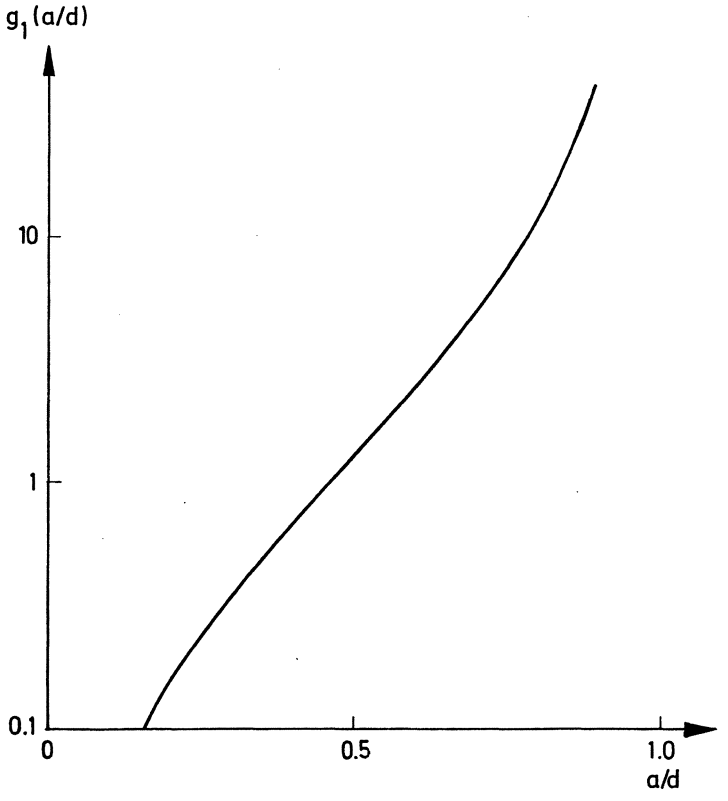

Fig 4.7 The function $g_1(a/d)$ used in (4:12)

termined. By introducing these values in (4:1), the influence of volume stresses can be analysed by means of the Fictitious Crack Model:

$$w(i) = \sum_{j=i}^{n} K(i,j)P(j) + C(i)F + w_V(i) \qquad (4:13)$$

where $w_V(i)$ represents the separation of the nodes in the node pair i when the structure is subjected to a certain distribution and intensity of volume stresses. The values of $w_V(i)$ are derived from linear elastic FEM calculations and consequently they can easily be converted to being relevant also for other intensities, specimen dimensions and for other values of the Young's modulus.

One limitation of the calculation method described above is that it is necessary to know the crack propagation path in advance. However, this is often the case due to symmetry of geometry and loads, existence of weak zones, test results or experience for example. If the crack propagation path is known in advance, then there are many advantages for using this method. When the values of the constants K(i,j), C(i), D(i) and D_F are determined once, the calculations can easily be carried out by solving the system of 2n+1 equations for different notch depths, different specimen dimensions, different values of the Young's modulus and different shapes of the σ-w curve. The influence of volume stresses can also be analysed. The solving of the 2n+1 equations (normally $n<40$ is sufficient) requires much less computer capacity than analysing the global stiffness matrix of the structure and consequently the calculation costs are reduced considerably.

4.3 Calculation method II: the super position principle

Sometimes it is impossible to predict the crack propagation path in advance, in which case the calculation method I is useless. When using the method of superposition the first step is to apply the load F_1 to the linear elastic structure in Fig 4.8a, which gives the stress $\sigma(1,i)$ in each node i. The load F_1 is chosen so that the tensile strength is reached at the crack tip, i.e. $\sigma(1,1)=f_t$.

The second step is to "open" node 1 and to introduce opening forces across the crack at this node, see Fig 4.8b. The intensity of the forces must depend on the width of the "fictitious" crack according to the σ-w curve and on the area which is represented by the forces. For the simple straight-lined σ-w curve in Fig 4.6a, the intensity of the forces increases linearly from 0 to $a_1 b f_t/2$ when w increase from 0 to w_c and the forces are 0 when

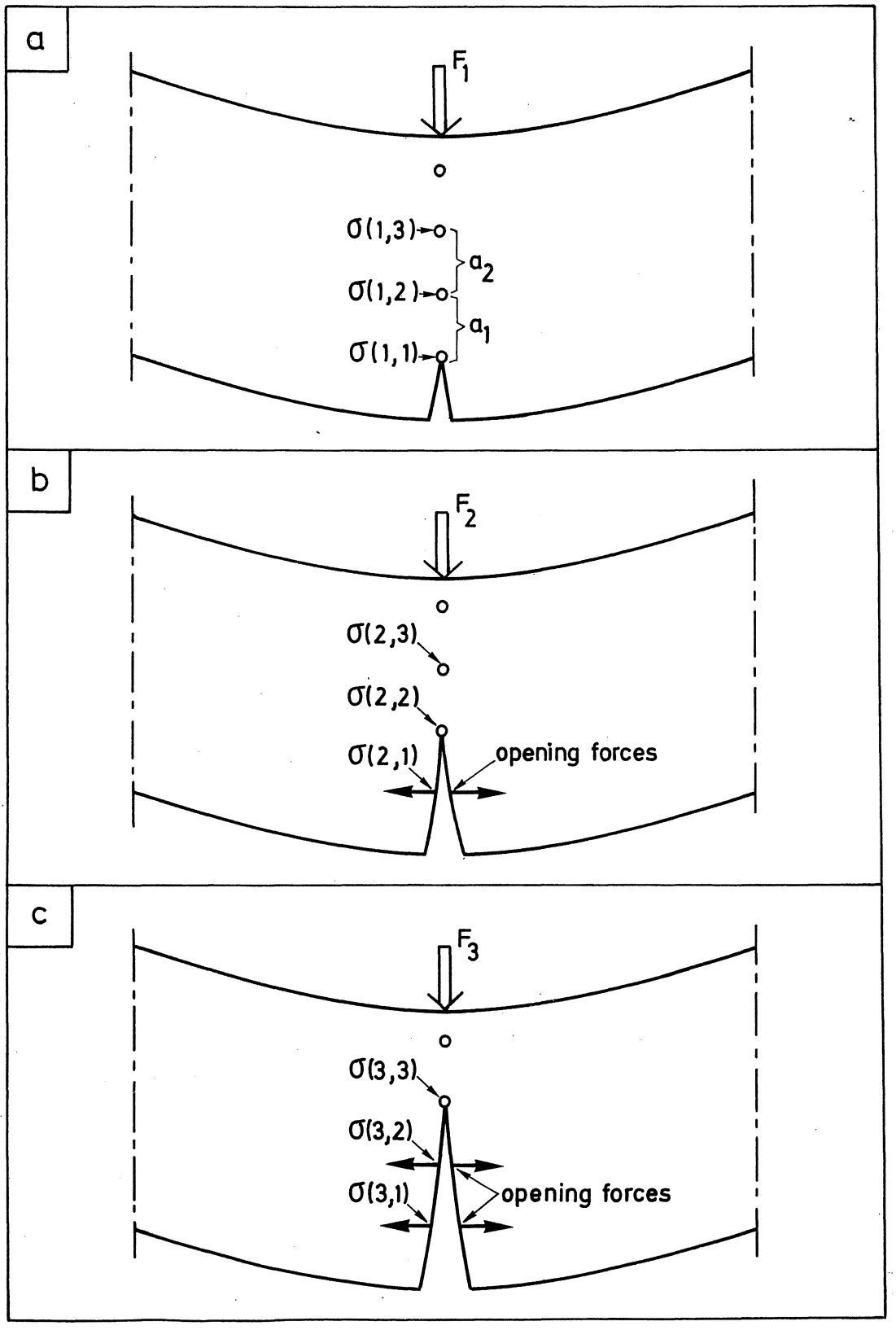

Fig 4.8 Schematic illustration of the three first load steps in calculation method II (superposition).

$w > w_c$. b is the width of the structure perpendicular to the plane and a_1 is defined in Fig 4.8a. The load F_2 is chosen so that $\sigma(1,2)+\sigma(2,2)=f_t$ which means that, when loadcase 1 and 2 are combined, the tensile strength is reached at node 2. The total load is then F_1+F_2 and the stresses at the different nodes are given as $\sigma(1,i)+\sigma(2,i)$. The stress at node 1 due to load F_2 is negative (the forces at this node want to widen the crack) and consequently the total stress at node 1 decreases according to the σ-w curve.

The third step, see Fig 4.8c, is to "open" node 2 and to introduce opening forces across the crack at this point. The intensity of these forces increases linearly from 0 to $(a_1+a_2)bf_t/2$ when w increases from 0 to w_c (if the σ-w curve is approximated with a single, straight line). The load F_3 is chosen so that $\sigma(1,3)+\sigma(2,3)+\sigma(3,3)=f_t$ and the calculations are carried out exactly as for the second step. In this way it is possible to follow the crack growth through the material.

The simple example above illustrates a crack propagating along a straight line. However, by using this method it is possible to chose the propagation direction of the fracture zone after each calculation step. Then the first principal stress is calculated at the tip of the fracture zone and the propagation takes place along a path perpendicular to the first principal stress or, as the possible directions of propagation are limited to the directions of the element sides, along the element side which deviates less from the theoretical propagation direction.

This calculation method is much more expensive than calculation method I as it is necessary to invert the global stiffness matrix of the structure for each calculation step. Also, there are no simple methods of converting the calculation results for one specific dimension so that they are relevant for other dimensions. Therefore method I is much more efficient when it can be used.

4.4 Element wide fracture zones

For the calculation methods described in 4.2 and 4.3 inter element fracture zones and cracks are used. This means that the crack propagation path is bound to follow the sides of the elements. This gives rise to some problems if the direction of the propagation path is unknown. In Fig 4.9a an example of a theoretical direction of crack propagation is shown in a finite element mesh with square elements. The elements are numbered from (a,1) to (j,10). Normally the theoretical propagation path does not follow the ele-

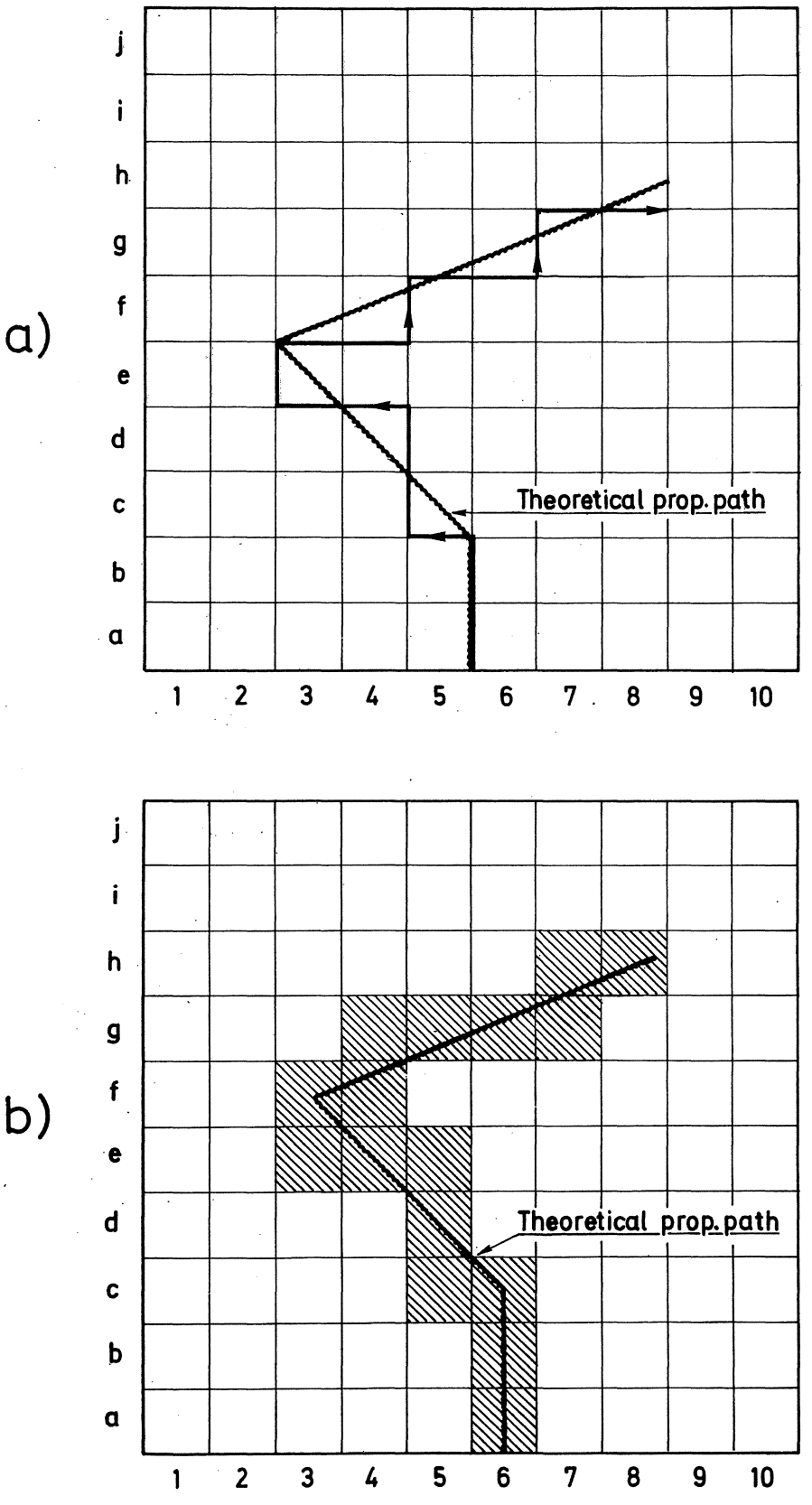

Fig 4.9 a) When inter element crack propagation paths are used, the crack is bound to follow the sides of the elements.

b) When element wide fracture zones are used, the stiffness of the elements is changed when the crack passes through.

ment sides but an approximate crack propagation path according to the Figure must be used in the calculations. The element mesh in the Figure is coarse and a finer mesh normally gives a better approximation. It is also possible to use other element shapes, for example, triangular elements sometimes give better possibilities to follow the theoretical propagation path more exactly. Another, but more complicated, method is to change the element mesh after each load step so that the element sides coincide with the direction of the propagation path.

For each load step nodes have to be "opened". This means that the number of nodes increases as the fracture zone propagates. This affects the stiffness matrix and complicates the calculations.

The problems discussed above are not unique for the Fictitious Crack Model but apply also to linear elastic finite element calculations. Some of the problems are solved for the linear elastic case if the Blunt Crack Band Model (Bazant and Cedolin, 1979) is used. In this model an element wide crack is used. When a crack passes through an element, the stiffness of the element is reduced to zero perpendicular to the direction of crack propagation but the stiffness parallel to the crack is not changed.

If the Blunt Crack Band Model is applied to the Fictitious Crack Model some problems are bound to arise. First, the σ-w curve is related to the absolute deformation of the fracture zone which means that the curve will be dependent on the element size if element wide fracture zones are used. This is a small problem as long the fracture zone propagates along a straight line parallel to the sides of rectangular elements, see Fig 4.9b. However, when the direction of the propagation path deviates from the direction of the element sides, for example when the fracture zone propagates from element (c,6) to (d,5), then the width of the element perpendicular to the propagation path varies along the path. This gives rise to difficulties when choosing the σ-w curve. Furthermore, when the fracture zone advances from element (c,6) to (d,5), the fracture zone will be tied at the node between the elements and consequently it is necessary to change the properties of at least one more element, in this case element (c,5). The same problem arises for elements (e,5), (e,3) and (g,4).

According to the discussion above it seems doubtful if there are any advantages in using element wide fracture zones for Fictitious Crack Model calculations. Inter element propagation paths are preferable, at least when the direction of the crack propagation path is known in advance.

4.5 Material parameters affecting the choice of the finite element mesh

When representing high stress gradients by means of FEM it is necessary to use a fine element mesh. For a linear elastic material the stress in front of the crack tip increases very rapidly as the distance from the notch tip decreases and consequently, in order to describe the stress distribution in a proper way, one has to use a great number of small elements and sometimes even a special crack tip element. The stress singularity disappears when there is a fracture zone in front of the crack tip and the stress distribution around the tip becomes smooth. This means that the stress field around the crack tip can be properly described by FEM even if a rather coarse element mesh is used. When discussing the choice of element size for Fictitious Crack Model calculations it is therefore necessary to consider the properties and behaviour of the fracture zone in the discussion.

The properties of the fracture zone are determined by the σ-w curve (Fig 3.4b). The behaviour of the fracture zone is also affected by the properties of the material outside the zone. These properties are determined by the σ-ε curve (Fig 3.4a).

In all the calculations presented in this thesis the σ-ε curve is approximated with a straight line according to Fig 4.10a, which ought to be reasonable for most cementitious materials except when they are highly fibre-reinforced. The straight-lined σ-ε curve is defined by the Young's modulus (E) and the tensile strength (f_t).

In the calculations stepwise linear σ-w curves are used, see Fig 4.10b. The area under the curve corresponds to the amount of energy that is necessary to create one unit of area of a crack and consequently the area equals the fracture energy (G_F). This means that when the shape of the curve is known, the position of the σ-w curve is defined by the fracture energy and the tensile strength. The shape of the curve is defined by a function $h(w/w_c)$ and the σ-w curve can be expressed as:

$$\sigma(w) = f_t h(w/w_c) \qquad (4:14)$$

The notations in the equation are given in Fig 4.10. $h(w/w_c)=1$ when $w=0$ and $h(w/w_c)=0$ when $w=w_c$.

The brittleness of a material is characterized by the σ-ε and the σ-w curves. However, sometimes it is possible to replace these curves with a single, cha-

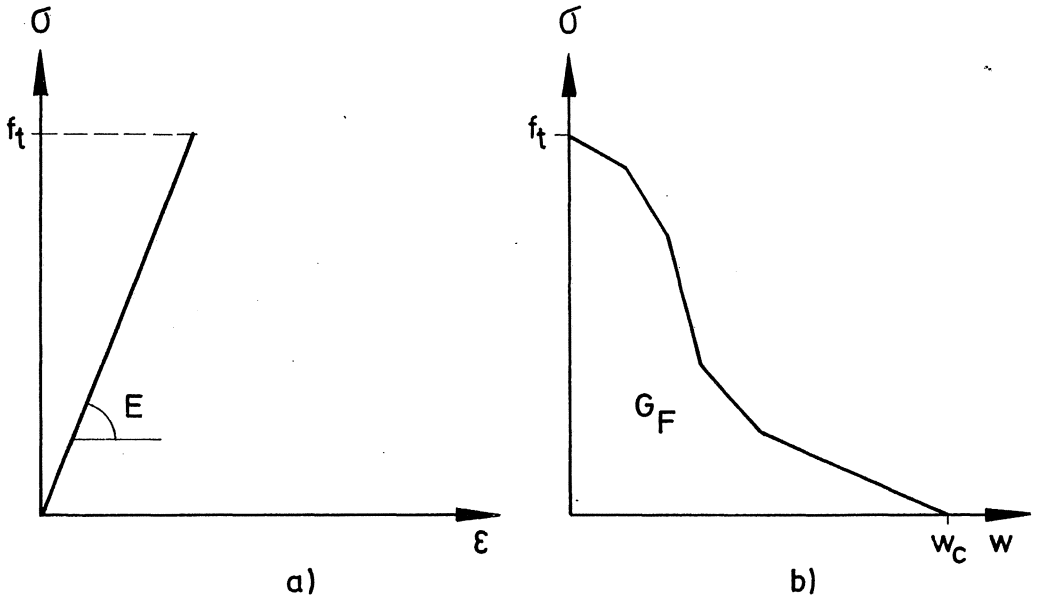

Fig 4.10 a) The σ-ε curve approximated with a single, straight line.
b) Normally stepwise linear σ-w curves are used in the calculations.

racteristic parameter. When a crack propagates, energy is consumed by the fracture zone. At the same time elastic energy is released from the material outside the fracture zone. When the maximum load in a direct tensile test is reached, the elastic energy available for crack propagation is $F_c\delta/2=F_c^2/2k$, where F_c is the maximum load, δ is the corresponding deformation and k is the stiffness of the specimen. For a specimen with constant cross section $k=AE/\ell$ where A is the cross sectional area and ℓ is the specimen length. This means that the energy available for crack propagation is $F_c^2\ell/2AE$. The amount of energy that can be consumed by crack propagation is G_FA. By equating these two expressions for energy, we find that $\ell^* = 2G_FA^2E/F_c^2 = 2G_FE/f_t^2$, where ℓ^* is the length of the specimen when the energy available for crack propagation, at maximum load, equals the capability of energy consumption of the fracture zone. For a given shape of the σ-w curve the material then becomes more sensitive to crack propagation, and therefore more brittle, when the value of ℓ^* decreases. For practical reasons it is more suitable to use half this length to characterize a material and then the characteristic length (ℓ_{ch}) is defined as:

$$\ell_{ch} = G_FE/f_t^2 \qquad (4:15)$$

It must be observed that ℓ_{ch} should only be used for comparing materials with similar shapes of their σ-w curves. However, for materials with similar shapes of their σ-w curves, ℓ_{ch} is probably the best way of characterizing the brittleness; the shorter ℓ_{ch} is, the more brittle the material is.

In this work the well-known three-point bend test on notched and unnotched beams is analysed and the calculation method I (substructure) is normally used. For most of the calculations the necessary constants (K(i,j), C(i), D(i), D_F) were determined by use of the finite element mesh shown in Fig 4.11. As the three-point bend test is symmetrical it was only necessary to use half the beam in the calculations. The line of symmetry in the Figure defines the middle of the beam. The length/depth ratio of the beam is 4.

The finite elements are four node isoparametric membrane elements and triangular constant strain membrane elements respectively. For the FEM-calculations the program EUFEMI was used, which was developed at the Division of Solid Mechanics at the Lund Institute of Technology (Hernelind and Pärletun, 1974).

In order to study how well the behaviour of the material is described when the element mesh in Fig 4.11 is used and to see how the calculation results are affected when varying distances between the closing forces in the fracture zone are used, the load-deflection curves for three different beams were determined. The depths (d) of the beams were 0.2, 0.8 and 1.6 m respectively. For all the beams the ratio notch depth/beam depth (a/d) was 0.4 and the beam width (b) was 1 m. The σ-w curve was approximated by a single, straight line and the values of G_F, E and f_t were 100 N/m, 40,000 MPa and 4 MPa respectively, which gives a ℓ_{ch}-value of 250 mm. These material properties represent a normal concrete quality (see Chapter 7).

The calculation results are presented in Fig 4.12. The unbroken curves represent calculations where closing forces act at each node in the fracture zone which means that the distances between the forces are d/40. The dashed curves represent calculations where closing forces act at each second node in the fracture zone and the distances between the closing forces are then d/20. In the Figure the initial slope according to the linear elastic solution is also shown. This slope was calculated by use of (4:12).

The agreement between the initial slope of the curves and the slope according to the linear elastic solution seems excellent. This implies that the finite element mesh used is sufficiently fine for describing the behaviour

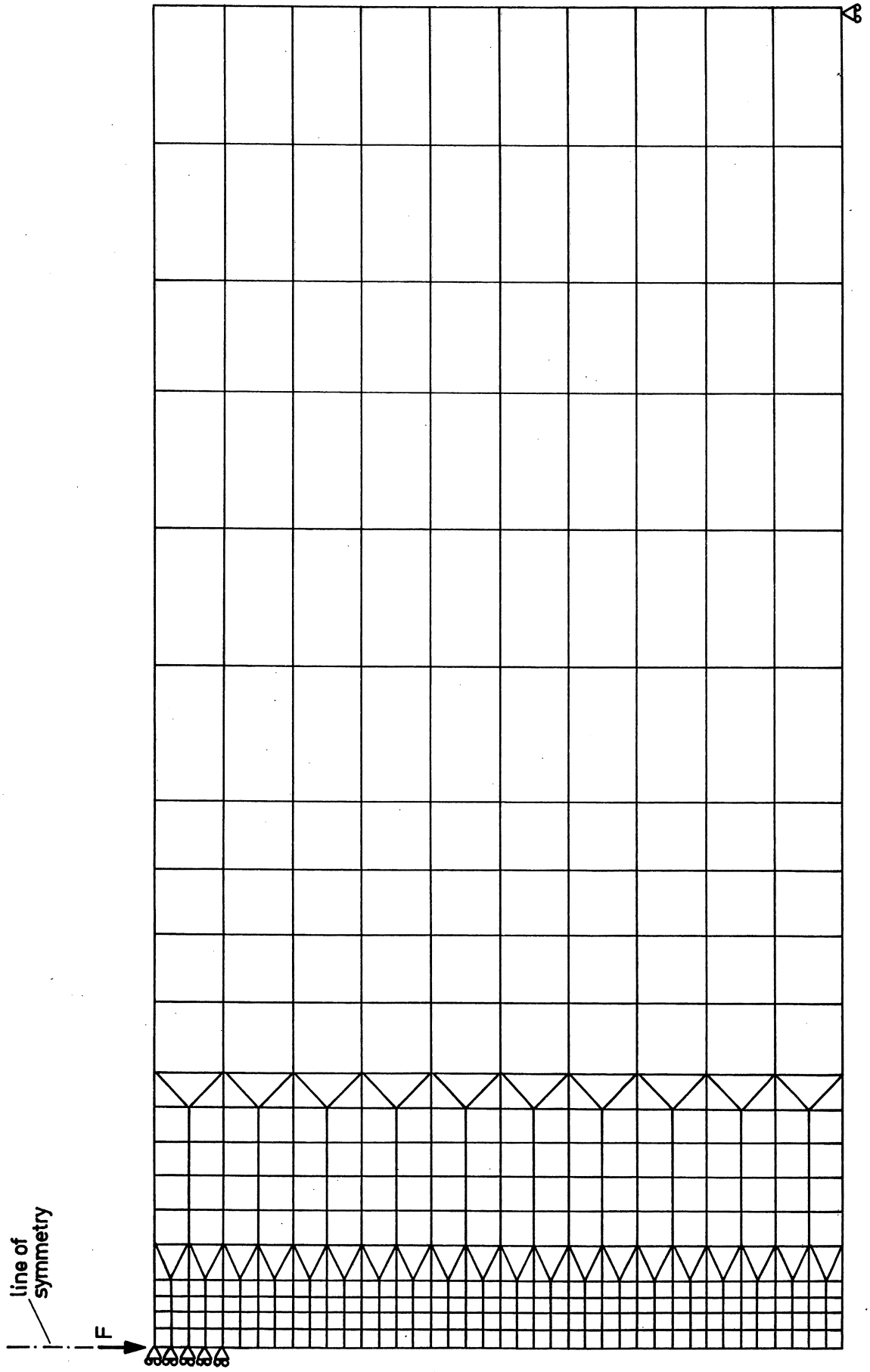

Fig 4.11 The finite element mesh used during the analyses.

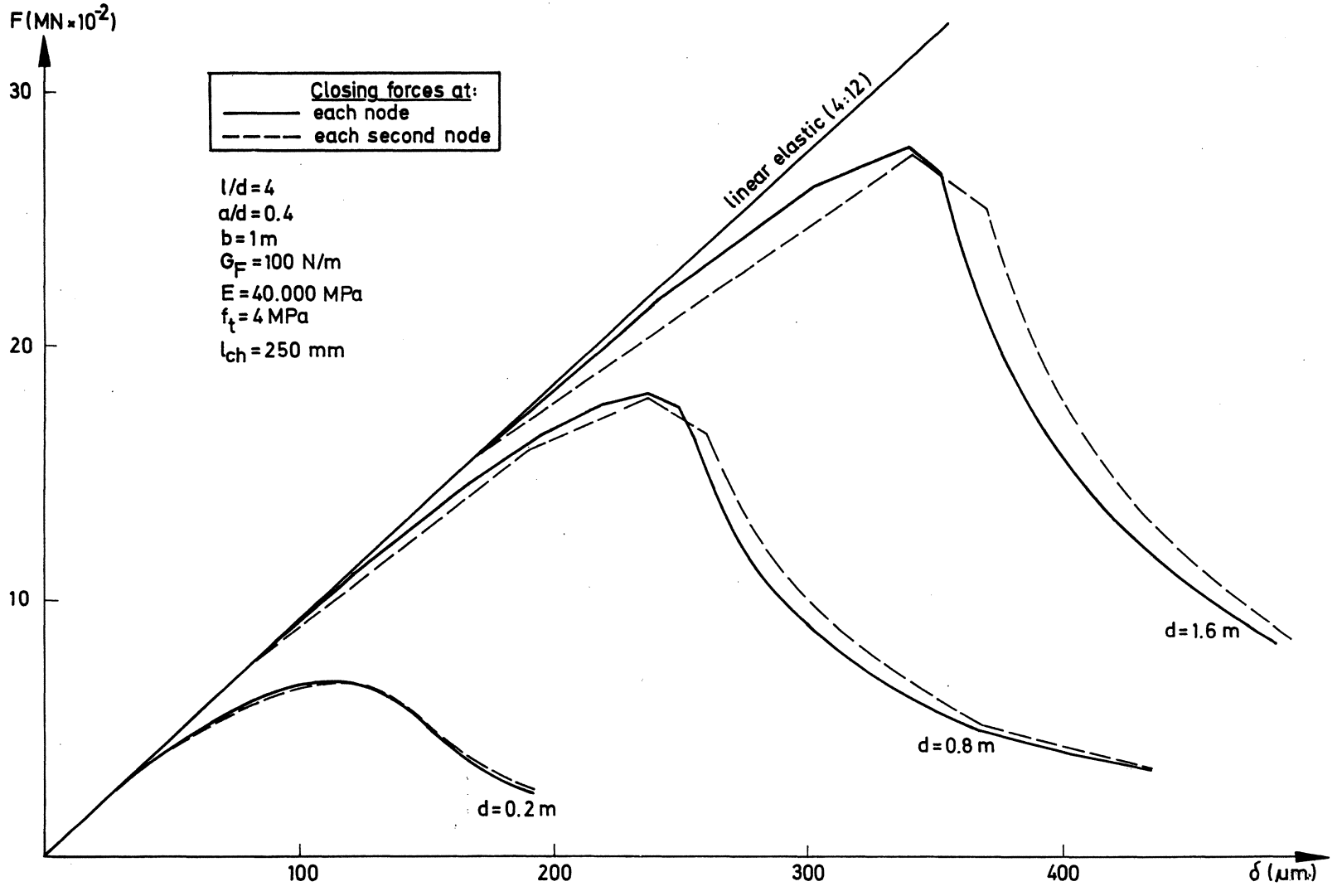

Fig 4.12 Calculated load-deflection curves for different beam depths and different distances between the closing forces in the fracture zone. The straight line represents the linear elastic solution according to (4:12).

of the material outside the fracture zone.

There are differences between the curves representing different distances between the closing forces. The differences increase as the beam depth increases but the agreement also seems suprisingly good for the largest beam. This implies that the properties of the fracture zone can be described in a reasonable way even when the distances between the closing forces are wide. For the largest beam the distances between the closing forces are 40 and 80 mm respectively which correspond to about 15 to 30 % of the characteristic length. However, these figures are naturally also dependent on the absolute dimensions of the structure. For example, for small structures ($d/\ell_{ch}<1$) it is necessary to decrease the distances between the closing forces.

Other calculation results presented by Petersson and Gustafsson (1980) support the results above which prove that the Fictitious Crack Model describes the crack propagation in a proper way, even if the finite element mesh is relatively coarse and the distances between the closing forces are wide. However, it seems unsuitable to use larger distances between the closing forces than 0.2 ℓ_{ch}, which for concrete corresponds to 40-80 mm.

5 THE FRACTURE ZONE

5.1 The width of the fracture zone

The strain measurements presented in Fig 3.2 indicate that the fracture zone in concrete propagates along a narrow band and that the width of the zone is small in the stressed direction. Direct observations of stable crack propagation in fine-grained mortar (maximum aggregate particle size = 0.3 mm) was reported by Mindess and Diamond (1980). They used a scanning electrone microscope (SEM) in order to study the region in front of a notch in compact tension specimens. Their results show that branch cracks exist and sometimes also two or more parallel cracks develop simultaneously but the width of the cracked zone is very limited, in this case less than a few tenths of a millimeter, i.e. similar to the size of the maximum aggregate particles.

Modéer (1979) used an indirect method in order to study the development of the fracture zone in front of a notch in a bent mortar beam. The surface of the beam was covered with a water film. When the widening of the fracture zone reached a certain value the micro-cracks absorbed water from the surface. This reduced the reflexions from the surface which could be registrated by use of a camera. According to these tests it seems that the width of the fracture zone is limited to a band less than a few millimeter wide.

In order to study the development of the fracture zone, stable tensile tests were carried out. The tests were performed in the very stiff tensile testing machine presented in Chapter 8. The material used was concrete with a maximum aggregate particle size of 8 mm and the water-cement-ratio was 0.6. The specimens were cast in steel moulds and stored in lime saturated water (+20^{o}C) until one day before testing. During the last day before testing the specimens were insulated with plastic foil. The tests were performed 7 days after casting. The specimens were kept in the air for a few minutes while they were fixed into the testing machine which means that the surfaces became slightly dry. During the tests water was sprayed on all the surfaces but one. When the fracture zone developed, water was absorbed by the zone due to capillary forces and the zone could be observed as a dark area on the "dry" surface.

The results from two tests are presented here. The mean stress-deformation curve for the two tests is shown in Fig 5.1. The "dry" surface was photographed in the 9 positions defined on the curve in the Figure.

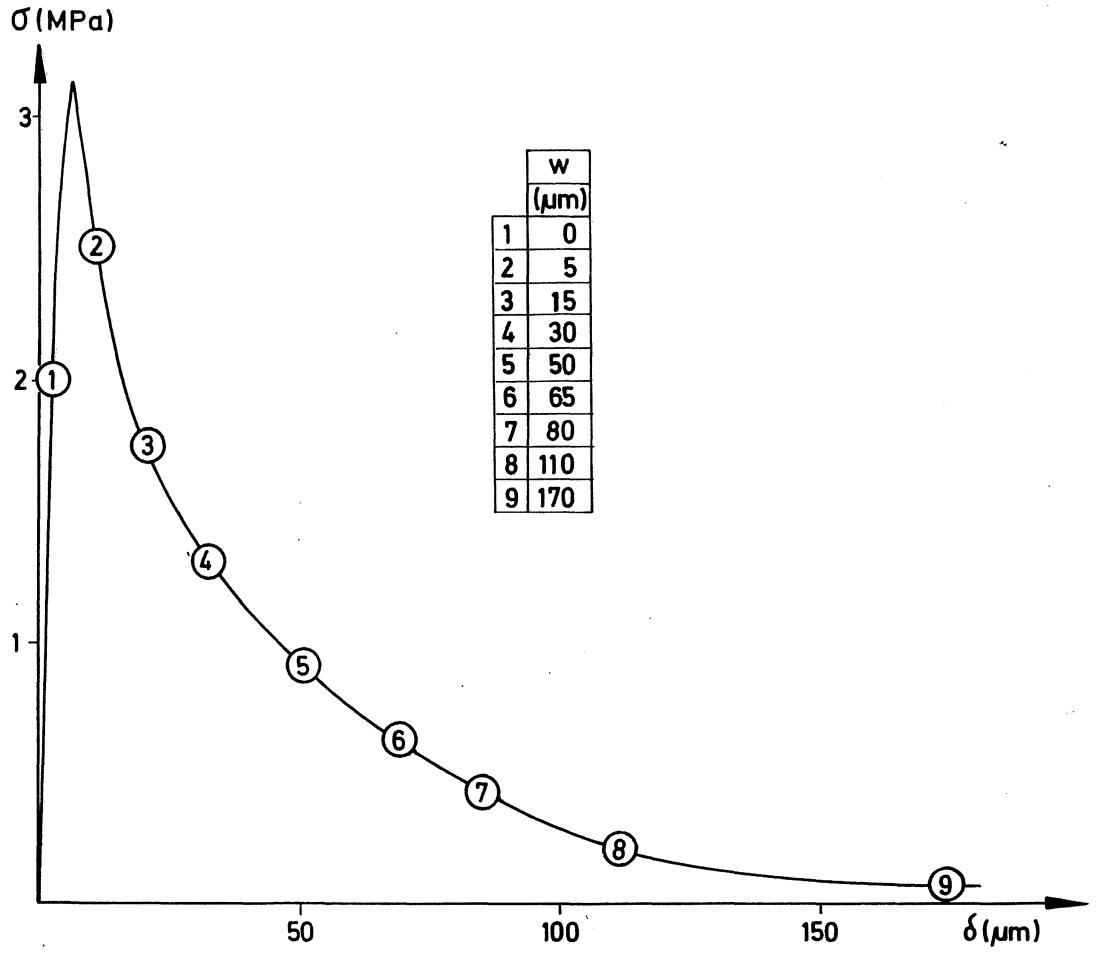

Fig 5.1 The mean stress-deformation curve for the two tests presented in Fig:s 5.2-5.3. The figures on the curve correspond to the positions for the photos in Fig:s 5.2-5.3. w = widening of the fracture zone.

The results from one of the tests are presented in Fig 5.2. The surface is cast against a steel mould which means that the surface is covered with a thin layer of cement paste and therefore no aggregate particles can be seen. The first sign of a fracture zone can be observed in photo No 3 where small, dark lines have developed on both sides of the specimen. This photo is taken when the widening of the fracture zone is about 15 μm and the stress has decreased to about 60 % of the tensile strength. The fracture zone ought to start developing already when the tensile strength is reached but the microcracks are too narrow to be able to transport water until the position of the load-deformation curve corresponding to photo No 3 is reached. In photo No 4 the wet band has spread through the specimen. In photo No 5 there is a small jump in the wet band and at this position a narrow crack can be distinguished and in photo No 6 the crack can be seen very clearly. This means

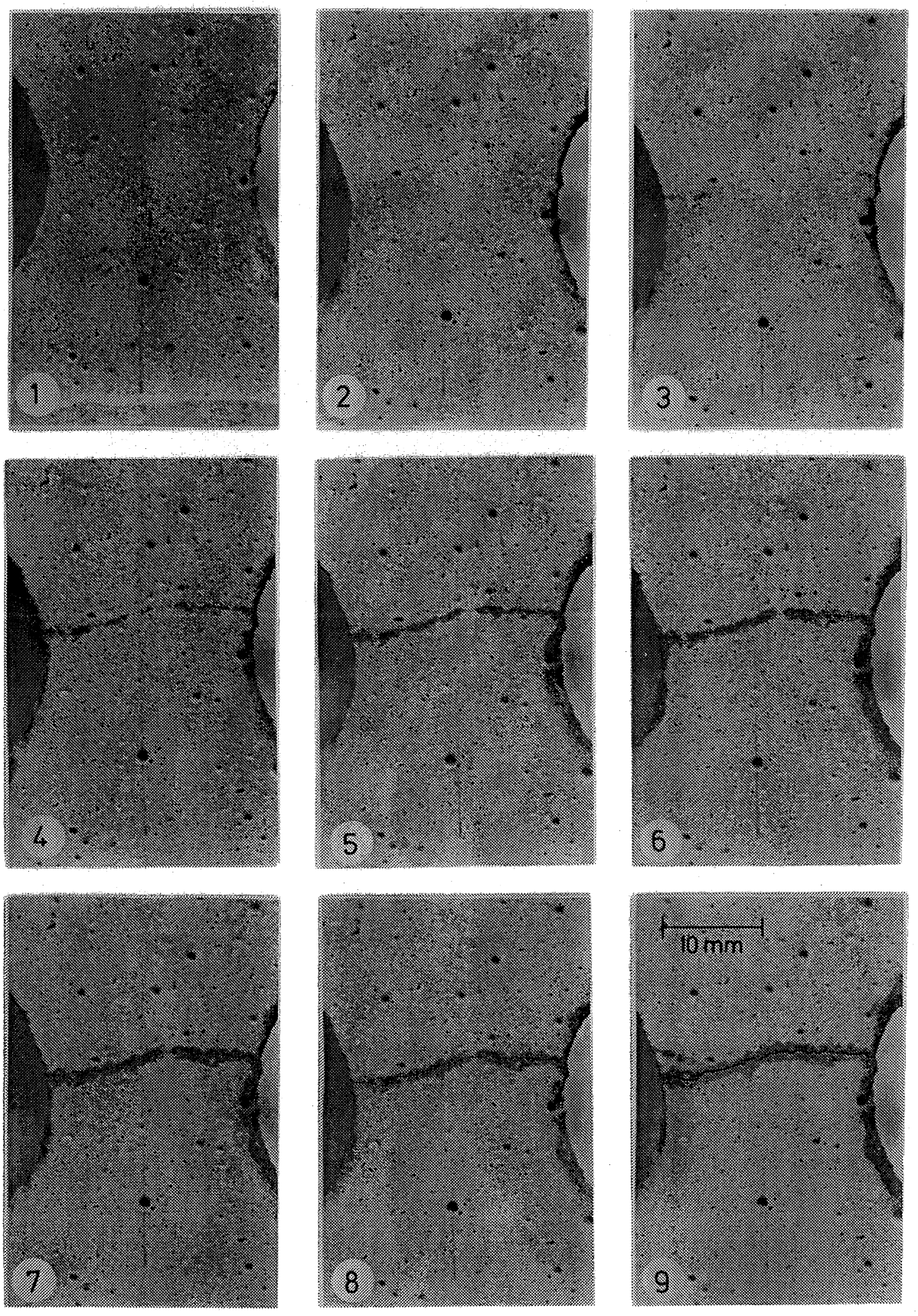

Fig 5.2 The development of the fracture zone during a direct tensile test. The surface is cast against a steel mould. The photos correspond to the positions on the load-deformation curve in Fig 5.1.

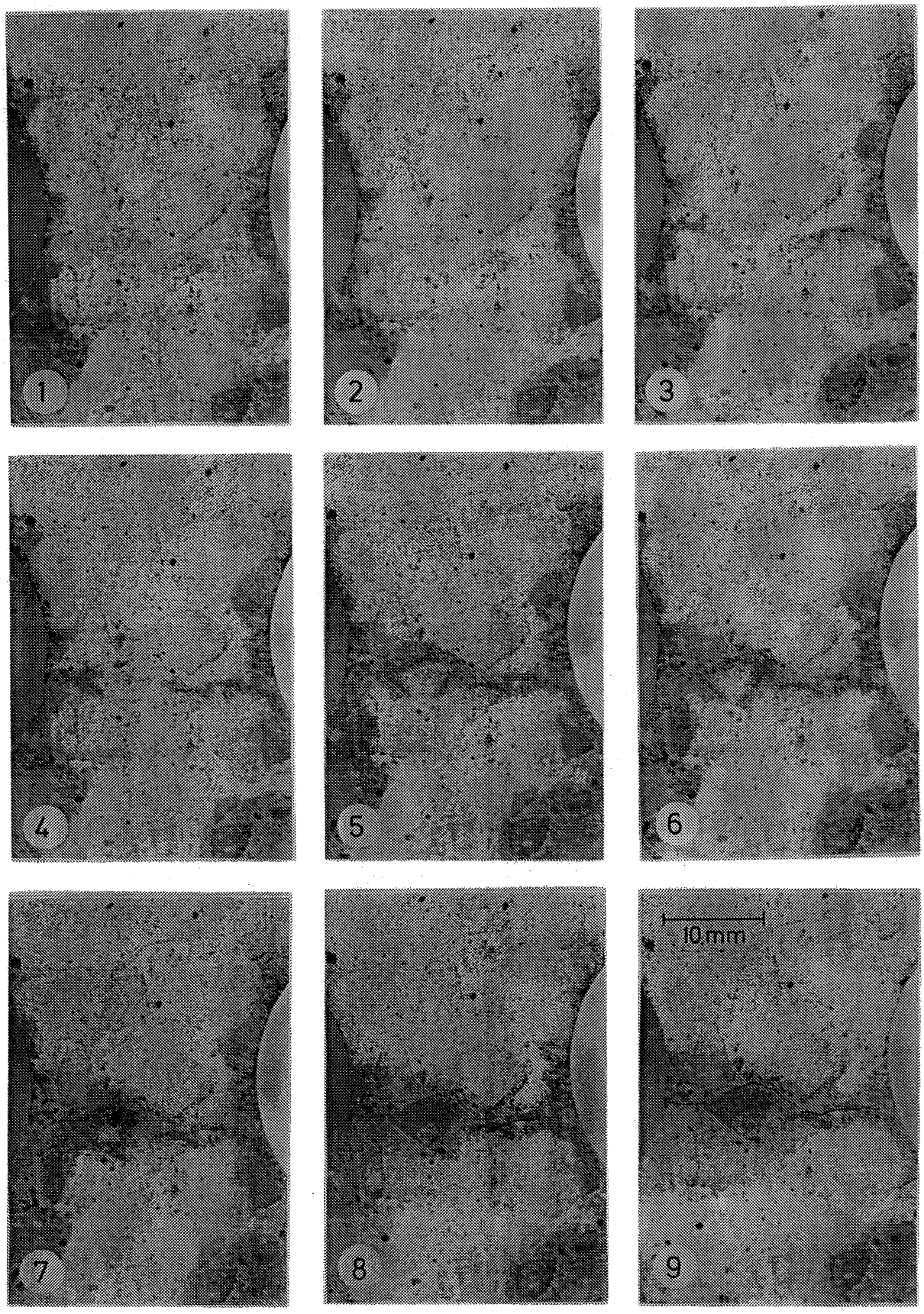

Fig 5.3 The development of the fracture zone during a direct tensile test. The surface is sawn. The photos correspond to the positions on the load-deformation curve in Fig 5.1.

that the crack becomes visible when the widening of the fracture zone is about 25-50 μm. It can be observed that the material is still able to transfer 25 % of the maximum stress when a visible crack has developed across the specimen. In photo No 9 the widening of the fracture zone is 170 μm but the material is still able to transfer some percentage of the maximum stress. In this photo a branch crack has developed on the left side of the specimen. This branch crack is probably caused by the extraction of an aggregate particle from the cement paste inside the specimen.

The results in Fig 5.2, and also the other test results discussed above, indicate that the width of the fracture zone is small in the stressed direction. However, these observations are made on surfaces which are cast against steel moulds and therefore the results are not representative for the material inside the specimen. For this reason a specimen was divided by using a saw and then tested in the stiff testing machine. The results for the sawn surface are presented in Fig 5.3. Unfortunately the surface was already partly wetted at the start of the test and the dark areas in photo No 1 have nothing to do with the fracture zone.

The fracture zone is first seen in photo No 3 when the widening of the zone is about 15 μm. In photo No 4 it can be seen how the fracture zone starts developing around an aggregate particle and in photo No 5 the zone has developed almost completely around the aggregate particle. This means that the fracture zone is considerably wider in this case compared with the case in Fig 5.2. The width of the fracture zone seems to be of the same magnitude as the size of the maximum aggregate particles, i.e. about 8 mm in this case. This is quite natural as the aggregate particles have to be extracted from the cement paste before the final collapse of the specimen. However, normally a width of the fracture zone corresponding to the maximum aggregate particle size can be considered as small and therefore the Fictitious Crack Model should be usable for describing the development of the zone.

5.2 The development of the fracture zone

The development of the fracture zone can be analysed by use of the Fictitious Crack Model. In Fig 5.4 the fracture zone and the stress distribution in front of a notch tip in a beam subjected to three-point bending are shown for different positions on the load-deflection curve. The beam depth is 0.2 m, the notch depth 50 mm and the beam length 0.8 m. In the calculations the σ-w curve is approximated with a single, descending, straight line and

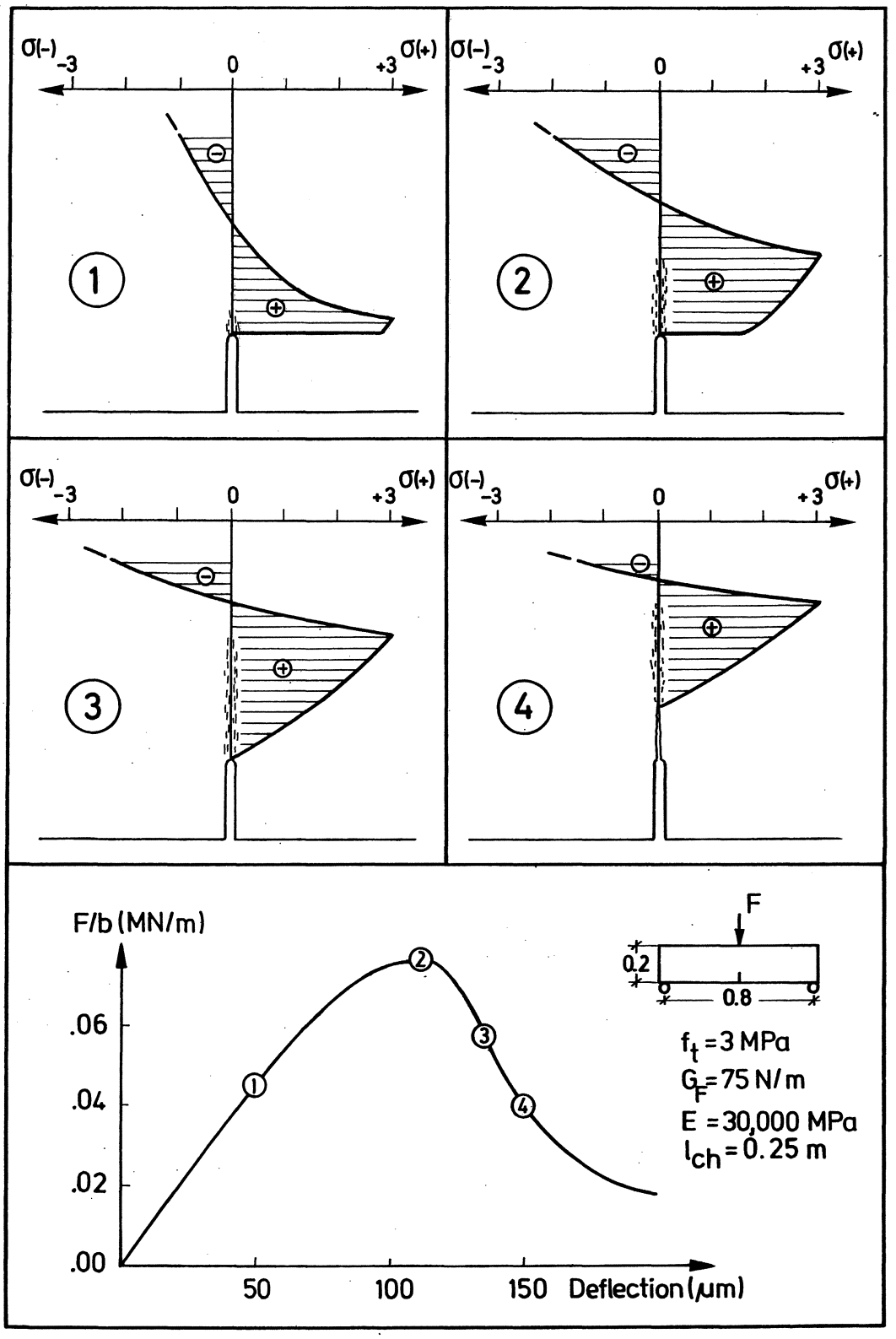

Fig 5.4 The fracture zone and the stress distribution in front of the notch tip for different positions of the load-deflection curve. The Figure is relevant for a 0.2 m deep notched beam (a/d=0.25) in three-point bending and the material properties correspond to a normal concrete quality.

f_t, E and G_F are 3 MPa, 30,000 MPa and 75 N/m respectively, i.e. ℓ_{ch} = 0.25 m, which corresponds to a normal concrete quality. The σ-ε curve is approximated with a straight line.

In this Chapter all the diagrams are relevant for ℓ_{ch} = 0.25 m. They can however easily be converted to be relevant also for other values of ℓ_{ch} by use of the proportionality factor d/ℓ_{ch}.

The fracture zone starts developing as soon as the specimen in Fig 5.4 becomes subjected to load. In the first position of the load-deflection curve in the Figure, a small fracture zone has developed. No stresses exceed the tensile strength. This gives a much more realistic description of the stress distribution than the linear elastic solution which always, at least theoretically, includes a stress singularity. When the maximum load is reached, the depth of the fracture zone is about 50 mm and the stress distribution is quite different compared with the linear elastic one. These calculations are relevant for a 200 mm deep beam. For smaller beam depths, 50 mm is not unusual in tests, the influence of the fracture zone will be even more pronounced and it seems quite obvious that it is necessary to consider the effect the fracture zone has on the fracture process. It can be observed that the material at the notch tip is able to transfer stress even when the maximum load is reached and a real crack, i.e. a crack with stress-free surfaces, will not propagate until position 3 of the load-deflection curve is reached. This is very interesting as it clearly indicates that it is necessary to separate the criterion for the fracture load, which is normally the most interesting, from the criterion for crack propagation. Finally, at position 4 a real crack has advanced a distance of about 30 mm.

In Fig 5.5 the load is shown as a function of the position of the tip of the fracture zone (defined as the distance from the notch tip) for different relative notch depths. The curves are relevant for 0.2 m deep, normal quality concrete beams in three-point bending. For the curve representing the unnotched beam (a/d=0) the fracture zone will not propagate until the tensile strength is reached at the bottom of the beam but for the notched beams the fracture zone, due to the stress concentrations, starts developing as soon as the specimen becomes loaded. The circles on the curves correspond to the positions where a real crack starts propagating and consequently, before these points are reached, the curves show the depth of the fracture zone. The depth of the fracture zone decreases as the notch depth increases which is explai-

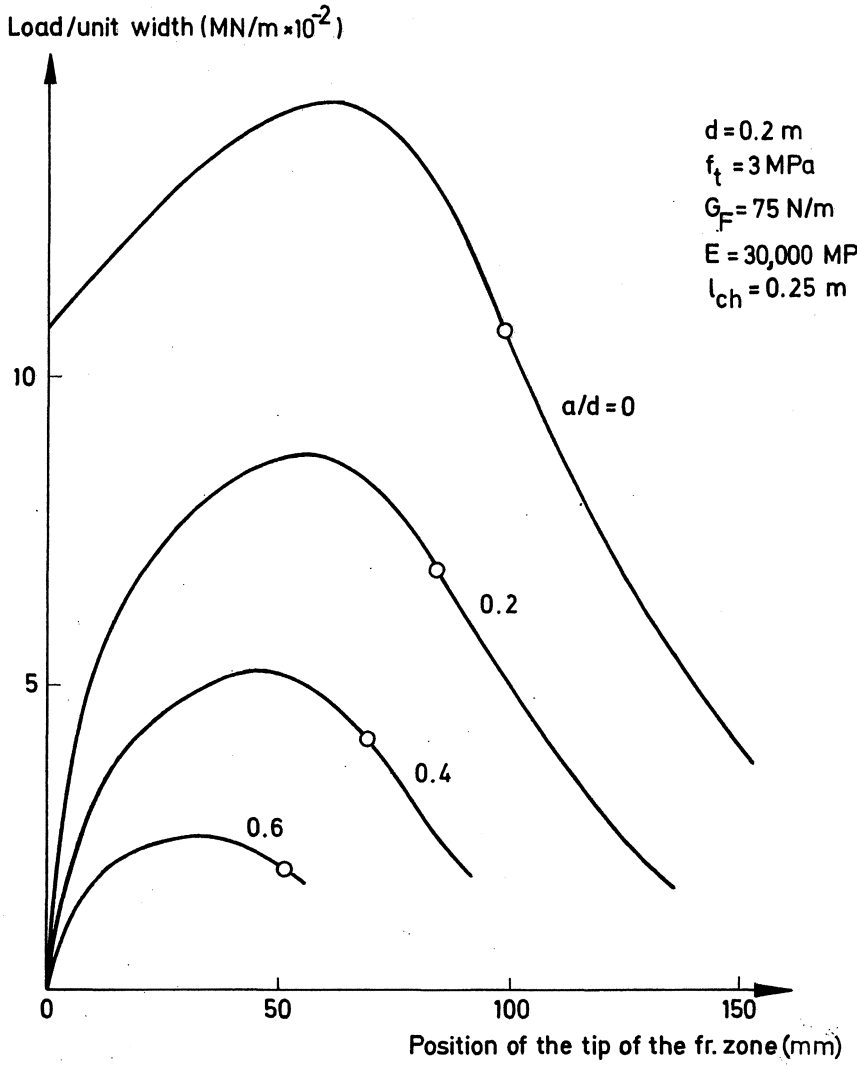

Fig 5.5 The load as a function of the position of the tip of the fracture zone (defined as the distance from the notch tip) for different relative notch depths. The curves are relevant for 0.2 m deep beams in three-point bending. The dimensions and the material properties are the same as those used in Fig 5.4. The dots represent the positions where real cracks start propagating.

ned by the simple fact that the available space for the fracture zone decreases as the notch depth increases.

In Fig 5.6 the depth of the fracture zone at the maximum load is shown as functions of the beam depth for a normal concrete quality. Also here the available space plays an important role and the depth of the fracture zone increases with increasing beam depth. However, the increase in the depth of the fracture zone is less than proportional to the increase in the beam depth and consequently the ratio depth of the fracture zone/beam depth decreases with

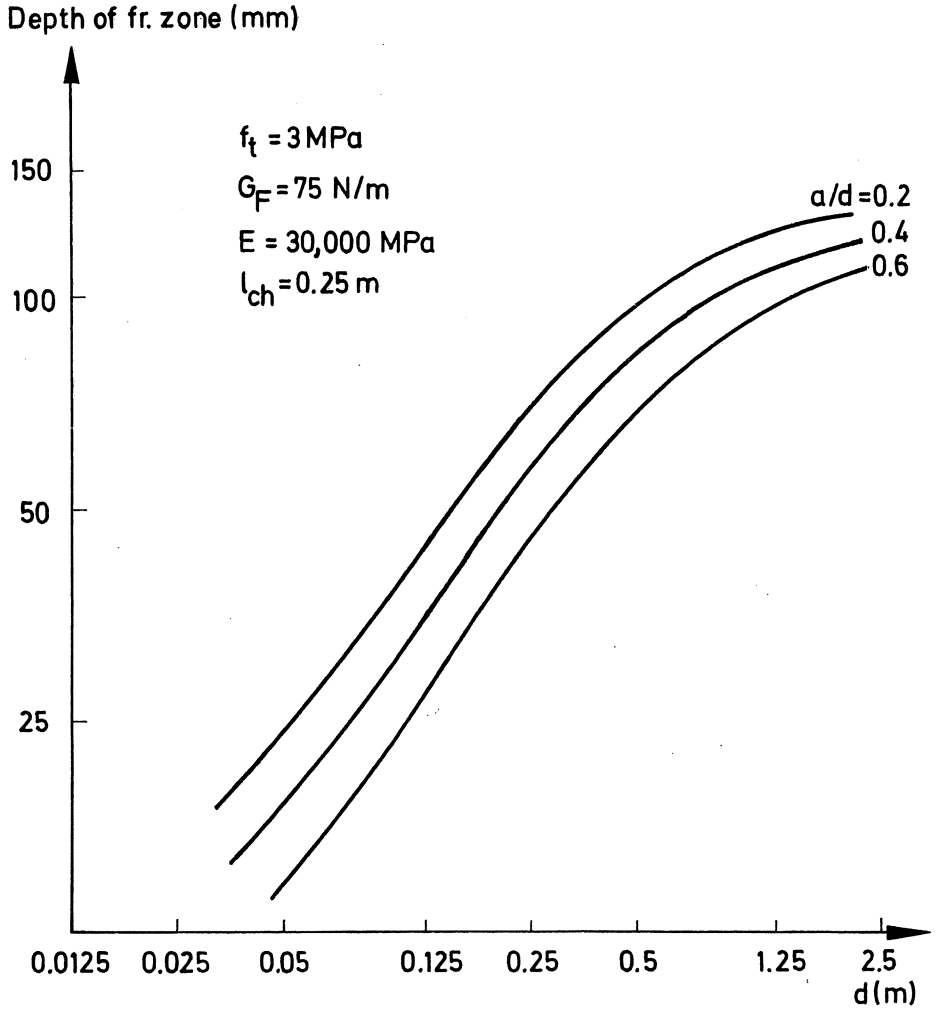

Fig 5.6 The depth of the fracture zone at the maximum load as function of beam depth for different relative notch depths. The curves are relevant for three-point bending and the material properties are the same as those used in Fig 5.4.

increasing beam depth. This means that the fracture behaviour of concrete and similar materials is size dependent which is illustrated by a number of examples in Chapter 6. For deep beams the depth of the fracture zone seems to reach a limiting value of about 125-150 mm. The limiting value ought to be dependent on the test technique, for example where the direct tensile test is concerned such a limiting value does not exist. Test results presented by Entov and Yagust (1975) indicate that high, local strains exist 50-100 mm in front of the notch tip in large, centrally notched tensile specimens and results presented by Sok, Baron and François (1979) show high strains several hundreds of millimeter in front of the notch tip in large double cantilever beams (the results according to Sok et al are probably a bit overestimated which is discussed in 6.5). These results confirm the calculation results showing that deep fracture zones develop in front of notches in concrete structures.

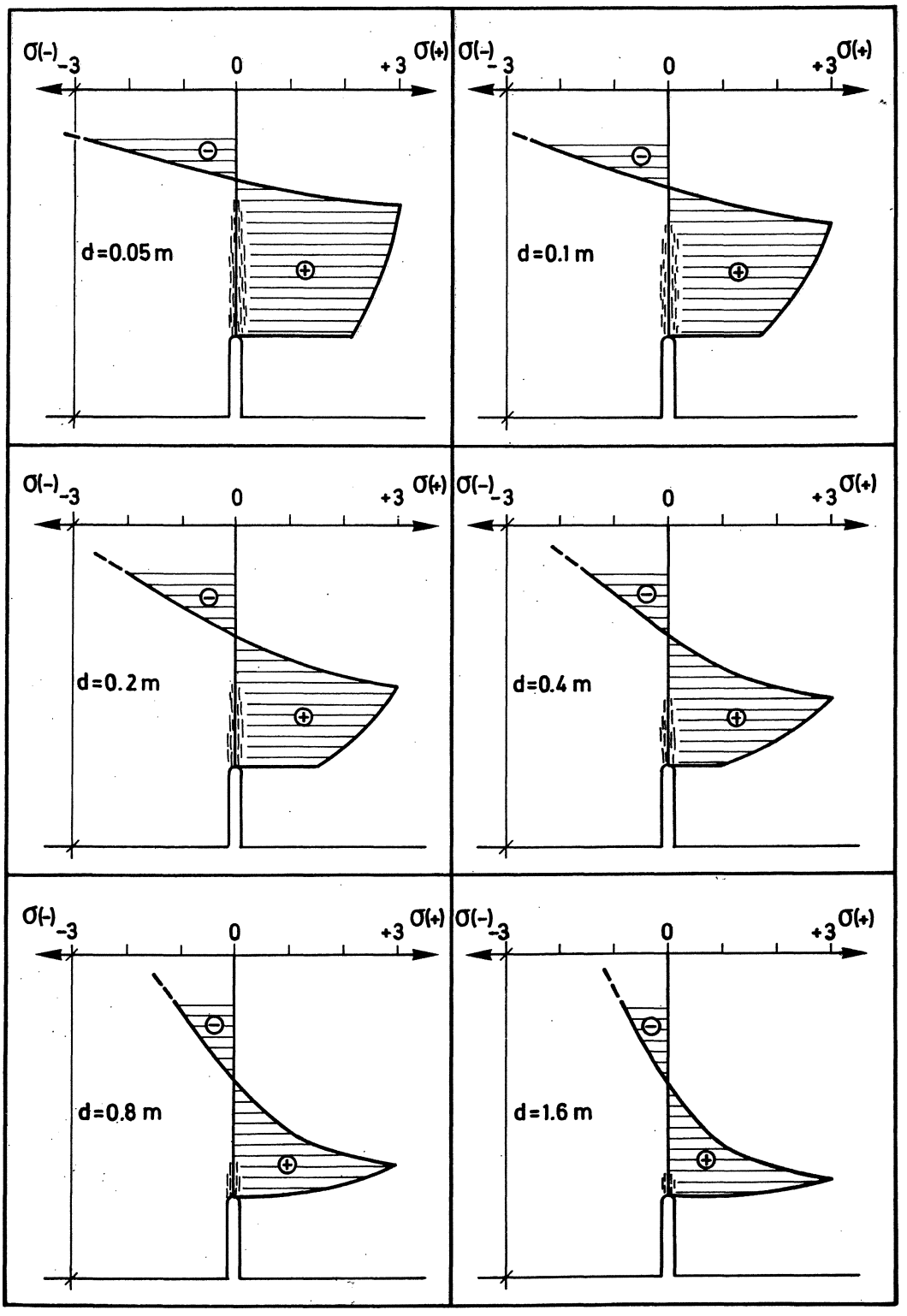

Fig 5.7 The fracture zone and the stress distribution in front of the notch tip at the maximum load for different beam depths. The Figure is relevant for three-point bending (a/d=0.25) and the material properties are the same as those used in Fig 5.4 (f_t=3MPa, G_F=75N/m, E=30,000MPa, ℓ_{ch}=0.25 m).

It is not only the depth of the fracture zone that is affected by the beam depth but also the stress distribution within the zone. In Fig 5.7 the stress distribution at the maximum load in front of the notch tip is shown for different beam depths. The relative notch depth is 0.25 and the results are relevant for a normal concrete quality. The stress transferring capability at the notch tip decreases as the beam depth increases and consequently a real crack starts propagating closer to the maximum load for deeper beams. The fracture zone is more efficient in reducing the stress concentrations at the crack tip for low values of the beam depth and the stress distribution becomes more similar to the distribution according to the linear elastic solution as the beam depth increases. This of course contributes to the size dependency of the fracture behaviour where concrete and similar materials are concerned.

6 THE FICTITIOUS CRACK MODEL vs OTHER APPROACHES

6.1 Introduction

Linear elastic fracture mechanics is the most frequently used approach for cementitious materials but the J-integral, the COD-approach and R-curves have also been applied to plain and fibre-reinforced concrete. All these approaches have, more or less successfully, been applied to metals and most of the work carried out in the field of fracture mechanics and concrete has therefore been concentrated on experimental tests, where the relevance for concrete of the existing approaches has been studied. This has resulted in numereous and often contradictory test data concerning K_c, G_c, J_c, COD_c and R-curves for example. In this Chapter these test data are compared with results derived by use of the Fictitious Crack Model and the usefulness of the approaches when applied to cementitious materials is also discussed.

Four different "model" materials have been analysed. The σ-ε curve is approximated with a straight line for all the materials but the σ-w curves are quite different and are presented in Fig:s 6.1-6.4.

If the shape of the σ-w curve is unknown then the straight line approximation (SL) according to Fig 6.1 is probably the most rational. For plain concrete this simple approximation often gives satisfying results, which is discussed later. Normal values of G_F and f_t for concrete are 100 N/m and 4 MPa respectively, see Chapter 7, and this means that w_c, i.e. the maximum widening of the fracture zone when it is still able to transfer stress, in this case is 0.05 mm.

The approximation according to Dugdale (D) in Fig 6.2 is probably most suitable for yielding materials such as mild steels and many qualities of plastics. The curve is used here as it is often referred to in the literature. In some special cases the curve can be used as a rough approximation for some qualities of fibre-reinforced concretes.

In Chapter 8 results showing the real shape of the σ-w curve for a number of concrete qualities are presented. According to these results, the curve in Fig 6.3 (C) seems to be the best two line approximation for most normal concrete qualities. This curve therefore describes the properties of the fracture zone in concrete in a more realistic and consequently a better way than the simple approximation in Fig 6.1.

The shape of the σ-w curve for fibre-reinforced materials is greatly dependent

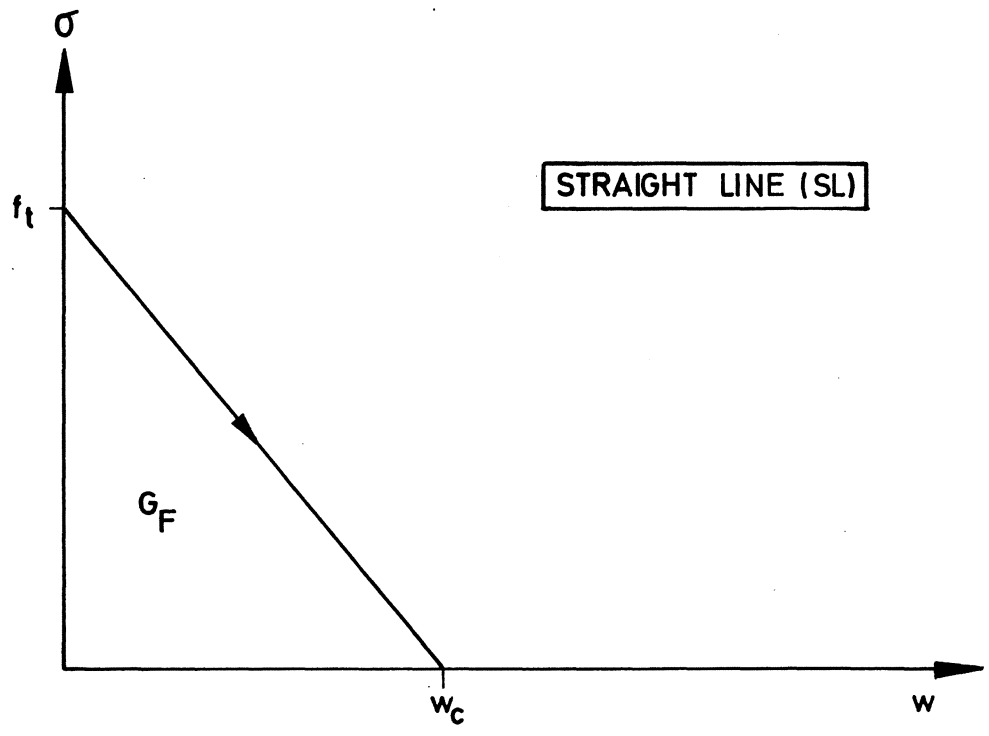

Fig 6.1 The σ-w curve approximated to a single, straight line (SL).

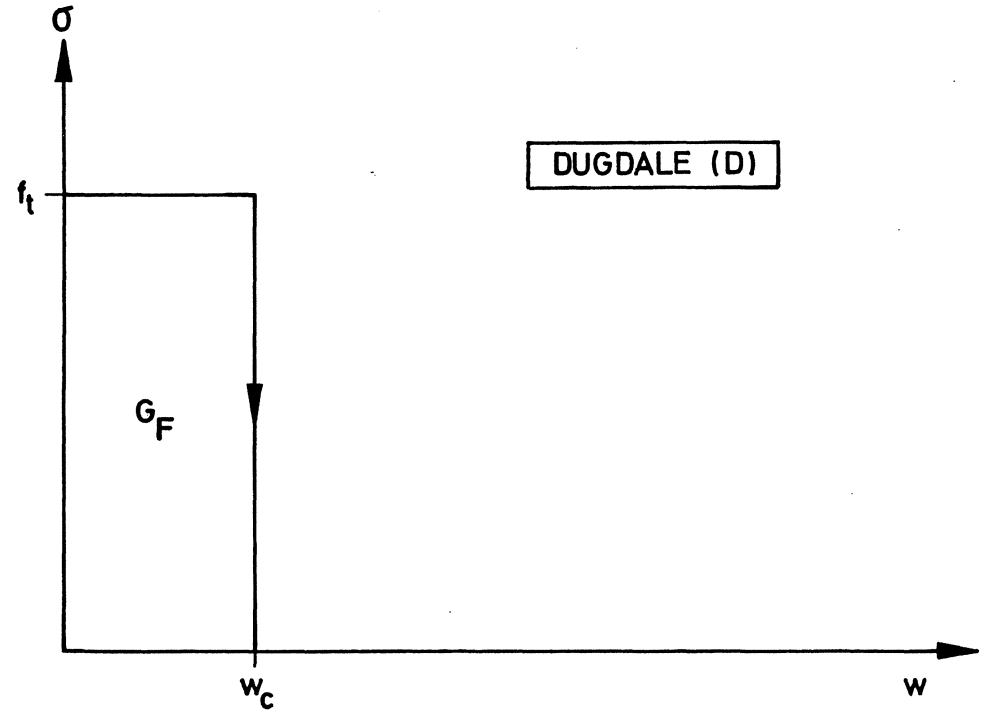

Fig 6.2 A σ-w curve according to Dugdale (D).

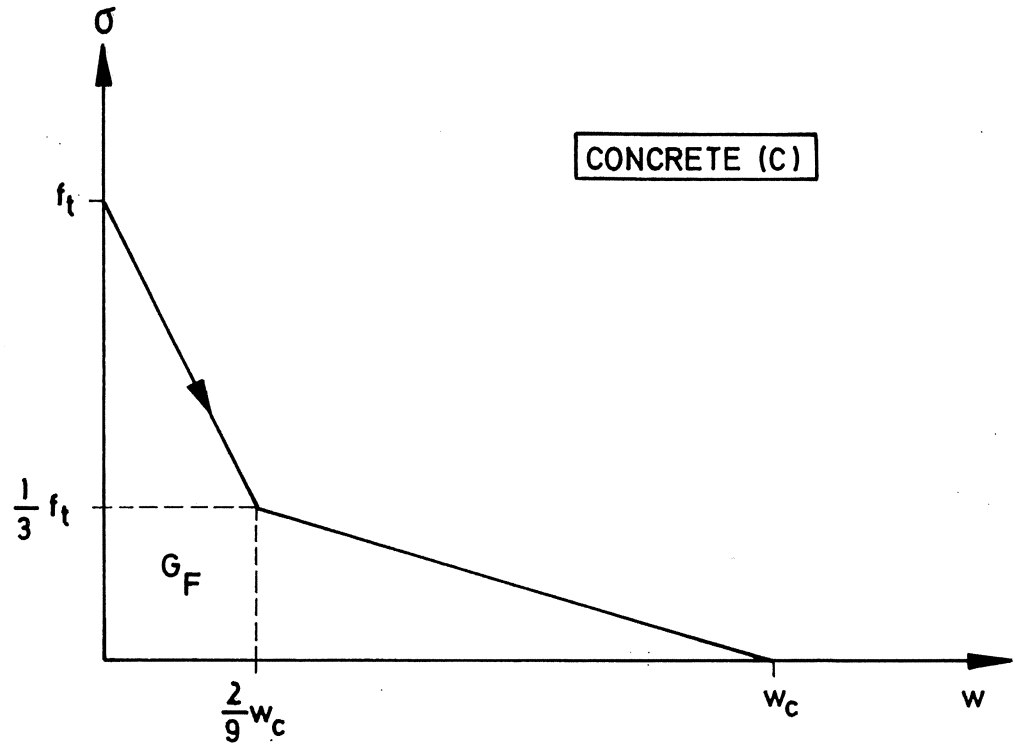

Fig 6.3 A two-line approximation of the σ-w curve that seems to be suitable for most normal concrete qualities (C).

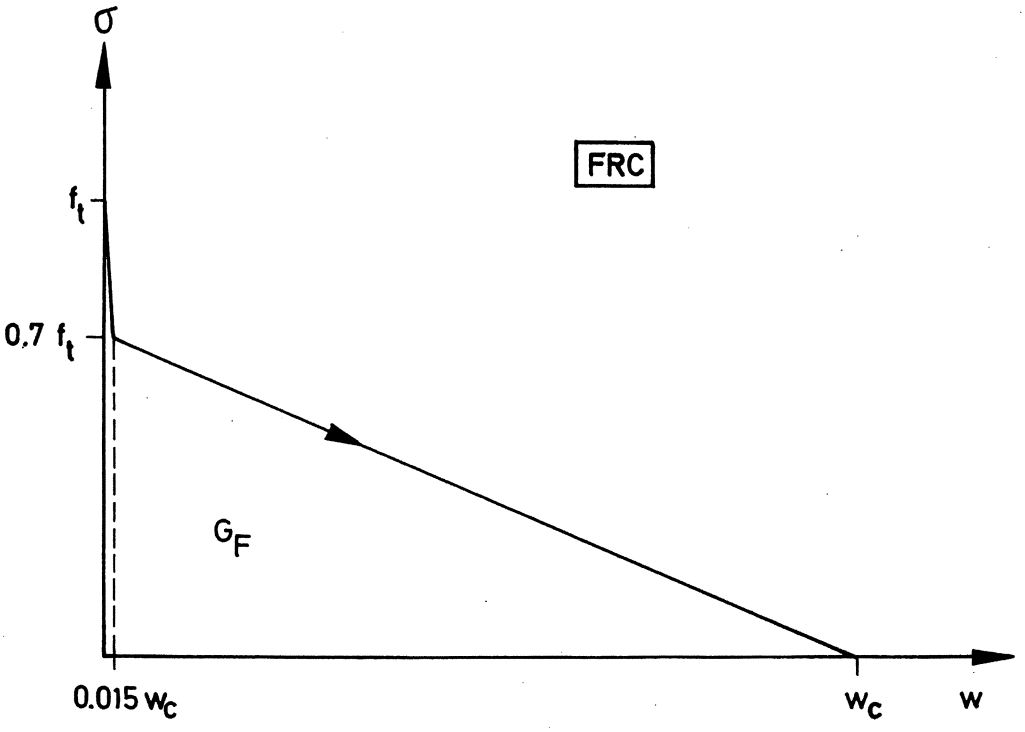

Fig 6.4 An example of a σ-w curve representing a fibre-reinforced material (FRC).

on the type of fibre and fibre content for example. The curve in Fig 6.4 shows an example of such a curve. If f_t is 4 MPa and G_F about 1400 N/m, then the initial slope of the curve is similar to that of concrete and w_c is about 1 mm. Then this curve ought to represent a fibre-reinforced concrete (FRC) with a fairly low percentage of short fibres.

The calculations in this Chapter mainly deal with the three-point bend test. In the calculations the finite element mesh in Fig 4.11 was used. In Fig 6.5 typical load-deflection curves for the four model materials are shown. The curves represent beams that are 0.2 m deep, 0.2 m wide, 0.8 m long and the relative notch depth is 0.4. For all the materials the Young's modulus and the tensile strength are 40,000 MPa and 4 MPa respectively. For the σ-w curve according to Fig 6.4 G_F is 1430 N/m, which, as mentioned above, corresponds to a fibre-reinforced concrete with a fairly low percentage of short fibres.

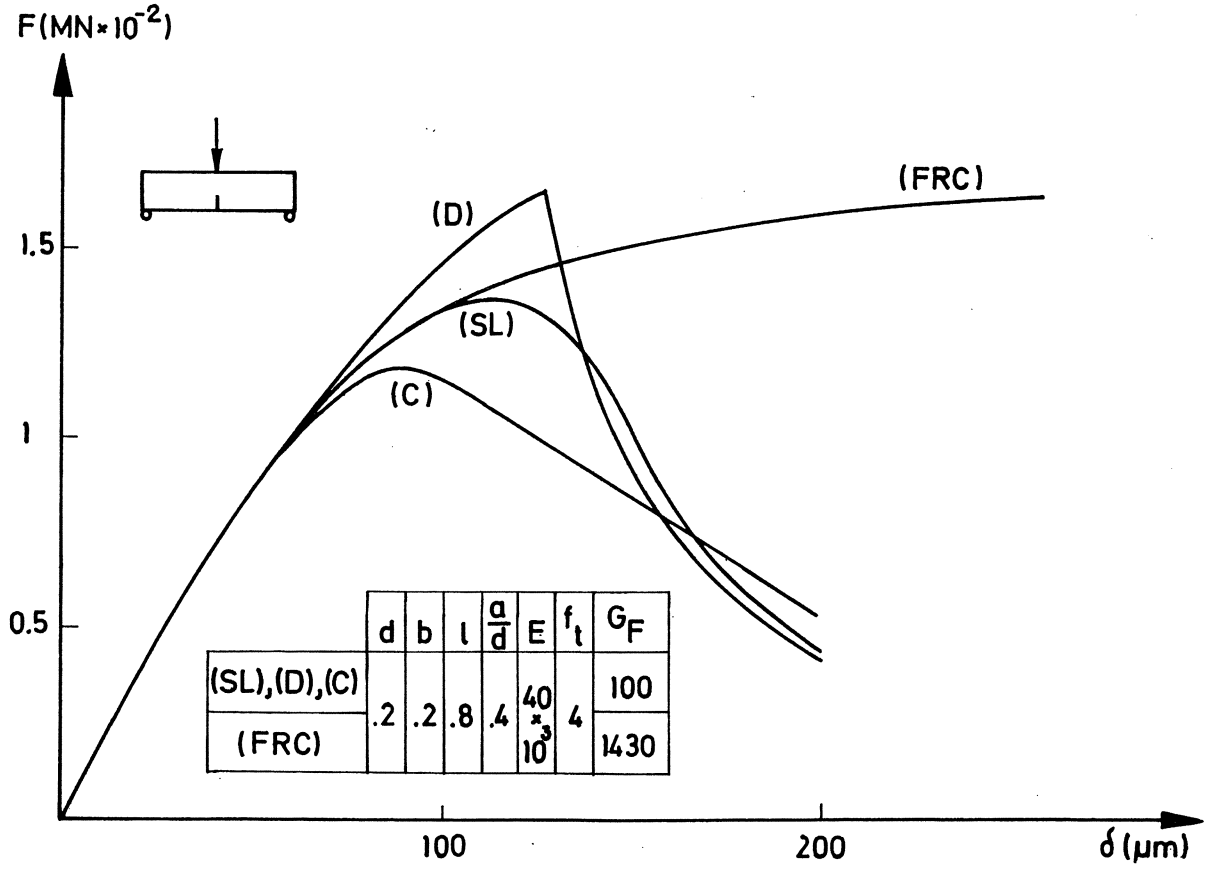

Fig 6.5 Calculated load-deflection curves for the four model materials presented in Fig:s 6.1-6.4. The curves are relevant for three-point bend tests on notched beams. The dimensions are m for d, b and ℓ, MPa for E and f_t and N/m for G_F.

For the other σ-w curves G_F is 100 N/m, which corresponds to a normal value for concrete. As can be seen, the shape of the σ-w curve considerably affects the calculation result. This means that the shape of the σ-w curve is an important parameter that has to be considered when analysing the fracture process of a material.

6.2 Linear elastic fracture mechanics

6.2.1 Notch sensitivity

In the literature results from a large number of linear elastic fracture mechanics tests on cementitious materials are reported, which are discussed in 6.2.2. The results from different tests are often conflicting and this has given rise to doubts about the usefulness of fracture mechanics, where concrete and mortar are concerned. Therefore, in order to study the applicability of fracture mechanics to cementitious materials, notch sensitivity tests have been carried out. The notch sensitivity is defined as f_f^{net}/f_f (net. flexural tensile strength/flexural tensile strength) where f_f^{net} for a three-point bend test on a notched beam is:

$$f_f^{net} = \frac{3\ell}{2b} \frac{1}{(d-a)^2} F_c \qquad (6:1)$$

where ℓ = beam length, b = beam width, d = beam depth, a = notch depth and F_c = fracture load. f_f equals f_f^{net} when a = 0.

The notch sensitivity for linear elastic materials has been dealt with by Ziegeldorf et al (1980). They showed that the notch sensitivity can be expressed as:

$$\frac{f_f^{net}}{f_f} = \frac{K_c}{f_f} \times \frac{1}{\sqrt{a}(1-a/d)^2 f(a/d)} \qquad (6:2a)$$

where f(a/d) for a three-point bend test is (Brown and Srawley, 1967):

$$f(a/d) = 1.93-3.07(a/d)+14.53(a/d)^2-25.11(a/d)^3+25.8(a/d)^4 \qquad (6:3)$$

(6:2a) can be expressed as:

$$\frac{f_f^{net}}{f_f} \times \frac{f_f \sqrt{d}}{K_c} = \frac{1}{\sqrt{a/d}(1-a/d)^2 f(a/d)} \qquad (6:2b)$$

By using (6:2b), the notch sensitivity as a function of the relative notch depth can be described by a single curve according to Fig 6.6.

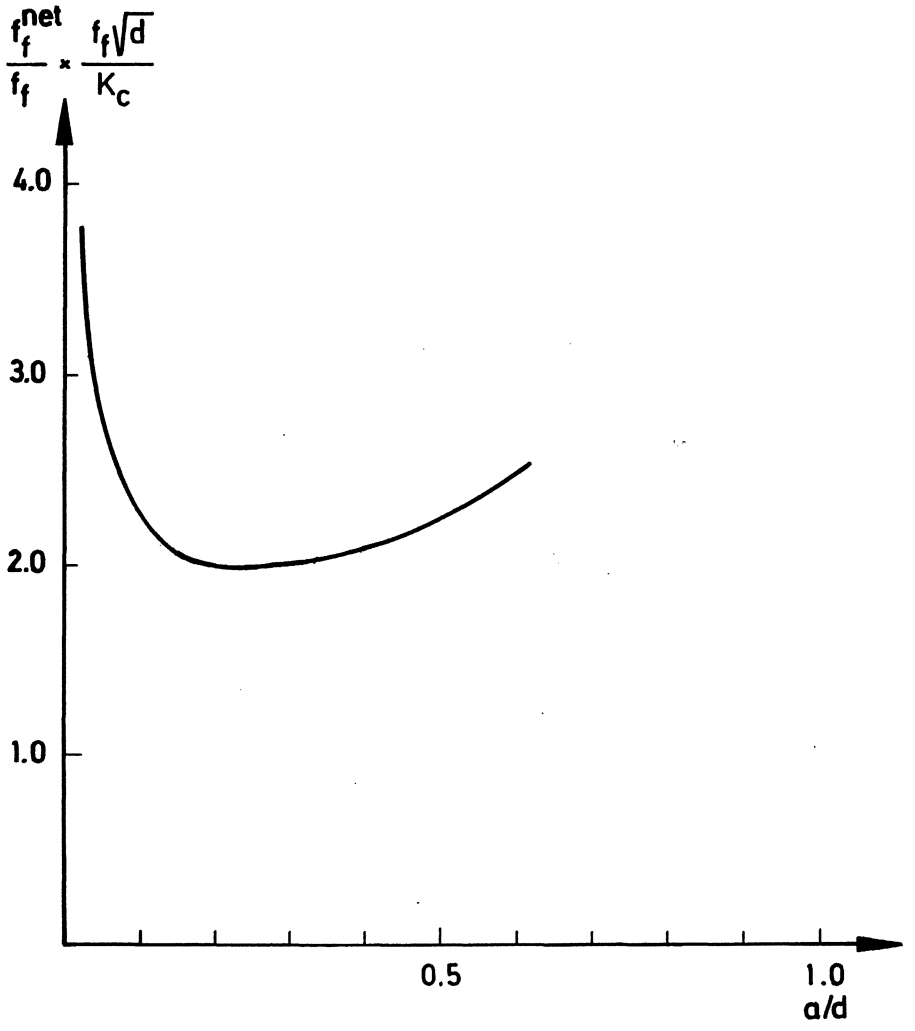

Fig 6.6 Notch sensitivity as a function of relative notch depth (a/d) and $f_f\sqrt{d}/K_c$ for materials that can be treated by means of linear elastic fracture mechanics.

The curve in Fig 6.6 shows that the beam is most notch sensitive when the relative notch depth is 0.2-0.3. The notch sensitivity increases with increasing beam depth and decreasing values of the parameter K_c/f_f. However, the curve is relevant only when linear elastic fracture mechanics is applicable, which considerably limits its usefulness. For example, when $f_f\sqrt{d}/K_c$ is less than 2, then the notch sensitivity exceeds 1 for all notch depths, which seems unrealistic. Furthermore, the notch sensitivity ought to reach 1 when the notch depth is zero but this is not the case which is explained by the fact that linear elastic fracture mechanics is normally not applicable when the relative notch depth is too small.

More realistic notch sensitivity curves can be determined by using the Fictitious Crack Model, see the unbroken lines in Fig 6.7. In the calculations the σ-w curve was approximated with a single straight line.

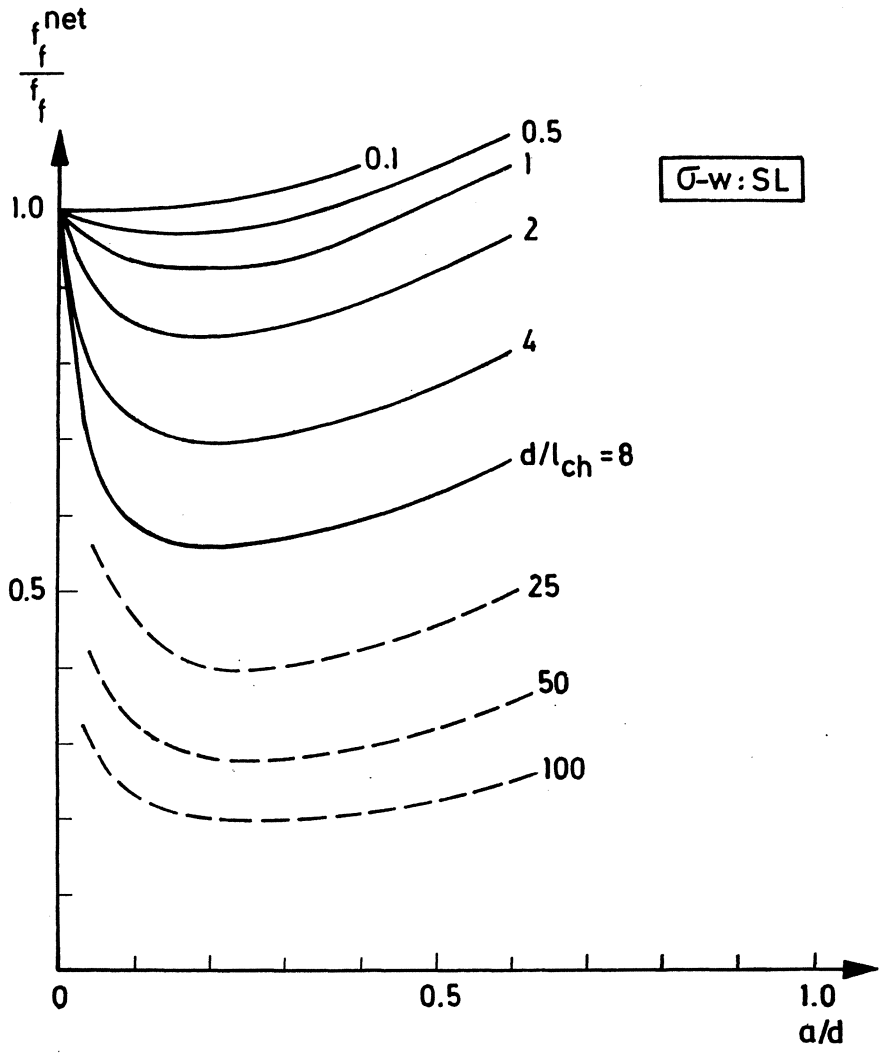

Fig 6.7 Notch sensitivity as function of relative notch depth and d/ℓ_{ch} calculated by means of the Fictitious Crack Model (unbroken lines) and linear elastic fracture mechanics (dashed lines) respectively. In the calculations a σ-w curve according to Fig 6.1 (SL) was used.

As can be seen in Fig 6.7, notch sensitivity is not a pure material property as it is dependent on the specimen dimensions. A normal value of ℓ_{ch} for concrete is 250 mm and consequently a 100 mm deep beam is relatively notch insensitive while a 1 m deep beam is considerably affected by a notch. A probable value of ℓ_{ch} for cement paste is 5-10 mm (Modéer, 1979) which means that this material is notch sensitive already at beam depths of 10-20 mm. The results in Fig 6.7 also imply that for notched beams with d/ℓ_{ch}-values less than about 1 the approximative fracture criterion $f_f^{net}=f_f$ is usable. However,

when using this simple criterion it must be remembered that f_f depends on specimen dimensions and fracture mechanical properties of the material, see 7.2.

The finite element mesh used in the calculations is too coarse to be used for d/ℓ_{ch}-values exceeding about 8 when the distances between the forces in the fracture zone are $0.2\ell_{ch}$. However, when d/ℓ_{ch} increases, the material becomes more "brittle" and the usefulness of linear elastic fracture mechanics increases. In 6.2.2 and 7.2 the critical strain energy release rate (G_c) and the tensile strength (f_t) are discussed and it is shown that when linear elastic fracture mechanics is applicable, $G_c \approx G_F$ and $f_t \approx f_f$. According to (2:8) and

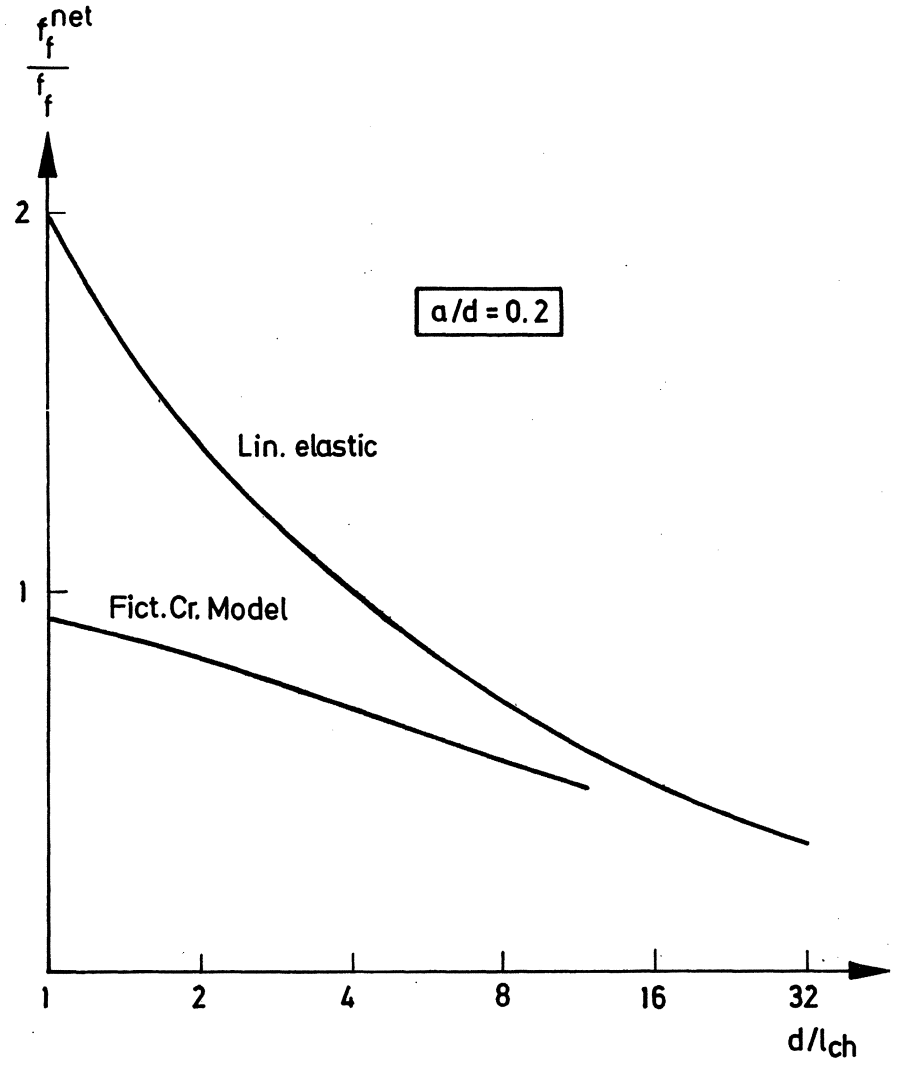

Fig 6.8 The notch sensitivity for the relative notch depth 0.2 as functions of d/ℓ_{ch}. The curves represent solutions according to the linear elastic fracture mechanics and the Fictitious Crack Model respectively.

(4:15) it is then obvious that $K_c/f_f \approx \sqrt{G_F E}/f_t = \sqrt{\ell_{ch}}$. This means that the linear elastic notch sensitivity curve in Fig 6.6 can be related to ℓ_{ch}. In Fig 6.8 the notch sensitivity for the relative notch depth 0.2 is shown as functions of d/ℓ_{ch}. The two curves represent solutions according to linear elastic fracture mechanics and the Fictitious Crack Model respectively. The curves are quite different where small values of d/ℓ_{ch} are concerned but the difference decreases as d/ℓ_{ch} increases. For practical applications therefore the linear elastic solution ought to be usable as an approximation for d/ℓ_{ch}-values exceeding about 10-20 when the difference between the curves is less than about 15 %.

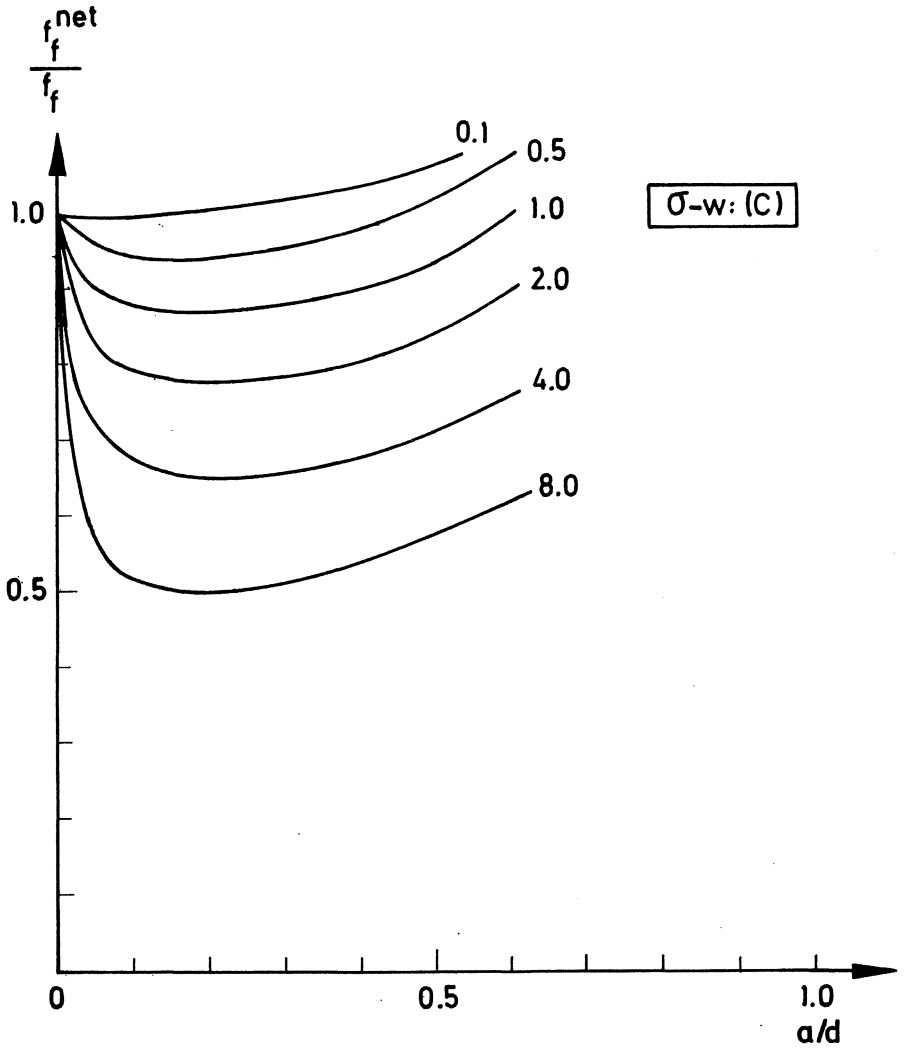

Fig 6.9 Notch sensitivity as function of relative notch depth and d/ℓ_{ch} calculated by means of the Fictitious Crack Model. In the calculations a two line approximation of the σ-w curve (C) according to Fig 6.3 was used.

In Fig 6.7 linear elastic notch sensitivity curves for d/ℓ_{ch}-values exceeding 25 are presented (dashed lines). These plus the curves determined by means of the Fictitious Crack Model give a complete set of notch sensitivity curves ranging from $d/\ell_{ch}=0.1$ to $d/\ell_{ch}=100$.

The notch sensitivity curves in Fig 6.9 represent materials with a two line approximation of the σ-w curve according to Fig 6.3. The differences between these curves and those presented in Fig 6.7 are small but the two line approximation of the σ-w curves seems to give a somewhat higher notch sensitivity. However, for practical applications the curves in Fig 6.7 ought to be sufficient for concrete. For fibre-reinforced materials the σ-w curves are often quite different and then notch sensitivity curves have to be calculated for each individual material.

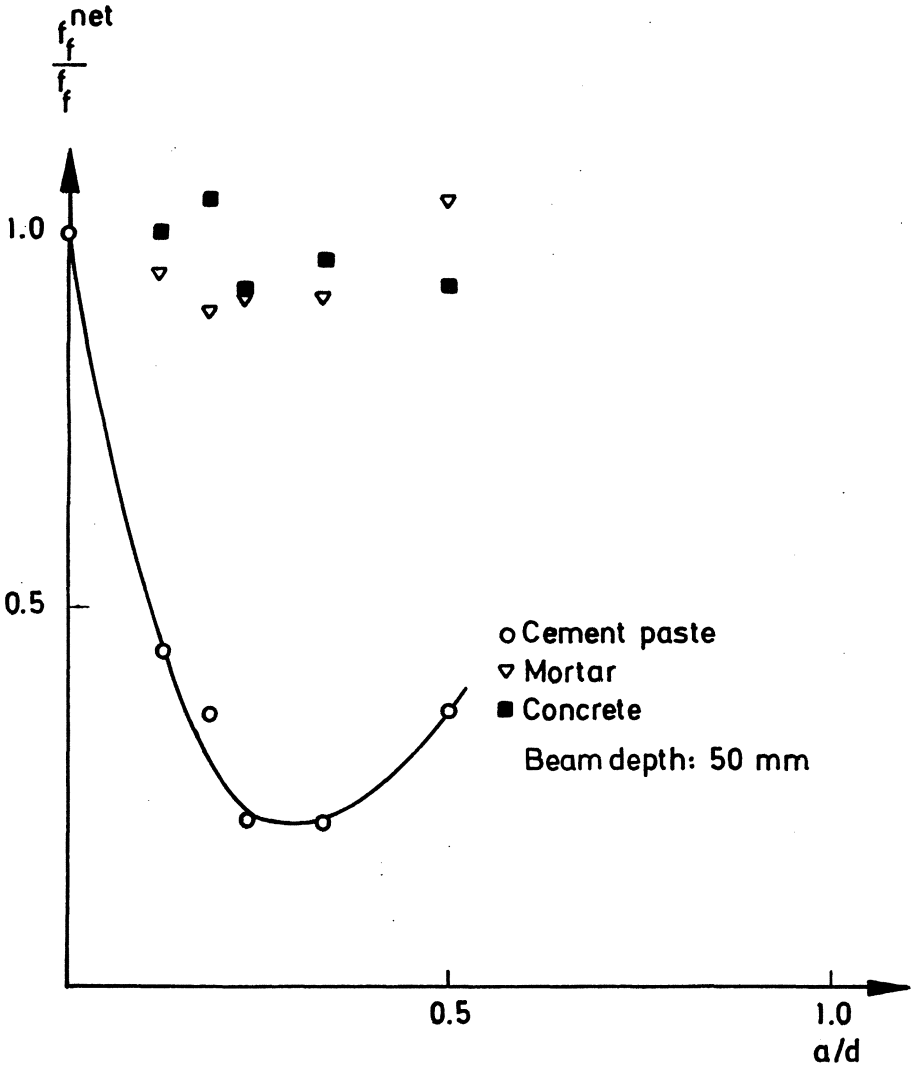

Fig 6.10 Experimental determined notch sensitivity curves for cement paste, mortar and concrete (Shah and McGarry, 1971)

In Fig 6.10 test results for concrete, mortar and cement paste are shown (Shah and McGarry, 1971). The results are derived from three-point bend tests on 50 mm deep beams. A normal value of ℓ_{ch} for concrete is 250 mm and for mortar 150 mm (see Chapter 7) which corresponds to d/ℓ_{ch}-values of 0.2 and 0.33 respectively. The test results show that concrete and mortar are, more or less, notch insensitive where the actual specimen size is concerned which agrees well with the theoretical curves in Fig 6.7. The results for mortar also show a minimum on the curve for a/d=0.2-0.3, exactly the same as for the theoretical curves.

The only available value of ℓ_{ch} for cement paste is 7 mm for a 7 days old paste (Modéer, 1979). In Chapter 7 it is shown that the ℓ_{ch}-value for concrete decreases rapidly with increasing age due to the fact that the tensile strength increases relatively faster than the fracture energy and the Young's modulus. The same ought to be relevant for cement paste and a d/ℓ_{ch}-value of 10-20 seems realistic in this case.

The test results indicate that cement paste is highly notch sensitive where the actual specimen size is concerned and the notch sensitivity is most pronounced when the relative notch depth is 0.25-0.30. This agrees well with the theoretical curves. However, the tests indicate a somewhat higher notch sensitivity than the calculations which is probably due to the lack of knowledge regarding the σ-w curve and the ℓ_{ch}-value of the actual cement paste and perhaps also to the testing conditions where for example shrinkage stresses can affect the results.

In Fig 6.11 other test results are presented (Gjørv, Sørensen and Arnesen, 1977), which are also carried out on three-point bent, 50 mm deep beams. In this case the agreement between the experimental and the theoretical curves for cement paste is good but the experimental curves indicate that both concrete and mortar are notch sensitive. This can be explained by the fact that the materials used were unconventional; the content of cement paste was about 52 % by volume in the concrete and 68 % by volume in the mortar! This definitely means that the ℓ_{ch}-values were much lower than those for ordinary concrete qualities.

The ℓ_{ch}-values for the materials used in the test ought to increase as the percentage of aggregate increases. Consequently the test results illustrate, in an excellent way, how the notch sensitivity increases with increasing d/ℓ_{ch}-values, exactly as for the theoretical curves. The entire amount of

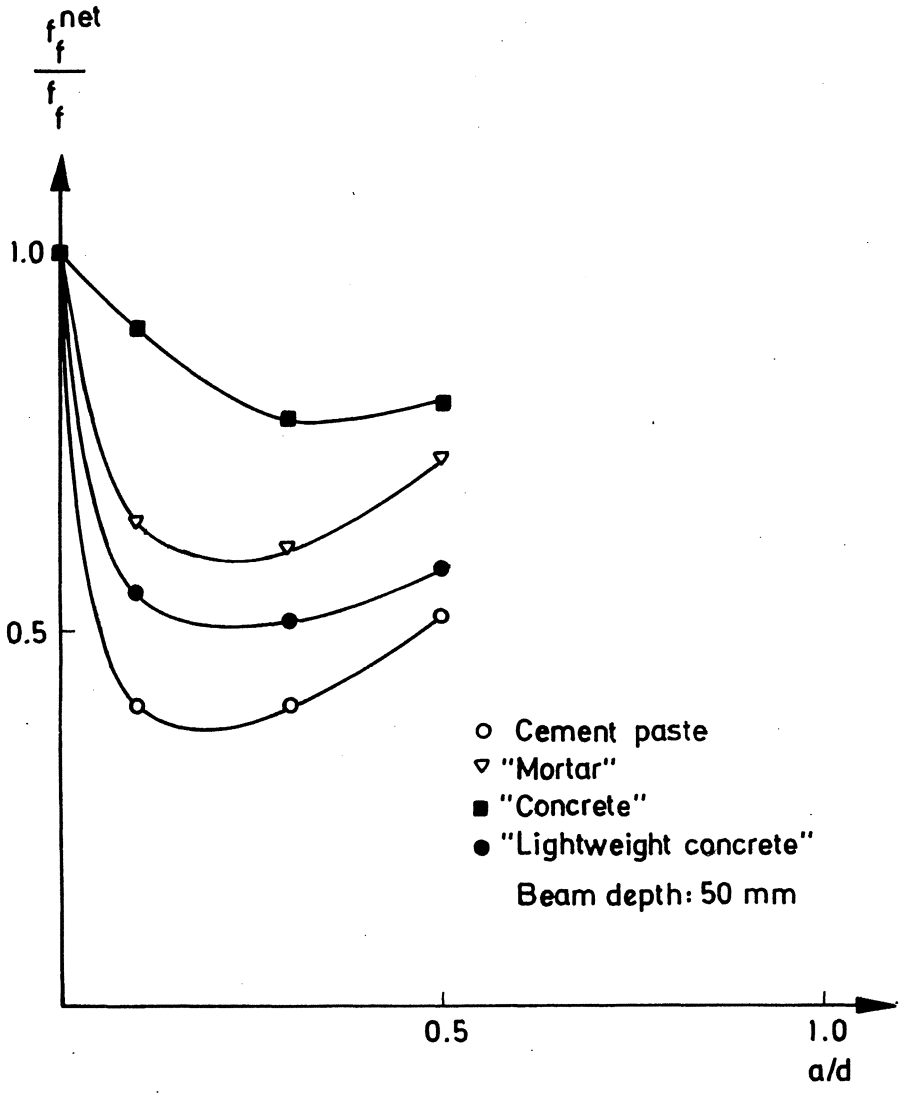

Fig 6.11 Experimental determined notch sensitivity curves for cement paste, "mortar", "concrete" and "light-weight concrete" (Gjørv, Sørensen and Arnesen, 1977)

aggregate in the light-weight concrete was expanded clay. The capability of this type of aggregate in preventing crack propagation is poor (see Chapter 7) and therefore the light-weight concrete ought to be almost as brittle as the cement paste which explains the position of the notch sensitivity curve for this material.

Experimental results in agreement with those in Fig 6.10 and Fig 6.11 are also reported by Higgins and Bailey (1976), Hillemeier and Hilsdorf (1977) and Ziegeldorf, Müller and Hilsdorf (1980).

6.2.2 K_c- and G_c-approaches

The critical strain energy release rate (G_c) represents the energy consumption per unit crack area at the crack tip when the crack propagates, i.e. the amount of energy necessary to create one unit of area of a crack. However, G_c is strictly defined only for linear elastic materials and where other materials are concerned, G_c is always an approximate value of the amount of energy necessary to create one unit of area of a crack.

The fracture energy (G_F) is another measure of the amount of energy necessary to create one unit of area of a crack. G_F equals the area under the σ-w curve and consequently G_F is not only defined for linear elastic materials but in principle for all materials in which cracks can propagate.

According to the definitions above it is obvious that G_c equals G_F where linear elastic materials are concerned. For this reason the ratio G_c/G_F ought to be useful as a measure of how well linear elastic fracture mechanics describes the fracture of a structure; the closer G_c/G_F is unity, the better the linear elastic fracture mechanics approximation is.

In Fig 6.12 the ratio G_c/G_F is shown as function of d/ℓ_{ch} and relative notch depth for a three-point bend test. The calculations are carried out by means of the Fictitious Crack Model. In the calculations K_c was first calculated according to (2:9) and (6:3) and then these results were converted to G_c by using (2:8). The σ-w curve was approximated to a single straight line (SL).

As can be seen in the Figure, the ratio G_c/G_F increases with increasing values of d/ℓ_{ch} and finally it ought to approach unity. This means:

$$\lim_{d/\ell_{ch} \to \infty} G_c = G_F \qquad (6:3)$$

and consequently, according to (2:8):

$$\lim_{d/\ell_{ch} \to \infty} K_c = \sqrt{G_F E} \qquad (6:4)$$

(6:3), (6:4) and (2:8) show that $K_c/\sqrt{G_F E} = \sqrt{G_c/G_F}$ and consequently the two ratios can be represented by the same curve in log-diagrams where the modulus of the logscale for $K_c/\sqrt{G_F E}$ is twice the modulus of the log-scale for G_c/G_F. In Fig 6.12 the ratio $K_c/\sqrt{G_F E}$ is represented by the vertical log-scale to the right.

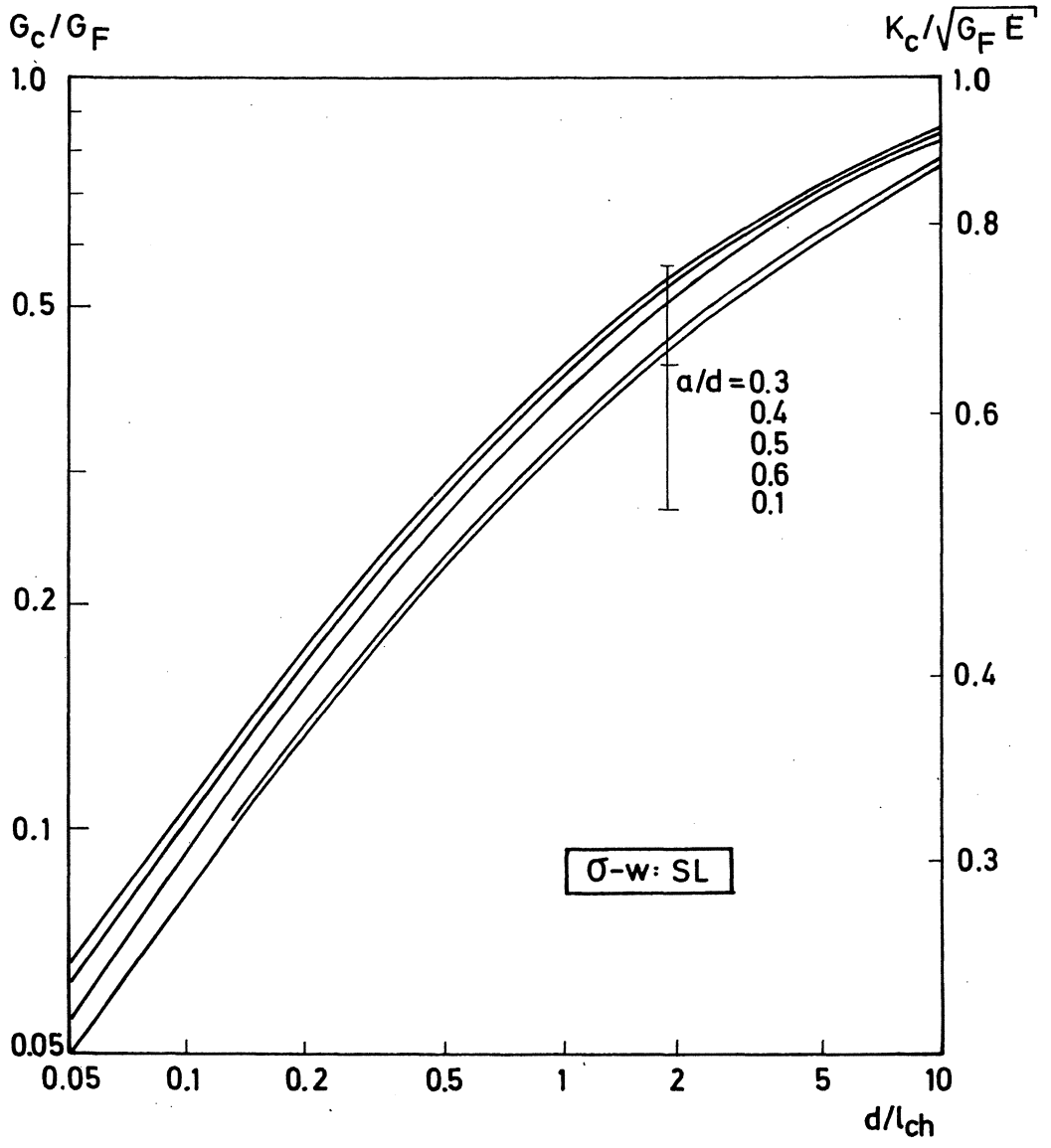

Fig 6.12 Theoretical values of G_c/G_F and $K_c/\sqrt{G_F E}$ as functions of d/ℓ_{ch} for different relative notch depths. The curves are relevant for three-point bend tests and the σ-w curve is approximated with a single, straight line (SL) according to Fig 6.1.

Normally the fracture load is the most interesting thing to study when analysing a structure by means of fracture mechanics. The fracture load is directly related to K_c, see (2:9), which means that when K_c deviates from the correct value by a certain amount then the fracture load, predicted by means of linear

elastic fracture mechanics, will also deviate from the true value by the same amount. For practical applications it seems reasonable to accept a deviation of about 10 % of the fracture load (or K_c) and consequently, according to Fig 6.12, if this criterion is to be fulfilled when linear elastic fracture mechanics is used, the value of d/ℓ_{ch} should exceed about 10. For concrete, which normally has a ℓ_{ch}-value of 200-300 mm, linear elastic fracture mechanics then is applicable only for beam depths greater than 2-3 m. In tests it has been customary to use beam depths of 25-300 mm, which correspond to d/ℓ_{ch}-values of 0.1-1 and then the K_c-value is only 30-60 % of $\sqrt{G_F E}$ and the G_c-value only 10-40 % of G_F. Furthermore, in this region K_c and G_c are strongly size dependent. This implies that the applicability of linear elastic fracture mechanics is extremely limited where concrete is concerned.

Cement paste has ℓ_{ch}-values less than 10 mm and consequently linear elastic fracture mechanics is useful only when the beam depth exceeds about 100 mm. However, in real structures cement paste is used only as a part of the concrete and mortar and in this case the thickness of the layer of paste never exceeds a few mm. This means that also where cement paste is concerned, which is normally considered to be a very brittle material, the usefulness of linear elastic fracture mechanics for practical purposes is very limited.

In Fig 6.12 curves representing different relative notch depths are shown but the dependency of the notch depth is more clearly illustrated in Fig 6.13, where G_c/G_F and $K_c/\sqrt{G_F E}$ are presented as functions of relative notch depth for different values of d/ℓ_{ch}. The curves in the Figure are relevant for a σ-w curve approximated with a single, straight line (SL). As can be seen in the Figure, G_c, and thus K_c, reach a maximum when a/d is about 0.25-0.30. In tests it is customary to use relative notch depths between 0.2 and 0.5. Within this region the influence of a/d on G_c and K_c is small and it is therefore difficult to detect this influence from experimental results.

In Fig 6.14 and Fig 6.15 the dependency of geometry and material parameters on K_c and G_c is shown regarding another approximation of the σ-w curve. In the calculations a two-line σ-w curve (C) according to Fig 6.3 was used. The shapes of the curves are similar to those in Fig 6.12 and Fig 6.13 but the values of K_c and G_c are lower for the same value of d/ℓ_{ch}. This means that the restrictions for the applicability of linear elastic fracture mechanics become even harder than when the σ-w curve is approximated with a single, straight line. This is contrary to the conditions according to the notch sen-

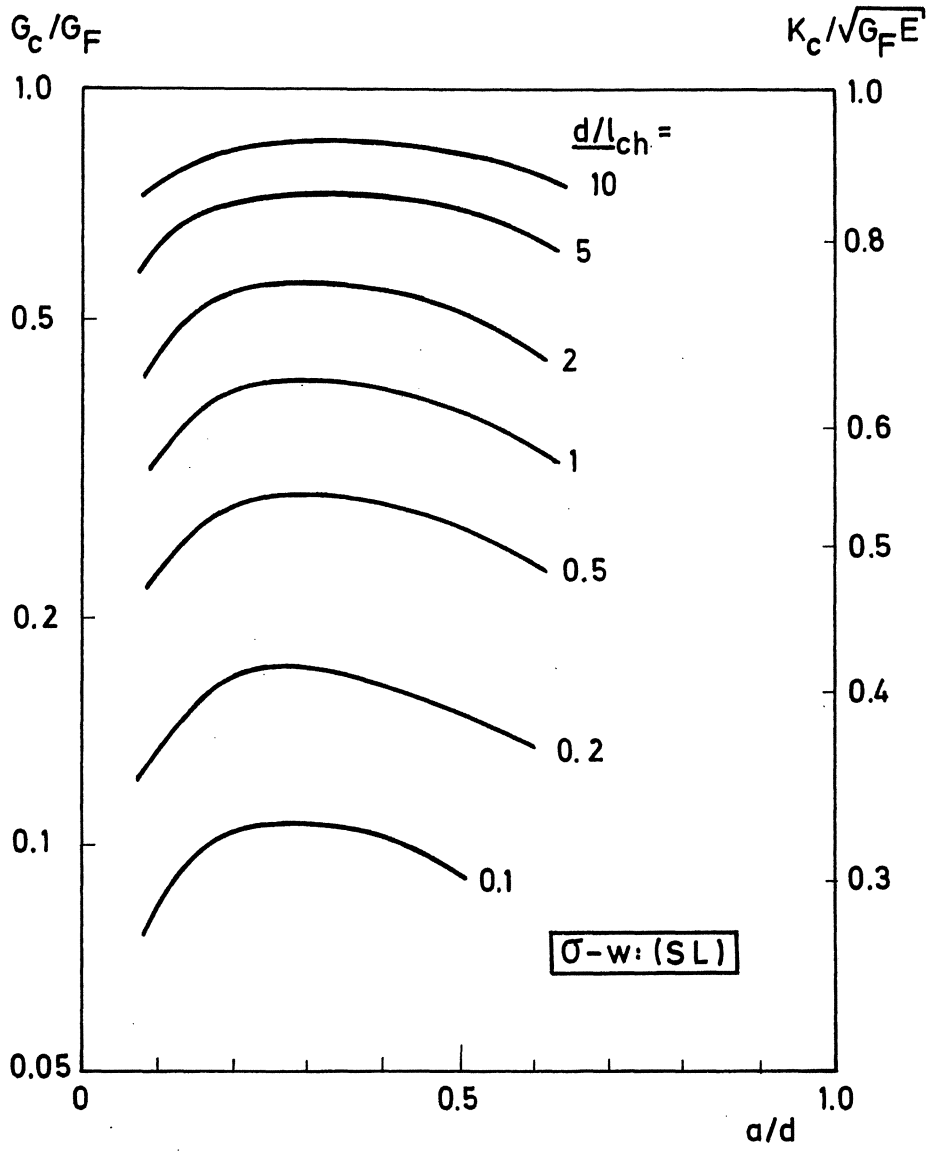

Fig 6.13 Theoretical values of G_c/G_F and $K_c/\sqrt{G_F E}$ as functions of relative notch depth for different values of d/ℓ_{ch}. The curves are relevant for three-point bend tests and the σ-w curve is approximated with a single, straight line (SL) according to Fig 6.1.

sitivity, which give a somewhat higher notch sensitivity for the two-line approximation of the σ-w curve than for the σ-w curve approximated with a single straight line. This can be explained by the fact that the notch sensitivity is not only affected by the maximum load of the notched specimen but also by the flexural tensile strength, which itself is affected by the shape of the σ-w curve. The ratio G_c/G_F (or $K_c/\sqrt{G_F E}$) therefore ought to be

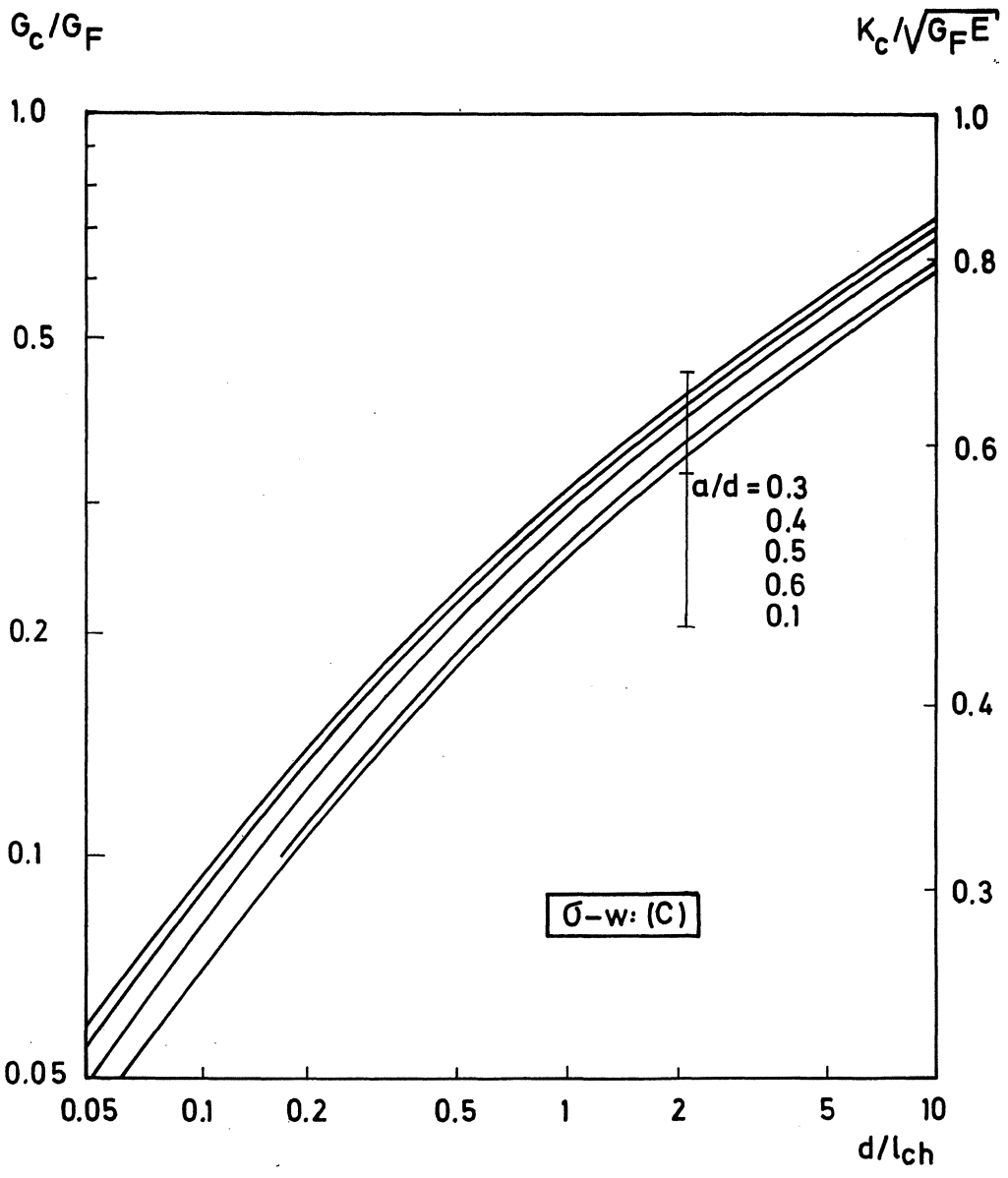

Fig 6.14 Theoretical values of G_c/G_F and $K_c/\sqrt{G_F E}$ as functions of d/ℓ_{ch} for different relative notch depths. The curves are relevant for three-point bend tests and the σ-w curve is approximated with two lines (C) according to Fig 6.3.

better as a measure of the applicability of linear elastic fracture mechanics than the notch sensitivity.

In Fig 6.16 theoretical values of G_c/G_F and $K_c/\sqrt{G_F E}$ are shown as functions of d/ℓ_{ch} for different approximations of the σ-w curve. The approximation according to Dugdale shows an upper limit of the curves but even when this

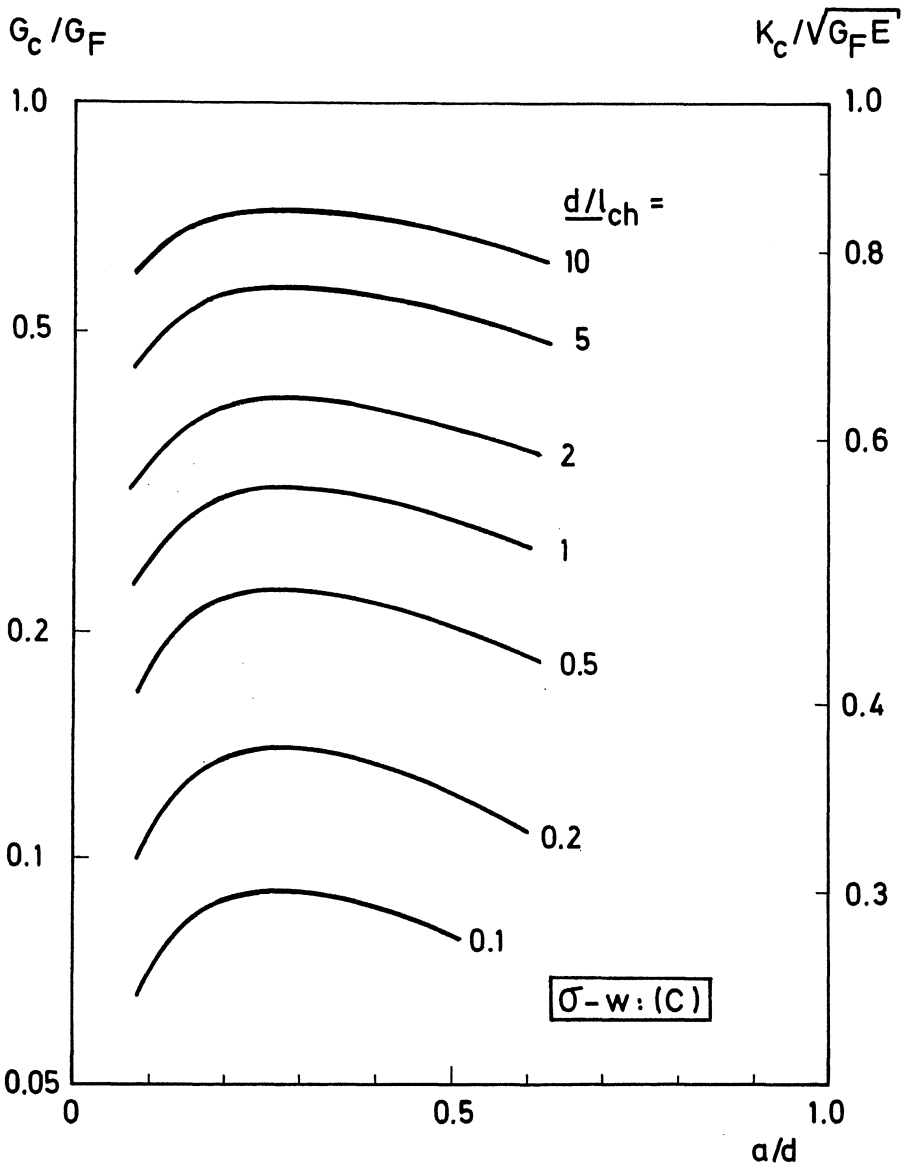

Fig 6.15 Theoretical values of G_c/G_F and $K_c/\sqrt{G_F E}$ as functions of relative notch depth for different values of d/ℓ_{ch}. The curves are relevant for three-point bend tests and the σ-w curve is approximated with two straight lines (C) according to Fig 6.3.

σ-w curve is used, the ratio d/ℓ_{ch} has to exceed about 3 if the difference between the calculated and the true fracture load is to be less than 10 %. For three-point bend tests on metals it is often prescribed that, in order to obtain relevant values of K_c, both the notch depth (a) and the ligament depth (d-a) must exceed $2.5(K_c/\sigma_y)^2$ (cf Knott, 1973), where σ_y is the yield stress. As discussed previously, $K_c \approx \sqrt{G_F E}$ when linear elastic fracture mechanics is

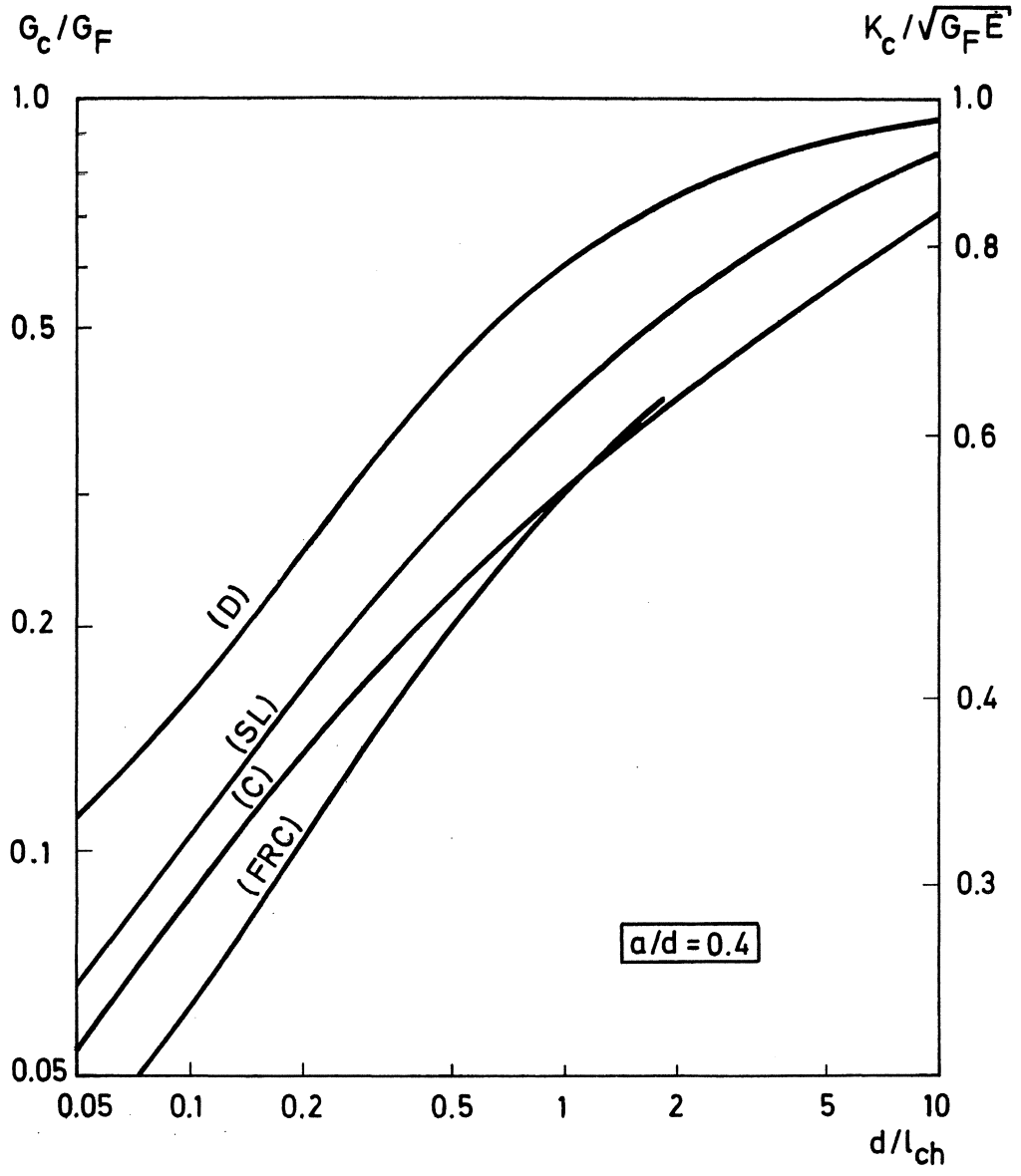

Fig 6.16 Theoretical values of G_c/G_F and $K_c/\sqrt{G_F E}$ as function of d/ℓ_{ch} for different approximations of the σ-w curve. The shapes of the σ-w curves are defined in Fig:s 6.1-6.4.

applicable. With $\sigma_y = f_t$ this means that $(K_c/\sigma_y)^2 = G_F E/f_t^2 = \ell_{ch}$ and for a/d = 0.5 the value of d/ℓ_{ch} has to exceed about 5 in order to obtain a relevant value of K_c for metals. This restriction of d/ℓ_{ch} for metals, which often have σ-w curves of the Dugdale type, seems to be in good agreement with the calculation results in Fig 6.16.

The more the σ-w curve deviates from the approximation according to Dugdale, i.e. the more concave the curve becomes, the lower the value of $K_c/\sqrt{G_F E}$ (or G_c/G_F) becomes for the same value of d/ℓ_{cn}. For fibre-reinforced concrete (FRC) the G_F-value is normally very large (Gustafsson, 1977) and the ℓ_{ch}-value is often several meters. This means that the FRC-curve is of interest only for very small values of d/ℓ_{ch} and this implies that linear elastic fracture mechanics is completely useless for this type of material.

It was mentioned above that the approximation of the σ-w curve according to Dugdale can sometimes be used for fibre-reinforced materials. This may seem slightly confusing as the two curves according to Dugdale and FRC are very different. However, the FRC-curve in the Figure is relevant for a material with a low content of short fibres. As the fibre content increases the σ-w curve becomes more similar to the σ-w curve according to Dugdale, but at the same time ℓ_{ch} increases and the ratio d/ℓ_{ch} decreases which means that the applicability of linear elastic fracture mechanics is very limited even if a σ-w curve according to Dugdale is relevant for the material.

Linear elastic fracture mechanics was first applied to concrete by Kaplan (1961). Some of his results are presented in Table 6:1. The values are re-

Table 6:1 G_c values determined by Kaplan (1961) and G_F values determined by three different methods for three concrete qualities and two different beam depths. W/C=water-cement-ratio.

Material	d (mm)	d/ℓ_{ch}	G_c (N/m) acc to Kaplan	G_F (N/m) acc to G_c and Fig 6.12	G_F (N/m) acc to G_c and Fig 6.14	G_F (N/m) acc to tests
Quartzite concrete W/C=0.6 $\ell_{ch} \approx 350$mm	75	0.2	12	79	97	85-105
	150	0.4	18	78	97	
Limestone concrete W/C=0.5 $\ell_{ch} \approx 100$mm	75	0.75	18	55	72	55-70
	150	1.5	27	59	79	
Mortar W/C=0.5 $\ell_{ch} \approx 150$mm	75	0.5	16	62	76	55-90
	150	1.0	25	66	87	

levant for three-point bend tests on notched beams with the relative notch depth 0.5. G_c was calculated from the fracture load by means of ordinary linear elastic relations. In the Table three different values of G_F are also presented; two of them are determined from G_c and Fig 6.12 and Fig 6.14 respectively and the third is determined from tests on similar materials, see Chapter 7. The ℓ_{ch}-values are estimated from experimental results, which are also presented in Chapter 7.

The G_c-values determined by Kaplan are markedly size dependent; when the beam depth increases from 75 to 150 mm the G_c-values increase by about 50 %. This size dependency almost disappears when G_c is converted to G_F by using the curves in Fig 6.12 or Fig 6.14. Also, the agreement between the converted G_F-values and those determined in tests seems to be good.

The two-line approximation of the σ-w curve used in Fig 6.14 ought to be relevant for normal concrete qualities, which is in good agreement with the results for the quartzite concrete. The existence of the "tail" of the two-line approximation of the σ-w curve probably is due to frictional forces when coarse aggregate particles are extracted from the cement paste, see Chapter 8. As is shown in Chapter 7, the crack passes through the aggregate particles where limestone concrete is concerned and no coarse particles are extracted from the cement paste. Therefore perhaps the single line approximation of the σ-w curve used in Fig 6.12 is better for this material.

Kaplan also carried out G_c-determinations for three different relative notch depths; 0.17, 0.33 and 0.5. The highest value of G_c was obtained when the relative notch depth was 0.33, which is in good agreement with the results in Fig 6.13 and Fig 6.15.

Since Kaplan carried out his tests a great number of similar determinations on concrete have been reported, for example Welsh and Haisman (1979), Moavenzadeh and Kuguel (1969), Naus and Lott (1969), Walsh (1972), Mindness and Nadeau (1976), Strange and Bryant (1979) and Carpinteri (1981). All these tests were performed on bent beams with depths between 25 and 375 mm. The determined K_c-values vary between 0.4 and 1.1. For a normal value of the Young's modulus (35,000 MPa) this corresponds to G_c-values between 5 and 35 N/m. Due to the small and varying specimen dimensions the results have often been conflicting and the results differ very much from normal values of $\sqrt{G_F E}$ and G_F, which for concrete are 2 $MN/m^{3/2}$ and 100 N/m respectively.

Entov and Yagust (1975) reported fracture mechanical tests on large, centrally notched specimens where the loading forces were acting at the notch centre. For the largest specimen, 100 x 2,000 x 2,500 mm^3, they reported K_c- and G_c-values of 1.9 $MN/m^{3/2}$ and 100 N/m respectively which is close to the probable true values of $\sqrt{G_F E}$ and G_F. For smaller specimen dimensions, 64 x 900 x 1,050 mm^3, the corresponding values were 1.4 $MN/m^{3/2}$ and 70 N/m respectively and this confirms the results above that it is necessary to use very large specimens in order to obtain consistent values of K_c and G_c.

Also in the case of cement paste a large number of test results of K_c and G_c are reported, for example Brown and Pomeroy (1973) and Nadeau, Mindess and Hay (1974). Very interesting results are reported by Higgins and Bailey (1976). They determined K_c of cement paste for different beam depths in three-point bending and found that K_c increases with increasing beam depth and "as the specimen size tends to infinity, so K_c appears to tend towards a limiting value". However, not even when the beam depth was 110 mm (which corresponds to a d/ℓ_{ch}-value of at least 10) had K_c reached its final value. These results are in good agreement with the theoretical results in Fig 6.12 and Fig 6.14.

Mai (1979) presented results of K_c, G_F, f_t and E for an asbestos-cement mortar composite. This is the only reference found where all the necessary parameters for the use of the curves in Fig 6.16 are determined. For this material Mai found that the fibres were extracted from the cement paste matrix at crack propagation. When a notched specimen of this type of material is subjected to load, one may assume a stress distribution according to Dugdale in front of the notch.

The material properties of the three different qualities of asbestos-cement mortar are presented in Table 6:2. In the Table test results of K_c according to Mai are also shown as well as K_c-values calculated from $\sqrt{G_F E}$ and the curve in Fig 6.16 (the tests were performed on three-point bent beams with the relative notch depth 0.4). As can be seen in the Table, the agreement between the test results and the calculated values is excellent, in spite of the simplified assumptions. This confirms the calculation results above and also implies that the Fictitious Crack Model is also suitable for fibre-reinforced materials.

According to the calculations, the tests and the discussion above the usefulness of linear elastic fracture mechanics seems to be very limited where cementitious materials are concerned. For plain and fibre-reinforced concrete linear elastic fracture mechanics is only applicable on large structures where the di-

Table 6:2 K_c-values according to tests and calculations for asbestos-cement mortar composites with the material properties given in the Table.

		mass fraction of fibres		
		5 %	10 %	15-20 %
d	(mm)	26	26	26
f_t	(MPa)	7.1	10.8	15.8
E	(MPa)	17,200	17,200	17,200
G_F	(N/m)	760	2,300	3,300
ℓ_{ch}	(mm)	260	340	230
d/ℓ_{ch}		0.10	0.08	0.11
K_c $(MN/m)^{3/2}$	acc. to $\sqrt{G_F E}$ and Fig 6.16	1.4	2.3	3.1
K_c $(MN/m)^{3/2}$	test results acc. to Mai	1.5	2.2	3.2

mensions are in meters. This also implies that it is very difficult to develop standard test methods that are suitable for laboratory determinations of K_c and G_c. Such test methods can perhaps be developed for cement paste but as this material in practice is always only a component of a matrix, where the properties of the cement paste are quite different from those determined for pure paste, such test methods would be of limited value.

6.3 The J-integral approach

In Chapter 2 the formal definition of the J-integral is presented (2:10). An alternative and equivalent definition of J is given by Rice, Paris and Merkle (1972):

$$J = \frac{1}{b}\int_0^{\delta} \left(-\frac{\partial F}{\partial a}\right)_{\delta} d\delta = \frac{1}{b}\int_0^{F} \left(\frac{\partial \delta}{\partial a}\right)_{F} dF \qquad (6:5)$$

where F is the load, b is the width of the specimen, a is the crack depth, δ is the deformation and consequently $(\partial F/\partial a)_{\delta}$ is the change of the load when the crack advances a distance ∂a and the deformation is δ.

(6:5) is illustrated in Fig 6.17 for three-point bending. The two curves in the Figure represent load-deflection curves for two notched beams with slightly different notch depths; a and $a+\Delta a$ respectively. From these curves the value of J at deformation δ_1 can be obtained as (compare 2:10):

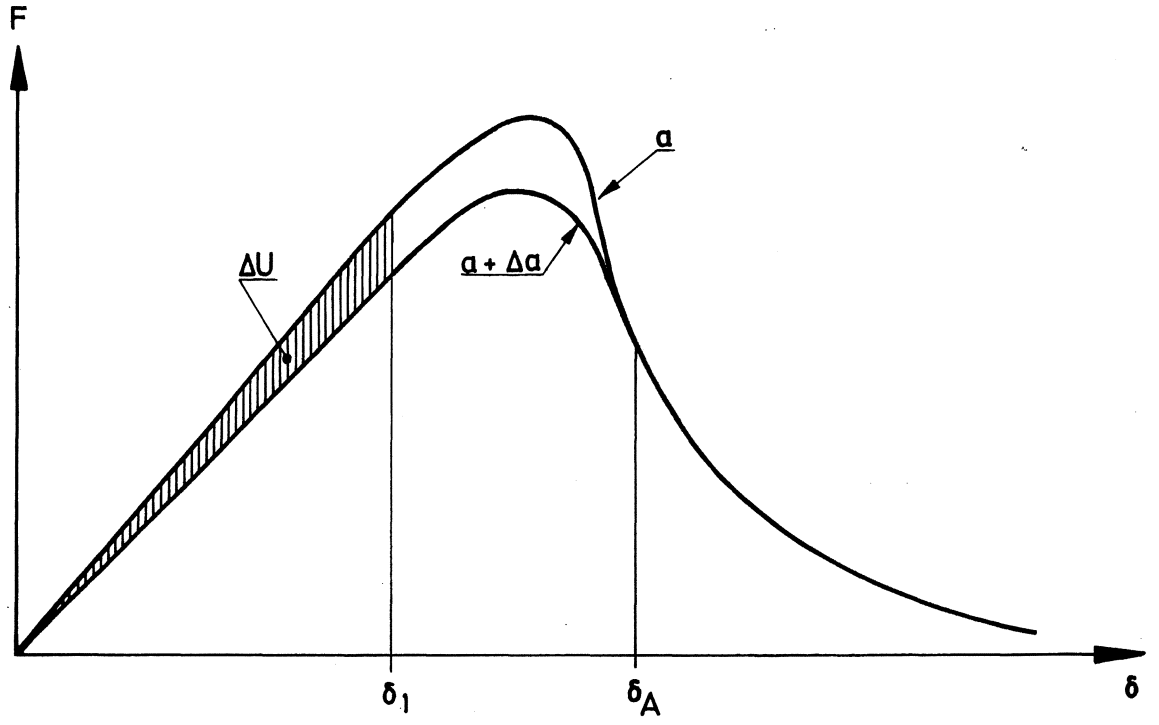

Fig 6.17 Illustration of (6:5) for a three-point bend test. $J = \frac{1}{b}(\Delta U/\Delta a)$ at δ_1.

$$J = \frac{1}{b}(\Delta U/\Delta a)_{\delta_1} \qquad (6:6)$$

where ΔU is the amount of energy represented by the area between the two curves from $\delta=0$ to $\delta=\delta_1$.

The two curves in Fig 6.17 are identical when the deflection exceeds δ_A. At δ_A a real crack, i.e. a crack with no stress-transferring capability, has advanced to a distance Δa in front of the notch with the original depth a and in front of the notch with the original depth $a+\Delta a$ a real crack will just start propagating. $\frac{1}{b}(\Delta U/\Delta a)_{\delta_A}$ thus represents the amount of energy necessary to create one unit of area of a crack and consequently J_c equals G_F when determined at the deflection corresponding to the start of real crack propagation. δ_A is probably the only point where J_c is a material property.

Unfortunately it is unsuitable, for several reasons, to define J at δ_A. In fact δ_A is strictly defined only for elastic materials, i.e. for materials where the unloading outside the fracture zone takes place along the same curve as the initial loading. For other materials the two curves in Fig 6.17 will never coincide exactly. Also, the J-integral approach is not relevant if

unloading takes place, which is obviously the case if J_c is defined at δ_A. This "unloading problem" in fact is a problem wherever J_c is defined as unloading always takes place in the fracture zone and consequently also in the material close to the fracture zone.

The most important aim when using fracture mechanics is to predict the fracture load. Unfortunately δ_A normally exceeds the deflection at the fracture load and it is consequently unsuitable to use J_c when determined at δ_A. For example, for fibre-reinforced materials δ_A represents the deflection where all the fibres bridging the crack at the notch tip are completely pulled out and of course this cannot be used as a fracture criterion for design purposes. As the most interesting, and only well defined, point of the load-deflection curve is the maximum load, this point has normally been used for J_c-determinations on cementitious materials. In Fig 6.18 theoretical values of J_c/G_F determined at the maximum load are shown as functions of d/ℓ_{ch} for the four model materials defined in Fig:s 6.1-6.4. The curves are relevant for three-point bending on notched beams with the relative notch depth 0.25 (in the calculations the area between the two load-deflection curves representing a/d=0.2 and 0.3 is analysed).

For a material with a σ-w curve according to Dugdale the deflection at the fracture load equals δ_A and consequently J_c then equals G_F for this type of material. Many yielding materials behave more or less as ideally elastic-plastic materials and this is probably the reason for the usefulness of the J-integral approach for many metals.

For more realistic σ-w curves of cementitious materials the applicability of the J-integral approach is more limited, at least for small values of d/ℓ_{ch}. When the usefulness of the J-integral is compared with that of the linear elastic approach, the ratios J_c/G_F and G_c/G_F should be compared. For example, if the linear elastic fracture mechanics approach is accepted for G_c/G_F-values exceeding 0.8 (corresponds to $K_c/\sqrt{G_F E} \approx 0.9$), then d/ℓ_{ch} has to exceed 8-10 if the σ-w curve is approximated with a single, straight line (see Fig 6.12). The corresponding value of d/ℓ_{ch} for J_c/G_F is about 1.0-1.5 which implies that J_c is much more useful as a fracture criterion than G_c. However, when the more realistic σ-w curve for concrete (C) is used, the applicability of the J-integral approach decreases and d/ℓ_{ch} has to reach 5, corresponding to beam depths of about 1.0-1.5 m for concrete, if the ratio J_c/G_F is to exceed 0.8. Also where the fibre-reinforced material is concerned the applicability of the J-integral seems poor but this type of material

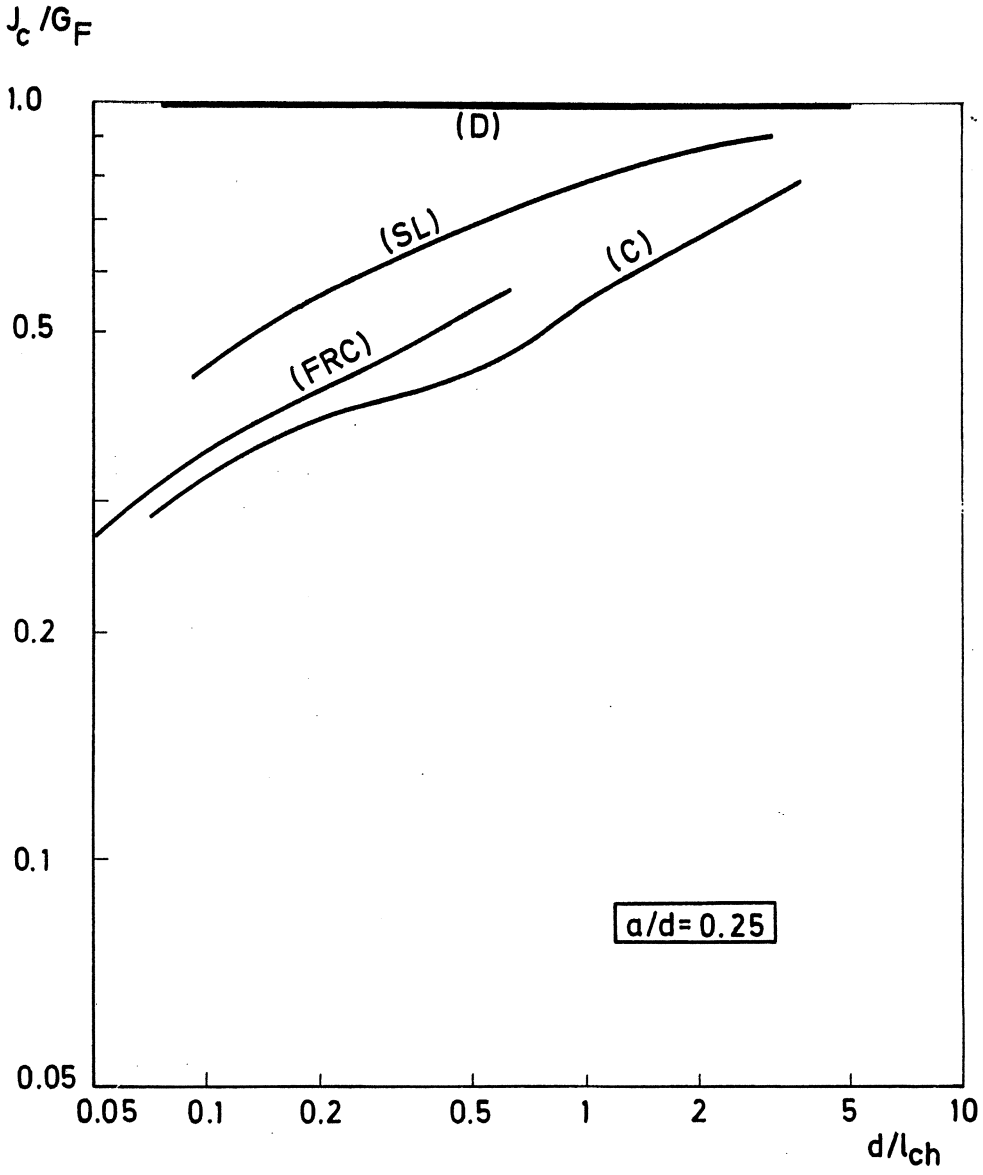

Fig 6.18 Theoretical values of J_c/G_F as functions of d/ℓ_{ch} for the four model materials defined in Fig:s 6.1-6.4. J_c is determined according to Fig 6.17 and the curves are relevant for three-point bending on notched beams with the relative notch depth 0.25.

has very individual σ-w curves and therefore the FRC-curve in the Figure should be regarded only as an example.

The irregularity of the (C)-curve in Fig 6.18 is due to the break-point of the σ-w curve when w equals 20 μm. When d/ℓ_{ch} is about 0.5, then the lower part of the σ-w curve, i.e. when w > 20 μm, affects the fracture load and thus the J_c/G_F-curve.

For experimental determination of J_c for cementitious materials it is custo-

mary to use a different method than the one described above.

By using moment (M) instead of force (F) and angle change (θ) instead of displacement (δ), then (6:5),according to Rice, Paris and Merkle (1975),can be written as:

$$J = \frac{1}{b}\int_0^M \left(-\frac{\partial\theta_{total}}{\partial d_\ell}\right)_M dM \qquad (6:7)$$

where d_ℓ is the depth of the uncracked ligament (d-a) and:

$$\theta_{total} = \theta_{no\ crack} + \theta_{crack} \qquad (6:8)$$

For a deeply notched specimen it is assumed that

$$\theta_{crack} = f\left(\frac{M}{d_\ell^2}\right) \qquad (6:9)$$

and from (6:8) and (6:9) it can be found that

$$\left(-\frac{\partial\theta_{total}}{\partial d_\ell}\right)_M = \left(-\frac{\partial\theta_{crack}}{\partial d_\ell}\right)_M = \frac{2M}{d_\ell^3} f'\left(\frac{M}{d_\ell^2}\right) = \frac{2M}{d_\ell}\left(\frac{\partial\theta_{crack}}{\partial M}\right)_{d_\ell} \qquad (6:10)$$

Substituting (6:10) into (6:7) and integrating gives:

$$J = \frac{2}{d_\ell b}\int_0^{\theta_{crack}} M d\theta_{crack} \qquad (6:11)$$

If the ligament is subjected mainly to bending but the load is applied by forces, then (6:11) can be written as:

$$J = \frac{2}{d_\ell b}\int_0^{\delta_{crack}} F d\delta_{crack} \qquad (6:12)$$

(6:12) represents the work done in loading, with the deformations with no crack present eliminated from the calculations. The evaluation of J_c at the fracture load when using this method is demonstrated in Fig 6.19.

Theoretical values of J_c/G_F as functions of d/ℓ_{ch} for the four model materials in Fig:s 6.1-6.4 are shown in Fig 6.20. J_c is calculated according to Fig 6.19 and is relevant for three-point bending on a beam with the relative notch depth 0.3. As can be seen in the Figure the ratio J_c/G_F is strongly affected by the beam depth and also by the shape of the σ-w curve. In order to explain the completely different behaviour of the material according to Dugdale

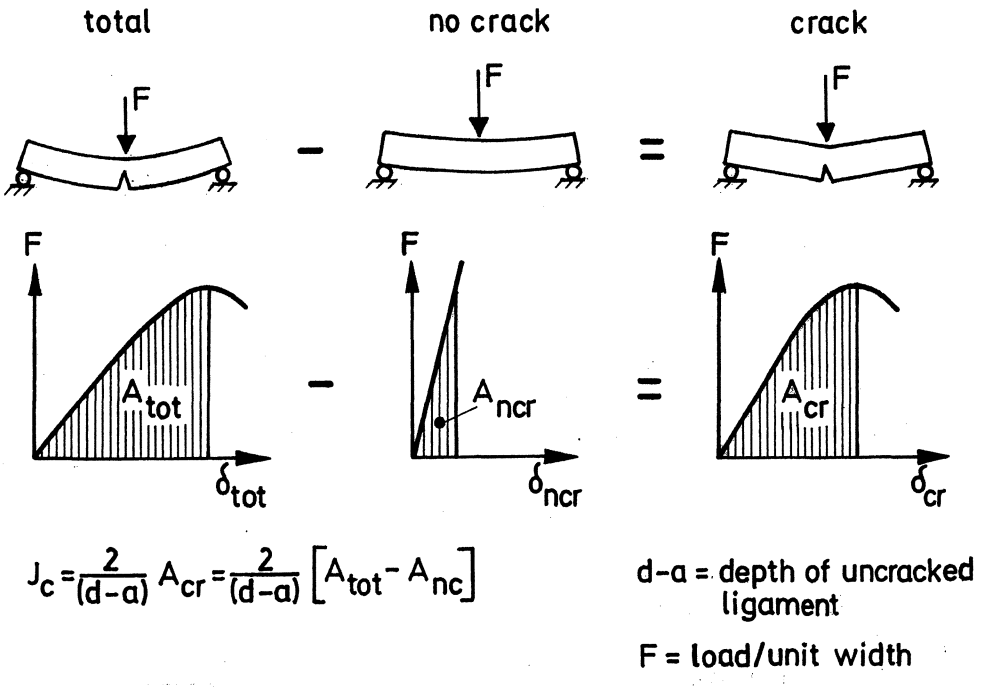

Fig 6.19 Experimental determination of J_c at three-point bending according to (6:12).

and the three others it is necessary to study the influence of the fracture zone. For a material according to Dugdale both the load and the deflection due to the presence of the crack increase as the fracture zone grows. The value of J at the start of real crack propagation therefore increases with the increasing value of the ratio depth of the fracture zone/depth of ligament. This ratio grows with decreasing values of d/ℓ_{ch} and consequently, as the crack starts to propagate when the fracture load is reached for this material, the ratio J_c/G_F decreases with increasing values of d/ℓ_{ch}. For the other three materials the crack starts to propagate after the maximum load is reached and this of course means that J_c determined according to Fig 6.19 becomes less than G_F. The start of crack propagation takes place closer to the fracture load for higher values of d/ℓ_{ch} and therefore the three J_c/G_F-curves increase with increasing values of d/ℓ_{ch}. However, for higher values of d/ℓ_{ch} the effect of the relative depth of the fracture zone ought to increase and then all the curves ought to decrease with increasing values of d/ℓ_{ch}. This can be seen in Fig 6.21 where J_c/G_F is shown as function of d/ℓ_{ch} for different relative notch depths when the σ-w curve is approximated with a single, straight line. For small values of a/d the curves increase in the beginning but when d/ℓ_{ch} exceeds about 1-2 they decrease. High values of the relative notch depth

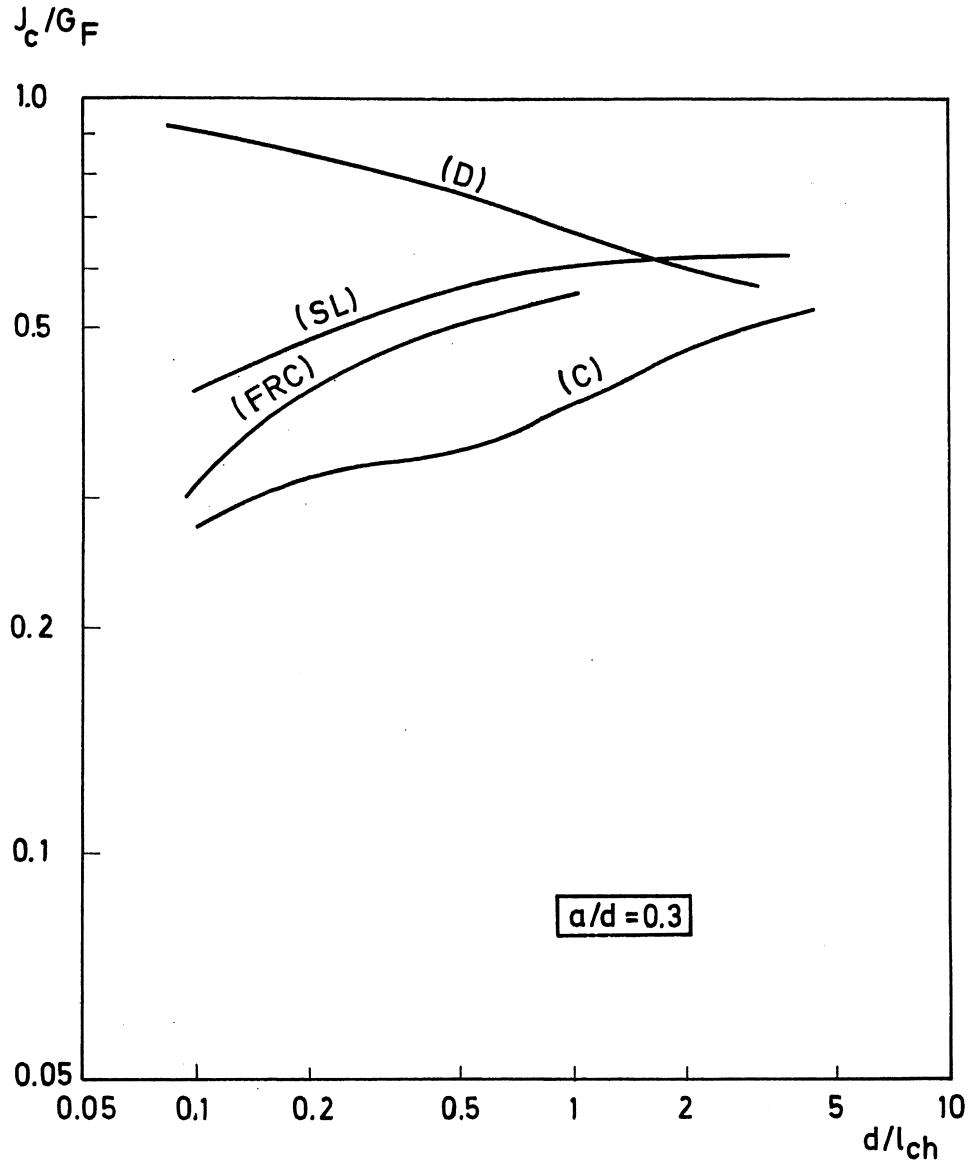

Fig 6.20 J_c/G_F as function of d/ℓ_{ch} for the four model materials defined in Fig:s 6.1-6.4. J_c is calculated according to Fig 6.19 and is relevant for three-point bending.

seem to give the best results for high values of d/ℓ_{ch}, but for small values of d/ℓ_{ch} the situation seems to be reversed due to the increased influence of the difference between the fracture load and the start of crack propagation.

In literature most J_c-determinations are carried out on fibre-reinforced concrete but at least one determination for concrete and cement paste is reported (Mindess, Lawrence and Kesler, 1973). By using the method in Fig 6.19 they determined J_c on 75 mm deep beams with the relative notch depth varying between 0.5 and 0.7. Their results of J_c and G_c are presented in Table 6:3, where the ratio J_c/G_c is also compared with theoretical values obtained from Fig:s 6.12 and 6.21. As can be seen in the Table the agreement between the

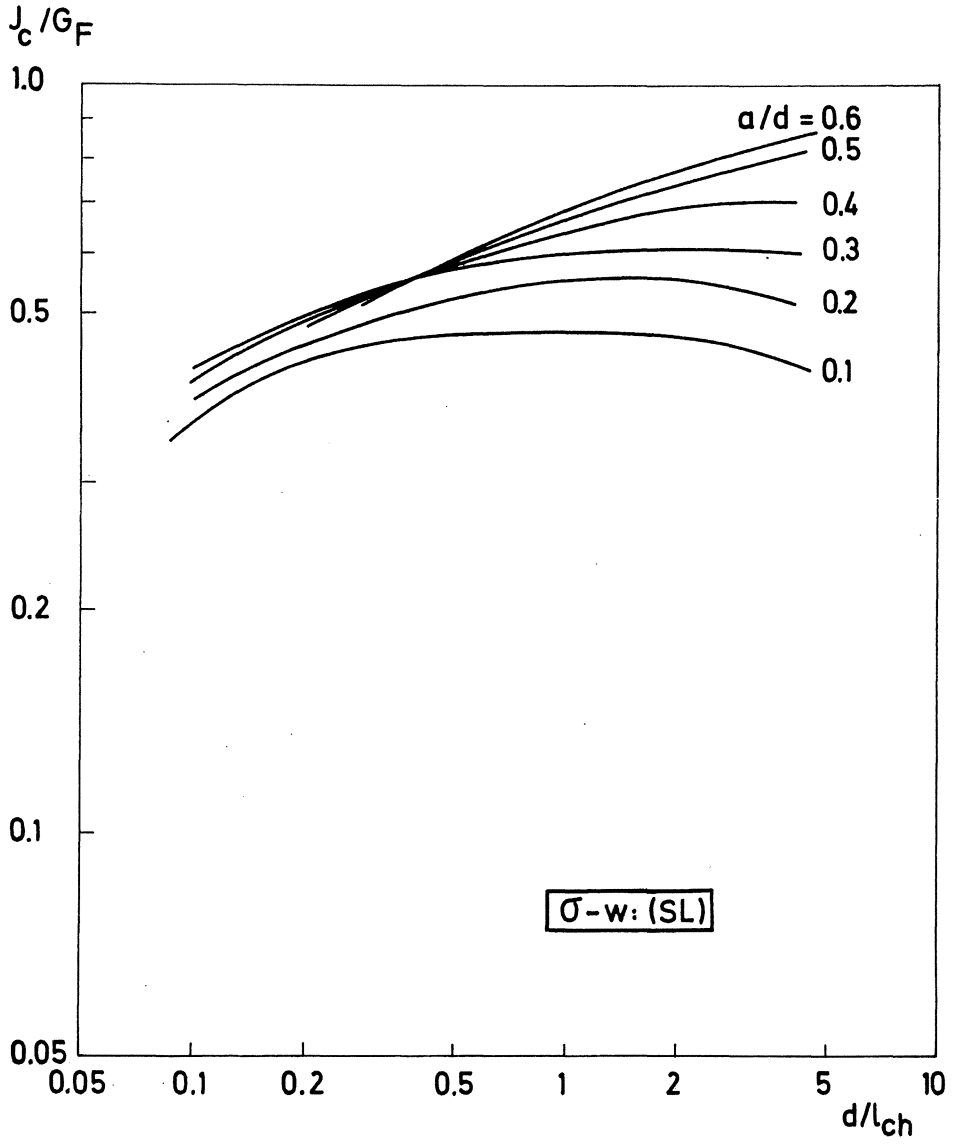

Fig 6.21 Theoretical values of J_c/G_F as function of d/ℓ_{ch} for different relative notch depths. J_c is calculated according to Fig 6.19 and the σ-w curve is approximated with a single, straight line (SL).

test results and the calculated values is good, in spite of the simplified assumptions.

Mindess et al also carried out J_c-determinations on steel-fibre reinforced concrete. They found that J_c is much more sensitive to the fibre content than G_c and consequently the ratio J_c/G_c increases with increasing fibre content, see Fig 6.22. Unfortunately it is very difficult to guess the shape of the σ-w curve for fibre-reinforced materials, which is probably dependent on the fibre content, and therefore it is impossible to quantitatively analyse the curve in Fig 6.22 by means of the Fictitious Crack Model. However, the ℓ_{ch}-value ought to increase with increasing fibre content and in Fig 6.23 theo-

Table 6:3 Test results of J_c, G_c and J_c/G_c for cement paste and concrete (Mindess et al, 1973). In the Table values of J_c/G_F calculated by using Fig:s 6.12 and 6.21 are shown as well.

	Estimations		Tests			Calculations
	ℓ_{ch} (mm)	d/ℓ_{ch}	G_c N/m	J_c N/m	J_c/G_c	J_c/G_c according to Fig:s 6.12, 6.21
Cement-paste	10	7.5	9-15	11-15	0.8-1.6	1.1-1.4
Concrete	250	0.3	17-18	40-43	2.2-2.5	2.7-3.0

retical values of J_c/G_c, calculated by using the Fictitious Crack Model, are shown as function of d/ℓ_{ch}. In the calculations the σ-w curve was approximated with a single, straight line and the relative notch depth was 0.5. The horizontal scale decreases to the right, which corresponds to increasing fibre content. As can be seen in the Figure, the shape of the curve is similar to that of the curve in Fig 6.22 and consequently the dependency of the fibre content on the ratio J_c/G_c can be qualitatively described by means of the Fictitious Crack Model.

Halvorsen (1980) carried out J_c-determinations for different beam depths on steel-fibre reinforced concrete. The beam depths were 75 mm and 150 mm respectively. The fibres were brass coated with irregular cross sections. The fibre content was probably 1.5 %. Halvorsen found that the value of J_c for the 150 mm deep beams was about twice the value for 75 mm deep beams. This indicates that J_c is strongly size dependent, which is in good agreement with the theoretical curves in Fig 6.20. The size dependency seems to increase when d/ℓ_{ch} decreases and this can explain the great size dependency reported by Halvorsen. In the tests the effect of the relative notch depth was also examined. No significant difference was obtained between J_c-values determined on beams with the relative notch depths 0.5 and 0.67 respectively.

Velasco, Visalvanich and Shah (1980) also studied the influence of notch depth on J_c for steel-fibre reinforced concrete. The beam depth was 76 mm and 1 % by volume of round, smooth steel fibres was used. Contrary to Halvorsen they found a substantial dependency on notch depth; J_c increased from 30 N/m to 60 N/m as the relative notch depth decreased from 0.75 to 0.50 and when the relative notch depth was 0.125 the J_c-value was 1600 N/m. These completely

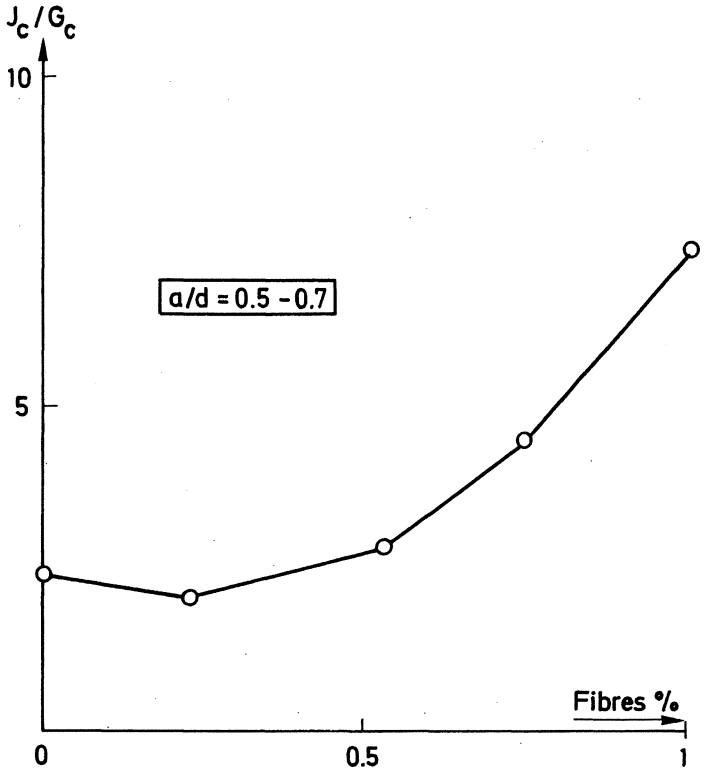

Fig 6.22 J_c/G_c as function of fibre content for a type of fibre-reinforced concrete (Mindess et al, 1973).

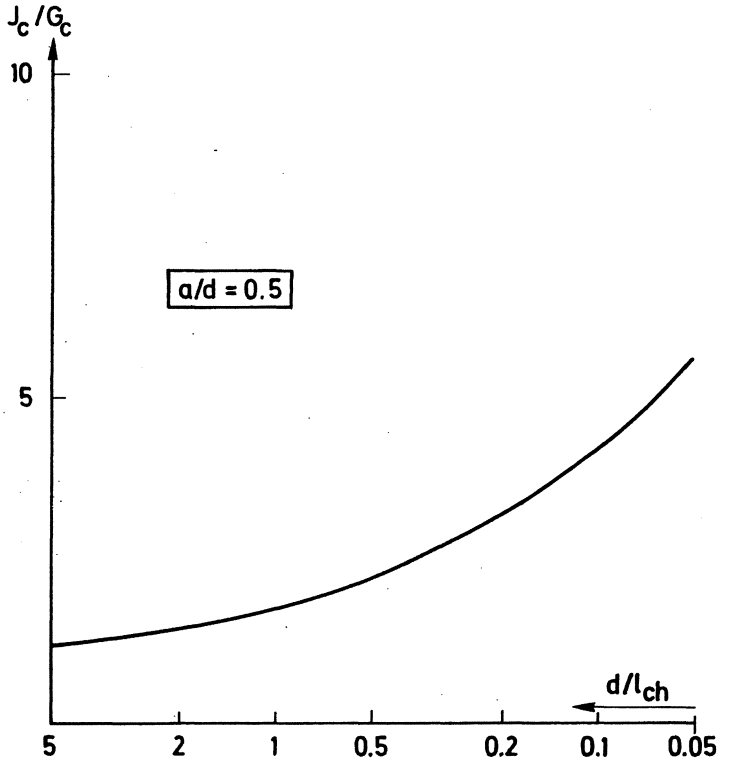

Fig 6.23 Theoretical values of J_c/G_c as function of d/ℓ_{ch}. J_c/G_c is calculated acc. to Fig:s 6.12 and 6.21. The relative notch depth is 0.5.

different results between two, fairly similar tests seem a little confusing. One explanation could be the difficulties in finding the position of the fracture load on the load-deflection curve, which is demonstrated in Fig 6.24. In the Figure typical load-deflection curves according to Velasco et al are shown for different relative notch depths. As can be seen in the Figure, there is a long horizontal part of the curves close to the fracture load and only a small, local variation of for example the fibre distribution can considerably change the position of the fracture load. In the Figure the positions of the fracture loads according to Velasco et al are shown. If other positions were chosen, which may be motivated at least where the deeply notched beams are concerned, then the J_c-values would be completely different.

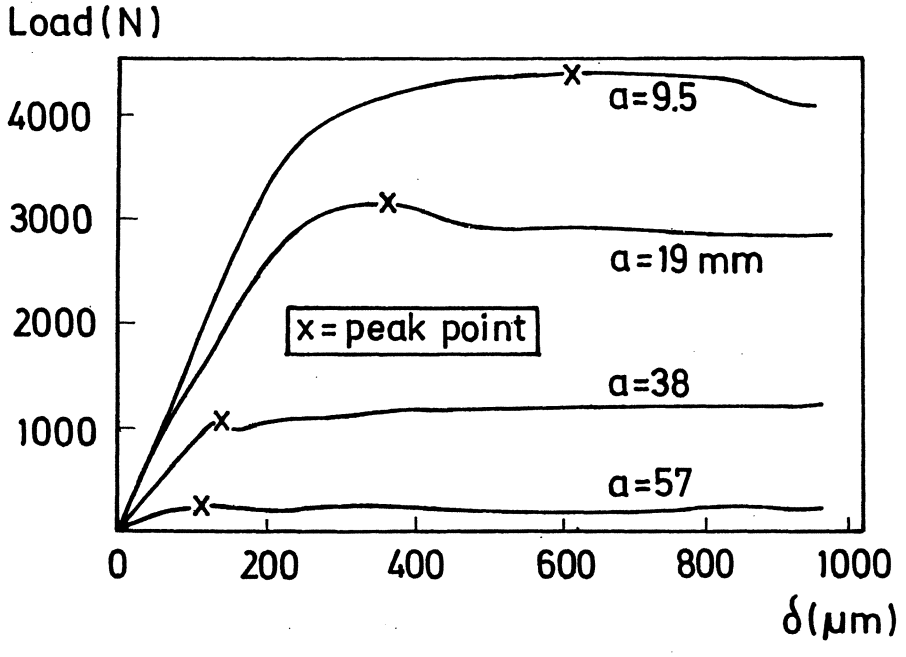

Fig 6.24 Load-deflection curves for different relative notch depths for a quality of steel-fibre reinforced concrete (Velasco et al, 1980).

According to the calculations, the test results and the discussion above it seems unsuitable to use J_c as a fracture criterion for cementitious materials of normal dimensions. J_c is too dependent on specimen size, notch depth and the shape of the σ-w curve for it to be useful. Also the difficulties of evaluating J_c, especially for fibre-reinforced materials, from the load-displacement curve makes the parameter unsuitable.

6.4 The crack opening displacement approach (COD)

The fracture zone is able to transfer stress as long as the widening of the zone is less than a critical value w_c (see Fig:s 6.1-6.4) but when this value is reached a real crack starts propagating. COD corresponds to the widening of the fracture zone at the crack tip. If COD_c is used as a criterion for the initiation of real crack propagation then it equals w_c and consequently COD_c is then a material property. However, as discussed before, it is the fracture load and not the initiation of crack growth that is the most interesting thing to study and then, when used as a criterion for the fracture load, COD_c is

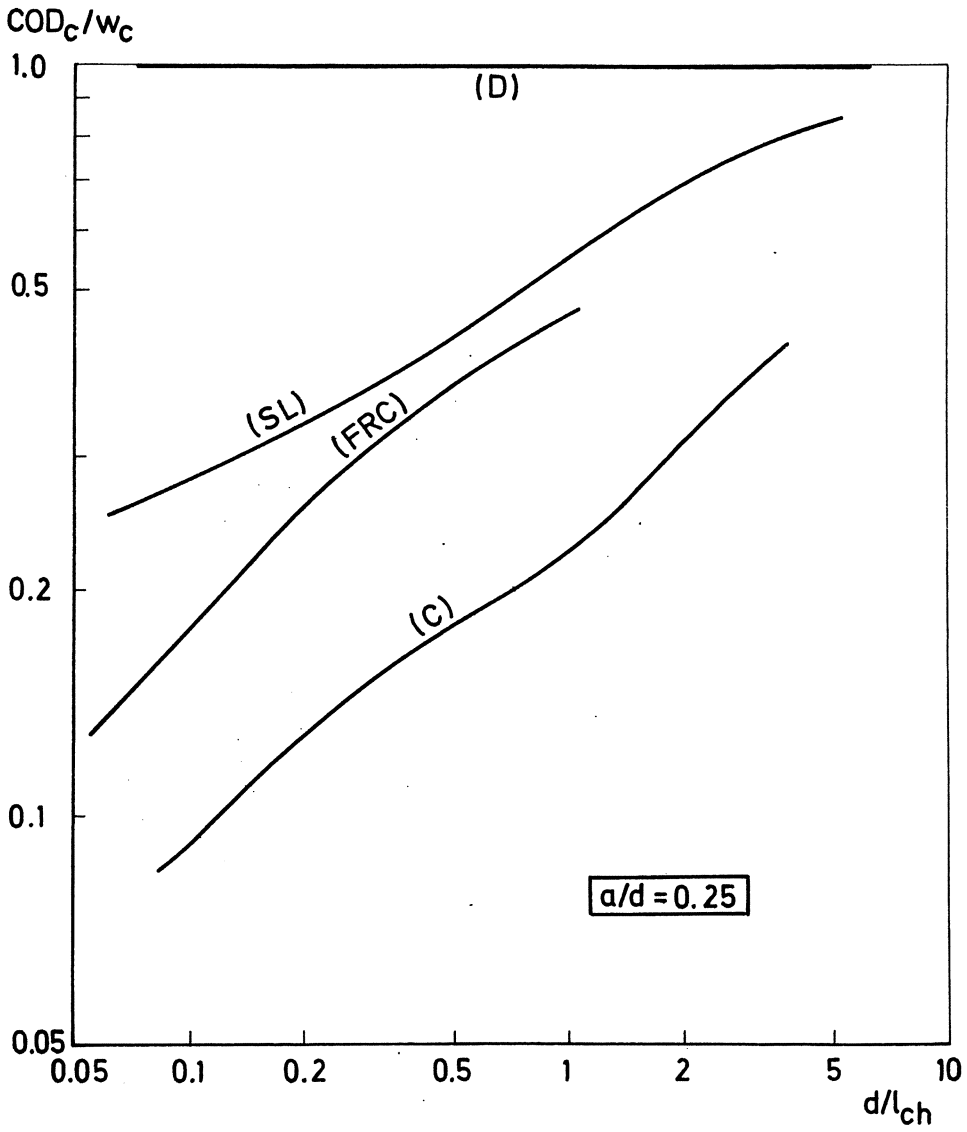

Fig 6.25 Theoretical values of COD_c/w_c as functions of d/ℓ_{ch} for the four model materials in Fig:s 6.1-6.4. The curves are relevant for three-point bending where the relative notch depth is 0.25.

normally an approximation. In Fig 6.25 theoretical values of COD_c/w_c are shown as function of d/ℓ_{ch} for the four model materials presented in Fig:s 6.1-6.4. COD_c is determined at the maximum load. The curves are relevant for three-point bending on beams with the relative notch depth 0.25.

Where materials with σ-w curves according to Dugdale are concerned, a real crack starts propagating when the fracture load is reached and consequently then COD_c/w_c always equals unity. This is probably the explanation for the fact that the COD-approach has sometimes been successfully applied on metals, which often have σ-w curves according to Dugdale. For most cementitious materials the σ-w curve is quite different and then the COD-approach is less useful, which can be seen in the Figure. COD_c increases greatly with increasing values of d/ℓ_{ch} and the more the shape of the σ-w curve deviates from the shape according to Dugdale, the less the applicability of the COD-approach is. Other calculations, which are not presented here, imply that COD_c is also slightly affected by the relative notch depth; the applicability of the COD-approach decreases with increasing relative notch depth.

The only application of the COD-approach to cementitious materials found in literature was published by Valesco, Visalvanish and Shah (1980). They determined COD_c at the fracture load for fibre-reinforced concrete (round, smooth steel fibres) and among other things they studied the influence of the relative notch depth. It is difficult to measure the displacement at the notch tip so they measured the Crack Mouth Displacement (CMD) instead, i.e.the displacement at the base of the notch and then they theoretically converted the CMD_c-values to COD_c-values.

Velasco et al found that COD_c was dependent on the relative notch depth; it decreased greatly with increasing relative notch depth. The same tendency, but less pronounced, can be found from calculations according to the Fictitious Crack Model. The very strong influence of the relative notch depth on COD_c reported by Velasco et al may be due to technical problems when evaluating the tests as it is very difficult, exactly as when determining the J-integral for fibre-reinforced materials, to define the position of the peak load on the load-displacement curve. However, it seems as COD_c, determined at the fracture load, is too dependent on specimen geometry and the shape of the σ-w curve to be useful as a fracture mechanics parameter where cementitious materials are concerned.

6.5 R-curve analysis

When calculating the resistance to crack growth it is necessary to know the actual crack depth (see 2.3.5), i.e.the notch depth (a) + the crack advance (Δa) and consequently the position of the crack tip has to be well defined. This is the case for metals which normally have a small fracture zone but for cementitious materials it is much more difficult to define the position of the crack front; should it be at the tip of the fracture zone, at the tip of the real crack (i.e. a crack with no stress-transferring capability) or somewhere in between? As the depth of the zone is often great, the definition of the position of the crack tip is of considerable importance.

A number of different methods for detecting the crack tip are reported in literature. Welsh and Haisman (1969) used the compliance technique (compliance=deflection/load). In this method the initial compliances of notched beams with different notch depths are first determined which makes it possible to find a relation between compliance and notch depth. Then a notched beam is loaded to a certain point of the load - deflection curve. The secant modulus of this point is compared with the compliance curve and thus the actual crack depth can be estimated. However, this method can only be used if the depth of the fracture zone is small as otherwise the fracture zone affects the compliance of the test beam but not the compliance curve. Therefore for cementitious materials, with large fracture zones, this method ought to be unsuitable.

The posititon of the tip of the visible crack is probably the most natural definition of the location of the crack tip but this location is affected by the method of observation; by the naked eye, by magnifying glass or by microscope. Strain measurements, acoustic emission measurements and other methods can also be used but the different ways of observing the crack tip give different crack depths (cf Sok, Baron and Francois, 1979) and consequently different K_R-curves which is shown in Fig 6.26. In the calculations of the curves the position of the crack tip was defined as the point where the widening of the fracture zone exceeds a critical value and the curves in the Figure represent different critical values ranging from 0 to 100 μm. The curves are relevant for three-point bending on beams with the relative notch depth 0.25 and the σ-w curve is approximated with a single, straight line. G_F is chosen to 75 N/m, f_t to 3 MPa and E to 30,000 MPa, which means that a real crack starts propagating when the widening of the fracture zone reaches 50 μm.

As can be seen in the Figure, the curves become quite different for different definitions of the position of the crack tip. When the critical value of the

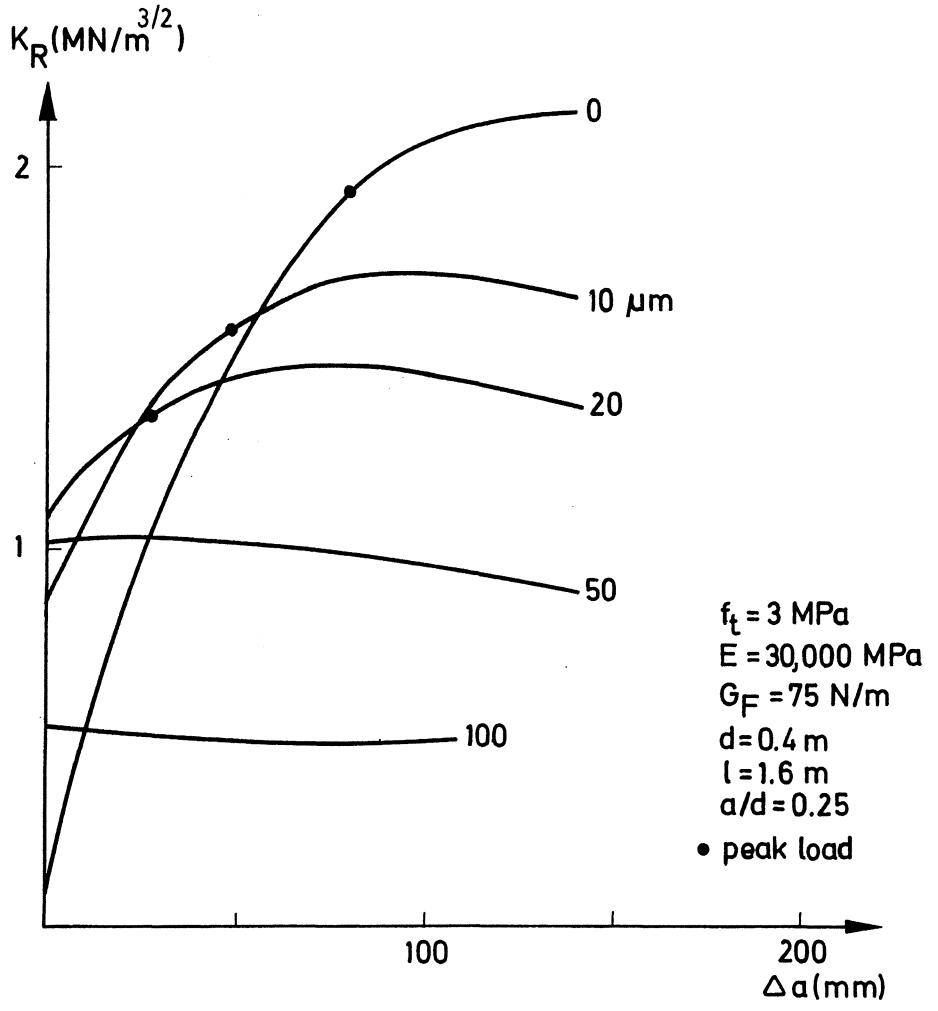

Fig 6.26 Theoretical K_R-curves for three-point bend tests on notched beams. The σ-w curve is approximated to a single, straight line. In the calculations the position of the crack tip was related to a critical value of the opening of the fracture zone and the six curves are relevant for different critical values ranging from 0 to 100 μm.

fracture zone is zero this corresponds to the tip of the fracture zone. This position can perhaps be roughly detected by means of acoustic emisson measurements or also by strain measurements. 50 μm correspond, in this case, to the tip of the real crack and consequently 10 μm and 20 μm represent positions somewhere in the fracture zone. It ought to be possible for the naked eye to observe "cracks" when their width exceeds about 25-50 μm, compare Chapter 5.

In the Figure the positions of the peak loads are shown for the curves representing the three smallest critical values of the widening of the fracture zone. As can be seen K_R increases also after the maximum load is reached. In the case of the curves representing the two largest critical values of the widening of the fracture zone the defined crack will not propagate until after the maximum load is reached.

In Fig:s 6.27-6.30 calculated K_R-curves for three-point bending are presented. In the calculations the position of the crack tip was defined as the point where the widening of the fracture zone equals 10 μm.

For Fig:s 6.27-6.28 the σ-w curve is approximated with a single, straight line and the material properties, which are given in the Figures, represent a normal concrete quality. In Fig 6.27 K_R-curves for different relative notch depths are presented and, as can be seen, the curves are just very slightly affected by the relative notch depth. However, for different beam depths, see Fig 6.28, the curves are very different and this implies that the K_R-curve is not useful as a material property for concrete.

For Fig:s 6.29-6.30 the σ-w curve is approximated according to Fig 6.4. With the actual material properties the material should then correspond to a fibre-reinforced concrete with a low percentage of short fibres. Also where this material is concerned the curves are strongly affected by the beam depth while the influence of the relative notch depth is less pronounced.

The only example found in literature regarding K_R-curves determined on bent beams of unreinforced cementitious materials was presented by Brown (1972). He determined K_R-curves for mortar and used the compliance technique, though somewhat modified, to find the actual crack depth. The tests were performed on 38 mm deep beams and the relative notch depth was 0.5. The results for 6 individual beams are presented in Fig 6.31.

The K_R-values are low which is probably due to the small specimen size but perhaps also to the method of determining the actual crack depth. However, the shapes of the curves are similar to those presented in Fig:s 6.27-6.28; the curves first increase with increasing crack advance until they reach a maximum and then they decrease.

Sok, Baron and Francois (1979) used very large double cantilever specimens, see Fig 6.32, in order to determine K_R-curves for concrete. Prestressed reinforcement was used parallel to the crack propagation path. This reinforcement is probably necessary as it prevents crack propagation perpendicular to the crack due to the high bending stresses. Such cracks in fact were also reported for the reinforced specimens (Sok, 1978) but they were stopped before they reached the reinforcement. These side cracks and probably also the reinforcement may affect the results.

The thickness of the specimen was reduced to one third along the crack propa-

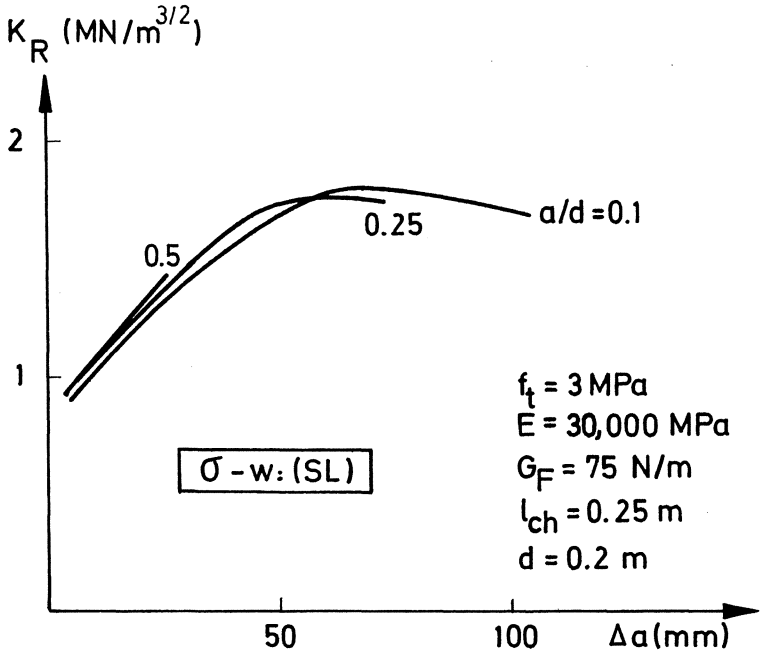

Fig 6.27 Theoretical K_R-curves for different relative notch depths. The curves are relevant for a normal concrete quality.

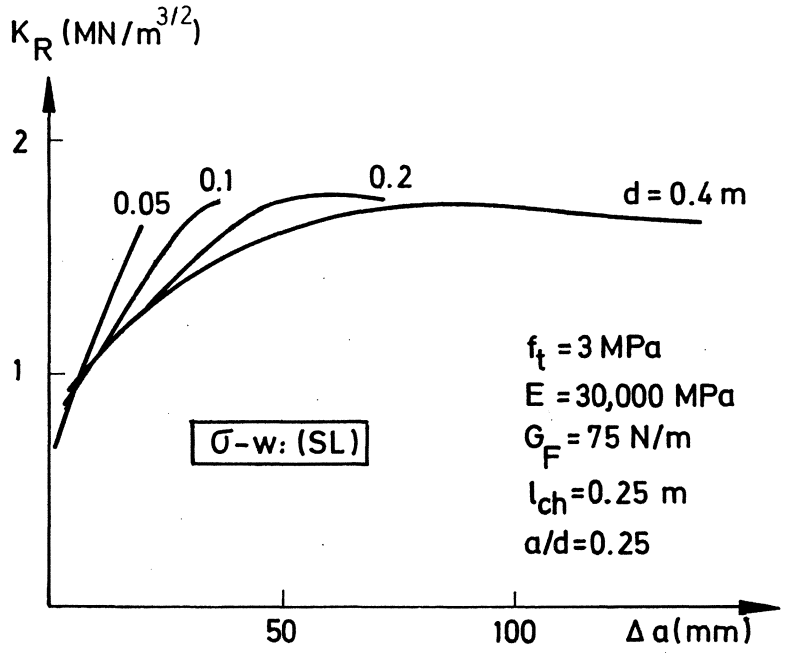

Fig 6.28 Theoretical K_R-curves for different beam depths. The curves are relevant for a normal concrete quality.

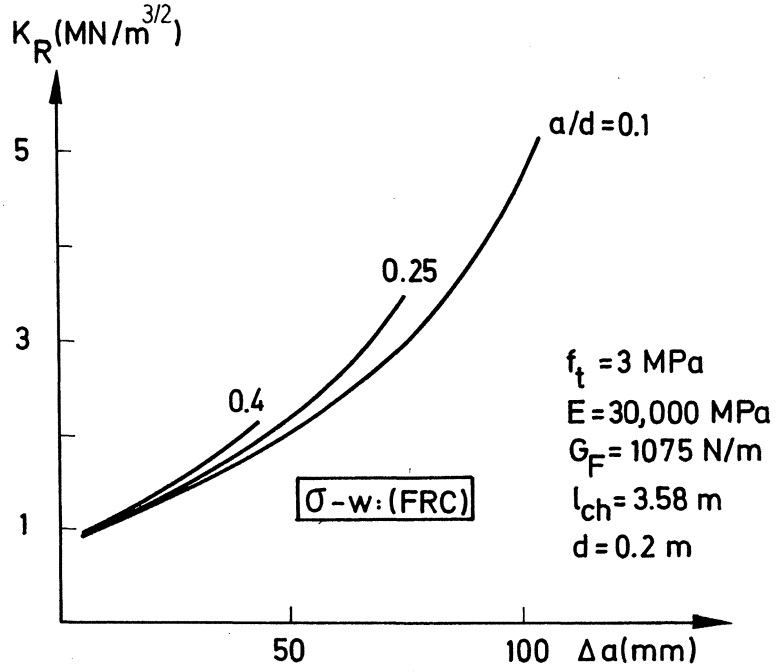

Fig 6.29 Theoretical K_R-curves for different relative notch depths. The curves represent a fibre-reinforced concrete with a low percentage of short fibres.

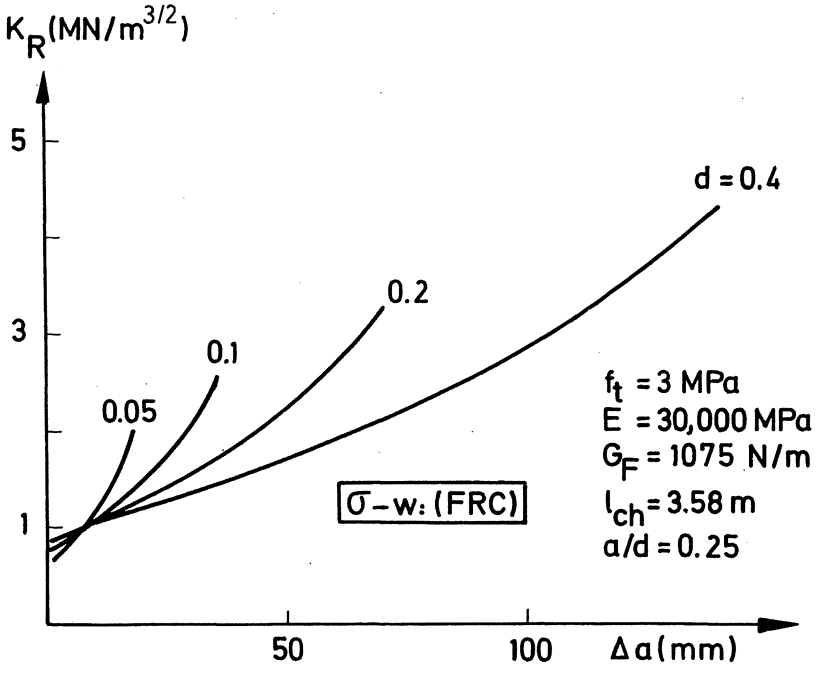

Fig 6.30 Theoretical K_R-curves for different beam depths. The curves represent a fibre-reinforced concrete with a low percentage of short fibres.

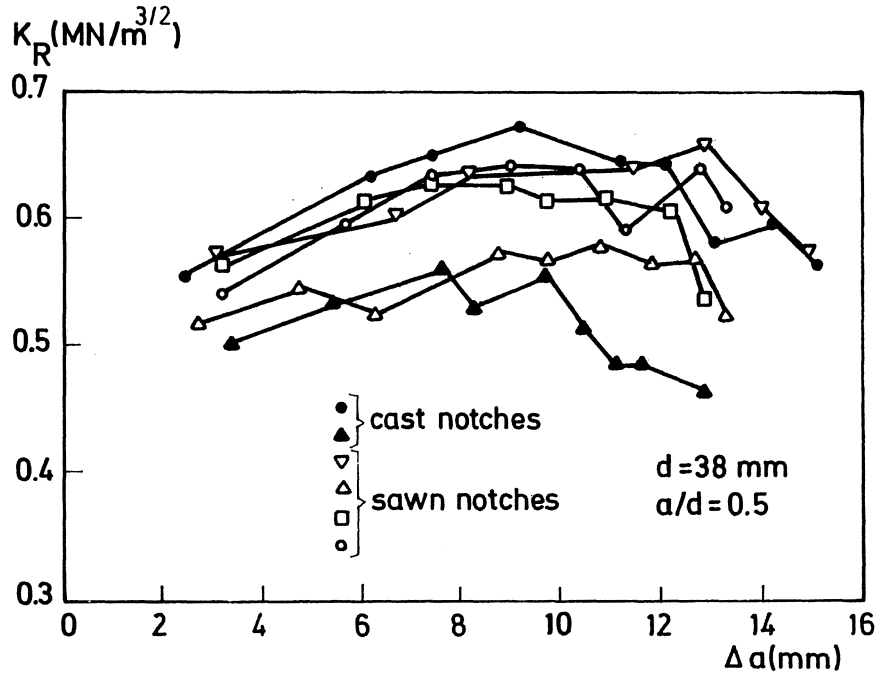

Fig 6.31 K_R-curves for six mortar beams (Brown, 1972).

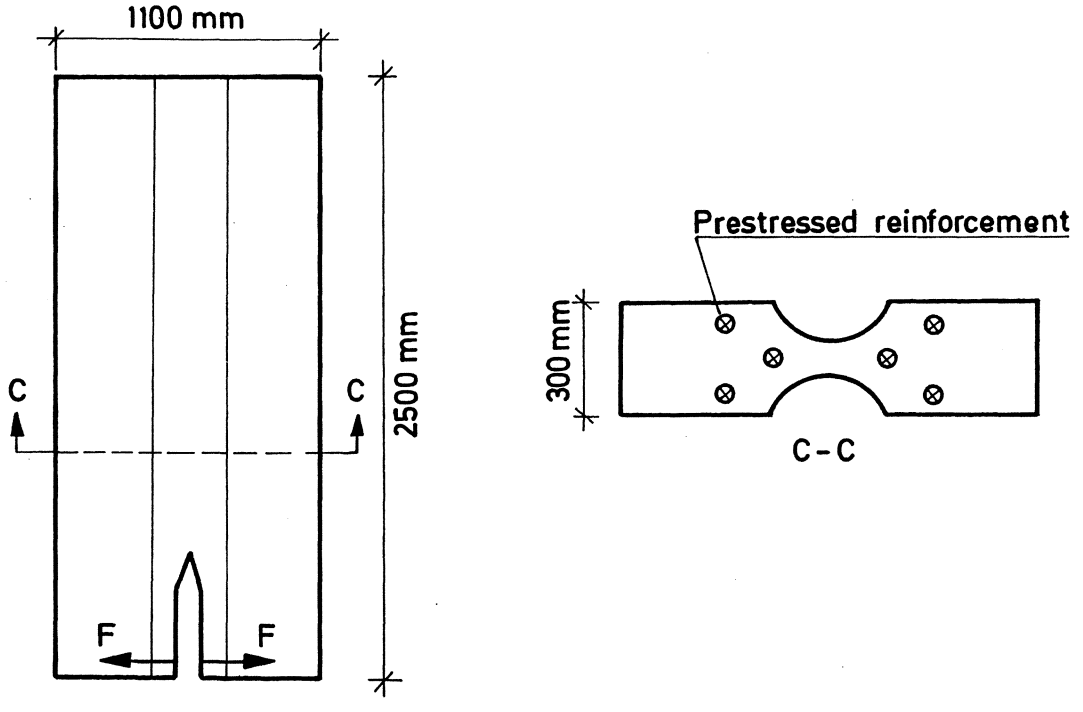

Fig 6.32 Double cantilever specimen used by Sok et al (1979) for determination of K_R-curves for concrete.

gation path. This varying thickness disturbs the stress distribution around the fracture zone. The fracture mechanics properties of the specimen are also markedly affected. The formal tensile strength is reduced to one third in the zone where the crack propagates and so is the fracture energy. This means that the ℓ_{ch}-value formally is increased three times and consequently, according to the results in Chapter 5, the depth of the fracture zone is markedly increased compared with the depth of the fracture zone in a specimen with constant thickness. According to the discussion above, this type of specimen seems unsuitable for fracture mechanics tests on cementitious materials.

In Fig 6.33 experimentally determined K_R-curves for different relative notch depths are shown for a fibre-reinforced concrete with 1 % round, smooth steel fibres distributed at random (Velasco, Visalvanich and Shah, 1980). The curves are determined on 76 mm deep beams in bending. In the Figure theoretical curves calculated by using the Fictitious Crack Model are presented as well. In the calculations a simplified σ-w curve according to Fig 6.34 was used, which seems suitable for this material (Hillerborg, 1980). In Fig 6.34 an experimentally determined (Petersson, 1980a) σ-w curve is also shown and the agreement between the theoretical and the experimental curves seems good. The Young's modulus is 30,000 MPa and the matrix crack is assumed to become visible when the widening of the fracture zone exceeds 10 μm.

As can be seen in Fig 6.33 the differences between the theoretical curves for different notch depths are small. From experiments it is probably very difficult to separate these curves and this explains the good agreement between the experimentally determined K_R-curves. However, when the beam depth increases, the slope of the theoretical K_R-curve decreases significantly and this implies that the K_R-curve cannot be used as a material property for this material either.

K_R-curves for an asbestos-cellulose cement composite have been determined by Mai, Foote and Coterell (1980). They studied the influence of beam depth on the K_R-curves and used beam depths between 25 and 200 mm. The relative notch depth was 0.3. The material contained 8 % asbestos fibres and 7 % cellulose fibres.

In Fig 6.35 the determined K_R-curves for the greatest and the smallest beam depths and corresponding calculated curves are presented. In the calculations it was assumed that the cellulose fibres did not affect the material parame-

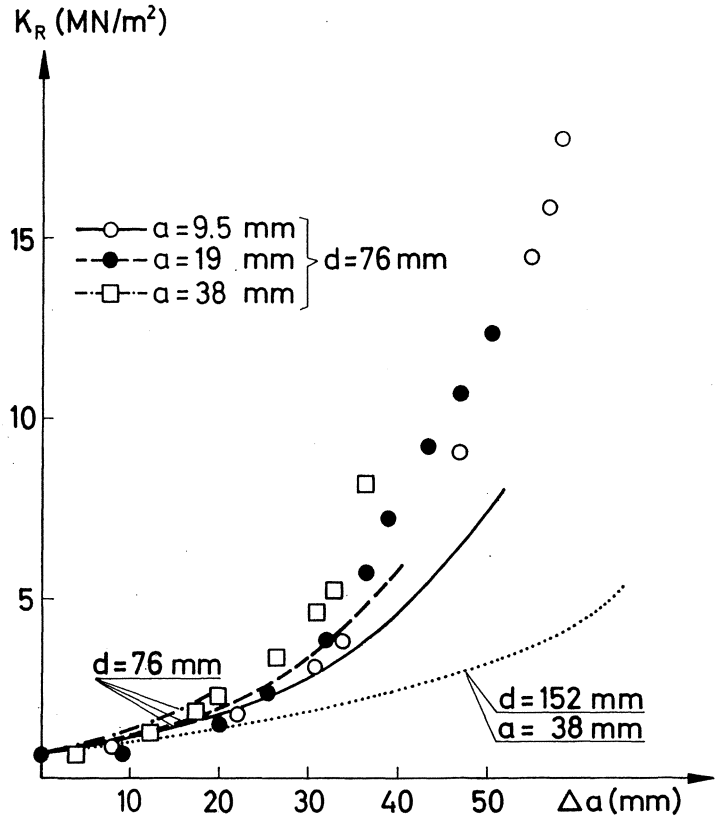

Fig 6.33 Experimentally (dots) and theoretically (lines) determined K_R-curves for fibre-reinforced concrete with 1 % round, smooth steel fibres distributed at random. During the calculations the σ-w curve was approximated according to Fig 6.34.

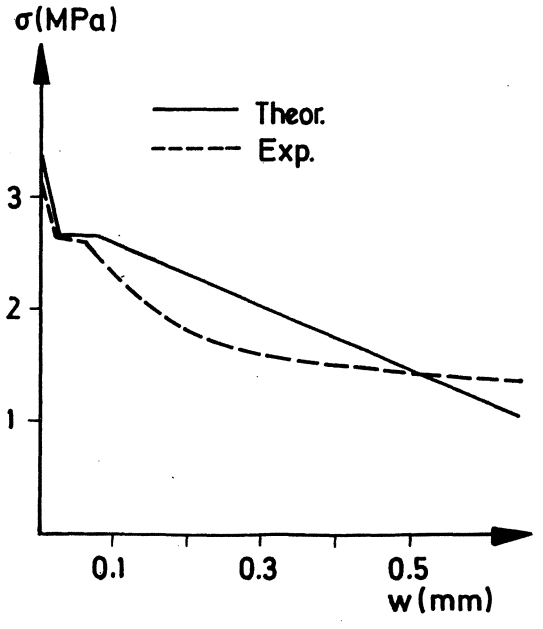

Fig 6.34 Experimentally and theoretically determined σ-w curves for a quality of fibre-reinforced concrete with 1 % of round, smooth steel fibres distributed at random.

ters very much and f_t, E and G_F were chosen according to Table 6:2, which means 9 MPa, 17,000 MPa and 1,500 N/m respectively.

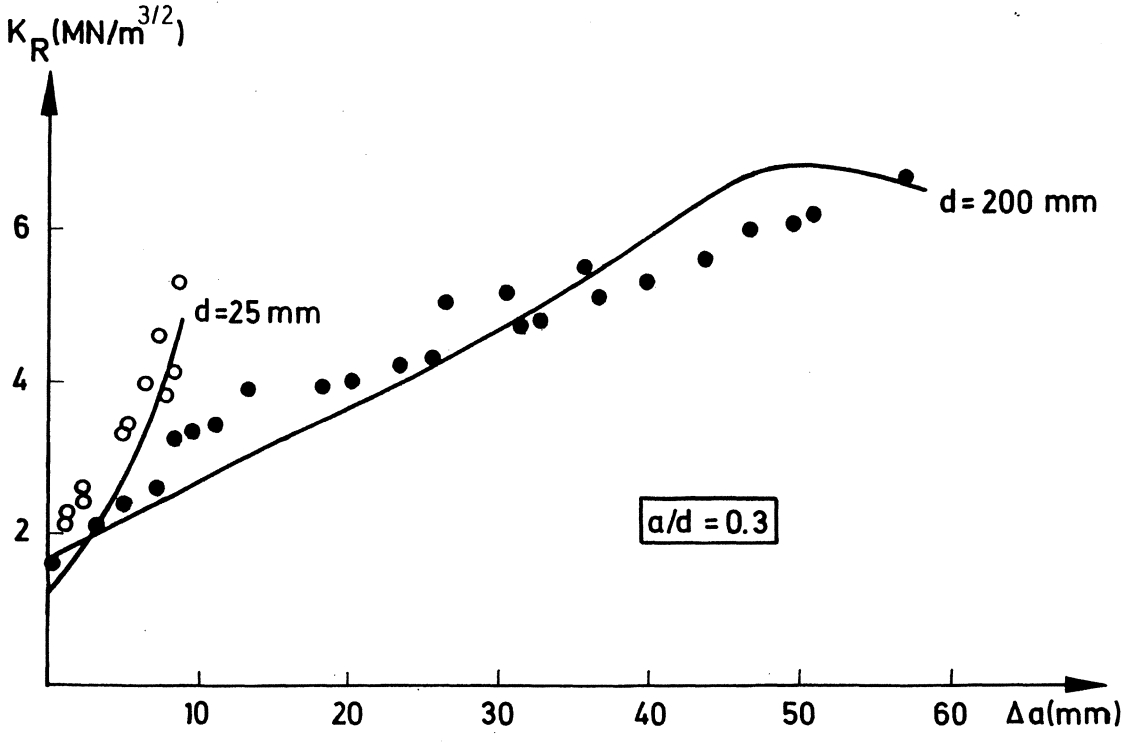

Fig 6.35 Experimental (dots) and theoretical (lines) K_R-curves of a quality of asbestos-cellulose cement composite for different beam depths. The experiments were carried out by Mai et al (1980).

The σ-w curve was approximated according to Dugdale and the matrix crack was assumed to become visible when the widening of the fracture zone exceeded 20 μm.

As can be seen in the Figure, the beam depth markedly affects the K_R-curves. This phenomenon is very well described by the theoretical curves calculated by means of the Fictitious Crack Model, in spite of the simplified assumptions.

According to the calculations, the test results and the discussion above it seems unsuitable to use K_R-curves as material properties for cementitious materials, at least for normally used dimensions. The curves are too dependent on the specimen dimensions and the notch depth.

6.6 Conclusions

The fracture zone significantly influences the fracture process of cementitious materials. The use of a single parameter seems insufficient for describing the complicated properties of the fracture zone and this explains why

the fracture mechanics approaches described above seem unsuitable. When the Fictitious Crack Model is used, the properties of the fracture zone are described by the σ-w curve and therefore this model offers a much more realistic and therefore better way of analysing the fracture process of cementitious materials than approaches normally used. Even if very simplified assumptions are used it is possible, by using the Fictitious Crack Model, to find out the limitations of the G-, J-, COD- and R-curve approaches where cementitious materials are concerned.

7 APPROXIMATIVE DETERMINATION OF THE σ-ε AND σ-w CURVES

7.1 Introduction

When using the Fictitious Crack Model it is necessary to know the σ-ε and σ-w curves for the material. If the σ-ε curve is approximated with a single, straight line, the curve is defined by the Young's modulus and the tensile strength. The σ-w curve is, if the shape of the curve is known, defined by the tensile strength and the fracture energy, see Fig 4.10. In this Chapter suitable methods for the determination of these properties are discussed and test results for a number of concrete qualities are also presented. As more or less standardized test methods already exist for the determination of the tensile strength and the Young's modulus, most of the work is concentrated on test methods by which the fracture energy can be determined.

7.2 Determination of the tensile strength (f_t) on prismatic specimens

7.2.1 Introduction

The main difficulty in carrying out direct tensile tests for concrete and other non-yielding materials on prismatic specimens is to achieve a uniform tensile stress across a section of the specimen, without inducing stress concentrations of too high a magnitude elsewhere. When the specimen is adapted to the testing machine by ordinary clamping grips, the grips give rise to stress concentrations and multiaxial stresses and the measured strength becomes less than the real tensile strength. By using sophisticated clamping grips (cf Johnston and Sidwell, 1968) the stress concentrations can be reduced but probably not eliminated. A way of attaching the specimen at the ends is to use an adhesive (Hughes and Chapman, 1965; Kadlecek and Spetla, 1966). However, the adhesive and the concrete normally exhibit different lateral strains when subjected to uniaxial stress due to their differences in Young's modulus and Poisson's ratio. Thus, shear stresses are produced between the two materials and in the region of the interface a principal stress that is greater than the axial tensile stress is then introduced, which most likely causes the fracture to occur at this interface. When using wet specimens it is also difficult to obtain a sufficiently strong joint. Consequently, when using ordinary clamping grips or adhesives, it is necessary to use necked specimens. A necked specimen has a varying cross sectional area, which is smallest at the middle of the specimen.

In order to avoid direct tensile tests it is customary to carry out indi-

rect tests, i.e. bend tests or splitting tests. However, these tests are greatly affected by specimen dimensions and are therefore unsuitable. In Fig 7.1 it is shown how the flexural tensile strength (f_f) depends on the ratio beam depth/characteristic length (d/ℓ_{ch}). The curves represent theoretical values, calculated by means of the Fictitious Crack Model, for wet specimens and specimens subjected to a certain degree and distribution of shrinkage stresses respectively, see below, and the dots represent test results. In the calculations the σ-w curve was approximated with a single, straight line. Similar results, for both bend tests and splitting tests, are presented in the literature (Wright, 1952; Mayer, 1967; Sabnis and Mirza, 1979; Modéer, 1979).

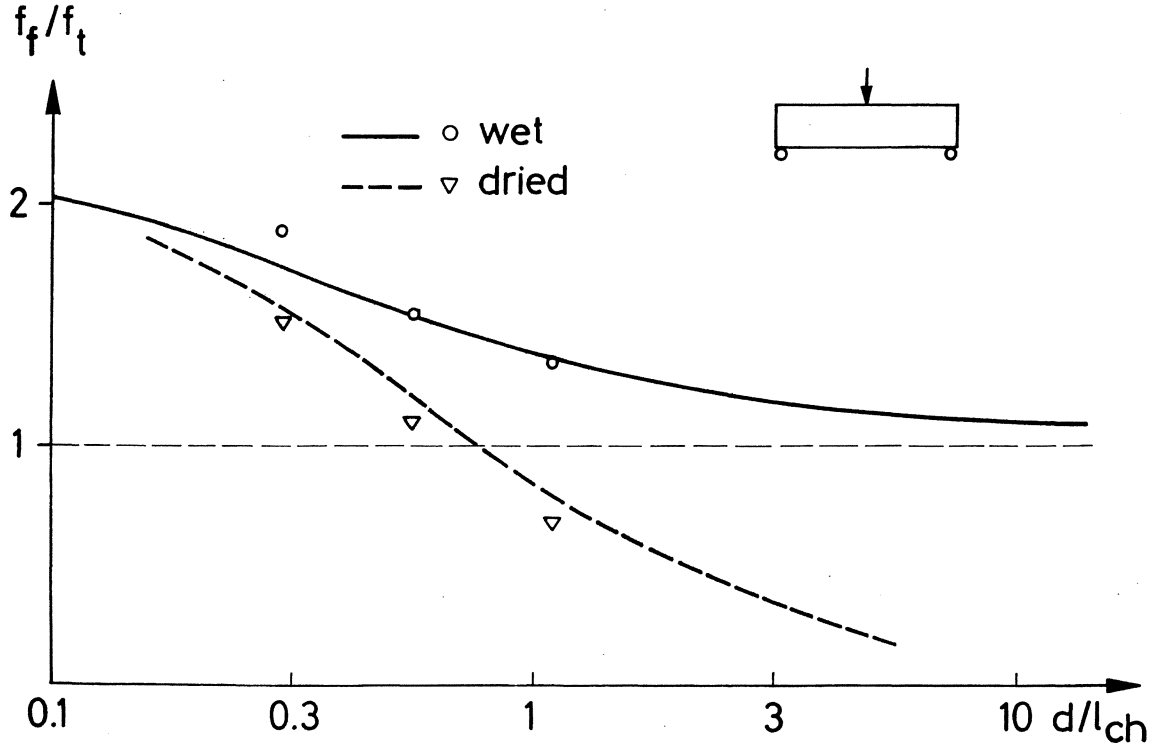

Fig 7.1 Flexural tensile strength/tensile strength (f_f/f_t) as a function of beam depth. The curves are calculated by means of the Fictitious Crack Model and the dots represent test results.

Some comments ought to be made about the results shown in Fig 7.1. The results are relevant for three-point bending and the flexural tensile strength is calculated as:

$$f_f = \frac{3F_c\ell}{2bd^2} \qquad (7:1)$$

where F_c = maximum load, ℓ = beam length, b = beam width and d = beam depth. This means that the influence of the transverse forces are ignored. This in-

fluence increases as the ratio beam length/beam depth decreases (Pfeiffer, 1968) and the flexural tensile strength calculated by use of (7:1) is always somewhat higher than the tensile strength. When the ratio beam length/beam depth is as high as 4, this influence is small but it explains why the unbroken curve in Fig 7.1 tends towards a value, which slightly exceeds unity when the beam depth increases. The disturbance of the stress field around the position of the applied load probably also affects the results slightly.

When calculating the curve representing beams subjected to drying shrinkage stresses, the stress distribution according to Fig 7.2 was assumed. In reality the distribution of course is much more complicated and affected by, for example, drying time and changes in the environmental climate. The intensity of the shrinkage stresses shown in Fig 7.2 produced the best agreement with test results.

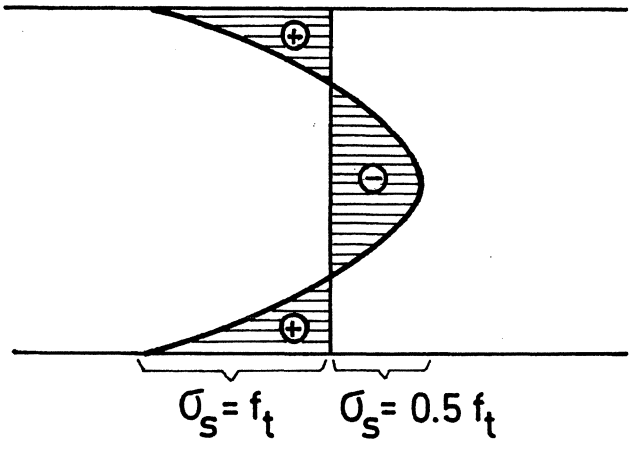

Fig 7.2 The shrinkage stress distribution used in the calculations in Fig 7.1. σ_s = shrinkage stress.

The tests were carried out on beams with square cross sections. The drying velocity was assumed to be proportional to the square of the beam depth (Hillerborg et al, 1977) and the beams with the depths 40, 80 and 160 mm were dried for 6, 24 and 96 h respectively. The specimens were dried on all surfaces which means that the stress distribution in the specimens became different compared with the distribution shown in Fig 7.2. The material used in the tests was a mortar (water-cement-ratio=0.65, maximum aggregate particle size =4 mm) and the ℓ_{ch}-value was assumed to be 150 mm.

In spite of the simplified assumptions the agreement between the calculated curves and the test results is good and it seems possible to describe the bend test on unnotched specimens by use of the Fictitious Crack Model. Among other

things it can be noticed in Fig 7.1 that the dependency of the beam depth on the flexural tensile strength increases when the specimen becomes subjected to shrinkage stresses.

7.2.2 Direct tensile tests on prismatic specimens

In Fig 7.3 and Fig 7.4 a new type of grip is presented by which it is possible to determine the tensile strength by direct tests on prismatic specimens. The grip consists of steel plates on to which wedge-shaped rubber inserts are glued. It is essential that the inserts are oriented according to Fig 7.3.

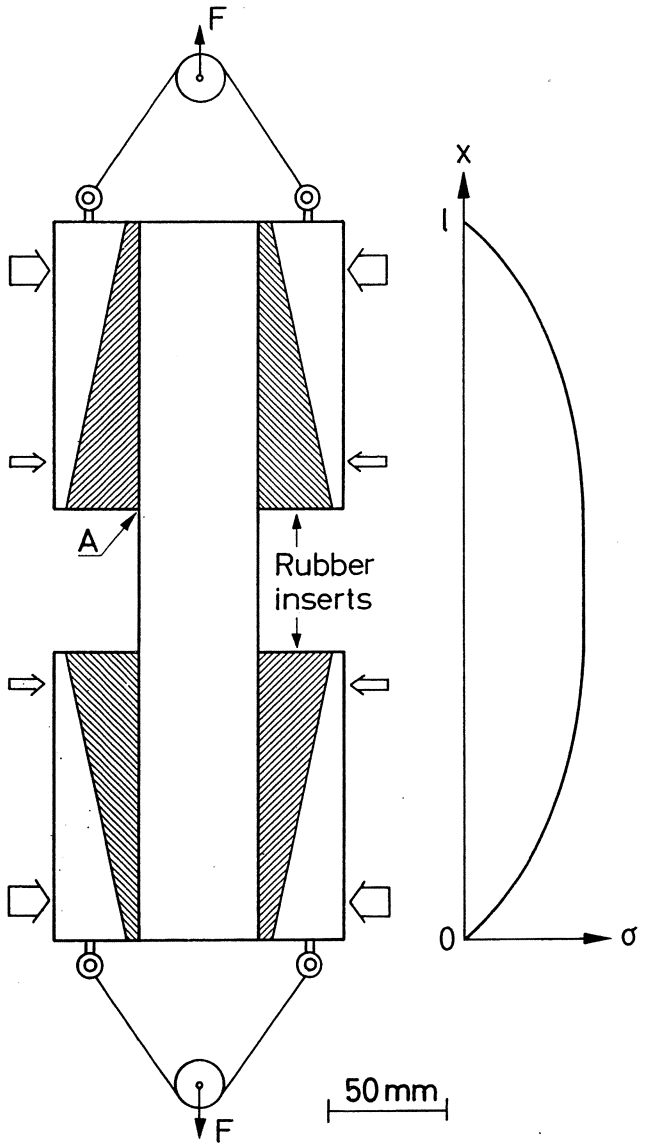

Fig 7.3 Grips for direct tensile tests. The wedge-shaped rubber inserts reduce the stress-concentrations to a minimum.

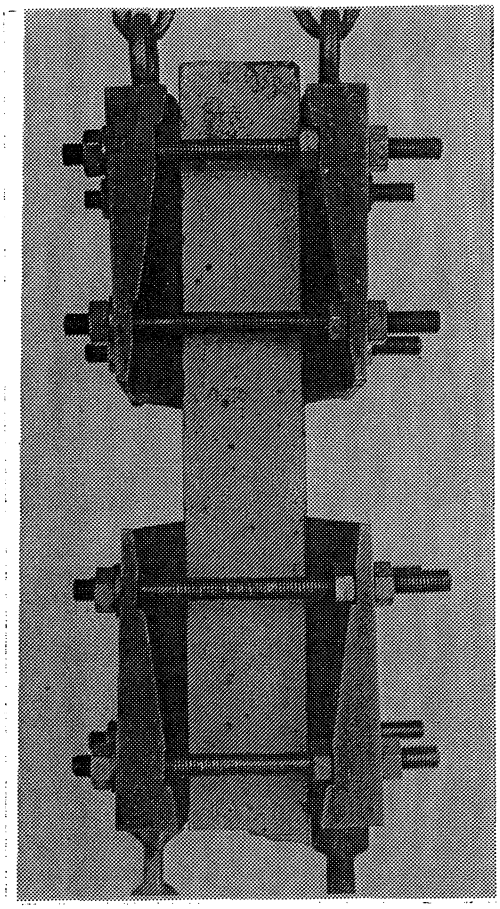

Fig 7.4 Tensile test using the grips in Fig 7.3.

Each part of the grip is pressed against the specimen at two points; one force near the end of the specimen and one lesser force close to the free part of the specimen.

The advantages of these grips compared to ordinary grips may be summarized as follows:

1. The clamping forces are greatest at the ends of the specimen and least at the ends of the grips close to the middle of the specimen. This means that the stress perpendicular to the tensile direction is small at the most critical cross section, i.e. at point A in Fig 7.3, and at this point the stress field becomes almost one dimensional.

2. Due to the variable stiffness of the wedge-shaped rubber inserts, the main part of the load is applied close to the ends of the specimen and consequently the axial stress grows gradually to its maximum value, which is shown in Fig 7.3.

3. The loading force at one point gives rise to a non-uniform stress distribution over the corresponding cross sectional area. The stress distribution becomes more uniform at a distance from the loading point. As the main part of the loading forces acts close to the ends of the specimen, the stress distribution becomes fairly uniform at the end of the grips. Consequently, the stress concentrations at point A become reduced to a minimum.

4. These grips make it possible to use prismatic specimens, which facilitate the manufacturing of test pieces. Specimens can also be sawn out from a structure.

The tensile tests presented in 7.5 below were carried out on 177 specimens. The fracture location distribution for the specimens examined in the test program is shown in Fig 7.5. The fracture location is defined as the distance between the position of the fracture load and the centre of the specimen.

In the Figure the position of the clamping grip is shown. As indicated in the Figure, the rubber insert deforms as the specimen becomes loaded and the contact between the insert and the specimen is lost over a distance of about 20 mm at the thick end of the insert and consequently the free part of the specimen increases, in this case, from 80 to about 120 mm in the test.

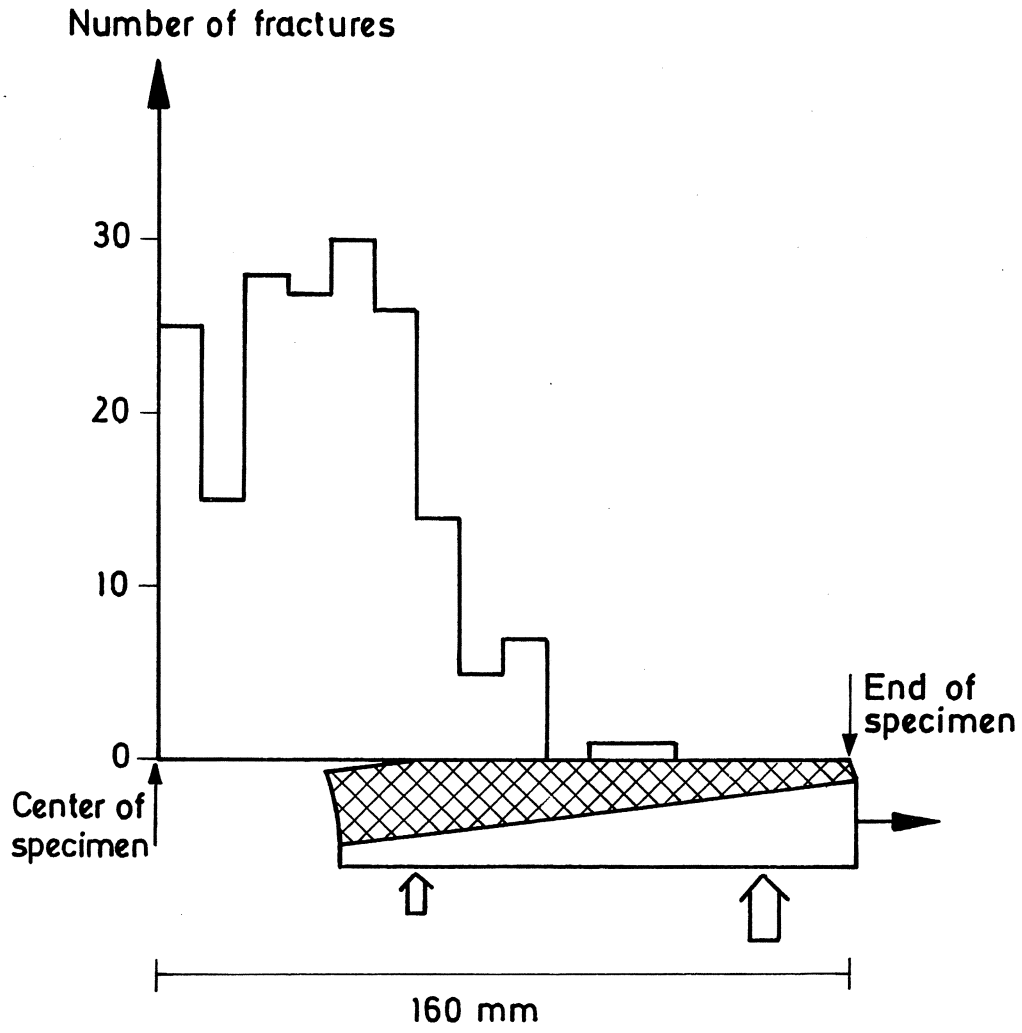

Fig 7.5 The fracture location distribution for the 177 direct tensile tests.

As can be seen in the Figure, the fracture locations are well distributed over the length of the free part of the specimen, which implies that no stress concentrations or multi-axial stresses affect the distribution and thus the fracture load. Of course there are a few fracture locations outside the free part of the specimen but this is quite natural due to the varying tensile strength along the specimen for an inhomogeneous material such as concrete.

The tensile strength determined by use of the grips described above has been compared with the flexural tensile strength for a number of concrete qualities (Petersson, 1981 and 7.5.5 below) and the ratio f_f/f_t seems to agree well with theoretical relations, which also implies that the grips are suitable for determining the direct tensile strength on prismatic concrete specimens.

7.3 Determination of the Young's modulus (E)

The static Young's modulus is a well defined material property for linear elastic, non-creeping materials only, otherwise the modulus is affected by, for example, loading velocity, load intensity and the number of load cycles. The dynamic Young's modulus (E_d) on the other hand is a well defined material property and for this reason it is the dynamic Young's modulus that has been determined in this work. The dynamic Young's modulus is always higher than the static Young's modulus, the difference is normally 10-20 % (Bastgen and Hermann, 1977).

In this thesis a method according to Vinkeloe (1962) has been used for determining the dynamic Young's modulus. The method is described briefly below.

According to Vinkeloe there exists a relation between the resonance frequency of a beam and the dynamic Young's modulus that can be expressed as:

$$E_d = \frac{f^2 M \ell^3 T}{C^2 I^2} \qquad (7:2)$$

where f is the resonance frequency, M is the mass of the beam, ℓ is the beam depth, T is a correction factor depending on the dimensions and the Poisson's ratio, C is a constant depending on the mode of oscillation and I is the moment of inertia for the beam.

For the first mode of oscillation the beam will oscillate around two points, which are located 0.224 ℓ from each end of the beam. In the tests these locations should coincide with the position of the supports. For the first mode of oscillation, which is used in this work, C is 3.56.

The dimensionless constant T is dependent on the Poisson's ratio and the ratio K/ℓ, where K for a beam with a square cross section equals beam depth/ $\sqrt{12}$. In Fig 7.6 T is given as a function of K/ℓ when the Poisson's ratio is 0.167. However, the curve is very little affected by the Poisson's ratio, for example, if Poisson's ratio is changed to 0, the value of T at $K/\ell=0.1$ decreases by 1.3 % and when $K/\ell=0.02$ (which is the case at the tests presented in 7.5) T decreases by 0.4 %.

In Fig 7.7 a schematic description of the test equipment used for determining the dynamic Young's modulus is shown. The specimen (4) is oscillating due to the vibrations caused by the vibrator (3). The frequency of the vibrator is controlled by a tone generator (1) and a frequency counter (2). The vibrations of the beam are registered by use of a pick-up (5) and an oscilloscope (6).

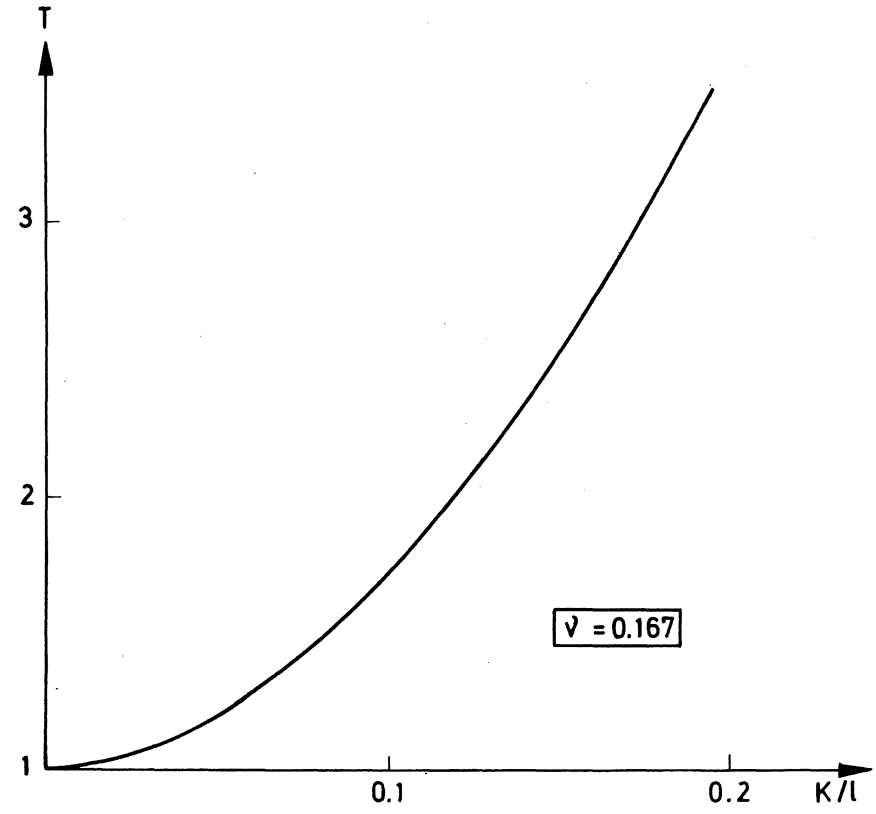

Fig 7.6 Correction factor T as a function of K/ℓ.

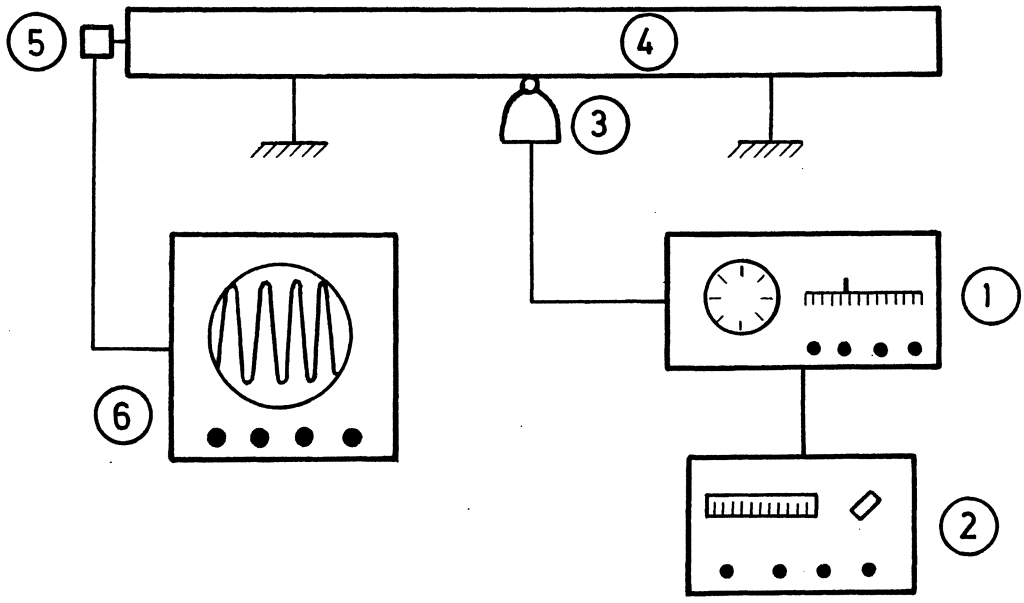

Fig 7.7 Testing equipment for measuring the resonance frequency and the Young's modulus on concrete beams. 1=tone generator, 2=frequency counter, 3=vibrator, 4=specimen, 5=pick-up, 6=oscilloscope.

The frequency is varied by use of the tone generator and the highest amplitude registered on the oscilloscope gives the resonance frequency and thus the dynamic Young's modulus.

7.4 Determination of the fracture energy (G_F)

7.4.1 Introduction

The fracture energy (G_F) is defined as the amount of energy necessary to create one unit of area of a crack and the principle when measuring G_F is therefore to let a crack propagate a well defined distance and measure the energy consumption due to the crack propagation. As discussed previously it is very difficult to define the position of the tip of a propagating crack and for this reason it seems necessary to measure the total energy consumption from the start of crack initiation until the crack has propagated right through the specimen as this gives a well defined length of the crack propagation path. It is essential that the fracture, i.e. the crack propagation, is stable as otherwise uncontrolled energy consumption due to dynamic effects will take place and it is also essential that the energy consumption outside the fracture zone is minimized. These problems are discussed in detail below.

There are a number of specimen types that can be used in order to obtain stable crack propagation, for example double torsion specimen (cf Wecharatana and Shah, 1980), compact tension specimen (cf Hillemeier and Hilsdorf, 1977), double cantilever beam (cf Chhuy, Benkirane, Baron and Francois, 1981) and also direct tensile test specimens (cf Evans and Marathe, 1968 and Chapter 8 below). However, the most simple specimen that can be used is a notched beam and in this case all the work is concentrated on the determination of the fracture energy by the use of three-point bending on notched beams.

Very few results of the fracture energy determined from stable tests are found in literature. Moavenzadeh and Kuguel (1969) measured the energy under the load-deflection curve for some qualities of cement paste, mortar and concrete. They related this energy to the actual crack surface and not to the net cross sectional area and therefore their results must be considered as some form of surface energies and not as fracture energies. Shah and McGarry (1971) also measured the energy under the load deflection curve and their results correspond to values of the fracture energy of 5-33 N/m for cement paste, 20-95 N/m for mortar and 30-135 N/m for concrete. It is however doubtful if all their

tests were carried out in a stable manner and at the evaluation of the tests the effect of the energy supplied by the weight of the beams was probably not considered. Harris, Varlow and Ellis (1972) found values of G_F for concrete of about 20-120 N/m but also in these tests it is doubtful if the effects of stability and energy supplied by the weight of the beams were considered. Modéer (1979) found G_F-values of about 10, 60 and 110 N/m for some qualities of cement paste, mortar and concrete. These tests have been carried out in a stable way and the tests were, at least to some extent, compensated for by the energy supplied by the weights of the beams. Fracture energy tests have also been carried out on fibre-reinforced materials (cf Harris, Varlow and Ellis, 1972; Ohigashi, 1978; Mai, 1979) but these results are not discussed here.

Even if there are some results of the fracture energy determined on notched beams, no investigations have been carried out in order to study the applicability of the test methods and the usefulness of G_F as a material property. For this reason the fracture energy and the usefulness of the three-point bend test for determining G_F are dealt with in detail below.

7.4.2 Stability conditions for three-point bend tests on notched beams

In order to obtain a relevant value of the fracture energy from a three-point bend test on a notched beam, the amount of energy supplied by the loading force and the weight of the beam must equal the amount of energy consumed by the crack propagation. This means that the energy consumption taking place outside the fracture zone in front of the crack tip has to be minimized. To fulfil this condition the fracture must be stable, otherwise energy consumption due to dynamic effects will occur.

In order to obtain a stable fracture it is necessary to use a displacement controlled testing machine as a load controlled machine always produces an unstable fracture when the maximum load is reached. The crack must also, for every point of the load-deflection curve, be able to consume the amount of energy that is released from the beam and the testing machine during the deformation.

Cooper (1977) and Modéer (1979) calculated conditions of stability for three-point bend tests on notched beams for the linear elastic case. According to their results it is almost impossible to obtain a stable fracture for cementitious materials unless the ratio notch depth/beam depth (a/d) is very large

and the test is performed in a very stiff testing machine. However, as discussed before, concrete is far from being an ideal linear elastic material and below it is shown how this makes it much easier to fulfil the conditions of stability.

In Fig 7.8 an example of a stable load-deflection curve (F-δ curve) is shown for a three-point bend test on a notched beam. The total amount of energy, Q_b, necessary to deflect the beam a distance δ_1 can be calculated from the F-δ curve. Q_b is affected by the strain energy release of the beam when the crack propagates as well as the amount of energy consumed by the slow crack propagation:

$$Q_b = \int_0^{\delta_1} F(\delta)d\delta \qquad (7:3)$$

In the total test arrangement, the energy release and consumption of the testing machine must also be considered. The stiffness, k, of the testing machine is defined as:

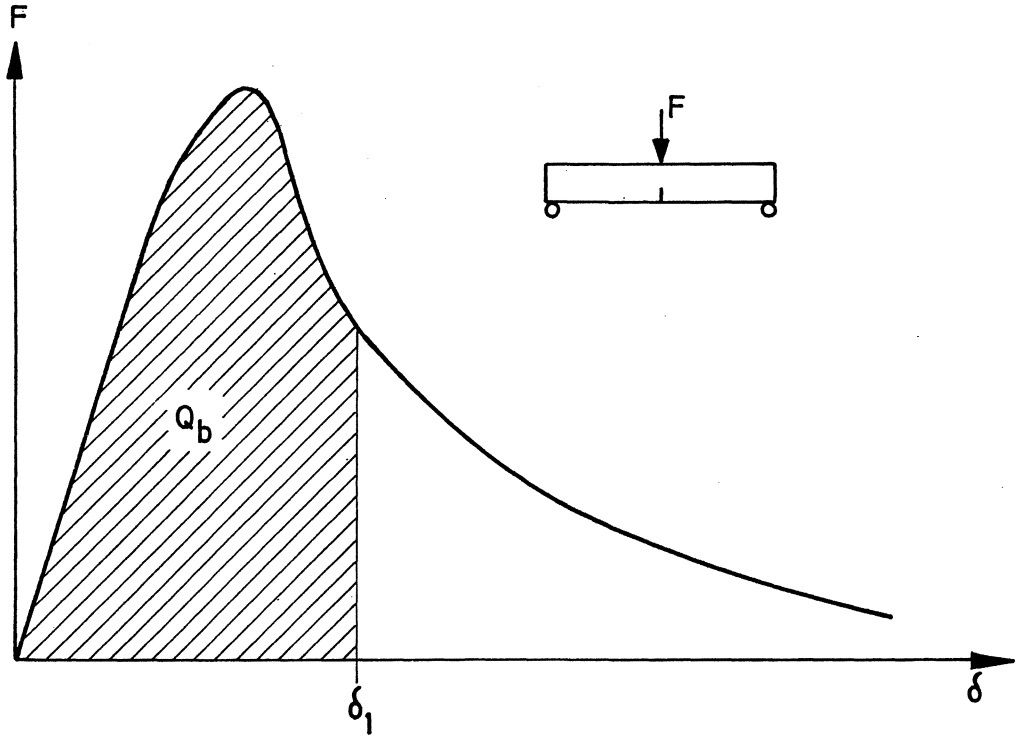

Fig 7.8 A load-deflection curve for a three-point bend test on a notched beam. The energy consumption necessary to deflect the beam a distance δ_1 is Q_b.

$$k = \frac{F}{\delta_M} \tag{7:4}$$

where F is the load applied to the testing machine and δ_M is the deformation of the testing machine due to the load F.

The stiffness of the testing machine determines the energy consumption of the testing machine, Q_M, when the beam is deflected a distance δ:

$$Q_M = \frac{F(\delta)\delta_M}{2} = \frac{(F(\delta))^2}{2k} \tag{7:5}$$

In order to obtain a stable fracture, the derivative of the total energy consumption has to be positive for any value of δ:

$$\frac{\partial(Q_b + Q_M)}{\partial\delta} = F(\delta) + \frac{F(\delta)}{k}\frac{\partial F(\delta)}{\partial\delta} > 0 \tag{7:6}$$

(7:6) gives the condition of stability:

$$k > -\frac{\partial F(\delta)}{\partial\delta} \tag{7:7}$$

(7:7) implies that the stiffness of the testing machine has to be greater than the steepest slope of the descending part of the F-δ curve, in order to obtain a stable fracture.

By use of the Fictitious Crack Model, F-δ curves can be calculated for different beam geometries and material properties. Conditions of stability can then be derived from (7:7). Results from such calculations are presented in Fig 7.9 b-f. In the calculations the σ-w curve was approximated with a single, straight line (SL). In Fig 7.9a conditions of stability for the linear elastic case according to Modéer (1979) are shown.

The geometrical parameters affecting the stability are ℓ/d, a/d and b (ℓ=beam length, d=beam depth, b=beam width and a=notch depth). The material properties affecting the stability, for a given shape of the σ-w curve, are the characteristic length (ℓ_{ch}) and the Young's modulus. The stability is also affected by the stiffness of the testing machine (k). The energy stored in the machine is directly proportional to E, b and 1/k and consequently directly proportional to Eb/k.

The curves in Fig 7.9 show that the conditions of stability are strongly affected by the d/ℓ_{ch}-value. A specimen of cement paste with a depth of 25 mm

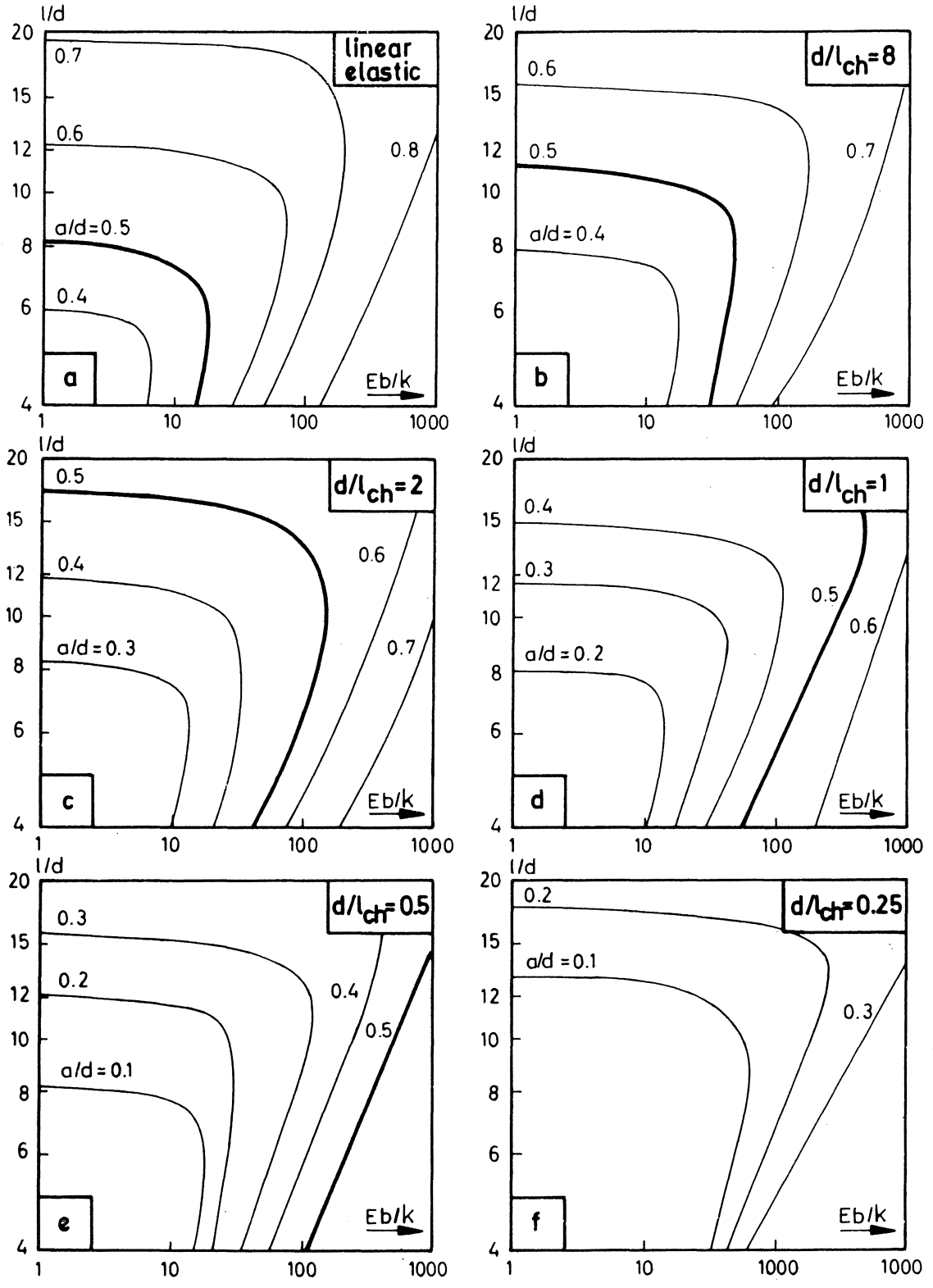

Fig 7.9 Conditions of stability for a three-point bend test on a notched beam. The areas of stability are limited by the curves and the axis. The Figure is relevant when the σ-w curve is approximated with a single, straight line.

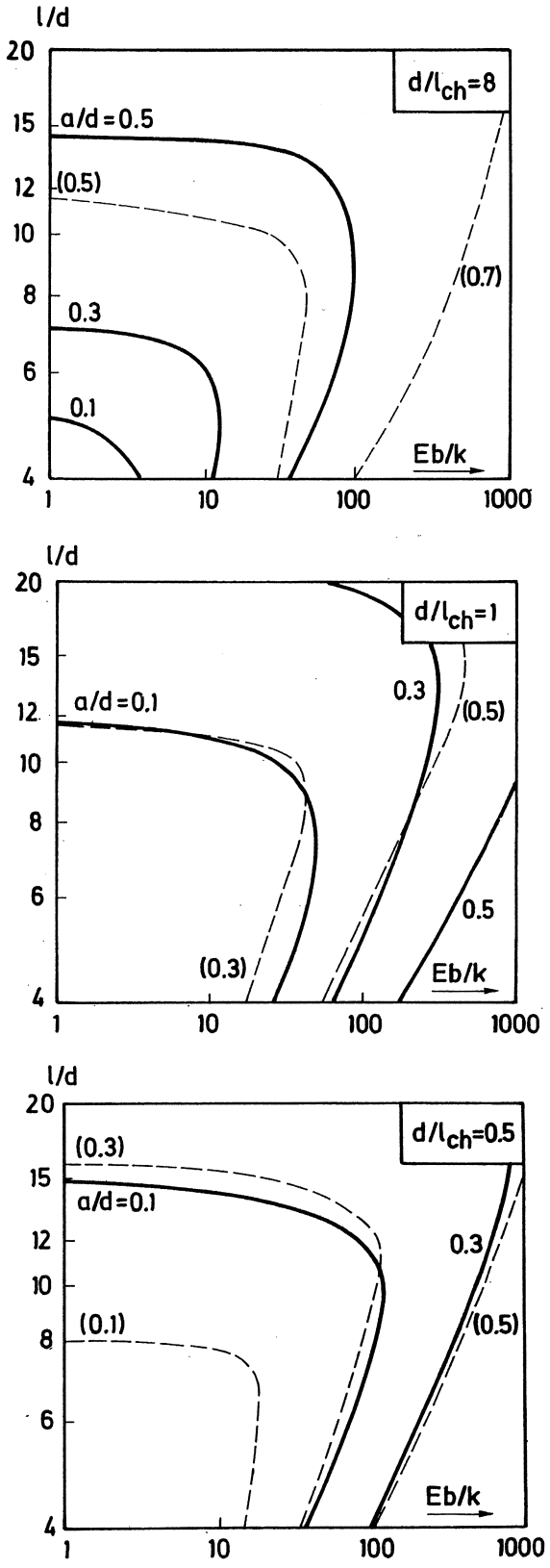

Fig 7.10 Conditions of stability for a three point-bend test on a notched beam. The curves are relevant for a two line approximation of the σ-w curve according to Fig 6.3 (unbroken lines) and the curves are compared with the results in Fig 7.9 (dashed lines).

has a d/ℓ_{ch}-value of about 2-4. Although this material is normally considered to be very brittle, the curves of stability noticeably differ from those calculated with the assumption of a linear elastic material. A concrete specimen with a depth of 50 mm has a d/ℓ_{ch} value of about 0.2. As seen in the Figure, these curves differ completely from the linear elastic case and the conditions of stability according to the linear elastic case are much too hard for concrete.

When determining G_F, all the beams have to fail in a stable manner, otherwise a systematic error will occur. When using the mean value of d/ℓ_{ch} about 50 % of the beams will fail in an unstable manner. This is a reason why the d/ℓ_{ch}-value ought to be increased somewhat before using Fig 7.9.

In Fig 7.10 conditions of stability are shown for three different values of d/ℓ_{ch} when the σ-w curve is approximated with two straight lines according to Fig 6.3 (unbroken lines). The dashed lines correspond to the results in Fig 7.9. As can be seen, the conditions of stability are considerably harder for the single line approximation of the σ-w curve than when the curve is approximated with two straight lines. This can be explained by the fact that the lesser the slope of the σ-w curves is directly after the maximum stress, the higher the fracture load becomes and, for the same value of G_F, the steeper the descending part of the load-deflection curve becomes, compare Fig 6.5. However, as the conditions of stability in Fig 7.9 are on the safe side, they can normally be used for concrete and similar materials, especially as the conditions are relatively mild. For example, for a concrete beam with the dimension 100 x 100 x 1000 mm^3 and the relative notch depth 0.5, the stiffness of the testing machine has to exceed about 10,000 N/mm in order to obtain a stable fracture (ℓ_{ch} and E are assumed to be 200 mm and 40,000 MPa respectively). Most modern testing machines fulfil this condition. Where fibre-reinforced materials are concerned other conditions of stability naturally have to be used but these materials normally have such high ℓ_{ch}-values that there are no problems in achieving stable fractures.

7.4.3 Evaluation of the G_F-test

When carrying out stable three-point bend tests, energy is not only supplied by the load but also by the weight of the beam. The effect of the energy supplied by the weight of the beam can be eliminated if the length of the beam is twice the distance between the supports according to Fig 7.11a. Of course shorter beam lengths can be used if the moment caused by the weight of the beam is compensated for by weights at the ends of the beam according to Fig 7.11b.

(Specimens according to Fig 7.11 are here called compensated beams). If this method is used then the fracture energy is directly obtained as:

$$G_F = \frac{A}{b(d-a)} \qquad (7:8)$$

where A = the area under the stable load-deflection curve, d=beam depth, a=notch depth and b=beam width.

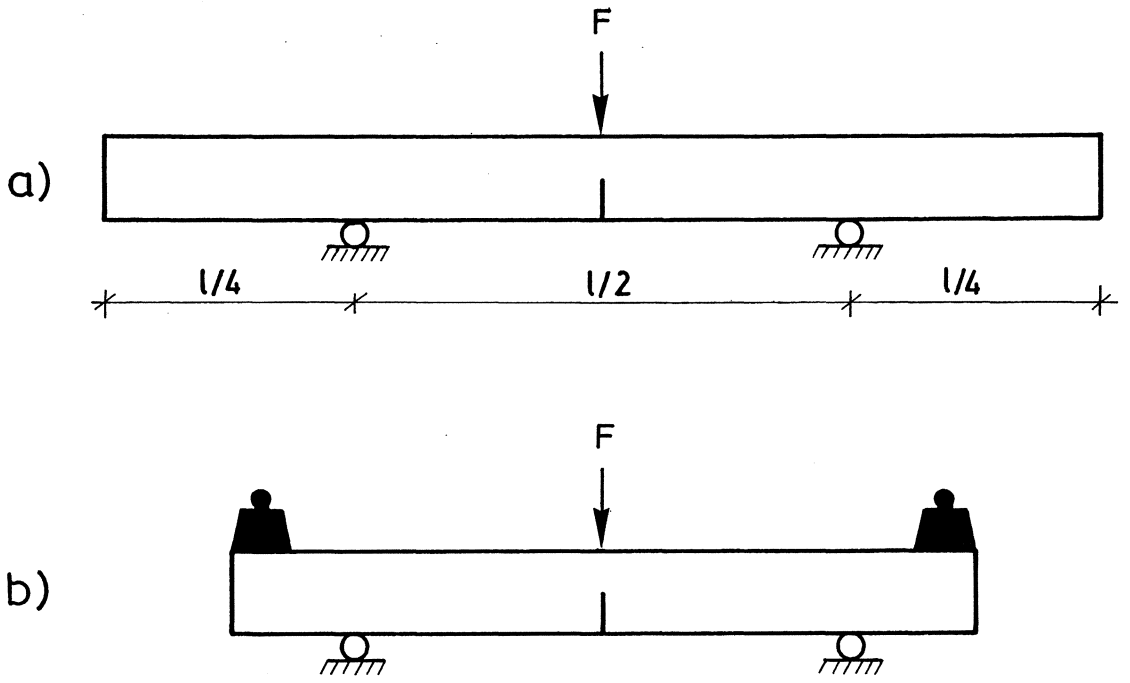

Fig 7.11 a) The energy supplied by the weight of the beam can be compensated for by using a beam with the length equalizing twice the distance between the supports

b) The energy supplied by the weight of the beam can also be compensated for by using weights at the ends of the beam.

When using the methods described in Fig 7.11 for evaluating G_F, some problems may arise. The beams have to be long which can give rise to problems in the performance of the test. Another problem is that there will be a long "tail" on the load-deflection curve, see Fig 7.12. Theoretically this tail will be infinitely long. The area under the curve is preferably measured by using a planimeter and then the long tail can cause problems. A small fault in the balance of the system can also give rise to substantial errors due to the long tail. For these reasons it would be better if the test could be stopped at a certain moment but this is only possible if the effect of the weight of the beam can be estimated.

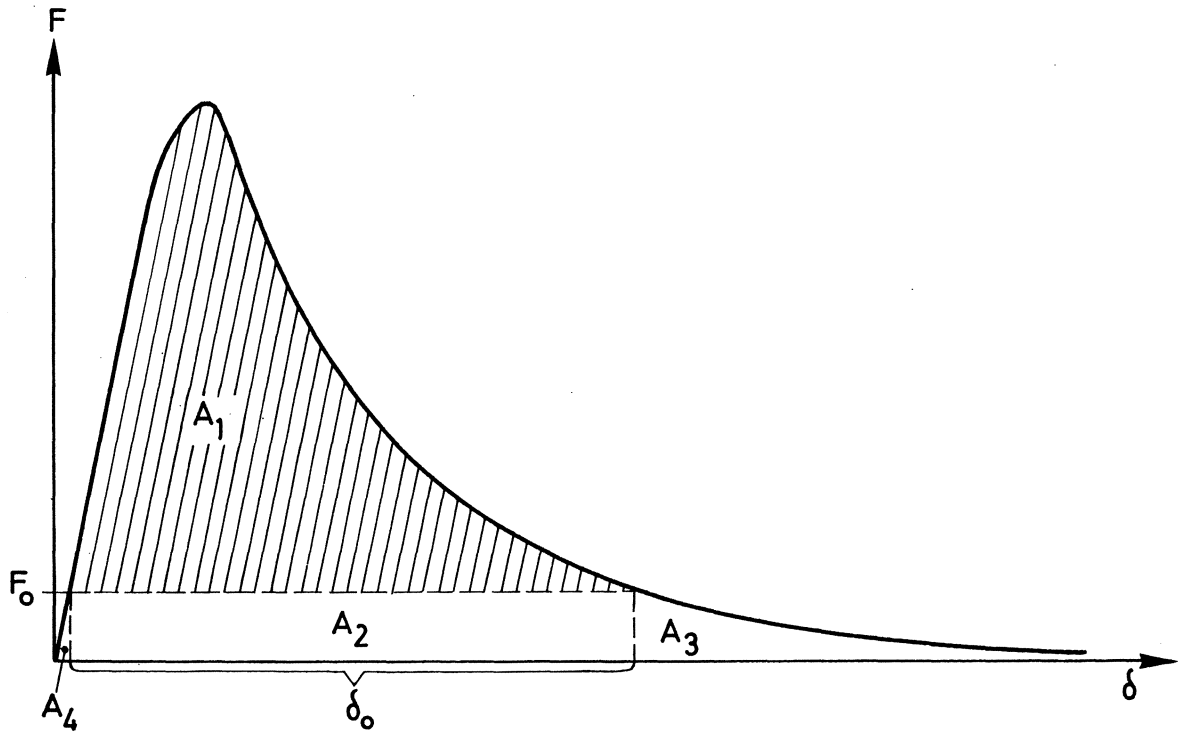

Fig 7.12 A load-deflection curve for a stable three-point bend test on a notched beam. The shaded area (A_1) defines the area under the load-deflection curve if there is no compensation for the energy supplied by the weight of the beam.

If there is no compensation for the effect of the weight of the beam, i.e. an uncompensated beam, then the beam will fail at a point corresponding to the load F_0 on the compensated load-deflection curve, see Fig 7.12. F_0 can be found by equating the moment due to F_0 and the moment due to the weight of the beam:

$$\frac{F_0 \ell}{4} = \frac{mg\ell^2}{8}$$

$$\Rightarrow$$

$$F_0 = \frac{mg\ell}{2} = \frac{Mg}{2} \qquad (7:9)$$

where m = weight per unit length of the beam, M = weight of the beam (between the supports) and g = 9.81 m/s^2.

When using the uncompensated beam for determining G_F the area under the load-deflection curve corresponds to the area A_1 in Fig 7.12. This method is useful only if it is also possible to estimate the energies corresponding to

A_2, A_3 and A_4 in the Figure. Normally A_4 is so small (less than 1 - 2 % of the total area) that it can be neglected. The area A_2 equals $F_o\delta_o$ (where δ_o is the deflection at the final fracture of the uncompensated beam) and consequently:

$$A_2 = \frac{Mg\delta_o}{2} \qquad (7:10)$$

For small values of the load (on the descending part of the curve) it is fair to assume that the beam is divided into two rectangular pieces which are only connected by the fracture zone, see Fig 7.13. It is assumed that the sides of the crack and the fracture zone are plane and that the compression zone is concentrated on a point at the top of the beam. This of course is an approximation as there always exists a compression zone at the top of the beam. However, it can be shown that the discussion below is relevant also when there exists a compression zone if the stress distribution over the remaining ligament is assumed to be uniformly changed as the depth of the fracture zone decreases.

For a given beam according to Fig 7.13 and defined material properties the depth of the fracture zone (d_F) is, when a real crack has started to propagate, reciprocally proportional to the deflection of the beam (δ), i.e.:

$$d_F = \frac{C_1}{\delta} \qquad (7:11)$$

where C_1 is a constant. Both the total closing force and the moment arm are proportional to d_F and consequently:

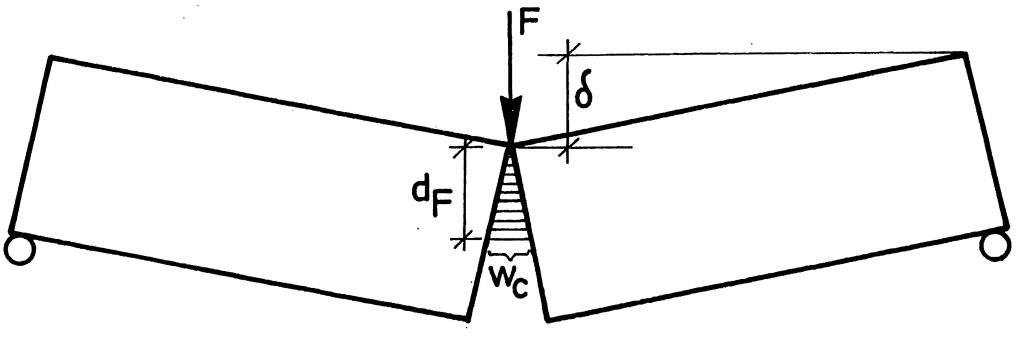

Fig 7.13 An approximative description of the last phase of a stable three-point bend test.

$$F(\delta) = \frac{C_2}{\delta^2} \qquad (7:12)$$

where C_2 is a constant. The area A_3 in Fig 7.12 then can be calculated as:

$$A_3 = \int_{\delta_o}^{\infty} F(\delta)d\delta = \int_{\delta_o}^{\infty} \frac{C_2}{\delta^2}\, d\delta = \frac{C_2}{\delta_o} = \frac{C_2}{\delta_o^2}\,\delta_o$$

and consequently, according to (7:9) and (7:12):

$$A_3 = F_o\delta_o = \frac{Mg\delta_o}{2} \qquad (7:13)$$

This means that the value of A_3 equals A_2 and, when using the uncompensated beam, the expression for G_F is:

$$G_F = \frac{A_1+Mg\delta_o}{b(d-a)} \qquad (7:14)$$

In order to study the relevance of (7:14), tests were performed on beams where the effect of the weight of the beam was compensated for by using weights according to Fig 7.11b. The total area under the load-deflection curve was determined and F_o was calculated by use of (7:9). After this the areas A_1, A_2, A_3 and A_4 according to Fig 7.12 could be determined and then the results derived from (7:14) could be compared with the true values determined by use of (7:8).

Two different beam depths were used, 50 mm and 200 mm respectively. The widths were 50 mm and the relative notch depths 0.5 for all the beams. Cast notches were used for the 200 mm deep beams and sawn notches for the 50 mm deep beams. The widths of the notches were 4 mm.

The mix proportions of the concrete used in the tests are presented in Table 7:1. Tests were performed for two different ages of the concrete, 7 and 28 days respectively.

Table 7:1 Mix proportions for the concrete used for analysing different evaluation methods of the G_F-test.

Cement (ordinary Portland)	367 kg/m^3
Water	220 kg/m^3
Aggregate 0-4 mm (not crushed)	837 kg/m^3
Aggregate 4-8 mm (crushed quartzite)	837 kg/m^3

The 200 mm deep beams were cast in plywood moulds and the 50 mm deep in steel moulds. The specimens were stored under wet sackcloth until the time for the test and the beams were kept wet during the testing. The loading velocity was chosen so that the maximum load was reached about 30 seconds after the test started.

In Table 7:2 the results for all the beams are shown. Results representing four alternative evaluation methods are presented. Alternative I corresponds to the area under the load-deflection curve for the uncompensated beam, which means that no corrections are made for the energy supplied by the weight of the beam. Alternative II means that the area A_2 is included when calculating G_F but not the area A_3. Alternative III corresponds to (7:14), which means that both A_2 and A_3 are considered. Alternative IV represents G_F-values calculated by use of the area under the load-deflection curve for beams where the energy supplied by the weight of the beam is compensated for and these values can therefore be considered to be true. In the last column of the Table the differences between Alternative III and Alternative IV, calculated as ((Alt III-Alt IV)/Alt IV) x 100 %, are shown.

As can be seen in the Table the energy supplied by the weight of the beam affects the results considerably. This is illustrated in Fig 7.14, where the areas A_1, A_2, A_3 and A_4 are shown for two of the beams used during the tests. For the 50 mm deep beam the G_F-value according to Alt I must be compensated for by about 50-60 % in order to correspond to the true value of G_F and for the 200 mm deep beam the compensation has to be about 150-250 %! However, in spite of the great effect of the weight of the beam, the results according to Alt III seem to be in good agreement with the true values. For the 21 50 mm deep beams there are only two G_F-values according to Alt III differing from the true values by more than 5,2 % and the differences between the mean values according to Alt III and Alt IV are only about 1 %. Due to the wide scatter in the test results, these small differences can normally be neglected. For the 200 mm deep beams the differences between the values according to Alt III and Alt IV are naturally greater but they are still astonishingly small compared with the great corrections that have to be carried out. No individual corrected value differs more than 15 % from the true value, only 3 out of 12 differ more than 10 % from the true value and the two mean values differ only by 7,8 % and 3,2 % respectively from the true mean values. The latter differences are negative and would decrease to 6,4 % and 1,8 % respectively if the area A_4 was considered, see Fig 7.14.

Table 7:2 G_F values evaluated by using different methods.

Age	Beam depth	G_F(N/m)				Difference between alt III and alt IV
		Alt I	Alt II	Alt III	Alt IV	
days	mm	no correction $G_F=A_1/(d-a)b$	no correction for A_3 $G_F=(A_1+A_2)/(d-a)b$	corrected for weight of beam acc. to (7:14)	true value	%
7	50	62.0	78.1	94.2	90.4	4.2
		56.2	71.1	86.0	87.6	-1.9
		47.9	62.5	77.1	79.6	-3.1
		53.2	71.5	89.8	88.1	1.9
		48.0	62.7	77.4	79.7	-2.9
		65.4	87.5	109.6	106.0	3.4
		63.7	83.8	103.8	101.0	2.8
		60.2	78.8	97.4	102.0	-4.5
		46.1	61.6	77.2	85.6	-9.8
		77.8	97.0	116.1	121.4	-4.4
mean values:		58.0	75.5	92.9	94.1	-1.3
7	200	44.2	85.9	127.7	130.5	-2.1
		33.0	64.3	95.5	101.4	-5.8
		31.4	67.2	103.0	116.3	-11.4
		23.2	54.8	86.4	87.2	-0.9
		24.2	54.2	84.2	98.8	-14.8
		36.8	73.4	110.0	124.0	-11.3
mean values:		32.1	66.6	101.1	109.7	-7.8
28	50	65.3	80.5	95.7	91.0	5.2
		65.2	82.0	98.7	96.0	2.8
		85.4	103.4	121.4	126.4	-4.0
		64.7	79.1	93.4	94.0	-0.6
		63.8	77.6	91.4	92.0	-0.7
		58.1	78.6	99.1	109.3	-9.3
		70.2	89.0	107.8	107.0	0.7
		58.3	74.8	91.3	90.7	0.7
		80.7	100.2	119.7	114.0	5.0
		58.2	73.1	88.0	90.3	-2.5
		55.2	75.4	95.6	101.1	-5.4
mean values:		65.9	83.1	100.2	101.0	-0.8
28	200	41.5	89.1	136.6	138.2	-1.1
		36.7	73.6	110.5	120.3	-8.2
		44.2	82.4	120.6	119.0	1.3
		47.0	84.8	122.7	122.0	0.6
		36.4	70.8	105.2	114.4	-8.0
		38.2	83.1	128.0	134.0	-4.4
mean values		40.7	80.6	120.6	124.6	-3.2

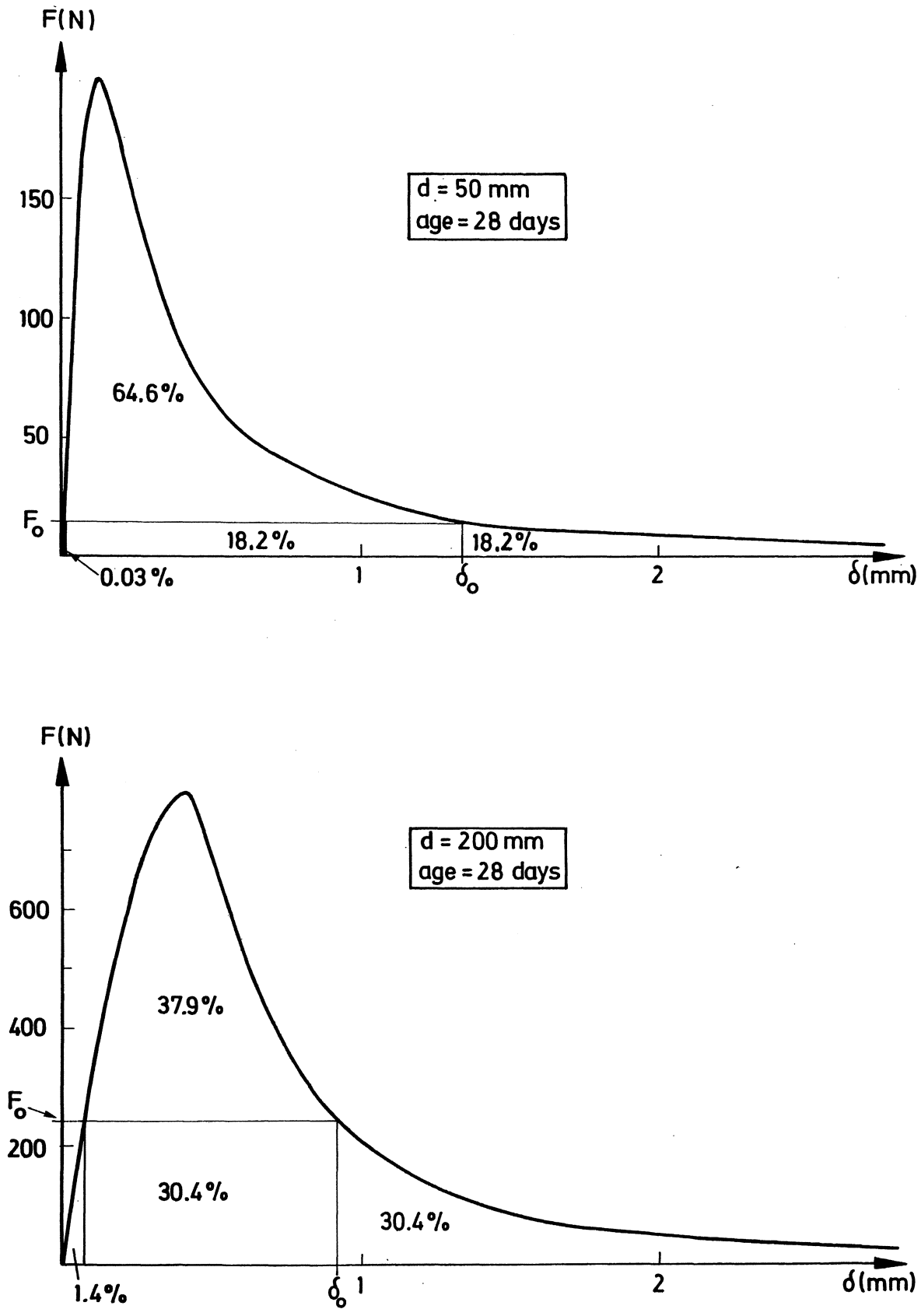

Fig 7.14 Illustration of the areas A_1, A_2, A_3 and A_4 for two beams used in the tests. The curves correspond to beam depths of 50 mm (top) and 200 mm (bottom) respectively.

As mentioned before the evaluation method according to Alt III has some advantages compared with the evaluation method according to Alt IV; smaller specimens can be used and it is easier to measure the area under the load-deflection curve. As the differences between the results from the two methods are so small, the test method according to Alt III, i.e. according to (7:14), seems preferable in most cases.

7.4.4 G_F as a material property

A material property must fulfil two criterions; it must be independent of specimen geometry and it must be independent of the type of loading. In order to check whether the fracture energy fulfils these criterions, G_F-determinations were carried out on four different specimen geometries, see Fig 7.15, of which two were subjected to three-point bending and two to direct tension.

The types of specimens denoted I and II are notched beams, which were tested in three-point bending. The depths of the beams were 50 mm and 200 mm respectively. These beams are in fact indentical to those used in the tests presented in 7.4.3, which means that the energy supplied by the weight of the beam was compensated for by using weights and G_F was evaluated by the use of (7:8). The concrete quality used is shown in Table 7:1. The testing procedure and the preparation of specimens are discussed in 7.4.3 but a few supplementary comments have to be made. For both the beam dimensions the relative loading velocity was the same, which means that the ratio load/maximum load as a function of the time was identical for the two types of beams. The maximum load was reached about 30 seconds after the start of the test. Cast notches were used for the 200 mm deep beams and sawn notches for the 50 mm deep beams. When cast notches are used, the material close to the notch tip will be disturbed during the casting. This disturbance ought to affect the G_F-value more for small beams than for large beams and for the 200 mm deep beams this influence on the G_F-value is assumed to be small. When sawn notches are used there is no such disturbance of the material in front of the notch tip.

G_F was also determined by using completely different specimen types denoted III and IV. The specimens were cast in steel moulds and were stored in the same way as the beams until one day before testing. During the last day these specimens were insulated with plastic foil and stored in the air.

By using the stiff tensile testing machine described in Chapter 8 stable tensile tests were carried out on the two latter types of specimens. The area under the load-deformation curve includes not only the amount of energy consu-

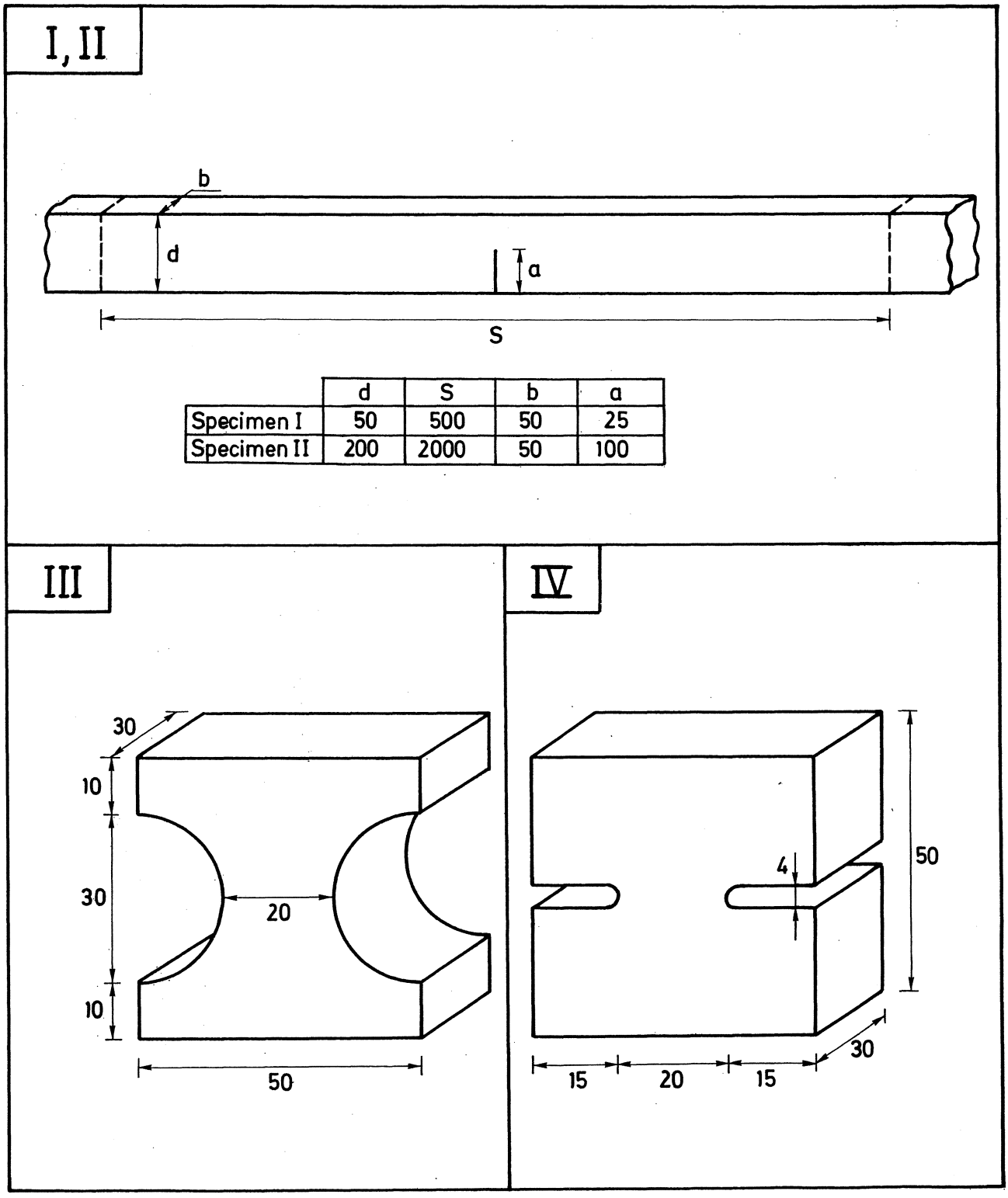

	d	S	b	a
Specimen I	50	500	50	25
Specimen II	200	2000	50	100

Fig 7.15 The four types of specimens used in the tests. The dimensions are given in mm. S=length between the supports.

med by the fracture zone but also the amount of energy consumed by the material outside the fracture zone before the tensile strength is reached, compare Chapter 3. In order to obtain the energy consumed by the fracture zone, the shaded area in Fig 7.16 must therefore be substracted from the total area under the curve. The shaded area is defined by the increasing part of the σ-δ curve and the unloading curve for the material outside the fracture zone. The unloading curve is assumed to be parallel with the initial slope of the σ-δ curve, compare 8.1. G_F then is calculated as the reduced area divided by the cross sectional area of the specimen. The loading velocity was chosen so that the maximum load was reached about 60 seconds after the start of the test. All the tests were carried out on wet specimens, exactly the same as for the beams.

The results are presented in Fig 7.17 and Fig 7.18. As can be seen in the Figures, the mean values of G_F for the 7 days old concrete varies between 86 N/m and 109 N/m and for the 28days old concrete between 98 N/m and 124 N/m. These variations must be considered as small, especially if they are compared with the variations between the values of the critical strain energy release rate (G_c) for the same specimens, see Fig 7.19. The mean values of G_c vary between 3 N/m and 23 N/m for the different specimen geometries. The G_c-values are calculated by use of ordinary linear elastic relations (of course there are no G_c-values for the unnotched specimen as G_c is defined only for notched structures) and E is assumed to be 30,000 MPa, which ougth to be a normal va-

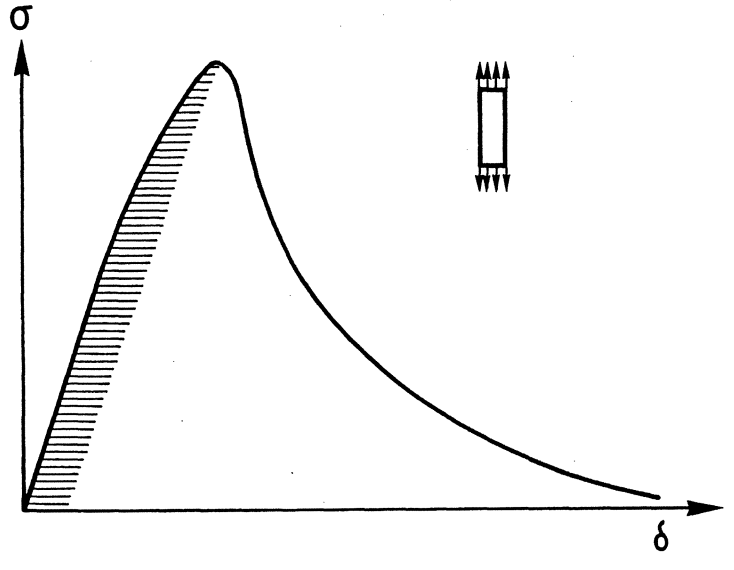

Fig 7.16 When determining G_F by using a stable tensile test, the energy consumption due to irreversible strains outside the fracture zone, i.e. the shaded area in the Figure, must be substracted from the total energy consumption.

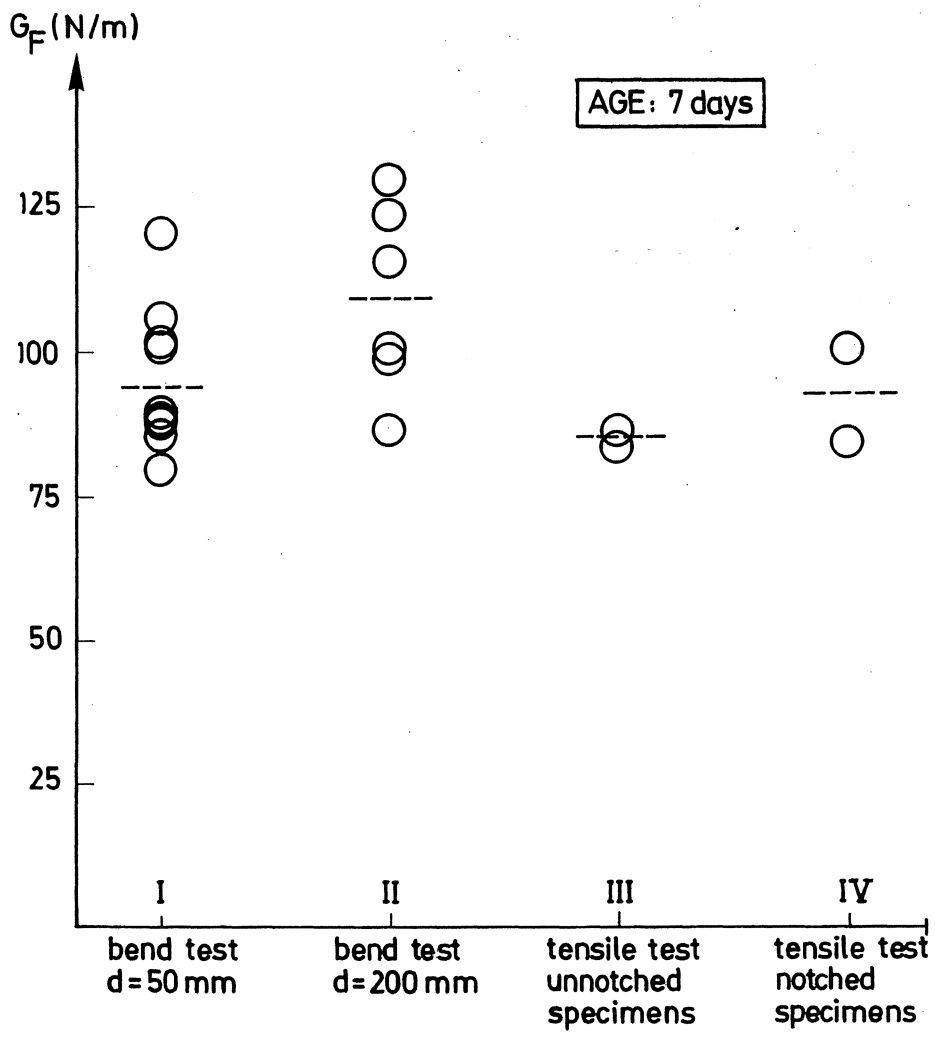

Fig 7.17 G_F-values for a 7 day old concrete determined on different types of specimens. Each circle represents a single specimen and the dashed lines represent mean values.

lue of the static Young's modulus for this material. It can be noted that the differences between the G_c-values for the different beam depths are in good agreement with the calculation results presented in Fig 6.14.

According to these test results, G_F seems to be useful as a material property for concrete and it is superior to the critical strain energy release rate. However, G_F seems to be slightly affected by the beam depth. There are some possible explanation for this size dependency and one of these is that the energy consumption outside the fracture zone due to the non-linearity of the σ-ε curve may affect the G_F-value more for deep beams than for low ones. Normally the energy consumption outside the fracture zone is assumed to be negligible. In order to study whether this assumption is realistic or not, finite element calculations were carried out on notched beams with different beam depths and the development of the stress field around the crack propagation

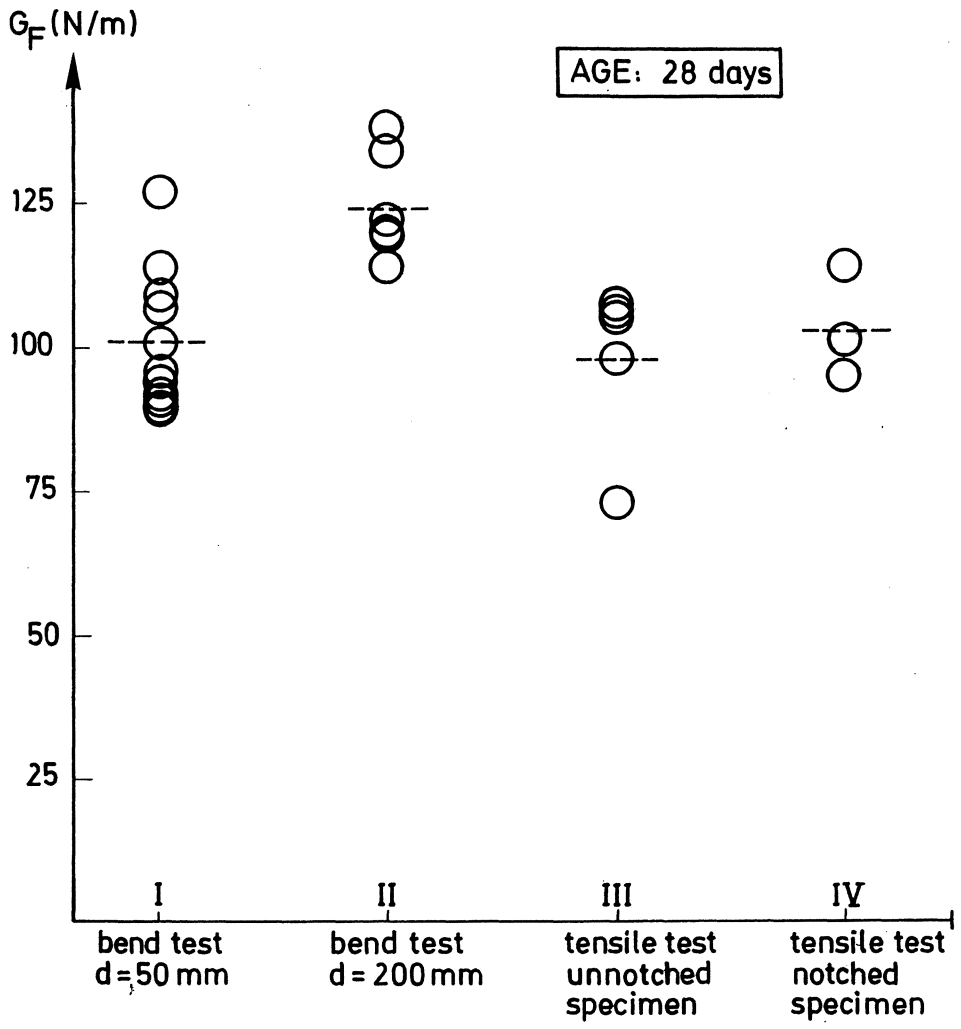

Fig 7.18 G_F-values for a 28 day old concrete determined on different types of specimens. Each circle represents a single specimen and the dashed lines represent mean values.

path was registered during the propagation of the fracture zone. By comparing the stress field with non-linear σ-ε curves for concrete, the energy consumption outside the fracture zone can be estimated. Of course more complicated non-linear finite element calculations would give better results (the non-linear zone around the fracture zone would probably be slightly larger), but for rough estimations the simple method described above ought to be useful.

The finite element mesh used in the calculations is presented in Fig 7.20. Due to the symmetry only half the beam had to be considered. The two beams used in the calculations correspond to the beams used in the tests presented above (d x b x ℓ = 50 x 50 x 500 mm^3 and 200 x 50 x 2000 mm^3, a/d = 0.5). The calculations were carried out by use of calculation method II (superposition), see 4.3, and in the calculations the σ-w curve was approximated with a straight line.

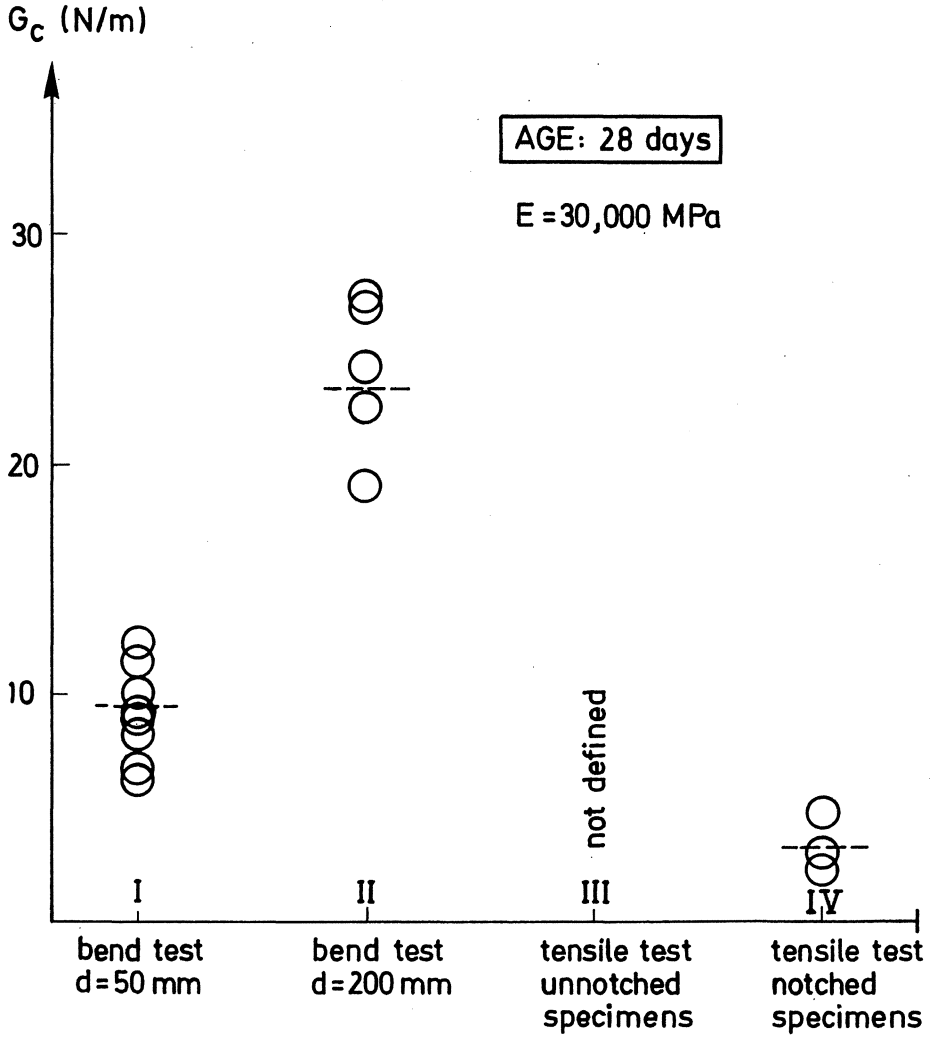

Fig 7.19 G_c-values (critical strain energy release rate) for a 28 day old concrete determined on different specimen geometries. Each circle represents a single specimen and the dashed lines represent mean values.

The highest value of the first principal stress obtained in the calculations was registered for each element. In Fig 7.21 lines connecting points with identical maximum values of the first principal stress are presented for the two beam depths (observe the different vertical scales). The curves are obtained by use of interpolation between the stresses in the middle of the elements. The results are relevant for a material with a ℓ_{ch}-value of 250 mm, i.e. a normal concrete quality. The unbroken lines are calculation results, while the dashed lines are estimations. It is assumed that the extension of the non-linear tensile zone is zero at the top of the beam, which is explained by the fact that a compression zone must always exist in this region, even when the fracture zone has almost reached the top of the beam.

The results in Fig 7.21 are of interest only if they can be compared with a

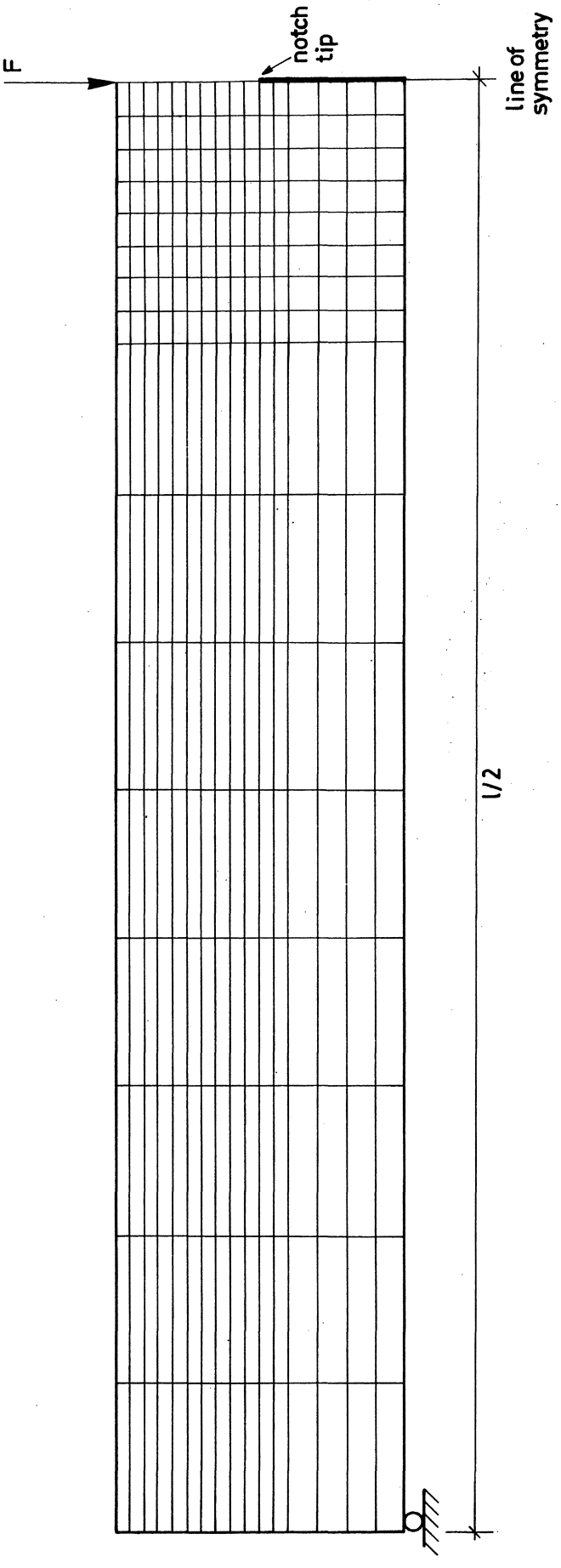

Fig 7.20 Finite element mesh used in the calculations in 7.4.4.

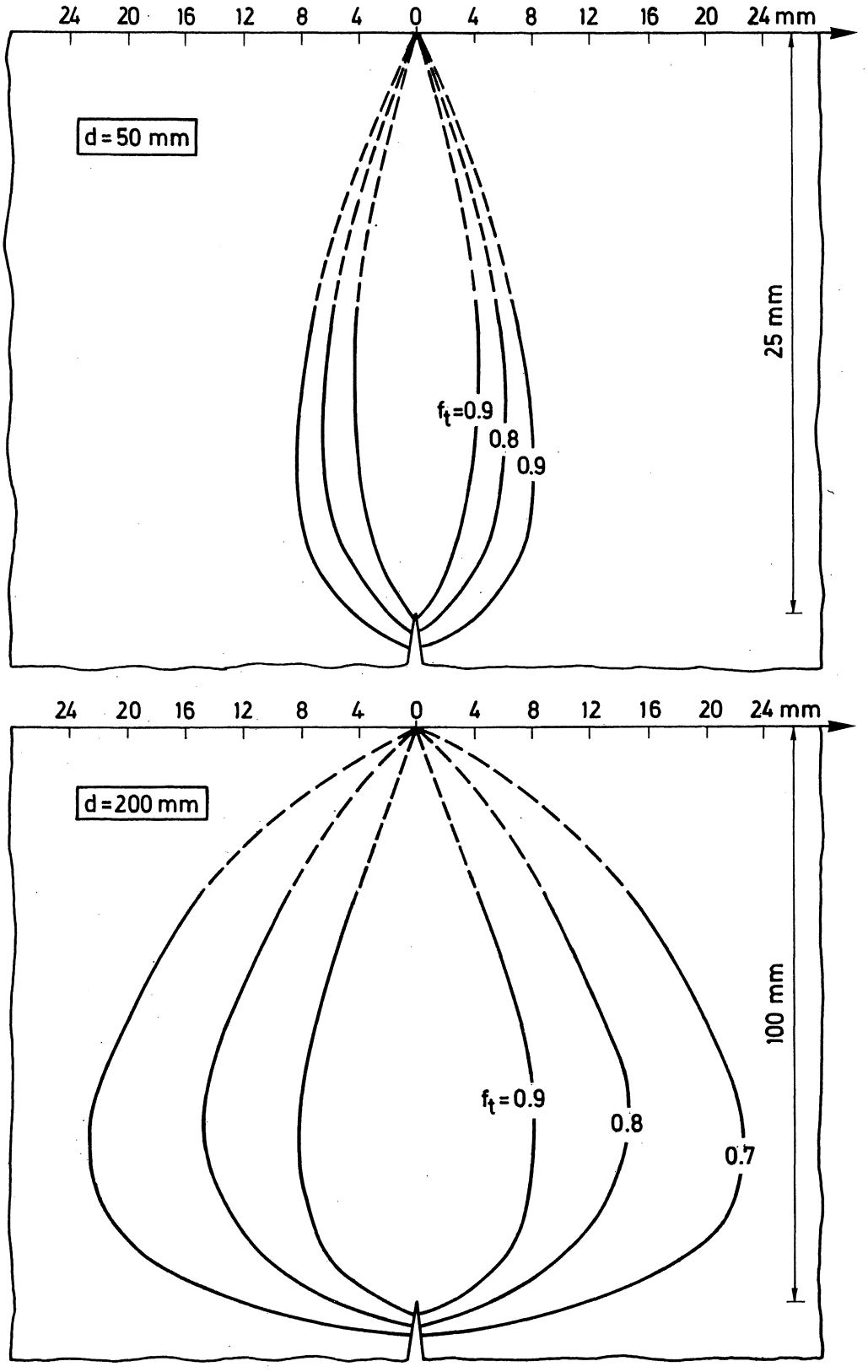

Fig 7.21 Lines connecting points with identical maximum values of the first principal stress. The results are relevant for 50 mm deep (top) and 200 mm deep (bottom) beams respectively.

non-linear σ-ε curve for concrete. According to test results presented by Hughes and Chapman (1966) and Evans and Marathe (1968) the σ-ε curve for concrete seems to be almost linear up to 70 % of the tensile strength and the total strain seems to be about twice the elastic strain at the fracture stress. If the unloading curve for each point is assumed to be parallel with the initial slope of the curve, then the σ-ε curve in Fig 7.22 can be used as an approximation for the concrete quality used in the tests ($f_t \approx 3.5$ MPa, $E \approx 30{,}000$ MPa).

As the irreversible deformations seem to be very small up to 70 % of the tensile strength, it is only the material volume inside the line denoted 0.7 f_t in Fig 7.21 that has to be considered when estimating the energy consumption due to the non-linear σ-ε curve. In order not to underestimate this energy consumption it can be assumed that the total material volume inside the line denoted 0.9 f_t has been subjected to the stress f_t, the material volume between the lines denoted 0.9 f_t and 0.8 f_t has been subjected to the stress 0.9 f_t and so on.

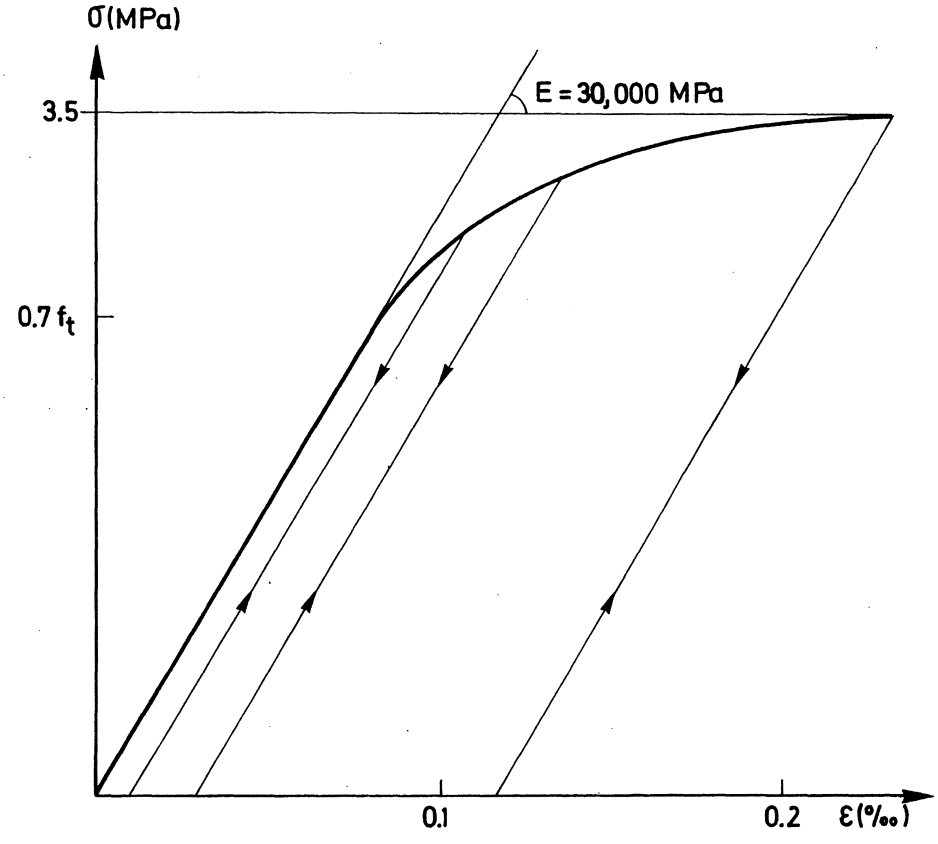

Fig 7.22 An approximate non-linear σ-ε curve for the concrete quality used in the tests and the calculations.

On these assumptions the energy consumption due to the non-linearity of the σ-ε curve is about 3.3 Nmm for the 50 mm deep beam and about 26 Nmm for the 200 mm deep beam, which means that the G_F value is overestimated by about 2.5 N/m for the low beam and by about 5 N/m for the deep beam (b=50 mm for both the beams). These values are probably overestimations but yet they can be considered as small and it seems as though the effect of the energy consumption due to the non-linearity of the σ-ε curve can normally be neglected. However, as G_F is overestimated more for the deep beam than for the low beam, this explains, at least to some extent, the small discrepancy between the G_F-values determined on beams of different depths.

As mentioned before the same relative loading velocity was used for both the beam depths when G_F was determined by use of the three-point bend test. This however means that the loading velocity in the fracture zone must be higher for the 200 mm deep beam than for the 50 mm deep beam as the fracture zone has to propagate a longer distance in the deeper beam. It has not been investigated how the loading velocity in the fracture zone affects the results but it may cause a small size dependency of G_F. Furthermore, it is almost impossible to obtain identical curing conditions for concrete specimens of different sizes. For example, the temperature always rises more in a large specimen than in a small one during the curing period and this normally affects the development of the material properties. This means that G_F can be slightly different for different sizes of specimens, even if they are cured in the same environment. These effects can never be eliminated.

As can be seen there are many explanations to why G_F for concrete can be size dependent. For this reason the very small variation of the G_F-values determined by the use of quite different methods and different specimen geometries must be accepted and G_F can be considered to be a useful material property for concrete.

7.4.5 Suitable specimen dimensions for the G_F test

There are many factors that must be considered when choosing suitable specimen dimensions for the G_F-test. These factors are listed and discussed below.

1. The capacity and dimensions of the testing machine limit the range of possible specimen dimensions. It must also be possible to handle the specimen during the test.

2. The fracture must be stable. A suitable specimen geometry can be chosen from the material properties, the stiffness of the testing

machine and Fig 7.9. Points 1 and 2 often greatly limit the possibilities of choosing specimen geometry.

3. The energy consumption due to irreversible deformations in the specimen outside the fracture zone, which is discussed in 7.4.4, must be minimized. To fulfil this the a/d-value should not be too small. The a/d-value ought to be equal to or larger than 0.5.

4. The scatter ought to be minimized. G_F is a mean value over the area through which the crack runs. This area decreases and the scatter increases when the depth of the notch increases. For this reason, a small a/d-value ought to be chosen. However, this opposes point 3. An a/d-value of 0.5 can be used as a compromise.

5. Energy consumption due to irreversible processes at the supports may occur. This is minimized if the beam is long and slender.

6. If the G_F-test is carried out on an uncompensated beam, see 7.4.3, it is then suitable if the fraction of energy supplied by the weight of the beam is as small as possible, as this is less controlled than the energy supplied by the testing machine. The fraction of energy supplied by the weight is minimized if the beam is small and the ratio beam depth/beam length is large. This is contrary to point 5. The resistance to irreversible processes at the supports, the specific gravity and the fracture mechanical properties of the material will determine from case to case whether point 5 or point 6 is the most important factor. (Point 6 should not be considered if compensated beams according to Fig 7.11 are used).

7. The beam has to be representative of the material. The dimensions will then be determined by the largest irregularities in the material. A fair assumption is that the smallest dimensions of the specimen ought to exceed the size of the largest irregularities (aggregate particles, pores, etc) at least four times.

8. Another factor that has not been discussed so far is the effect of the radius of the crack tip. This ought to be as small as possible and not exceed the dimensions of the irregularities in the material.

All the points listed above cannot be fulfilled at the same time. One has to compromise. However, point 2 must always be fulfilled, the fracture has to be stable under any condition.

7.5 Experimental investigation of the fracture mechanical properties of concrete

7.5.1 Testing procedure

Tests were performed in order to study three fundamental fracture mechanical properties of concrete; the dynamic Young's modulus (E_d), the fracture energy (G_F) and the tensile strength (f_t). Besides these properties the flexural tensile strength (f_f) and the compression strength (f_c) were also determined. All these properties can be determined on a single specimen, which is demonstrated in a simple example in Fig 7.23.

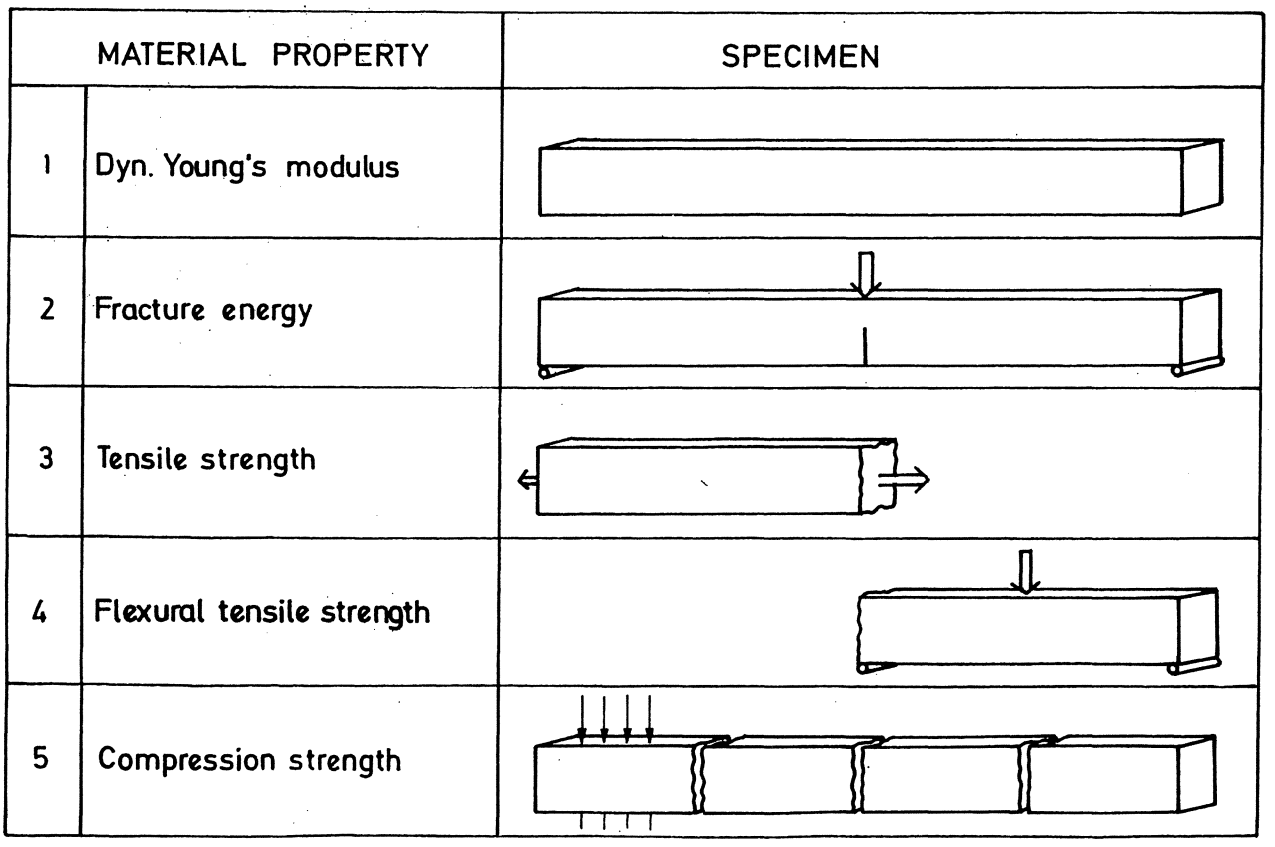

Fig 7.23 Test program for determining most of the fundamental mechanical properties of concrete on a single specimen.

In the tests the program described in Fig 7.23 was used for determining all the properties except the compression strength, which was determined on specimens with dimensions better fitted for available testing equipment. All the tests were performed on wet specimens.

First the dynamic Young's modulus was determined by use of the method described in 7.3. The specimen dimensions were 50 x 50 x 640 mm^3. After this a 4 mm

wide and 25 mm deep notch was sawn in the middle of the beam. The notched beam was subjected to three-point bending in order to determine the fracture energy and the test arrangement is presented in Fig 7.24. The distance between the supports was chosen as 600 mm, which with the actual testing machine (stiffness ≈ 5,000 N/mm) always resulted in stable fractures, compare Fig 7.9. As this test arrangement does not allow compensation for the energy supplied by the weight of the beam, the evaluation method according to (7:14) had to be used. For all the specimens the ligament was measured after the test by use of vernier callipers. A typical load-deflection curve for a G_F-test on concrete is shown in Fig 7.25.

During the G_F-test the beam was divided into two 320 mm long pieces. One of these was used for determining the tensile strength by use of the method presented in 7.2. The other piece was used for determining the flexural tensile strenght by use of three-point bend tests where the distance between the supports was 200 mm. The supports used in these tests were the same as those used in the G_F-tests, see Fig 7.24.

Finally the compression strength was determined on cubes with a side length of 40 mm. The cubes were sawn out from beams with the dimensions 40 x 40 x 160 mm^3 and the load was applied to the sawn surfaces.

The five test methods are illustrated in Fig:s 7.26-7.30.

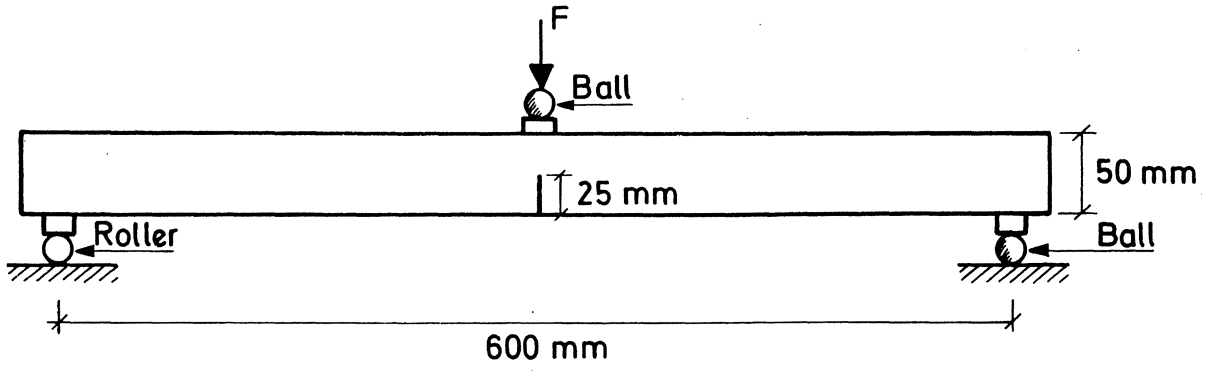

Fig 7.24 Test arrangement used for the G_F-test.

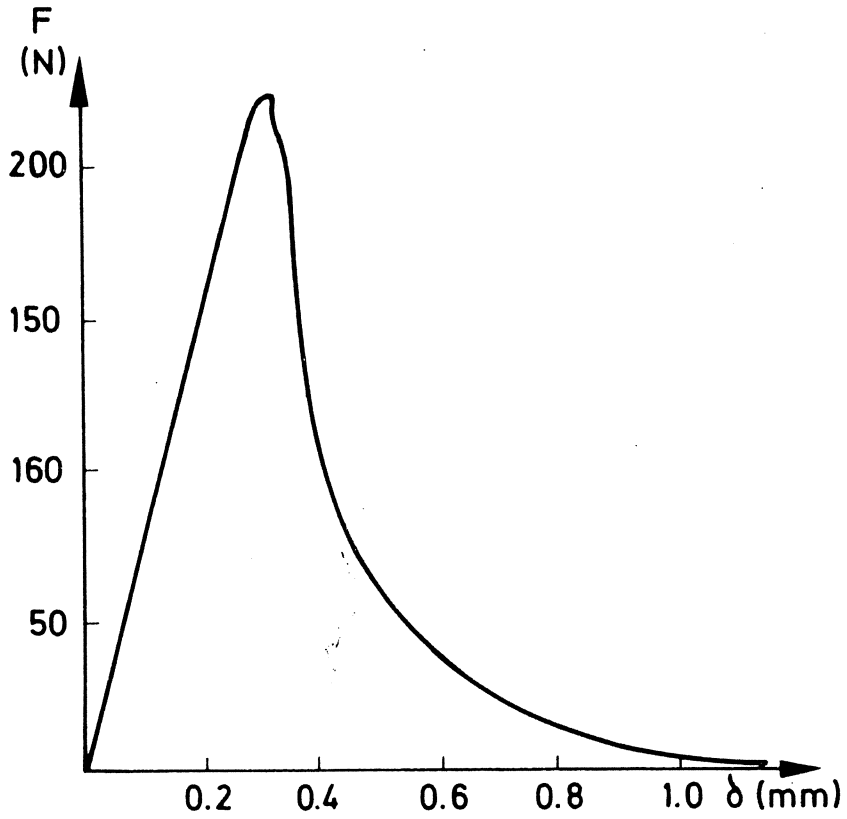

Fig 7.25 A typical stable F-δ curve from the G_F-tests. The deformation includes the deformations of the testing machine. The curve is relevant for mix 1 in Table 7:3 below.

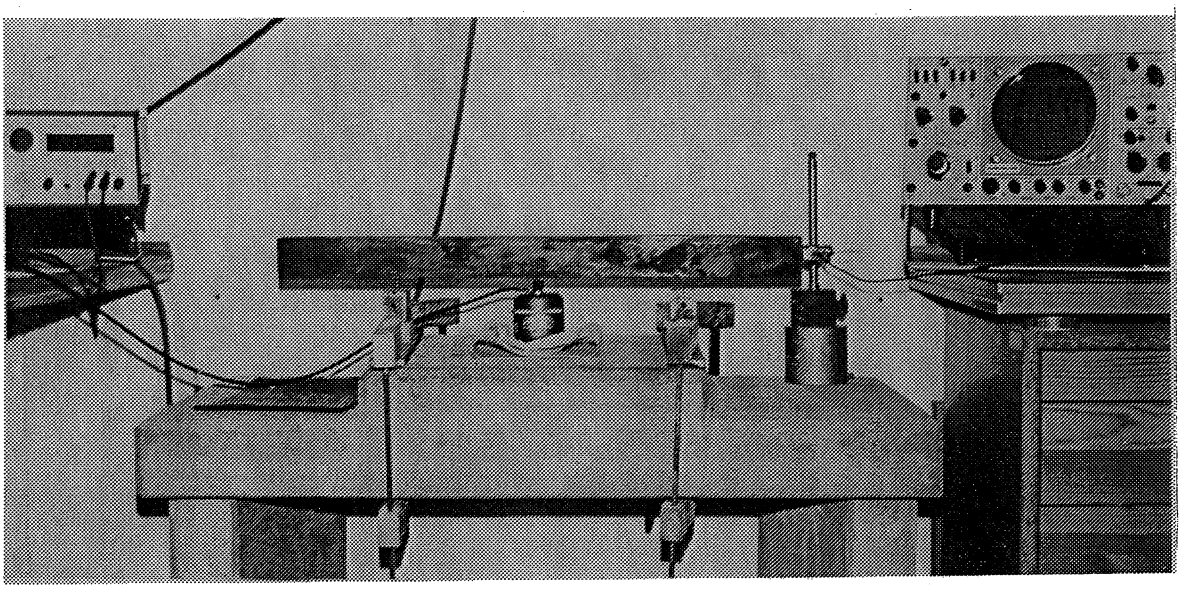

Fig 7.26 Determination of the dynamic Young's modulus (E_d).

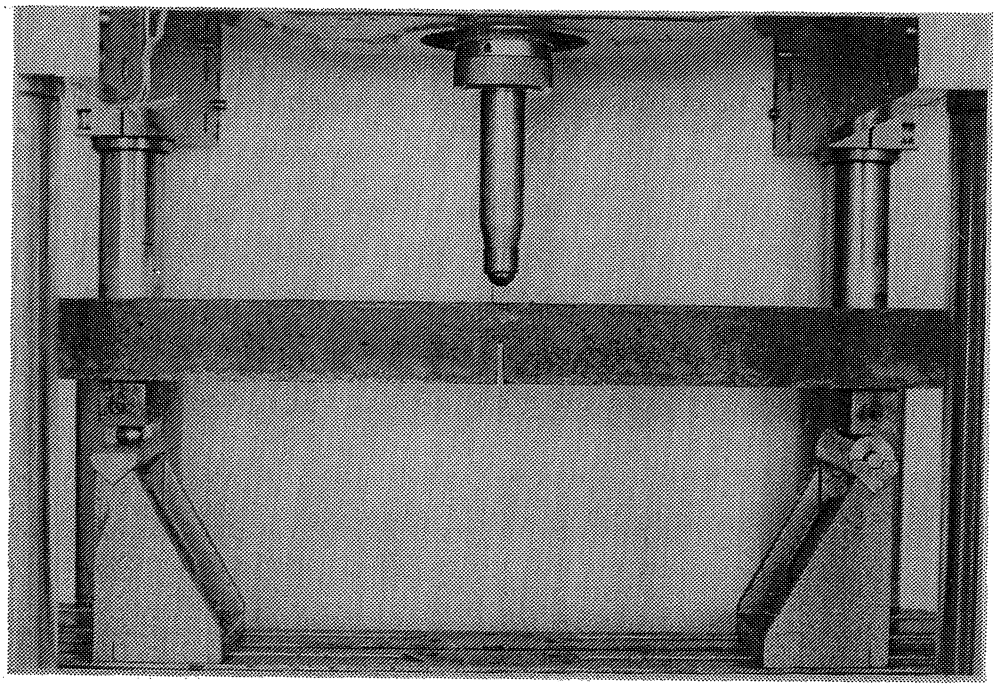

Fig 7.27 Determination of the fracture energy (G_F).

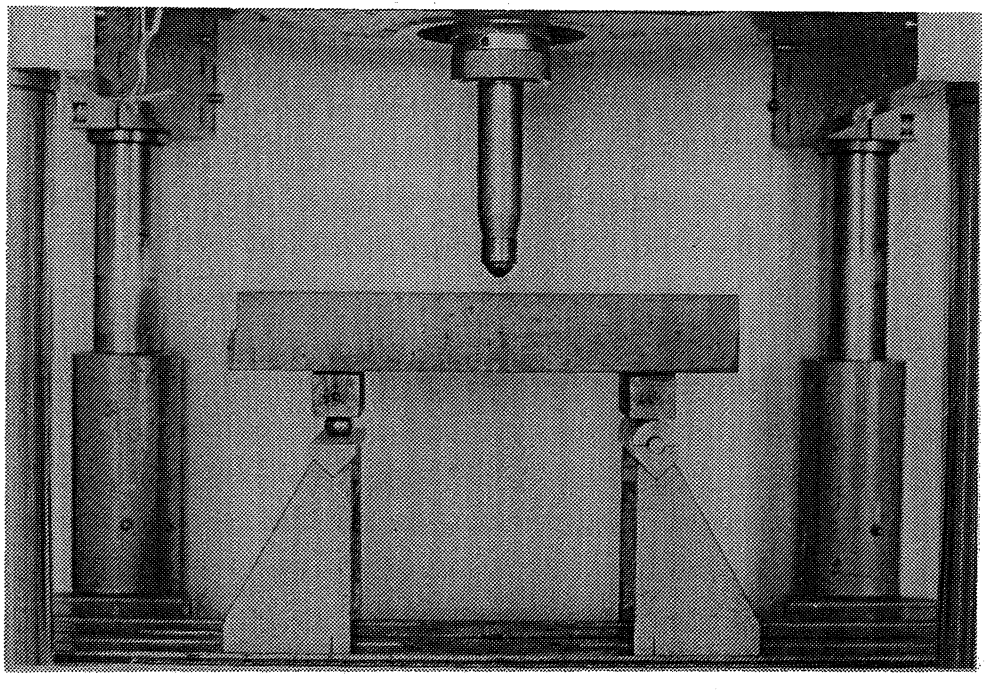

Fig 7.28 Determination of the flexural tensile strength (f_f).

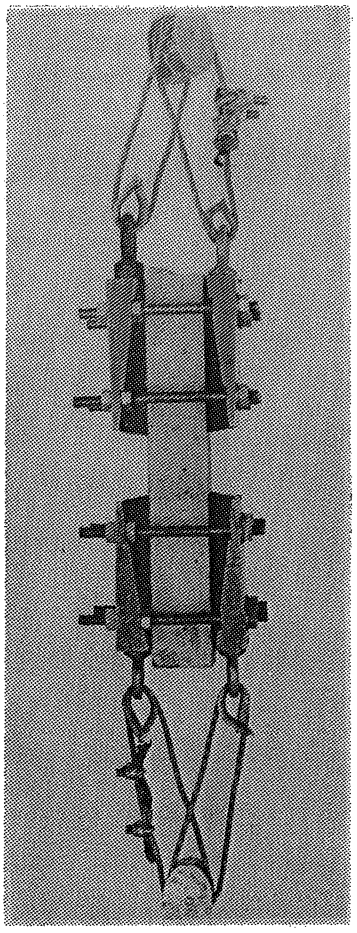

Fig 7.29 Determination of the tensile strength (f_t).

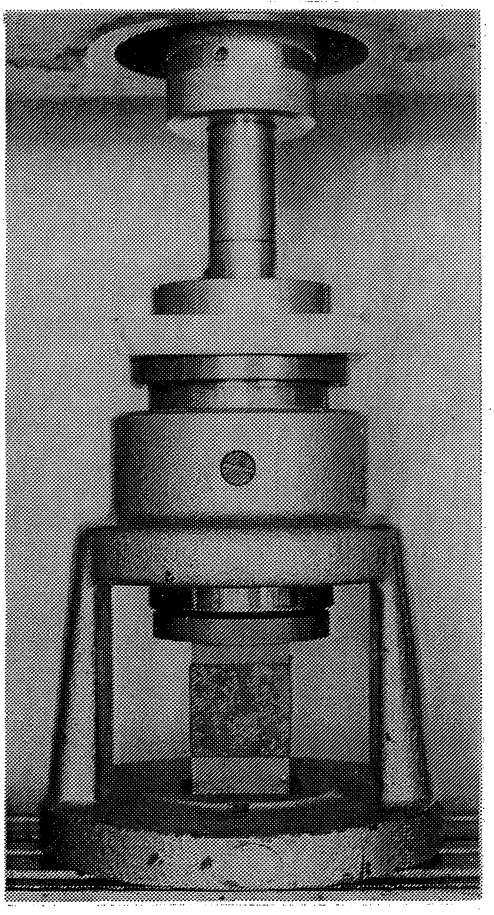

Fig 7.30 Determination of the compression strength (f_c).

7.5.2 Materials and mix proportions

The experiments were carried out in order to study the effect of the following factors on the fracture mechanical properties of concrete; type of aggregate, water-cement-ratio, volume fraction of cement paste, maximum aggregate particle size and age of concrete. The factors were varied one by one and the mixing proportions and the testing ages for the concrete qualities that were studied are presented in Table 7:3. Ordinary Portland cement was used. The same quality of aggregate 0-4 mm, nature material (not crushed) with a modulus of fineness of 2.5, was used in all the mixtures and the content of aggregate 0-4 mm was always 43 % by volume of the total aggregate content. When varying the maximum aggregate particle size, aggregate >4 mm was composed according to Table 7:4.

As can be seen in Table 7:3, there are no differences between the mixtures 1, 7, 10, 13 and 17. This concrete composition and age can be considered to be a reference concrete quality.

Table 7:3 The mixtures and testing ages for the concretes used in the tests. The factor that was studied for each case is marked with a circle. (Q=crushed quartzite, G=gravel (sea-bottom material), LS=crushed lime-stone, EC=expanded clay).

Mixture	Type of aggregate >4 mm	Water-Cement-Ratio	Cement Paste / Aggregate (Vol)	Maximum Particle Size (mm)	Age of concrete (days)	Cement-Sand (0-4)-Gravel(>4)-Ratio (by weight)
1	(Q)	0.5	0.5	12	28	1.0:2.04:2.71
2	(G)	0.5	0.5	12	28	1.0:2.04:2.77
3	(LS)	0.5	0.5	12	28	1.0:2.04:2.64
4	(EC)	0.5	0.5	12	28	1.0:2.04:0.72
5	Q	(0.3)	0.5	12	28	1.0:1.55:2.05
6	Q	(0.4)	0.5	12	28	1.0:1.80:2.38
7	Q	(0.5)	0.5	12	28	1.0:2.04:2.71
8	Q	(0.7)	0.5	12	28	1.0:2.55:3.38
9	Q	0.5	(0.4)	12	28	1.0:2.60:3.44
10	Q	0.5	(0.5)	12	28	1.0:2.04:2.71
11	Q	0.5	(0.6)	12	28	1.0:1.68:2.23
12	Q	0.5	0.5	(8)	28	1.0:2.04:2:71
13	Q	0.5	0.5	(12)	28	1.0:2:04:2.71
14	Q	0.5	0.5	(16)	28	1.0:2.04:2.71
15	Q	0.5	0.5	12	(2)	1.0:2:04:2.71
16	Q	0.5	0.5	12	(7)	1.0:2.04:2.71
17	Q	0.5	0.5	12	(28)	1.0:2:04:2.71
18	Q	0.5	0.5	12	(91)	1.0:2.04:2.71

Table 7:4 Composition of aggregate >4 mm.

Max particle size (mm)	Aggregate 4-8 mm	Aggregate 8-12 mm	Aggregate 12-16 mm
8	100 %	-	-
12	50 %	50 %	-
16	33 1/3 %	33 1/3 %	33 1/3 %

7.5.3 Preparation of specimens

For each concrete mixture 6 specimens (50 x 50 x 640 mm^3) were cast on two different occasions, i.e. a total of 12 specimens for each mixture. The specimens were stored in 100 % RH and +20°C during the first 24 h after casting and then stored in lime saturated water (+20°C) until the time for testing. After the E_d-test the 25 mm deep notch was sawn by using a diamond saw. All the tests were carried out on wet specimens. The compression strength was tested for each mixture on six specimens, which were sawn out from two beams.

7.5.4 Results

The results from the tests are presented in Table 7:5 and Fig:s 7.31-7.35. In Table 7:5 90 % confidence intervals of the compression strength and the flexural tensile strength are shown. The 90 % confidence intervals of f_t, E_d, G_F and ℓ_{ch} are presented in Fig:s 7.31-7.35. When calculating the confidence intervals of ℓ_{ch}, the mean values and the standard deviations of f_t, E_d and G_F were used.

7.5.5 Discussion

As can be seen in Fig 7.31, all the fracture mechanical parameters are greatly affected by the quality of the aggregate. The two stronger aggregates, crushed quartzite and gravel, produce higher values of G_F than the two weaker aggregates, crushed lime-stone and expanded clay. The explanation being the difference of the crack propagation path. For the stronger materials, especially for gravel, the crack runs around the aggregate particles, producing a large crack surface and a high value of G_F. For the weaker materials the crack runs through the aggregate particles, consequently making the crack surface and G_F small, see Fig 7.36. A strong aggregate material with a strong bond probably also causes a more complex micro-crack formation in the paste than a weak aggregate material with a poor bond. Naturally the fracture energy is also affected by the G_F-value of the aggregate, at least when the crack passes through the aggregate particles, which explains the very low value for the concrete containing expanded clay.

When a composite is subjected to load there will always be stress concentrations in the material due to the difference between the Young's modulus of the components. These stress concentrations decrease as the difference between the Young's modulus of the components decrease. According to the test results it seems as though the Young's modulus of the lime-stone is low and this is one

Table 7:5 The compression strength and the flexural tensile strength for the concrete qualities used in the test. The figures represent 90 % confidence intervals.

Mixture No.	Characteristic Parameter		Compr. Strength (MN/m^2) 40 mm cube	Flex. tens. Strength MN/m^2 Beam depth=50 mm
1	Aggre-gate	Crushed Quarzite	52.3-54.8	7.3-7.7
2		Gravel agg. (Sea-bottom-mat.)	38.2-49.5	6.4-7.0
3		Crushed Lime-stone	58.0-61.6	7.5-8.1
4		Expanded Clay	17.8-21.8	3.9-4.2
5	Water-Cement-Ratio	0.3	83.1-88.7	8.5-8.9
6		0.4	71.2-76.8	8.2-8.6
7		0.5	52.3-54.8	7.3-7.7
8		0.7	28.4-31.1	5.3-5.6
9	Vol. cem. p. / Vol. aggr.	0.4	53.7-58.0	7.1-7.6
10		0.5	52.3-54.8	7.3-7.7
11		0.6	51.0-57.7	6.9-7.4
12	Max. Particle Size (mm)	8	47.1-58.3	7.3-7.7
13		12	52.3-54.8	7.3-7.7
14		16	53.3-57.2	6.9-7.5
15	Age of Concrete (days)	2	24.6-27.5	3.5-3.9
16		7	38.6-46.2	5.7-6.2
17		28	52.3-54.8	7.3-7.7
18		91	59.4-66.6	7.8-8.2

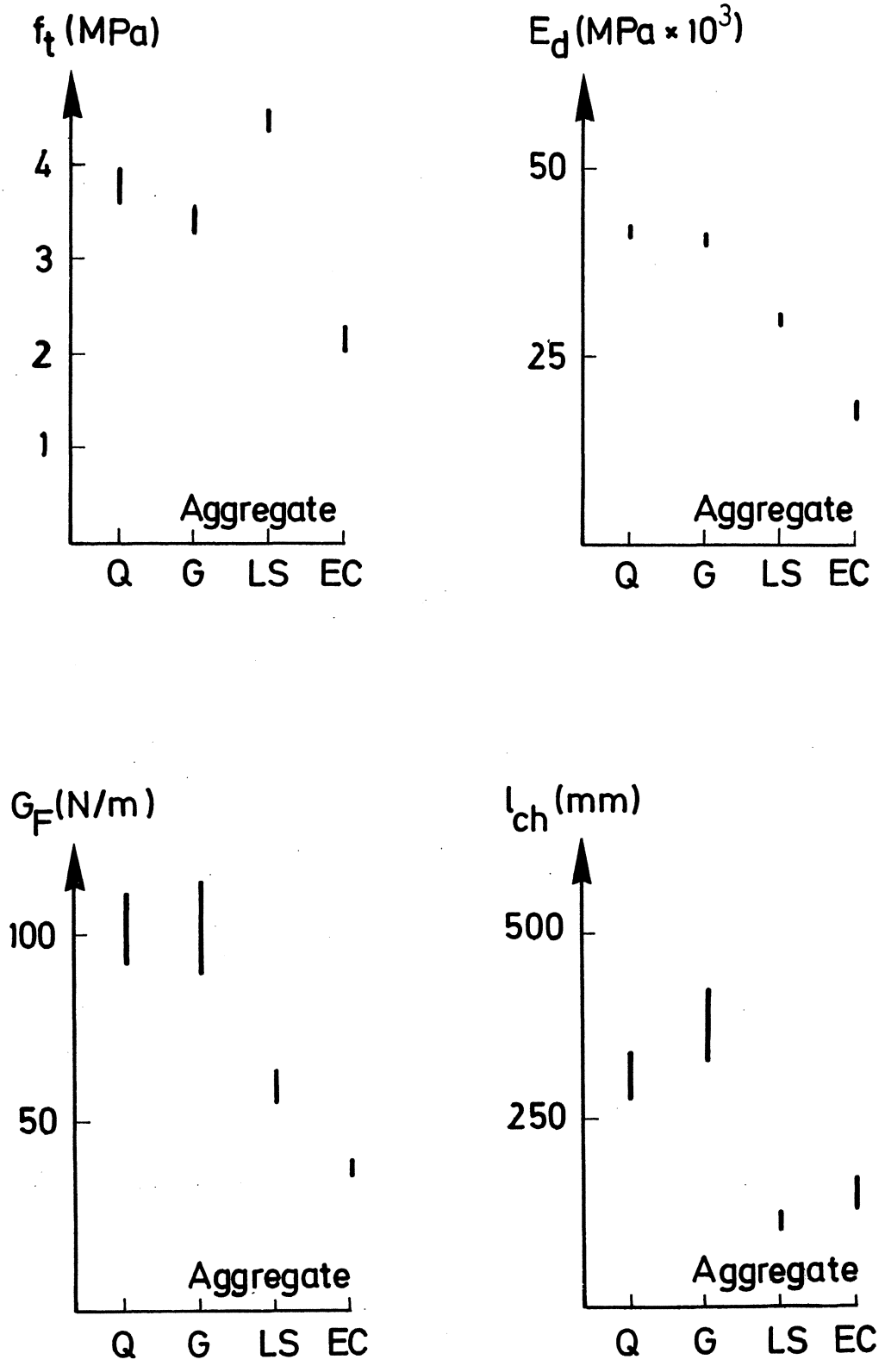

Fig 7.31 Relations between the fracture mechanical properties and the quality of aggregate. M=crushed quartzite, G=gravel, LS=crushed limestone, EC=expanded clay. (Mix 1-4).

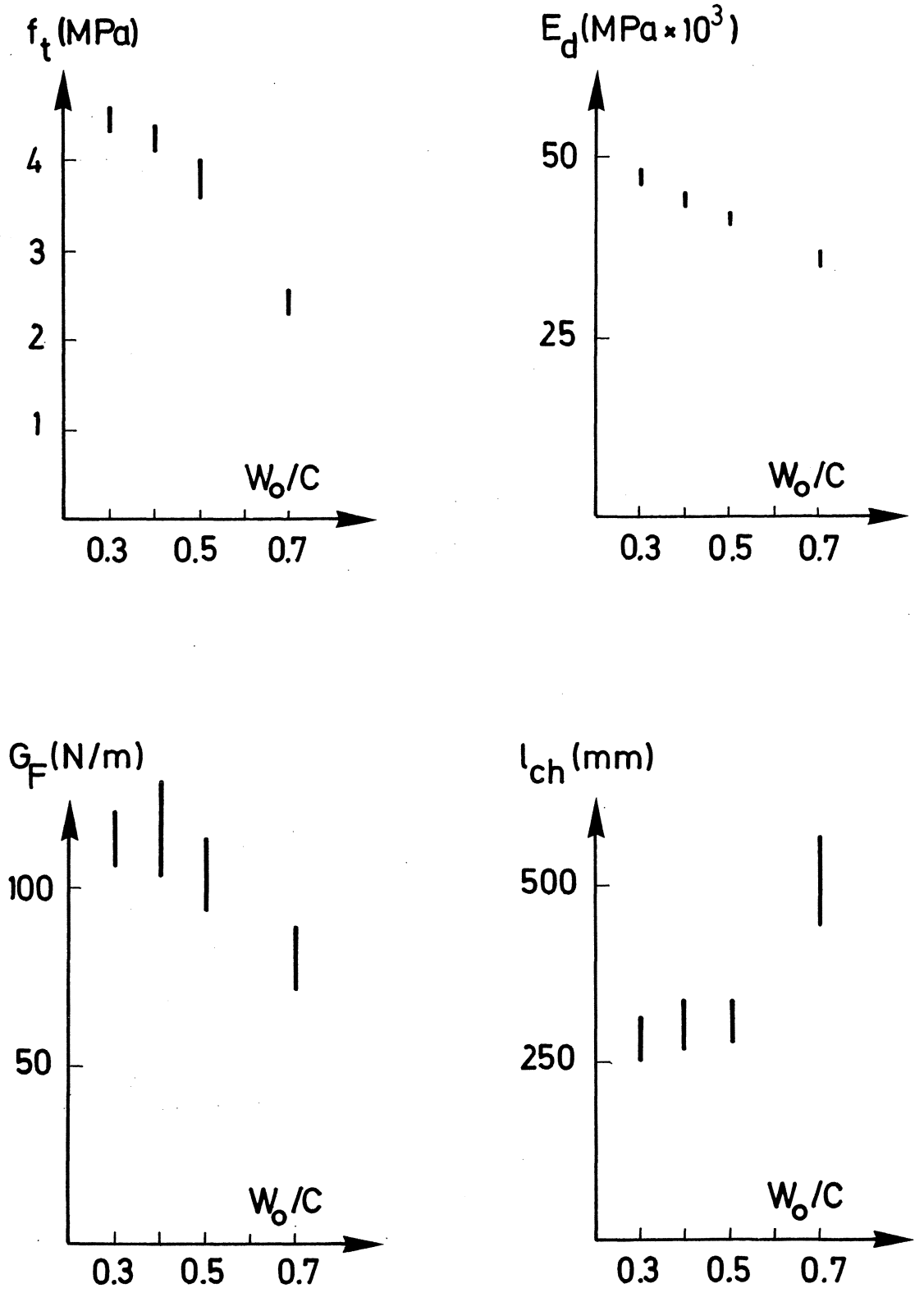

Fig 7.32 Relations between the fracture mechanical properties of the concrete and the water-cement-ratio. (Mix 5-8). W_o/C=water-cement-ratio.

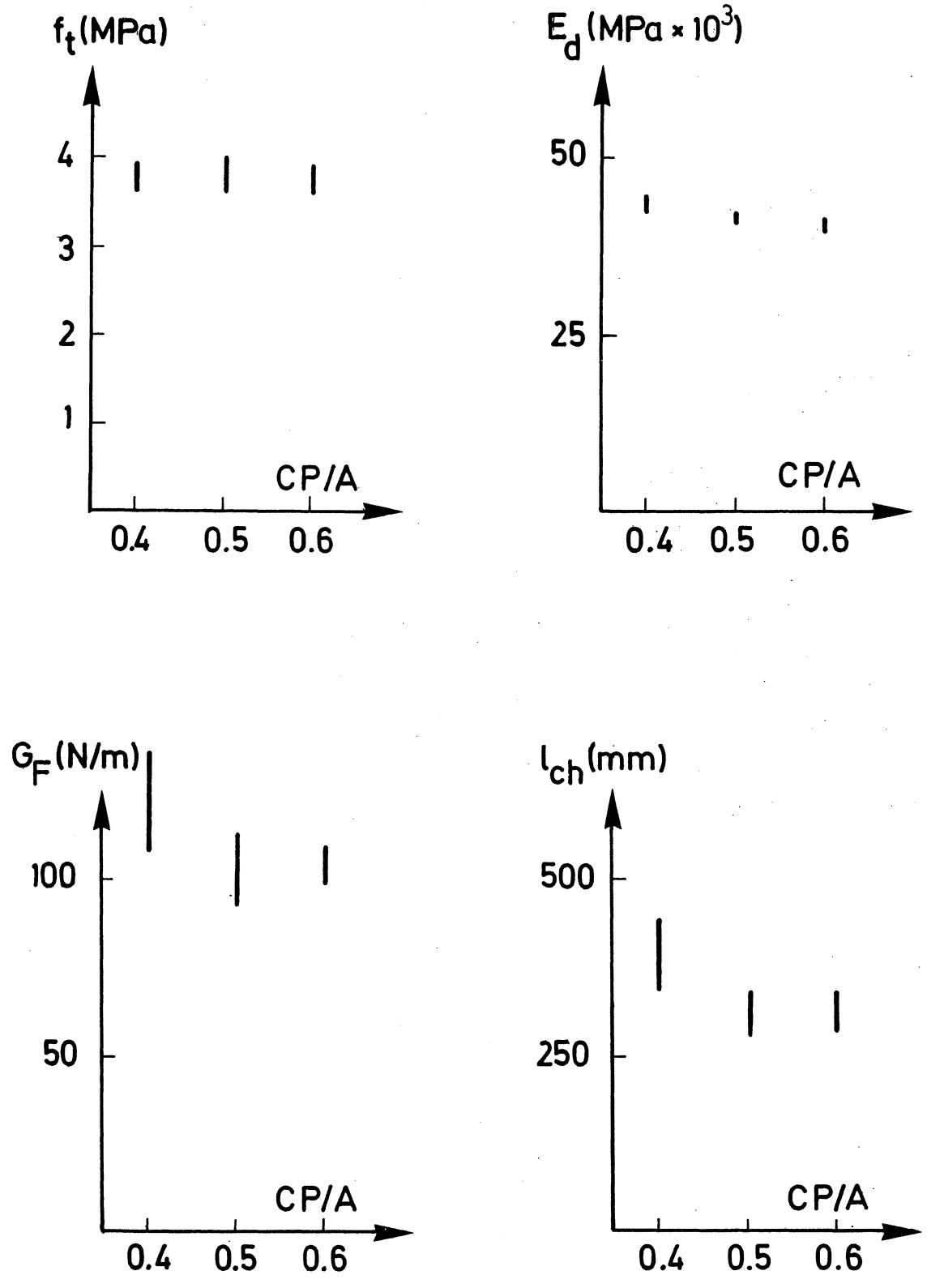

Fig 7.33 Relations between the fracture mechanical properties of the concrete and the ratio volume cement paste/volume aggregate (CP/A). (Mix 9-11).

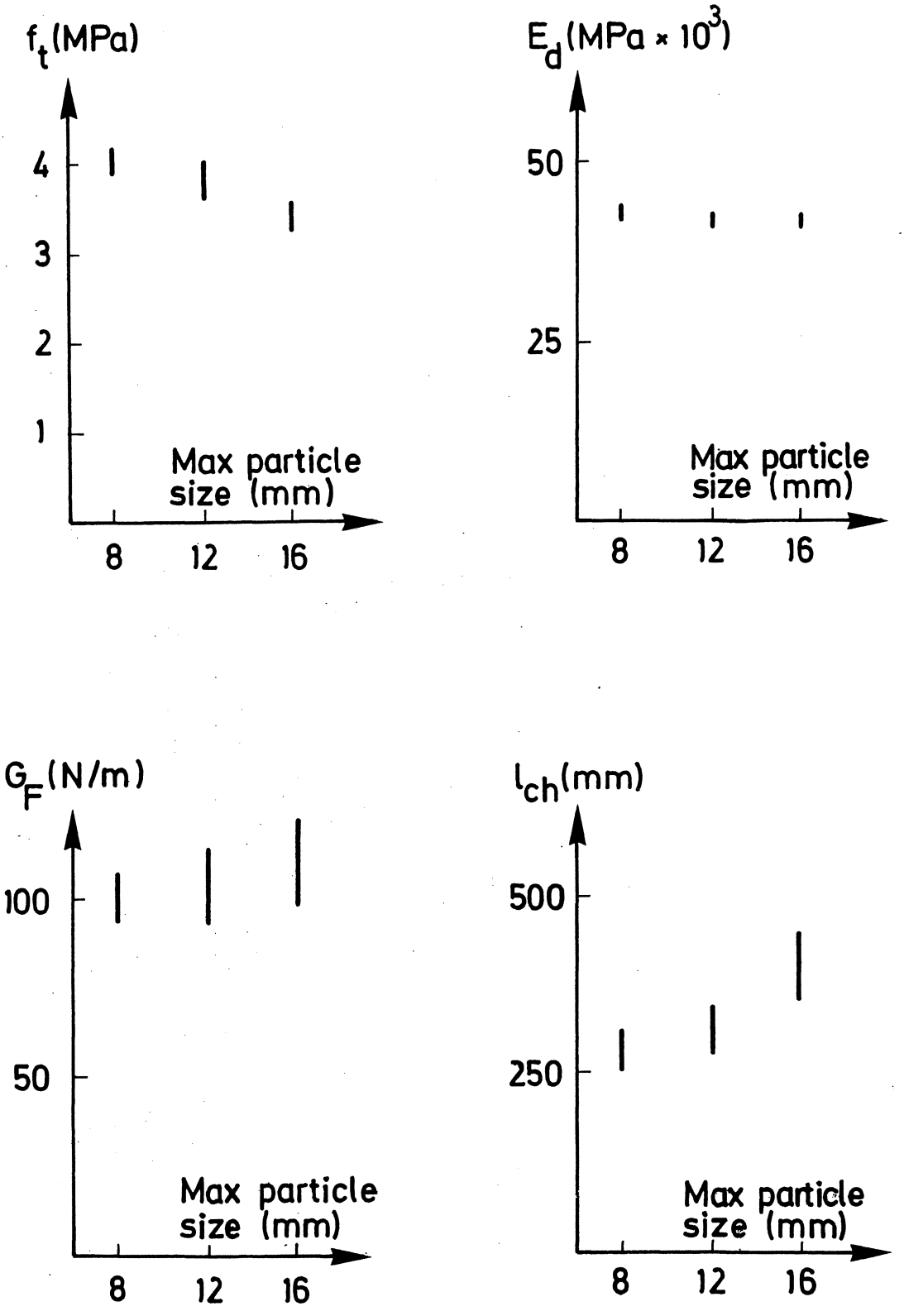

Fig 7.34 Relations between the fracture mechanical properties of the concrete and the maximum particle size of aggregate. (Mix 12-14).

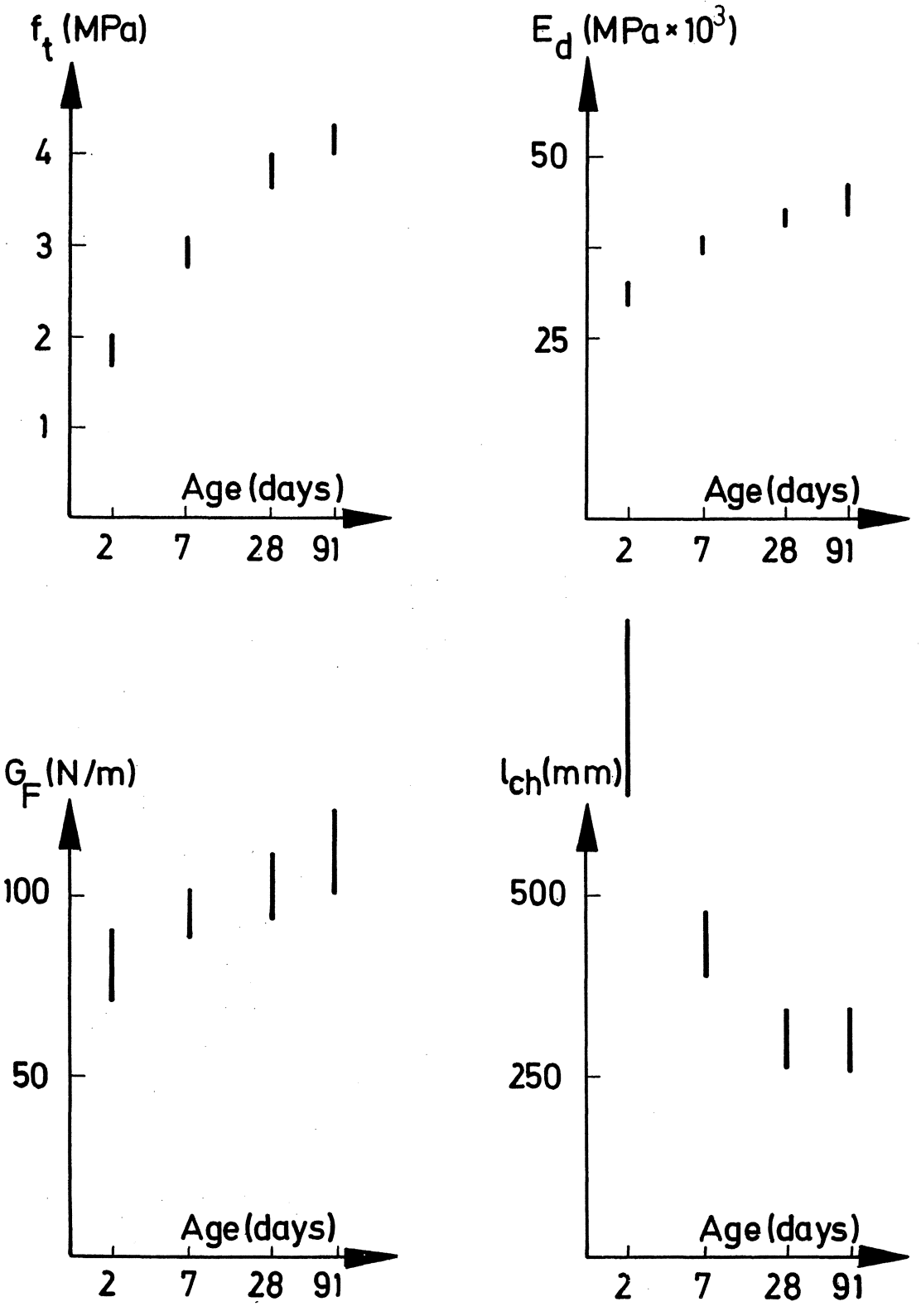

Fig 7.35 Relations between the fracture mechanical properties of the concrete and the age of the concrete. (Mix 15-18).

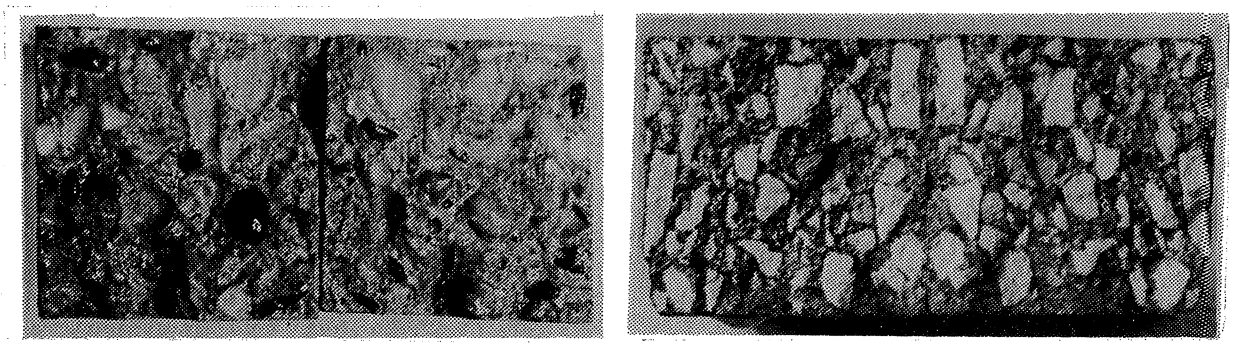

Fig 7.36 In the gravel concrete (left) aggregate particles are extracted from the paste, while the fracture surface runs through the particles in the lime-stone concrete (right).

explanation for the high tensile strength of the lime-stone concrete. Another explanation is that the adhesion between the aggregate particles and the cement paste is probably better for the lime-stone than for the other types of aggregate.

The low value of G_F for the lime-stone concrete together with the high value of f_t produces a low value of ℓ_{ch}. This material, and also the concrete containing expanded clay, can therefore be considered as much more "brittle" than the two concrete qualities containing crushed quartzite and gravel respectively.

The tensile strength and the Young's modulus decrease, as expected, when the water-cement-ratio increases, see Fig 7.32. Also G_F decreases when the water-cement-ratio increases, at least when the water-cement-ratio exceeds 0.4. ℓ_{ch} seems to be constant for water-cement-ratios up to 0.5 after which ℓ_{ch} increases markedly. This implies that concrete with a high strength is more "brittle" than a concrete with low strength.

The tensile strength seems to be independent of the volume fraction of aggregate, see Fig 7.33, while the Young's modulus naturally increases with increasing aggregate content as the Young's modulus of the aggregate is higher than the Young's modulus of the cement paste. G_F seems to increase somewhat with an increasing volume fraction of aggregate. This can be explained by the fact that the closer the aggregate particles are packed, the more complex the crack propagation path is and the larger the crack surface and fracture energy become. ℓ_{ch} also increases somewhat with an increasing volume fraction of aggregate. G_F and E_d seem to be insensitive to the maximum aggregate particle size, see Fig 7.34, while f_t decreases and ℓ_{ch} increases with increasing size of the largest aggregate particles.

f_t, E and G_F increase with increasing age of the concrete, see Fig 7.35. ℓ_{ch} decreases considerably with increasing age of the concrete up to about one month, after which it seems to stabilize. The reason for the great age dependency is that f_t increases relatively faster than G_F and E_d with increasing age, see Fig 7.37.

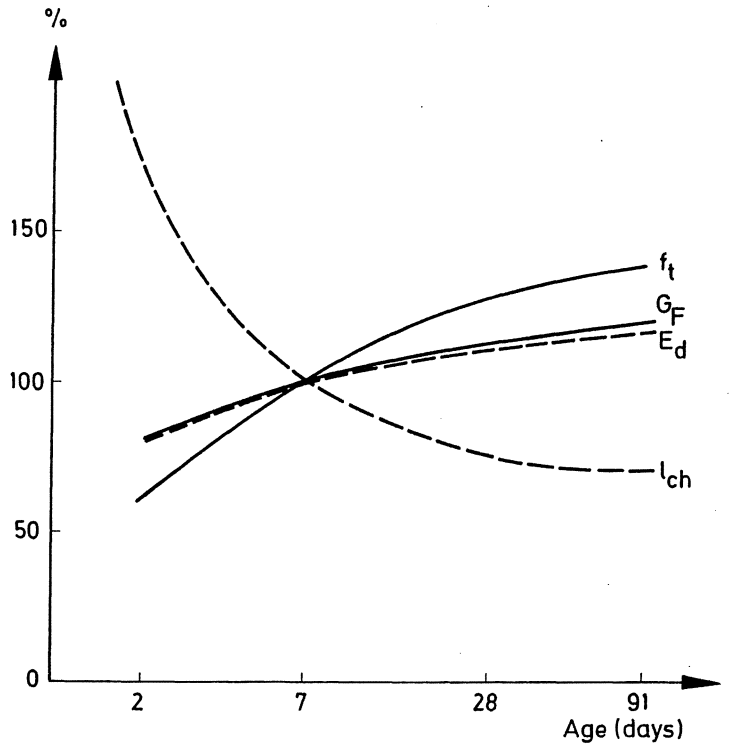

Fig 7.37 f_t increases at a relatively higher rate than G_F and E_d as the age of the concrete increases and therefore ℓ_{ch} decreases markedly as the age increases.

According to the test results above, the fracture energy for most concrete qualities seems to be 70-140 N/m. The characteristic length varies between 100 and 700 mm but normally it is 200-400 mm.

In Table 7:5 values of the flexural tensile strength (f_f) are given for the concrete qualities used in the tests. This makes it possible to compare the experimental results of f_f/f_t with theoretical estimations. In Fig 7.38 the values of f_f/f_t for the different concrete qualities are shown as a function of d/ℓ_{ch} and in the Figure a theoretical relation calculated by use of the Fictitious Crack Model is also presented. In the calculations the σ-w curve is approximated with a single, straight line (SL).

There is a wide scatter in the test results but it is quite obvious that the ratio f_f/f_t decreases with increasing values of d/ℓ_{ch}. This effect is well

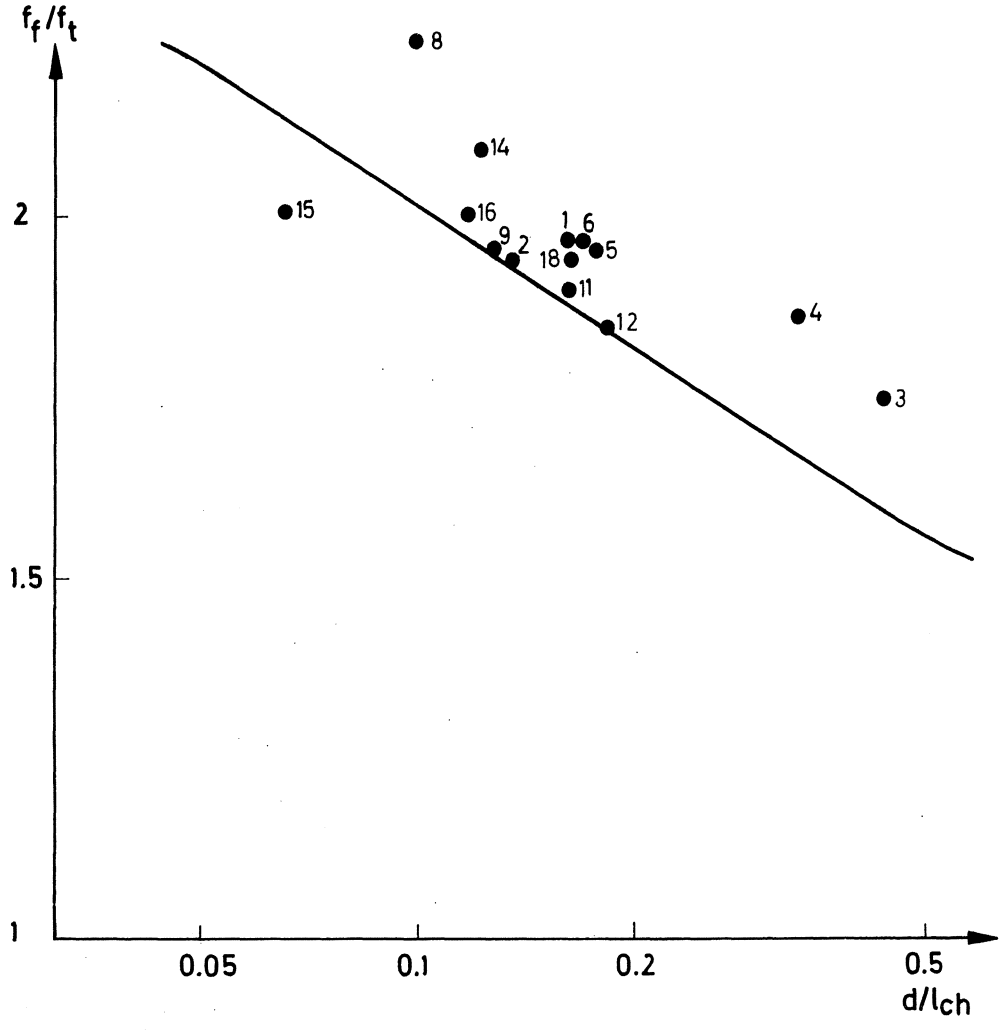

Fig 7.38 f_f/f_t as function of d/ℓ_{ch}. The dots represent different concrete qualities (the figures correspond to the mixtures defined in Table 7:3) and the curve represents a theoretical relation calculated by means of the Fictitious Crack Model.

described by the theoretical curve in spite of the simplified assumptions (the σ-w curve is approximated to a straight line, the effect of the non-linearity of the σ-ε curve is not considered and so on). This implies that the Fictitious Crack Model, together with the material properties presented above, is suitable for describing the fracture process for concrete.

8 DETERMINATION OF THE σ-w CURVE FROM A STABLE TENSILE STRESS-DEFORMATION CURVE

8.1 Introduction

As discussed in Chapter 3, the complete, stable tensile stress-deformation curve (σ-δ curve) can be considered to consist of two parts; one part representing the relation between stress and relative strain for the material outside the fracture zone and one part representing the relation between stress and absolute deformation of the fracture zone, see Fig 3.4. Fig 8.1 illustrates how the σ-ε curve for the material outside the fracture zone and the σ-w curve for the fracture zone can be determined from a stable stress-deformation curve.

The fracture zone does not start developing until the tensile strength is reached and consequently ε equals δ_A/ℓ_g and w equals 0 for the stress σ_1 on the

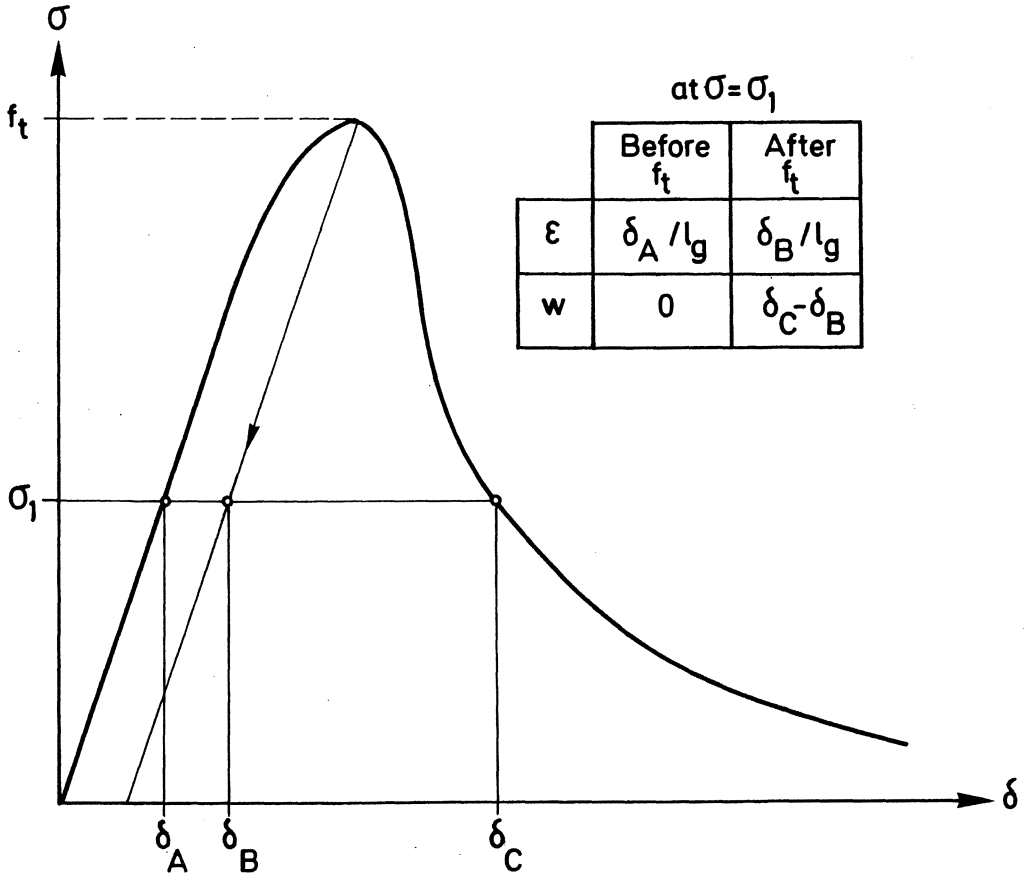

Fig 8.1 Determination of the σ-ε curve for the material outside the fracture zone and the σ-w curve for the fracture zone from a stable tensile stress-deformation curve (σ-δ curve).

increasing part of the stress-deformation curve. σ_1 and δ_A are defined in Fig 8.1 and ℓ_g is the gauge length for the deformation measurements. The stress decreases when the fracture zone starts developing and consequently the material outside the fracture zone becomes unloaded. In the Figure the unloading curve for the material outside the fracture zone is assumed to be parallel with the initial slope of the σ-δ curve. In real materials the unloading curve may be slightly different due to creep effects for example. However, if the gauge length for the deformation measurements is not too great, then a small error in the slope of the unloading curve has a very little effect on the distance δ_C-δ_B in the Figure for all values of σ_1, compare test results below. A small fault in the slope of the unloading curve thus affects the σ-w curve very little and therefore the assumed slope ought to be useful. On the descending part of the stress-deformation curve ε then equals δ_B/ℓ_g and w equals δ_C-δ_B for the stress σ_1.

Very few investigations regarding the stable stress-deformation curve (or stable stress-strain curve) for concrete are reported in literature. The reason for this is probably that it is necessary to use a very stiff tensile testing machine in order to obtain a stable fracture and ordinary testing machines are normally too weak, see 8.2.

Hughes and Chapman (1966) reported 5 individual stable stress-strain curves. The tensile strengths of the concrete qualities tested ranged from 0.75 MPa to 1.5 MPa, which is much lower than for a normal concrete quality.

Evans and Marathe (1968) reported 9 individual stress-strain curves for concrete. The tensile strengths were also low in these tests, between 1.5 MPa and 3 MPa. The scatter between the individual curves was wide and for one concrete quality they found a value of the strain at the tensile strength of 0.8 $^{o}/_{oo}$, which seems quite unrealistic.

Heilmann, Hilsdorf and Finsterwalder (1969) carried out tensile tests on a great number of concrete specimens. Most of their specimens failed in an unstable manner but they reported at least two individual stable stress-strain curves. The tensile strength was less than 1.8 MPa for both the specimens, i.e. lower than for a normal conrete quality.

It is easier to obtain a stable fracture for a material with a high value of the characteristic length (ℓ_{ch}) than for a material with a low value, see 8.2. According to the results in 7.5.4, ℓ_{ch} seems to increase markedly with decreasing tensile strength and this is probably the reason why all the stable

stress-strain curves reported in the literature are relevant for concrete qualities with very low values of the tensile strength (a low value of the tensile strength may be due to shrinkage stresses).

In this Chapter a very stiff tensile testing machine of a new type is presented by which it is possible to follow the complete tensile stress-deformation curve also for normal concrete qualities. σ-w curves for a number of concrete qualities are presented as well.

8.2 Stability conditions for the direct tensile test

In Fig 8.2 a schematic illustration of a tensile test is shown. The testing arrangement consists of a number of springs with different stiffnesses:

k_1 = the stiffness of the testing machine

k_2 = the stiffness of, for example, steel rods, which can be coupled parallel with the specimen in order to make the testing arrangement stiffer (cf Evans and Marathe, 1968).

k_3 = the stiffness of the specimen outside the fracture zone

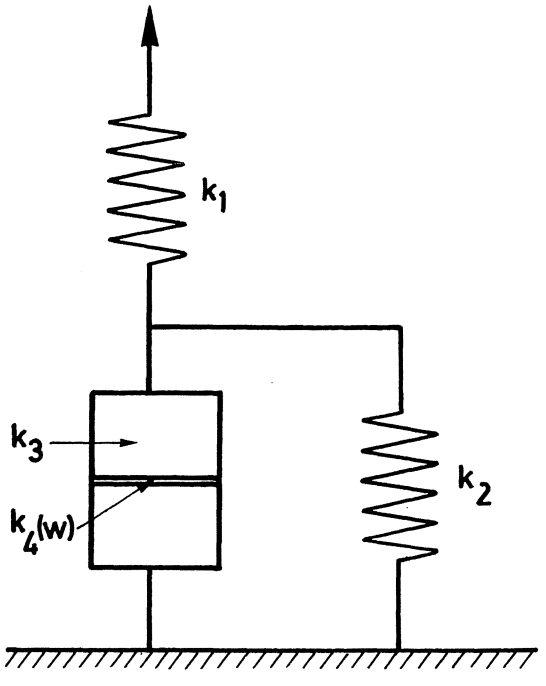

Fig 8.2 A schematic illustration of a direct tensile test. k_1, k_2, k_3 and $k_4(w)$ are the stiffnesses of the testing machine, of the rods, which are coupled parallell with the specimen, of the material outside the fracture zone and of the fracture zone respectively.

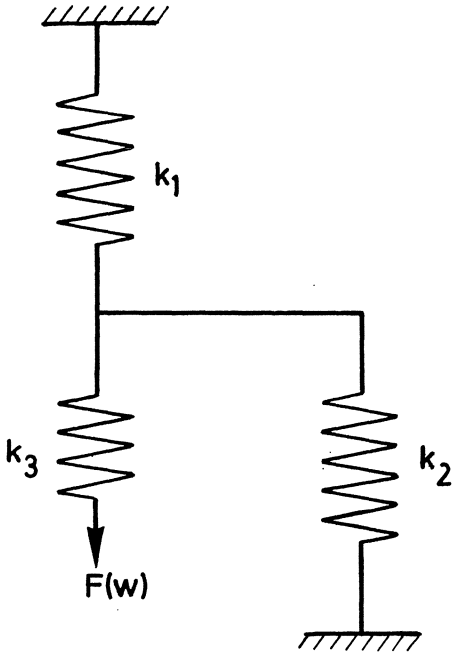

Fig 8.3 The system of springs used for the calculation of the stiffness (k_s) of the testing arrangement outside the fracture zone.

$k_4(w)$ = the stiffness of the fracture zone when the widening of the zone is w. This stiffness depends on the widening of the fracture zone according to the σ-w curve for the material.

The amount of energy (Q_F) necessary to widen the fracture zone from 0 to w is:

$$Q_F = A \int_0^w \sigma(w)dw \qquad (8:1)$$

where A is the cross sectional area of the specimen at the position of the fracture zone.

The amount of energy (Q_s) stored in the system of springs outside the fracture zone when the widening of the fracture zone is w can be expressed as (compare (7:5)):

$$Q_s = \frac{(F(w))^2}{2\,k_s} = \frac{A^2(\sigma(w))^2}{2\,k_s} \qquad (8:2)$$

where k_s is the stiffness of the system of springs shown in Fig 8.3. The springs with the stiffnesses k_1 and k_2 are parallel as they have to deform by the same amount when the load F(w) is changed. This means that the stiffness (k_s) of the system of springs in Fig 8.3 is:

$$k_s = \frac{1}{\frac{1}{k_2+k_1} + \frac{1}{k_3}} = \frac{k_3(k_2+k_1)}{k_1+k_2+k_3} \qquad (8:3)$$

If energy is consumed when the width of the fracture zone increases from w to w + dw, then the fracture will be stable and this gives the condition of stability for the direct tensile test (compare (7:6) and (7:7)):

$$\frac{\partial}{\partial w}(Q_F+Q_s) = A\sigma(w) + \frac{A^2\sigma(w)}{k_s}\frac{\partial\sigma(w)}{\partial w} > 0$$

$$k_s > -A\frac{\partial\sigma(w)}{\partial w} \qquad (8:4)$$

If the unloading curve for the material outside the fracture zone is assumed to be parallel with the initial slope of the curve (i.e. E) then the stiffness for the specimen (with a constant cross sectional area) outside the fracture zone is:

$$k_3 = \frac{AE}{\ell} \qquad (8:5)$$

where A is the cross sectional area of the specimen and ℓ is the specimen length.

By use of (8:3), (8:4) and (8:5) the following expressions are derived:

$$\frac{AE}{\ell}(k_1+k_2) > - A \frac{\partial\sigma}{\partial w}(k_1+k_2+\frac{AE}{\ell})$$

$$\Rightarrow$$

$$-E(k_1+k_2) < \ell \frac{\partial\sigma}{\partial w}(k_1+k_2) + \frac{\partial\sigma}{\partial w} AE$$

$$\Rightarrow$$

$$\ell < \frac{-\frac{\partial\sigma}{\partial w} AE - E(k_1+k_2)}{\frac{\partial\sigma}{\partial w}(k_1+k_2)}$$

$$\Rightarrow$$

$$\ell < - \frac{E}{\frac{\partial\sigma}{\partial w}} - \frac{AE}{k_1+k_2} \qquad (8:6)$$

(8:6) is the stability condition when the widening of the fracture zone is w. However, the fracture must be stable for all values of w and then the condition of stability becomes:

$$\ell < - \frac{E}{(\frac{\partial\sigma}{\partial w})_{max}} - \frac{AE}{k_1+k_2} \qquad (8:7)$$

where $(\frac{\partial\sigma}{\partial w})_{max}$ corresponds to the steepest slope of the σ-w curve.

If the σ-w curve is approximated with a single straight line, then the slope of curve is $-f_t/w_c$, where w_c is the maximum widening of the fracture zone, where it is still able to transfer stress, see Fig 6.1. For the single line approximation of the σ-w curve w_c equals $2\ G_F/f_t$ and thus the slope of the curve can be expressed as $-1/2 \times f_t^2/G_F$. The single line approximation of the σ-w curve is the most favourable case and for other shapes of the σ-w curve the steepest slope of the σ-w curve can be expressed as $-1/C \times f_t^2/G_F$, where C is a constant between 0 and 2 and C is dependent only on the shape of the σ-w curve. According to test results below the steepest slope of the σ-w curve for concrete seems to be about twice the mean slope and then the value of C becomes about 1 for this material.

The condition of stability for the direct tensile test can now, according to

(8:7) and (4:15), be written as:

$$\ell < C\frac{G_F E}{f_t^2} - \frac{AE}{k_1+k_2} = C\ell_{ch} - \frac{AE}{k_1+k_2} \qquad (8:8)$$

As can be seen from (8:8), the specimen length must be less than $C\ell_{ch}$ in order to obtain a stable fracture, even if an infinitly stiff testing machine is used. This means that the maximum length of the specimen for concrete is about 200-300 mm and for cement paste about 10-20 mm. However, these lengths are considerably reduced when the weakness of the testing machine is considered, which is illustrated in Fig 8.4. In the Figure the condition of stability according to (8:8) is illustrated for different values of the cross sectional area. The curves are relevant for ℓ_{ch} = 250 mm, E = 40,000 MPa and C = 1, i.e. a normal concrete quality. The horizontal axis in the Figure represents the stiffness of the testing machine (k_1) but of course this stiffness can be replaced by k_1+k_2, see (8:8), where k_2 is the stiffness of the rods, which can be coupled parallel with the specimen.

When carrying out tensile tests on concrete, all the specimen dimensions ought to exceed the size of the maximum aggregate particles a few times. This means that the smallest possible cross sectional area for a fine grained concrete should be about 500 mm^2 and for practical reasons the specimen length ought to exceed at least 40 mm. Even for these small specimen dimensions the stiffness of the testing machine has to exceed about 100,000 N/mm in order to obtain a stable fracture and the necessary stiffness increases rapidly with increasing specimen dimensions.

Normally it is impossible to attach the specimen to the testing machine without introducing weaknesses in the testing system. These weaknesses naturally affect the stability and in reality the conditions of stability are therefore harder than those given in (8:8) and Fig 8.4.

According to the results and the discussion above it seems quite obvious that ordinary testing machines are too weak to be useful for stable tensile tests on concrete. In order to obtain a stable fracture it is necessary to make the testing machine stiffer by use of rods which are coupled parallel with the specimen or to use special, very stiff testing machines. Such a testing machine, by which the complete tensile stress-deformation curve for concrete can be determined, is described below.

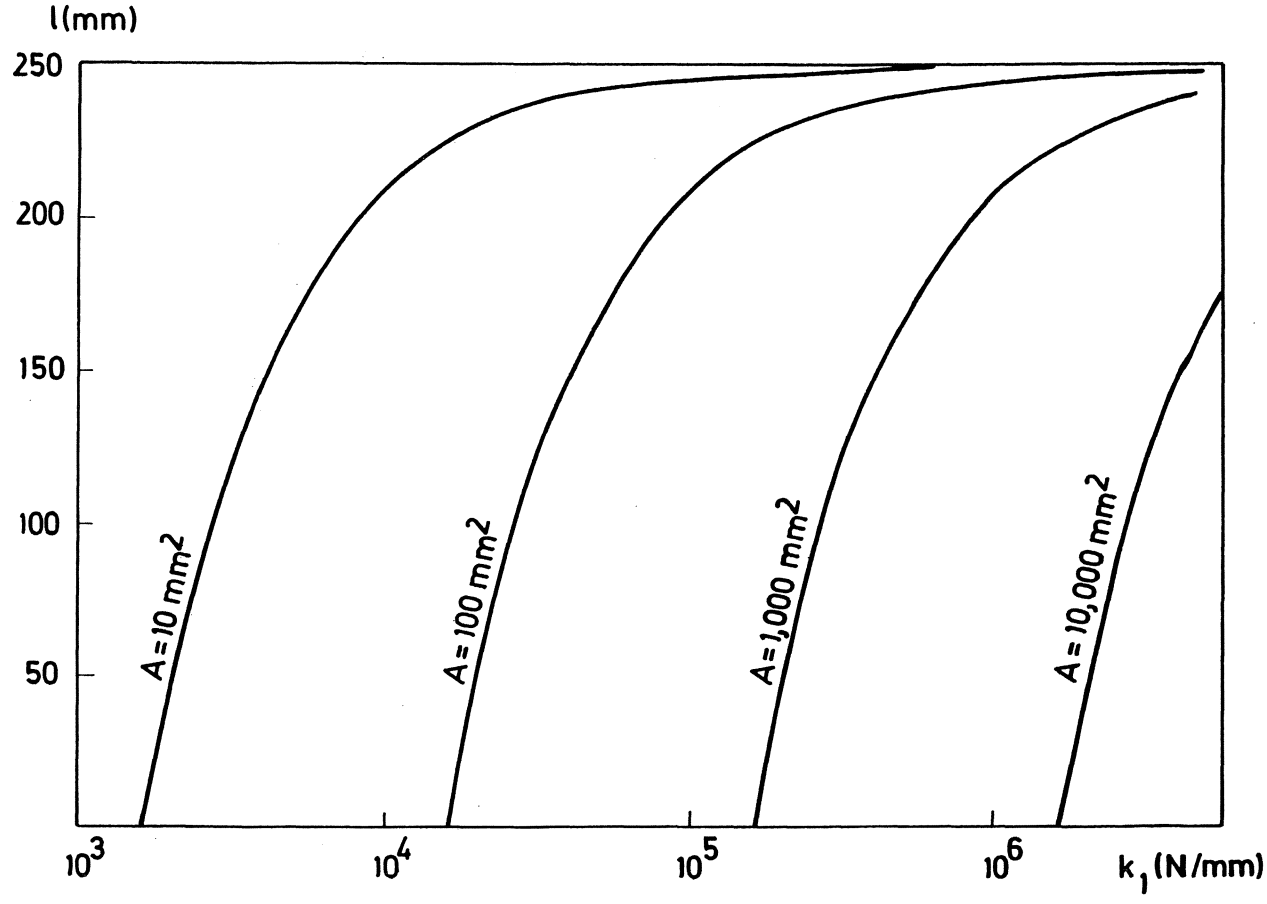

Fig 8.4 Conditions of stability for the direct tensile test. The curves represent the left limits of the areas of stability. The curves are relevant when ℓ_{ch} is 250 mm, E=40,000 MPa and the constant C in (8:8) is 1. ℓ=specimen length, A=cross sectional area of the specimen and k_1=the stiffness of the testing machine.

8.3 A stiff testing machine for stable tensile tests on concrete and similar materials

In Fig 8.5 and Fig 8.6 a new type of tensile testing machine is shown by which it is possible to carry out stable tensile tests on concrete specimens. Three aluminium columns (ϕ120 mm) are fixed between two concrete blocks and cylindrical heating elements are attached to the columns. The specimen is fixed (glued) in special holders between the concrete blocks. The aluminium columns expand when they are heated and then the specimen becomes subjected to load. The load is registered by strain gauges, which are attached to one of the holders and

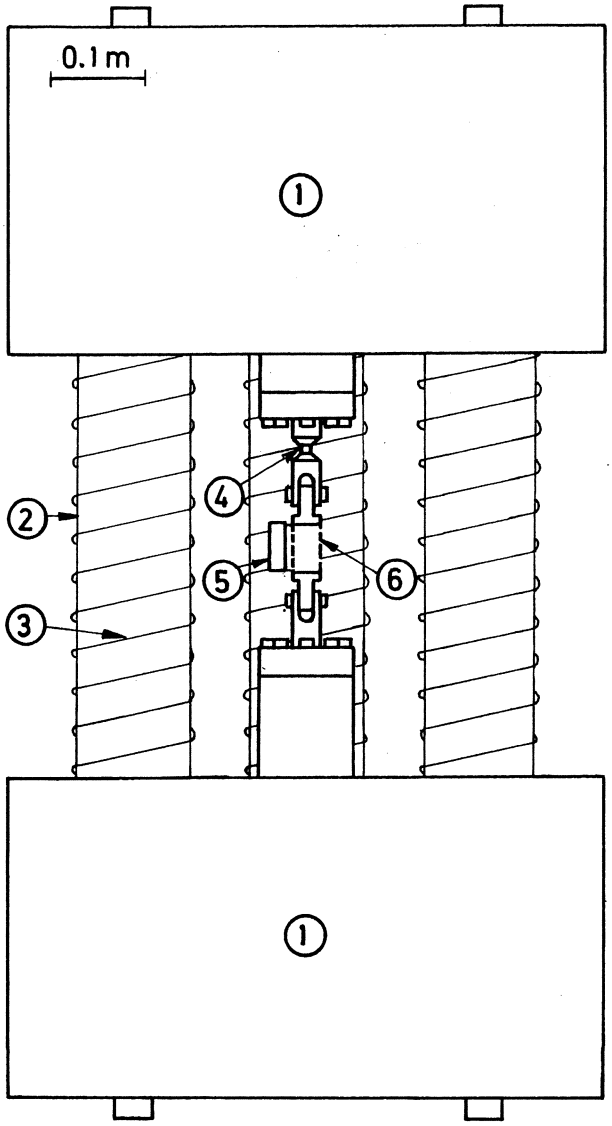

Fig 8.5 A stiff tensile testing machine for determination of the complete stress-deformation curve. 1=concrete block, 2=aluminium column, 3=heating element, 4=strain gauges for load registration, 5=inductive deformation transducer for deformation registrations, 6=specimen.

the deformations are registered by inductive deformation transducers, which are fixed directly on the specimen. During the test the aluminium columns are insulated with mineral wool in order to keep the temperature around the specimen constant, see Fig 8.7.

Coils of tubes (inner diameter=4 mm) surround the aluminium columns and kerosene tempered by a thermostat can circulate in the tubes. This makes it possible to keep the temperature in the aluminium columns constant during the time necessary (about 1 h) to obtain a sufficiently strong joint between the specimen and the holders and to cool the column during the test and thereby

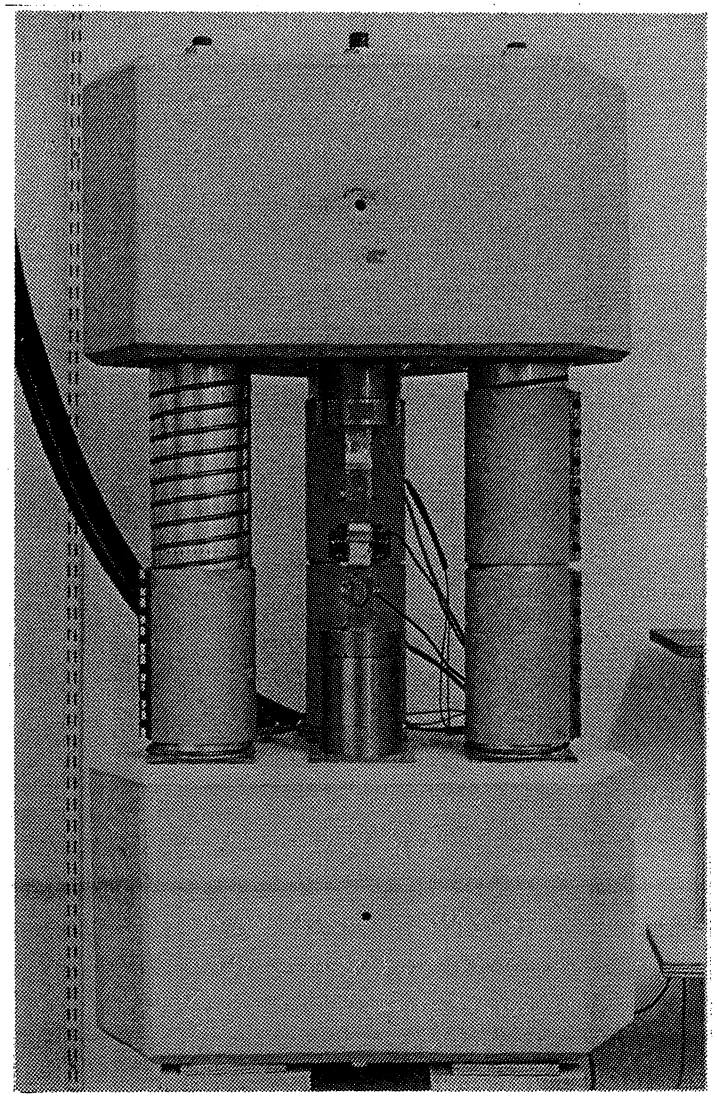

Fig 8.6 The stiff tensile testing machine. One of the heating elements is removed and the coils of cooling tubes can be seen on the left aluminium column.

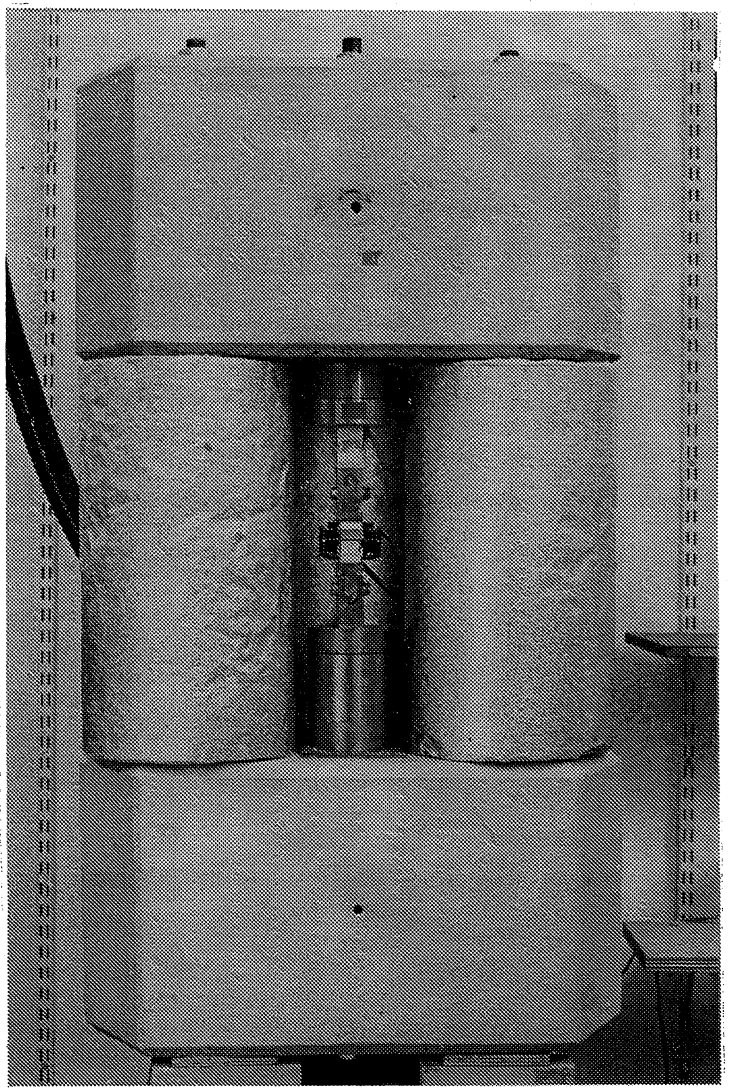

Fig 8.7 During tests the aluminium columns are insulated with mineral wool.

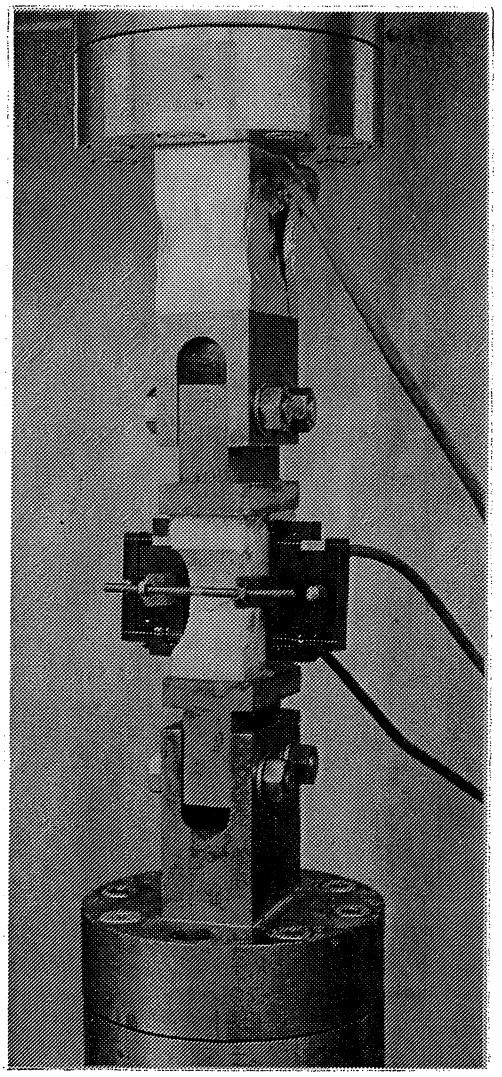

Fig 8.8 The specimen between the holders in the stiff tensile testing machine. The inductive deformation transducers are attached directly on the specimen.

cause unloading of the specimen. The columns can also be cooled when a test is finished, which greatly decreases the required time between two tests.

The thermal coefficient of expansion for aluminium is 24×10^{-6} K^{-1} and the deformation of the testing machine will be 1 mm if the temperature in the 450 mm long aluminium columns is increased by 93 K. As the temperature of aluminium can be raised to at least 200-300^{o}C without losing its elastic behaviour at low stresses, the deformation capacity of the testing machine is at least 2 mm. This can be compared with the deformation capacity necessary to follow the complete tensile stress-deformation curve for concrete, which is normally less than 0.2 mm.

The maximum effect for the 6 heating elements (two on each column) is 2,200 W. If all this energy was absorbed by the columns then the increase of the temperature would be about 6 K/s (the density of aluminium is 2,700 kg/m^3 and the specific heat capacity is 880 Ws/kg K), which corresponds to about 38 μm/min. In reality some of the energy is lost and the deformation velocity for the testing machine can be chosen, by varying the effect, between 0 and 30 μm/min. Of course the loading velocity can be increased if other heating elements are used.

In Fig 8.8 it is shown how the specimen is fixed between the supports by using an adhesive (type Epoxy). The part of the holder closest to the specimen is fixed to the other part of the holder by frictional forces caused by clamping bolts. This means that the gap between the holders can be adjusted, which is necessary when attaching the specimen.

When the specimen is fixed in the testing machine by using an adhesive, it is necessary to use a necked specimen, see 7.2. However, even if a necked specimen is used it is difficult to obtain a sufficiently strong joint if the specimen is wet. This problem is solved if the ends of the specimen are allowed to dry in the air for a couple of hours before the time for the test, while all the other surfaces are insulated by plastic foil. This method makes it possible to keep the narrow section of the necked specimen wet and the end surfaces dry. Before this drying process the ends of the specimen ought to be sandpapered in order to remove the thin layer of weak cement paste, which always exists on the surface of concrete.

8.4 Experimental determination of the σ-w curve for concrete

8.4.1 Testing procedure

By use of the stiff tensile testing machine presented in 8.3, stable tensile tests were carried out on a number of concrete qualities. In order to obtain a stable fracture and to get a sufficiently strong joint between the specimen and the holders in the testing machine, it is necessary to use small, necked specimens. For this reason the specimen type denoted III in Fig 7.15 was used in most tests. The deformations were measured on two opposite sides of the specimen by use of two inductive deformation transducers (gauge length 40 mm) and the mean value was registered. The deformation velocity was about 20 μm/min, which means that the duration of each test was 5-10 minutes.

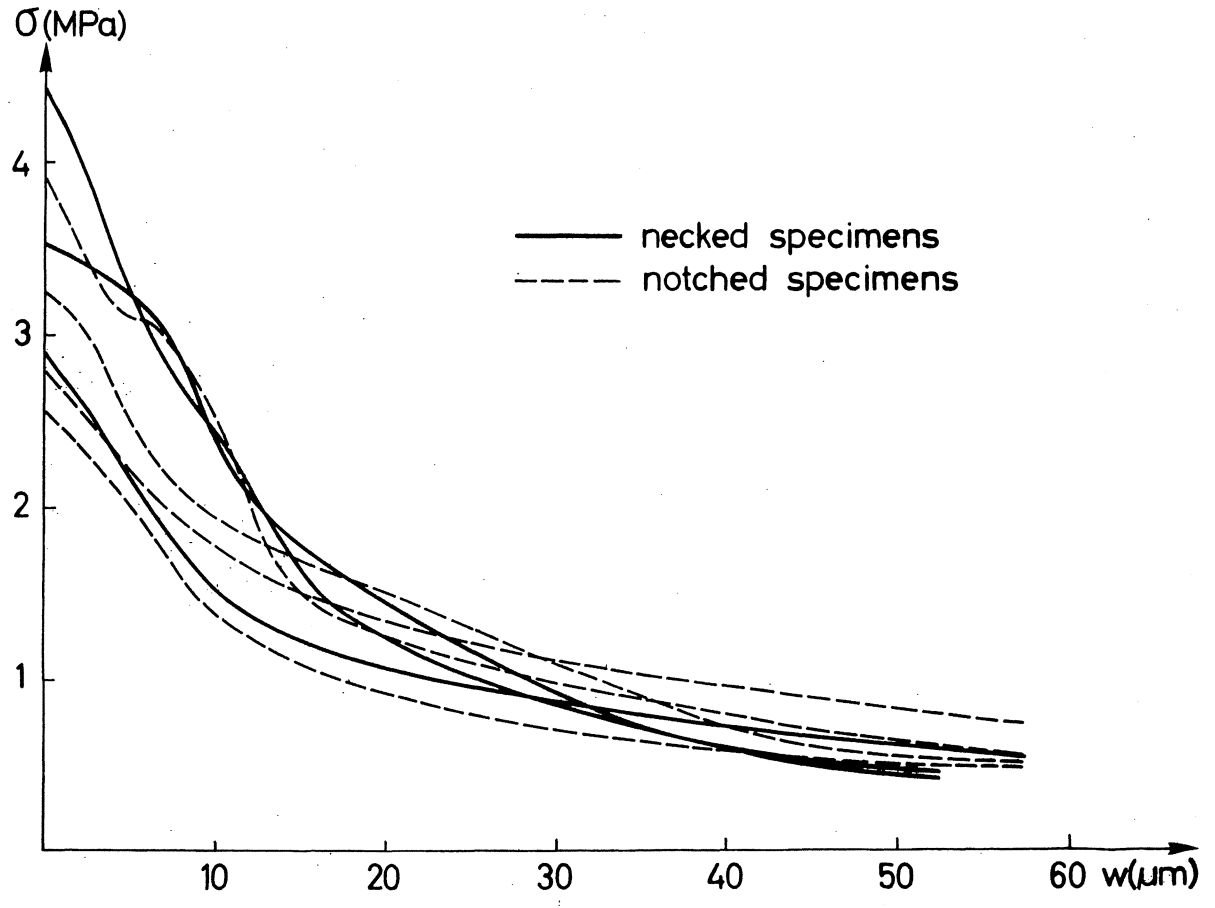

Fig 8.9 σ-w curves for necked and notched specimens respectively for the concrete quality in Table 7:1 (28 days). The specimens correspond to type III and type IV in Fig 7.15.

The shape of the stress-deformation curve (σ-δ curve) is naturally affected by the geometry of the specimen. In order to study how the shape of the specimen affects the σ-w curve, stable tensile tests were carried out on necked and notched specimens respectively, corresponding to the specimen types III and IV in Fig 7.15. The σ-w curves were determined according to the method presented in 8.1. These tests in fact are identical to the tensile tests presented in 7.4.4 and Fig 7.18. The concrete quality used is presented in Table 7:1 and the tests were performed when the concrete was 28 days old.

The results are presented in Fig 8.9 and it seems, even if the scatter is wide, as though there are no significant differences between the σ-w curves representing the two specimen geometries. The results in Fig 8.9 are in good agreement with the fact that concrete is normally relatively notch insensitive when small specimens and small notch depths are concerned, see 6.2. This implies that the σ-w curves are representative for the material, even if the curves are determined on notched specimens.

8.4.2 Materials and mix proporptions

Tests were carried out in order to study the effect of the water-cement-ratio, the maximum aggregate particle size and the age of the concrete on the σ-w curve. The four concrete qualities tested are presented in Table 8:1.

Table 8:1 The concrete qualities used in the tests.

		Mix 1	Mix 2	Mix 3	Mix 4
Cement (ordinary Portland)	kg/m^3	370	296	296	370
Water	kg/m^3	185	207	207	185
Aggregate	kg/m^3	1755	1755	1755	1755
Max aggr particle size	mm	8	8	2	8
Age at the testing	days	28	28	28	7
Water-cement-ratio		0.5	0.7	0.7	0.5

8.4.3 Preparation of specimens

For each concrete quality three specimens were cast in steel moulds. The specimens were kept in lime saturated water (+20°) until one day before testing. During the last day the ends of the specimens were allowed to dry while the other surfaces were insulated by plastic foil. The plastic foil was not removed until the start of the test, i.e. the specimens were also insulated during the time in the testing machine when the adhesive was hardening. The ends of the specimens were sandpapered one day before the test.

8.4.3 Results and discussion

Fig 8.10 shows the three stress-deformation curves for the concrete quality corresponding to mixture 4 in Table 8:1. When measuring the deformations a 40 mm effective gauge length was used. As can be seen in the Figure, the concrete is able to transfer stress even when it is considerably deformed and the curves differ completely from σ-δ curves for linear elastic materials. It can also be observed that the descending parts of the curves are far from being straight lines.

In Fig:s 8.11-8.13 σ-δ curves for different concrete qualities are shown. Each curve represents the mean value of three specimens. The values of the tensile strength (f_t) and the fracture energy (G_F) corresponding to these σ-δ curves are slightly higher than expected compared with the values in 7.5.4. However, the composition of the concretes used for the stable tensile test is different

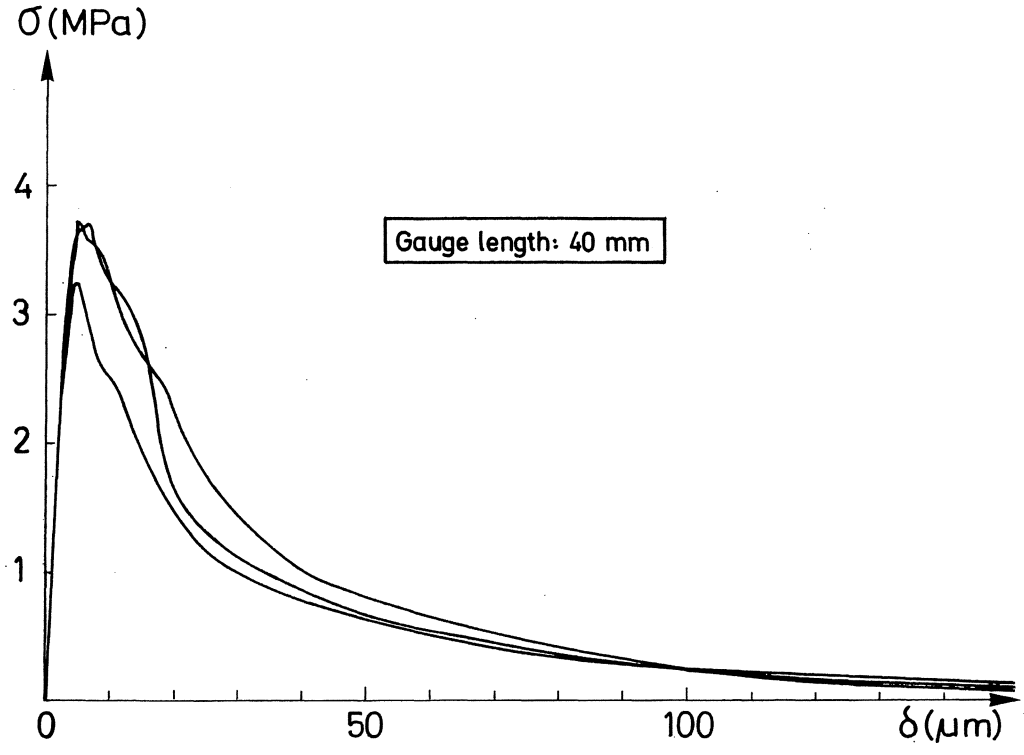

Fig 8.10 Stress-deformation curves for the concrete quality corresponding to mixture 4 in Table 8:1.

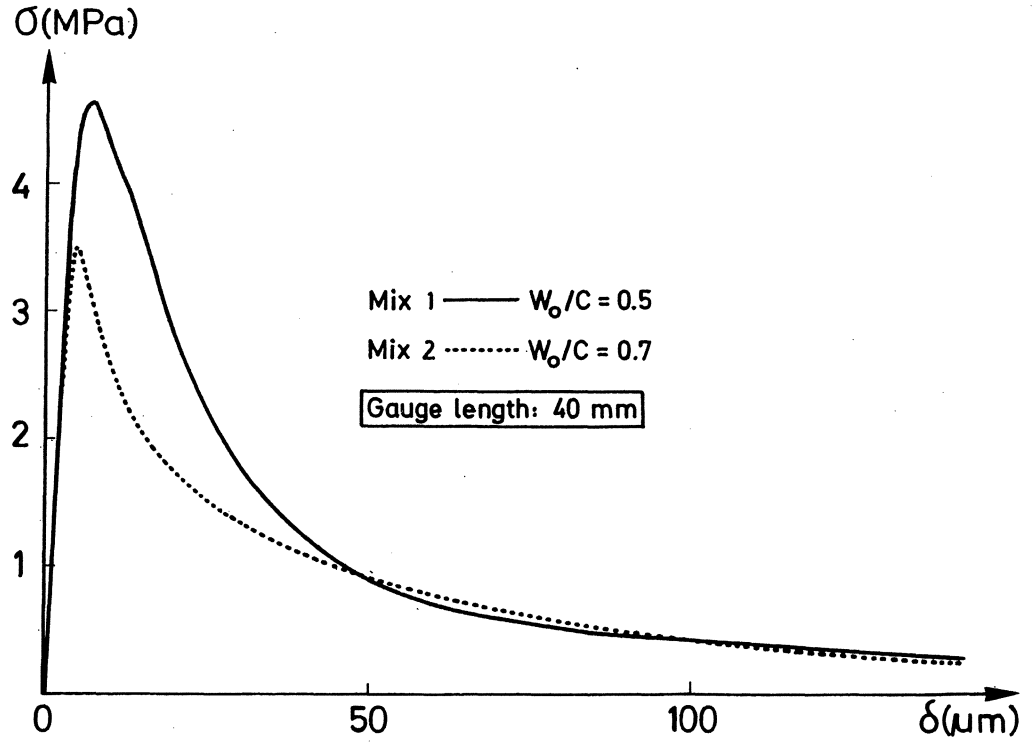

Fig 8.11 Mean stress-deformation curves for concrete qualities with different water-cement ratios (mix 1 and mix 2 in Table 8:1).

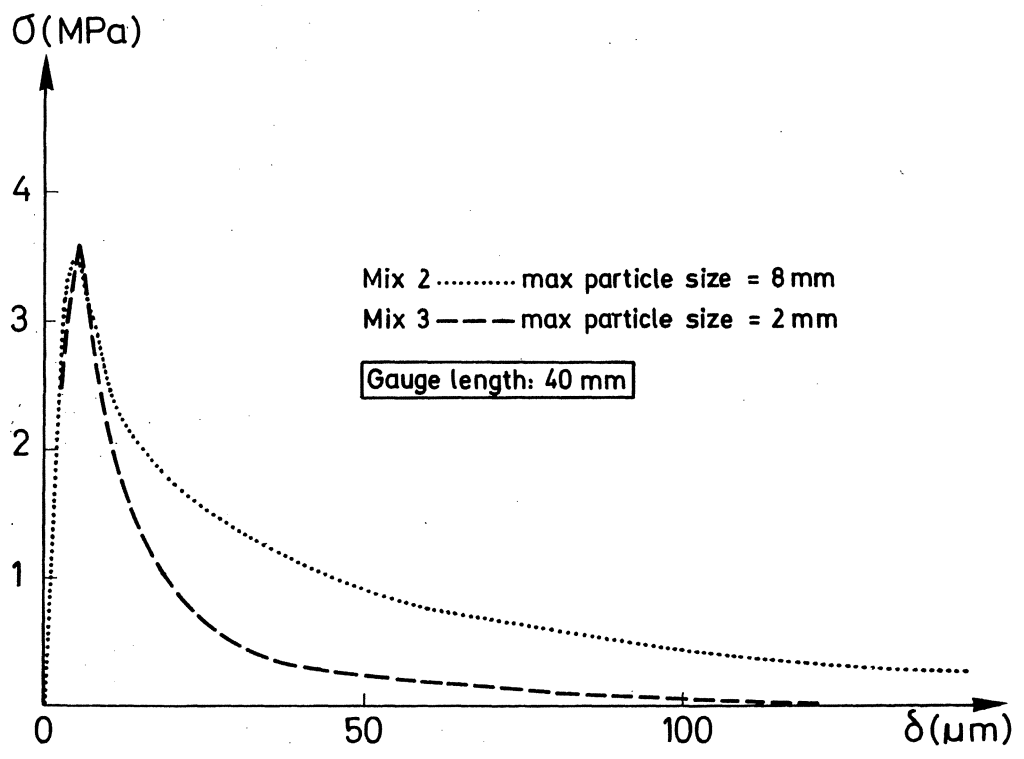

Fig 8.12 Mean-stress-deformation curves for concrete qualities with different maximum aggregate particle sizes (mix 2 and mix 3 in Table 8:1).

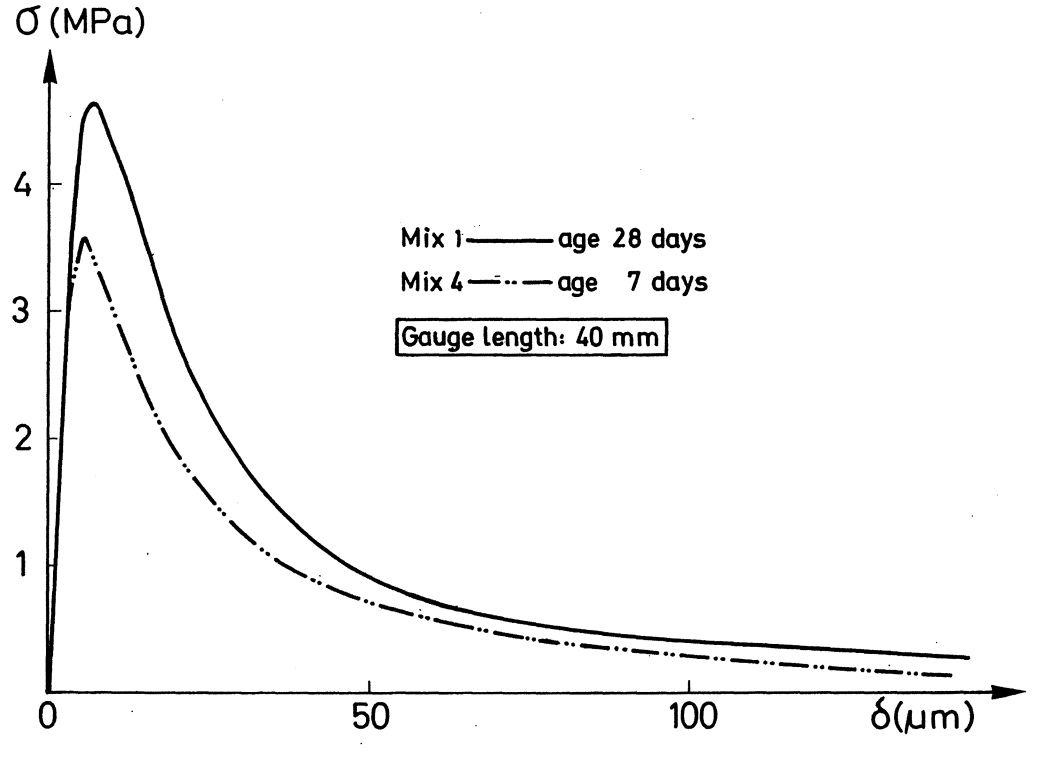

Fig 8.13 Mean stress-deformation curves representing different ages of the concrete (mix 1 and mix 4 respectively).

compared with the concretes used in 7.5. The tensile tests for each concrete quality are only carried out on three specimens and this of course gives rise to rather uncertain values of f_t and G_F, which is another possible explanation for the differences between the results from the two tests.

In Fig 8.11 curves representing concrete qualities with different water-cement-ratios are presented (mix 1 and mix 2 in Table 8:1). The curves differ in the beginning but when the deformation exceeds 50 μm they become almost identical.

The curves in Fig 8.12 represent concrete qualities with different maximum particle sizes (mix 2 and mix 3 respectively). The main difference between the curves is that the concrete with coarse aggregate seems to be able to transfer stress at higher deformations than the concrete with fine aggregate. This indicates that the stress transferring capability at high deformations is due to frictional forces when the coarse aggregate particles are extracted from the cement paste. These tests are carried out on concretes where the aggregate particles have a higher strength than the cement paste and consequently the aggregate particles are extracted from the cement paste when a crack propagates. For concretes where the strength of the cement paste is higher than the strength of the aggregate (for example lime-stone concrete, light-weight concrete or high-strength concrete) the crack will pass through the aggregate particles and it is then probable that these materials will have a lower stress transferring capability at high deformations than materials where the aggregate particles are extracted from the cement-paste.

In Fig 8.13 curves representing different ages of the concrete are presented. The effect of decreasing age on the σ-δ curve seems to be similar to the effect of increasing water-cement-ratio, compare Fig 8.11.

In order to describe the properties of the fracture zone it is not the σ-δ curves but the σ-w curves that are of interest. In Fig 8.14 the σ-w curves for the four concrete qualities used in the test are presented.

In Fig 8.15 the σ-w curves are shown in an alternative way; σ and w on the axes in Fig 8.14 are replaced by σ/f_t and w/w_c, i.e. Fig 8.15 shows the shape functions ($h(w/w_c)$) of the curves according to (4:14). In the Figure a σ-w curve approximated with two straight lines is also presented and this curve is identical to the σ-w curve (C) in Fig 6.3. For this approximation of the σ-w curve w_c is $3.6\ G_F/f_t$ and this expression for w_c has also been used for the real σ-w curves. As can be seen in the Figure, the shapes of the σ-w curves for the four different concrete qualities are about the same and the two-line approxi-

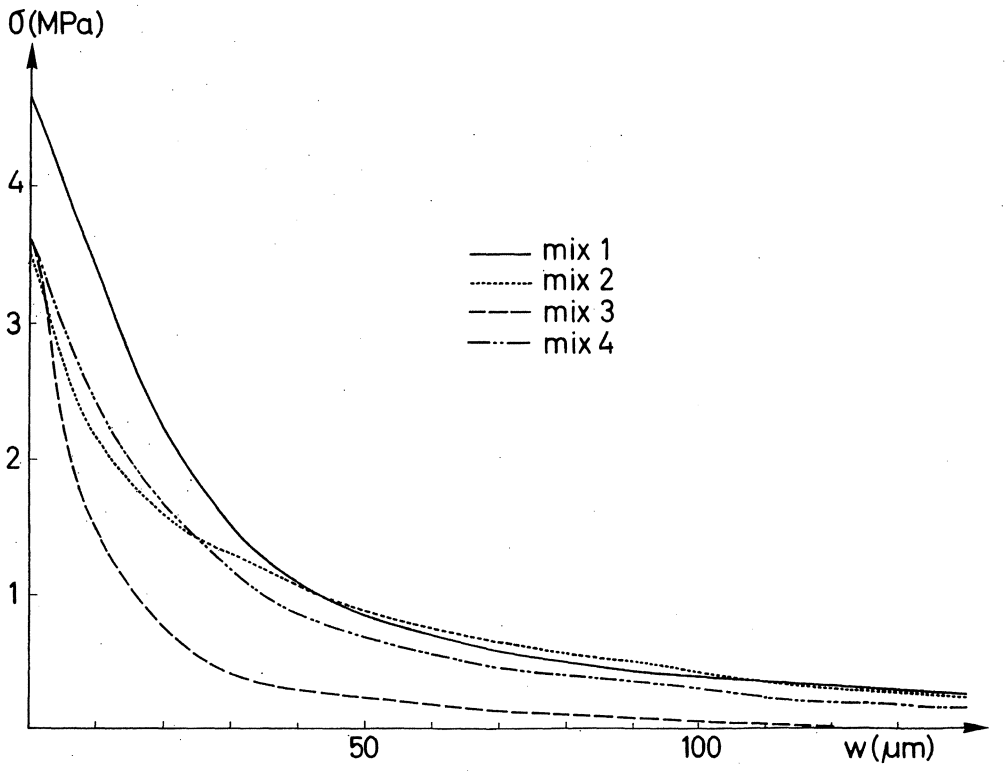

Fig 8.14 σ-w curves for the four concrete qualities presented in Table 8:1.

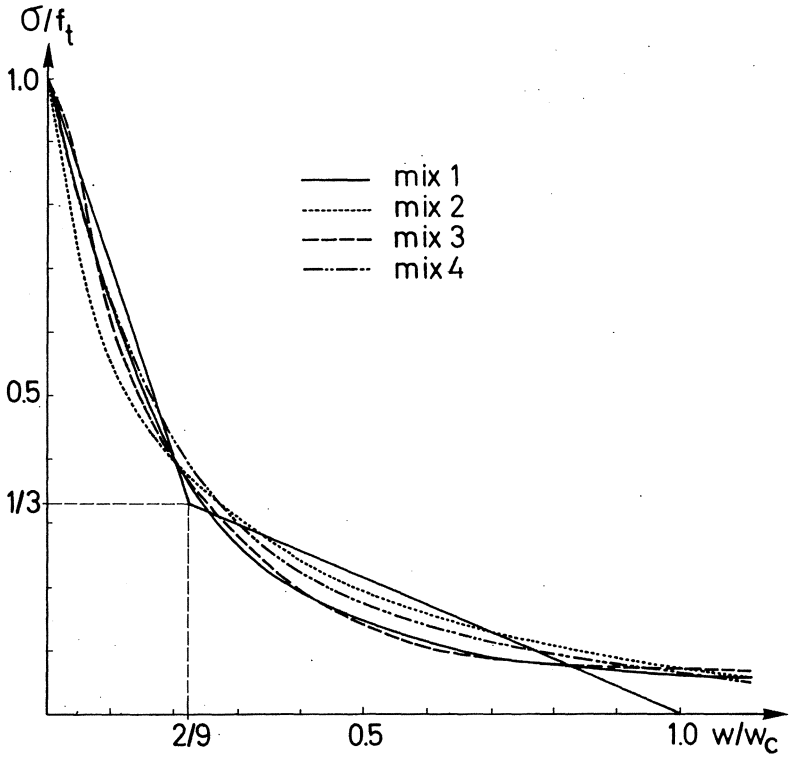

Fig 8.15 σ/f_t as function of w/w_c for the four concrete qualities presented in Table 8:1. The σ-w curve approximated with two straight lines corresponds to the curve in Fig 6.3.

mation of the σ-w curve shown in the Figure seems suitable for these concrete qualities.

For all the concrete qualities used in the test the aggregate particles are extracted from the cement-paste at crack propagation. The shape of the σ-w curve may be different if the crack passes through the aggregate particles. However, the shape of the σ-w curves shown in Fig 8.15 ought to be realistic for most concrete qualities and this means that the σ-w curve can be determined when the tensile strength (f_t) and the fracture energy (G_F) are known, see 4.5. A consequence of this is that no "complicated" stable tensile tests have to be carried out in order to determine the σ-w curve for concrete but the curve can be determined by use of the "simple" f_t- and G_F-tests presented in Chapter 7.

In Fig 8.16 load-deflection curves for a notched beam subjected to three-point bending are shown. The unbroken lines represent experimental results from the

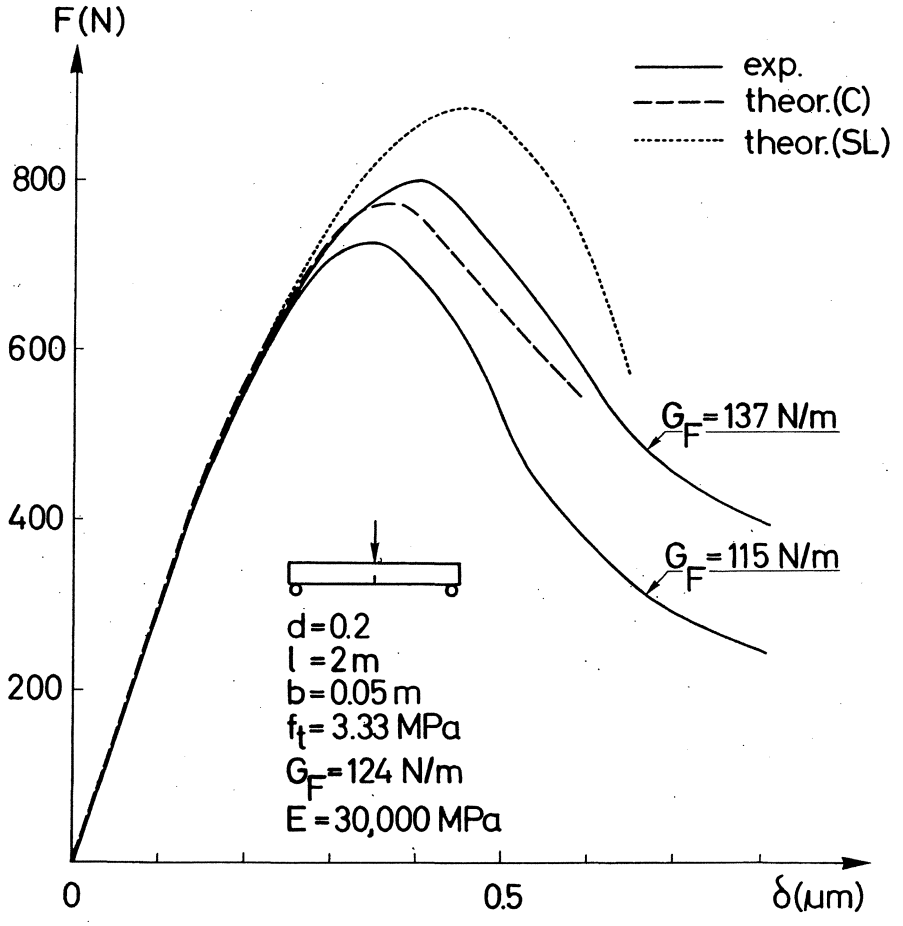

Fig 8.16 Experimental and theoretical load-deflection curves for three-point bend tests on notched beams. In the calculations the σ-w curve was approximated according to Fig 6.1 (SL) and Fig 6.3 (C) respectively.

tests on the 200 mm deep beams presented in 7.4.4 and Fig 7.18. In the tests six beams were tested in order to determine the fracture energy and the two experimental curves in Fig 8.16 correspond to the two beams, which produced the highest and the lowest value of the fracture energy respectively. The theoretical curves, calculated by means of the Fictitious Crack Model, correspond to two different approximations of the σ-w curve; the single line approximation (SL) according to Fig 6.1 and the two line approximation (C) according to Fig 6.3 (which is identical to the approximation in Fig 8.15) respectively. The mean value of G_F for the concrete quality is about 124 N/m (see test results in Fig 7.18) and f_t is about 3.33 MPa (see results in Fig 8.9, which are relevant for this concrete quality). These values were used in the calculations and the Young's modulus was assumed to be 30,000 MPa. As can be seen in the Figure the theoretical curve according to the two-line approximation of the σ-w curve is in good agreement with the experimental curves. Together with calculation results presented in Chapter 6 this implies that the shape of the σ-w curve presented in Fig 6.3 and Fig 8.15 is suitable for normal concrete qualities.

9 REFERENCES

Andersson, H. and H. Bergkvist (1970). Analysis of a non-linear crack model. *J. Mech. Phys. Solids*, Vol 18, pp. 1-28.

Barenblatt, G.J. (1962). The mathematical theory of equilibrium crack in the brittle fracture. *Advance in Applied Mechanics*, Vol 7, pp. 55-125.

Bastgen, K.J. and V. Hermann (1977). Experience made in determining the static modulus of elasticity of concrete. *Materiaux et Constructions*, Vol 10, pp. 357-364.

Bažant, Z.P. and L. Cedolin (1979). Blunt crack band propagation in finite element analysis. *J. of Engineering Mechanics Division*, Vol 105, No EM 2, pp. 297-315.

Brown, J.H. (1972). Measuring the fracture toughness of cement paste and mortar. *Magazine of Concrete Research*, Vol 24, pp. 185-196.

Brown, J.H. and C.D. Pomeroy (1973). Fracture toughness of cement paste and mortars. *Cem. and Concr. Res.*, Vol 3, pp. 475-480.

Brown, W.F. and J.E. Srawley (1967). *Plane Strain Crack Toughness Testing of High Strength Metallic Materials*. ASTM-STP 410.

Carlsson, J. (1976). *Fracture Mechanics*. Ingenjörsförlaget, Katrineholm, Sweden (in Swedish).

Carpinteri, A. (1981). Experimental determination of fracture toughness parameters K_{IC} and J_{IC} for aggregative materials. *Advances in Fracture Research*. 5th International Conference on Fracture, Cannes 29 March-2 April, 1981. pp. 1491-1498. Ed. D. Francois, Pergamon Press.

Chhuy, S., M. E. Benkirane, J. Baron and D. Francois (1981). Crack propagation in prestressed concrete. Interaction with concrete. *Advances in Fracture Research*. 5th International Conference on Fracture, Cannes 29 March-2 April, 1981. pp. 1507-1514. Ed. D. Francois, Pergamon Press.

Cooper, G.A. (1977). Optimization of the three-point bend test for fracture energy measurement. *J. of Materials Science*, Vol 12, pp. 277-289.

Dugdale, D.S. (1960). Yielding of steel sheets containing slits. *J. of Mech. Phys. Solids*, Vol 8, pp. 100-104.

Entov, V.M. and V.T. Yagust (1975). Experimental investigation of laws governing quasi-static development of macrocracks in concrete. *Mechanics of Solids*, Vol 10, pp. 87-95.

Evans, R.H. and M.S. Marathe (1968). Microcrackning and stress-strain curves for concrete in tension. *Materiaux et Constructions*, No 1, pp. 61-64.

Gjørv, D.E., S.I. Sørensen and A. Arnesen (1977). Notch sensitivity and fracture toughness of concrete. *Cem. and Concr. Res.*, Vol 7, pp. 333-344.

Griffith, A.A. (1921). The phenomena of rupture and flow in solids. *Phil. Trans. Roy. Soc.*, series A221, pp. 163-198.

Gustafsson, P.J. (1977). *Fracture Mechanics Applied to Lightweight Concrete and Fibre-reinforced Concrete.* Report TVBM-5001, Division of Building Materials, University of Lund, Sweden (in Swedish)

Halvorsen, G.T. (1980). J-integral study of steel fibre reinforced concrete. *The Int. J. of Cement Composites*, Vol 2, pp. 13-22.

Harris, B., J. Varlow and C.D. Ellis (1972). The fracture behaviour of fibre reinforced concrete. *Cem. and Concr. Res.*, Vol 2, pp. 447-461.

Heilmann, H.G., H.H. Hilsdorf and K. Finsterwalder (1969). Festigkeit und Verformung von Beton unter Zugspannungen. *Deutscher Ausschuss für Stahlbeton*, Heft 203, W. Ernst & Sohn, Berlin (in German).

Hernelind, J. and L.G. Pärletun (1974). *EUFEMI* (manual for FEM-calculations). Div. of Solid Mechanics, Lund Institute of Technology, Sweden (in Swedish).

Higgins, D.D. and J.E. Bailey (1976). Fracture measurements on cement paste. *J. of Materials Science*, Vol 11, pp. 1995-2003.

Hillemeier, B. and H.K. Hilsdorf (1977). Fracture mechanics studies on concrete compounds. *Cem. and Concr. Res.* Vol 7, pp. 523-536.

Hillerborg, A., M. Modéer and P.E. Petersson (1976). Analysis of crack formation and crack growth in concrete by means of fracture mechanics and finite elements. *Cem. and Concr. Res.*, Vol 6, pp. 773-782.

Hillerborg et al (1977). *Compendium in Building Materials AK.* Lund Institute of Technology, Division of Building Materials, Lund, Sweden (in Swedish).

Hillerborg, A. (1980). Analysis of fracture by means of the fictitious crack model, particulary for fibre reinforced concrete. *Int. J. of Cement Composites*, Vol 2, pp. 177-184.

Hillerborg, A. and P.E. Petersson (1981). Fracture mechanical calculations, test methods and results for concrete and similar materials. *Advances in Fracture Research.* 5th International Conference on Fracture, Cannes 29 March-2 April, 1981. pp. 1515-1522. Ed. D. Francois, Pergamon Press.

Hughes, B.P. and G.P. Chapman (1965). Direct tensile test for concrete using modern adhesives. *Bulletin RILEM*, No 26, pp. 77-80.

Hughes, B.P. and G.P. Chapman (1966). The complete stress-strain curve for concrete in direct tension. *Bulletin RILEM*, No 30, pp. 95-97.

Janson, J. and J. Hult (1977). Fracture mechanics and damage mechanics, a combined approach. *J. de Mécanique Appliquée*, Vol 1, pp. 69-84.

Janson, J. (1978). Damage model for crack growth and instability. *Eng. Fracture Mechanics*, Vol 10, pp. 795-806.

Johnston, C.D. and E.H. Sidwell (1968). Testing concrete in tension and in compression. *Mag. of Conc. Res.*, Vol 20, pp. 221-228.

Kachanov, L.M. (1958). Time of the rupture process under creep conditions. *Izv. Akad. Nauk SSSR, Otd. Tekh. Nauk*, Vol 8, pp. 26-31.

Kadlecek, V. and Z. Spetla (1965). Effect of size and shape of test specimens on the direct tensile strength of concrete. *Bulletin RILEM*, No 36, pp. 175-184.

Kaplan, M.F. (1961). Crack propagation and the fracture of concrete. *J. of the American Concrete Institute*, Vol 58, pp. 591-609.

Knott, J.F. (1979). *Fundamental of Fracture Mechanics*. 3rd edition, Butterworths, London.

Mai, Y.W. (1979).Strength and fracture properties of asbestos-cement mortar composites. *J. of Materials Science*, Vol 14, pp. 2091-2102.

Mai, Y.W., R.M.L. Foote and B. Cotterell (1980). Size effects and scaling laws of fracture in asbestos cement. *The Int. J. of Cement Composites*, Vol 2, pp. 23-34.

Mayer, H. (1967). Die Berechnung von Durchbiegung von Stahlbetonbauteilen. *Deutcher Ausschuss für Stahlbeton*. W. Ernst & Sohn, Berlin (in German).

Mazars, J. (1981). Mechanical damage and fracture of concrete structures. *Advances in Fracture Research*. 5th International Conference on Fracture, Cannes 29 March-2 April, 1981. pp. 1499-1506. Ed. D. Francois, Pergamon Press.

Mindess, S. and J.S. Nadeau (1976). Effect of notch width on K_{IC} for mortar and concrete. *Cem. and Concr. Res.*, Vol 6, pp. 529-534.

Mindess, S., F.V. Lawrence and C.E. Kesler (1977). The J-integral as a fracture criterion for fibre reinforced concrete. *Cem. and Concr. Res.*, Vol 7, pp. 731-742.

Mindess, S. and S. Diamond (1980). A preliminary SEM study of crack propagation in mortar. *Cem. and Concr. Res.*, Vol 10, pp. 509-519.

Moavenzadeh, F. and R. Kuguel (1969). Fracture of concrete. *J. of Materials*, Vol 4, pp. 497-519.

Modéer, M. (1979). *A Fracture Mechanics Approach to Failure Analyses of Concrete Materials*. Report TVBM-1001, Division of Building Materials, University of Lund, Sweden.

Nadeau, J.S, S. Mindess and J.M. Hay (1974). Slow crack growth in cement paste. *J. of the American Ceramic Soc.*, Vol 57, pp. 51-54.

Naus, D. and J. Lott (1968). *Fracture Toughness of Portland Cement Concretes*. Report No 314, Dep. of Theoretical and Applied Mechanics, University of Ill., Urbana, Ill.

Naus, D.J. and J.L. Lott (1969). Fracture toughness of portland cement concretes. *J. of the American Concr. Inst.*, Vol 66, pp. 481-489.

Ohigashi, T (1978). Measurement of effective fracture energy of glass fibre reinforced cement. *Testing and Test Methods of Fibre Cement-Composites*. RILEM Symposium, 5th-7th April 1978, Ed. R.N. Swamy, pp. 67-78.

Petersson, P.E. (1980a). Fracture mechanical calculations and tests for fibre reinforced cementitious materials. *Advances in Cement-matrix Composites*. Proceedings, Symposium L, Materials Research Society, Annual meeting, Boston November 17-18, 1980, pp. 95-106.

Petersson, P.E. (1980b). Fracture energy of concrete: Method of determination. *Cem. and Concr. Res.*, Vol 10, pp. 78-89.

Petersson, P.E. (1980c). Fracture energy of concrete: Practical performance and experimental results. *Cem. and Concr. Res.*, Vol 10, pp. 91-101.

Petersson, P.E. and P.J. Gustafsson (1980). A model for calculation of crack growth in concrete-like materials. *Numerical Methods in Fracture Mechanics*, pp. 707-719. Pineridge Press, Swansen, U.K.

Petersson, P.E. (1981). Direct tensile tests on prismatic concrete specimens. *Cem. and Concr. Res.*, Vol 11, pp. 51-56.

Pfeiffer, G. (1968). *Berechnung und Bemessung von wandartigen Trägern*. Werner-Verlag, Düsseldorf (in German).

Rice, J.R. (1968). Path independent integral and approximate analysis of strain concentration by notches and cracks. *J. of Applied Mechanics, Transactions*, ASME, Vol 35, pp. 379-386.

Rice, J.R., P.C. Paris and J.G. Merkle (1973). Some further results of J-integral analysis and estimates. *Progress in Flow Growth and Fracture Toughness Testing*, ASTM STP 536, pp. 231-245.

Sabnis, G.M. and S.M. Mirza (1979). Size effects in model concretes? *J. of Struct. Div., ASCE*, Vol 105, pp. 1007-1020.

Shah, S.P. and F.J. Mc Garry (1971). Griffith fracture criterion and concrete. *J. of the Engineering Mechanics Division*, December 1971, pp. 1663-1676.

Sok, C (1978). Etude de la propagation d'un fissure dans un béton non armé. *Bull. Liaison Labo. P. et Ch.*, Vol 98, pp. 73-84 (in French).

Sok, C., J. Baron and D. Francois (1979). Mecanique de la rupture appliquee au beton hydralique. *Cem. and Concr. Res.*, Vol 9, pp. 641-648 (in French).

Strange, P.C. and A.H. Bryant (1979). The role of aggregate in the fracture of concrete. *J. of Materials Science*, Vol 14, pp. 1863-1868.

Velazco, G., K. Visalvanich and S.P. Shah (1980). Fracture behaviour and analysis of fibre reinforced concrete beams. *Cem. and Concr. Res.*, Vol 10, pp. 41-51.

Vinkeloe, R. (1962). Prüfverfahren zur ermittlung des dynamischen Elastizitätsmodulus von Betonprismen. *Tonindustrie Zeitung*, Vol 86, pp. 272-276 (in German).

Walsh, P.F. (1972). Fracture of plain concrete. *Indian Concr. Journal*, Vol 46, pp. 469-476.

Wecharatana, M. and S.P. Shah (1980). Double torsion tests for studying slow crack growth of Portland cement mortar. *Cem. and Concr. Res.*, Vol 10, pp. 833-844.

Welch, G.B. and B. Haisman (1969). The application of fracture mechanics to concrete and the measurement of fracture toughness. *Materiaux et Constructions*, Vol 2, pp. 171-177.

Wright, P.J.F. (1952). The effect of the method of test on the flexural strength of concrete. *Mag. of Concr. Res.*, Vol 4, pp 67-76.

Ziegeldorf, S., H.S. Müller and H.K. Hilsdorf (1980). A model law for the notch sensitivity of brittle materials. *Cem. and Concr. Res.*, Vol 10, pp. 589-599.